Copper dyes for dye-sensitized solar cells

Wills, Kathryn

Award date:
2014

Awarding institution:
University of Bath

Copper dyes for dye-sensitized solar cells

Kathryn Alison Wills

A thesis submitted for the degree of Doctor of Philosophy

University of Bath
Department of Chemistry

April 2014

Signed on behalf of the Faculty of Science

_____

Table of Contents

Acknowledgments

There are many people I would like to thank for their support, guidance and friendship over the course of this PhD. Some are based in Bath and have been involved in the day-to-day routine of this work; some have lived further afield but their contribution is no less valuable. Firstly I would like to recognise my excellent supervisors; Petra Cameron, Matthew Jones and Simon Lewis. Their guidance and input has been invaluable and I am thankful for all their help in what was a very interdisciplinary project. Thanks also go to our collaborators at CINVESTAV in Mexico for their computational work; Gerko Oskam, Humberto J. Mandujano-Ramírez and Gabriel Merino, and to Neil Robertson and Tracy Hewat at the University of Edinburgh for their assistance with the copper biquinoline fluorescence work.

I would also like to say thank you to the various group members over the years that made the days in the lab and office enjoyable and have been excellent colleagues and friends; Mario, Monika, Anthony, Paul, Matthew, Julia, Catherine, Tom, Kenneth, Shane, Becky, Ellie, Nikte, Huaining, Ralf, Adam and Wentao. Also, to Nat who worked brilliantly on the copper dye project with me for her final year undergraduate project. A particular mention goes to those close friends who were around in the last few months for coffee drinking and helpful chats when it was tough going, especially Catherine, Adam and Becca.

I would also like to thank the Doctoral Training Centre and all involved with it for providing me with some fantastic opportunities and a great support network over the years. Very importantly, many thanks go to the EPSRC for funding the research.

On a personal level, I would like to thank Nick and his family for unreservedly encouraging me to apply and take up my place in the DTC. I am also very grateful to my parents, brother, grandparents, other extended family and friends from outside of the academic world who have been so patient and supportive over the years. Your support is valued much more than you probably realise, or than I have probably ever told you!

Declaration of work done in conjunction with others

The computational experiments described in Chapter 5.7 and Chapter 7.3 were carried out by collaborators at CINVESTAV IPN, Dept. Fis Aplicada, Merida 97310, Yucatan, Mexico; Humberto J. Mandujano-Ramírez, Gabriel Merino and Gerko Oskam.

The synthesis and study of complex 1, described in Chapter 4, was done in conjunction with a final year undergraduate project student; Natalie Lang.

The emission spectroscopy data for complexes 20 and 40 was acquired using equipment at the University of Edinburgh with the assistance of Tracy Hewat and Neil Robertson.

The TiO_2 film thickness measurements quoted in Chapter 7 were carried out by Adam Pockett and Ralf Niemann.

Abstract

This thesis studies the application of copper(I) complexes as the sensitizing component of dye sensitized solar cells (DSCs). Ruthenium(II) polypyridyl complexes have been widely studied and shown great success for the past two decades; however the metal is rare and expensive. A copper(I) based DSC could offer a viable alternative to using ruthenium(II) dyes, taking into account the cost and sustainability advantages.

Interest in copper(I) DSCs has reignited over the past five years and the work in this thesis begins by reproducing the synthesis of one of the first reported complexes, [Cu(6,6'-dimethyl-2,2'-bipyridine-4,4'-dicarboxylic acid)$_2$][Cl]. A more detailed study of the dye and its properties will be described, including assessing the effect of TiO_2 film dye time on DSC performance, electrochemical studies and coupling the dye with a $Co^{2+/3+}$ mediator. In the following chapters, improvements to the basic 2,2'-bipyridine framework are investigated. An experimental and computational investigation with a [Cu(2,2'-biquinoline-4,4'-dicarboxylic acid)$_2$][$HNEt_3$] complex is presented, where the 2,2'-biquinoline ligand has been chosen as a bulkier, more conjugated alternative to the 2,2'-bipyridine ligand. Although DSC efficiencies with this complex are comparatively low, an investigation into possible reasons for this is described.

This thesis then considers functionalisation of a 2,2'-bipyridine ligand with halide and thiophene substituents. Several new ligands and copper(I) complexes are described and characterised. A top DSC efficiency of 1.41% was obtained with a [Cu(6,6'-dimethyl-[2,2'-bipyridine]-4,4'-diyl)bis(thiophene-2-carboxylic acid)$_2$][PF_6] dye. The synthetic route towards this complex and an analysis of its features, such as emissive behaviour, electrochemical properties and electron diffusion length, are described.

List of abbreviations and symbols

Chemical and experimental

Ac	acetyl
aq.	aqueous
Ar	aromatic
bipy	2,2'-bipyridine
Bu	butyl
conc.	concentrated
DMF	*N*,*N*-Dimethylformamide
DMSO	dimethylsulfoxide
Et	ethyl
Fmoc	fluorenylmethoxycarbonyl
FTO	fluorine-doped tin oxide
h	hour(s)
IPA	isopropanol
Me	methyl
min	minute(s)
O/N	overnight
rt	room temperature
s	second(s)
sat.	saturated
t-/tert-	tertiary
TBAHFP	tetrabutylammonium hexafluorophosphate (NBu_4PF_6)
4-TBP	4-tertbutylpyridine
wt	weight

Electrochemical and photochemical

$\mathbf{c_\mu}$	chemical capacitance
CE	counter electrode
CV	cyclic voltammetry/voltammogram
$\mathbf{E_{cb}}$	conduction band energy
$\mathbf{E_f}$	Fermi energy level
$\mathbf{E_{vb}}$	valence band energy
EIS	electrochemical impedance spectroscopy

E^0	standard electrode potential
$E^{0'}$	formal electrode potential
$E^{0\text{-}0}$	zero-zero transition energy
$E_{1/2}$	half wave potential
E_p^{ox}	peak oxidation potential
E_p^{red}	peak reduction potential
EQE	external quantum efficiency
eV	electron volts
FRA	frequency response analyser
HOMO	highest occupied molecular orbital
i_p^a	peak anodic current
i_p^c	peak cathodic current
IC	internal conversion
ISC	intersystem crossing
L_n	electron diffusion length
LUMO	lowest unoccupied molecular orbital
MLCT	metal to ligand charge transfer
n_c	free electron density
NHE	normal hydrogen electrode
n_t	trapped electron density
R_{ct}	charge transfer resistance
r_{rec}	recombination resistance
r_{tr}	transport resistance
RE	reference electrode
SCE	saturated calomel electrode
SHE	standard hydrogen electrode
τ_n	effective electron lifetime
WE	working electrode

Analytical and techniques

COSY	correlation spectroscopy
d	doublet
dd	double doublet
DFT	density functional theory
EPR	electron paramagnetic resonance

ESI-TOF	electrospray time-of-flight
HMBC	heteronuclear multiple-bond correlation spectroscopy
HMQC	heteronuclear multiple-quantum correlation spectroscopy
HRMS	high-resolution mass spectrometry
IR	infra-red
IPCE	incident photon to current efficiency
J	coupling constant
MALDI	matrix assisted laser desorption ionization
MHz	megahertz
m/z	mass to charge ratio
NMR	nuclear magnetic resonance
OCVD	open circuit photovoltage decay
q	quartet
s	singlet
t	triplet
TD-DFT	time-dependent density functional theory
UV	ultraviolet
Vis	visible

Photovoltaic devices

AM	air mass
DSC	dye-sensitized solar cell
FF	fill factor
I-V	current-voltage
J_{SC}	short-circuit current density
LED	light emitting diode
η	solar-to-power conversion efficiency
P_{in}	power input (solar power incident on the DSC)
P_{max}	maximum power point
PV	photovoltaic
V_{OC}	open-circuit photovoltage

Chapter 1 - Introduction

1. Introduction

This chapter briefly describes the history of photovoltaics and the context for current interest and research into non-fossil fuel derived energy sources. The structure and mechanisms of the dye-sensitized solar cell will be considered before presenting a literature review of developments in dye design and, more specifically, the use of copper(I) dyes.

1.1. Overview of photovoltaic technologies

Conversion of light energy into electricity, known as "the photovoltaic effect", was first reported in 1839 by Edmund Bequerel[1] and over the following years led to the development of the first solid state photovoltaic (PV) systems. Initially, these relied on either a layer of selenium, copper-copper oxide, lead sulfide or thallium sulfide. However, it was the rapid growth of the silicon electronics industry in the 1950s (i.e. the production of good quality silicon wafers) that resulted in PV devices producing useful amounts of power, initiating the growth of the sector as we know it today.

As the population, and thus the energy demands, of the world are forecasted to increase significantly in the coming decades, alternative, renewable, energy sources such as solar power are under widespread investigation. Energy security and availability are not the only motivators for moving away from our reliance on fossil fuels. Concern over anthropogenic climate change caused by increasing concentrations of greenhouse gases, such as carbon dioxide (CO_2), in the earth's atmosphere have resulted in international treaties (such as the Kyoto Protocol)[2] and CO_2 reduction targets being established. In the UK, national policy aims to reduce greenhouse gas emissions by 80% by 2050, relative to values from 1990.[3] In terms of energy policy, the European Union has a target to obtain 20% of its energy from renewable sources by 2020.[4]

Harnessing energy from the sun is the obvious choice when it comes to securing enough energy to meet the present and future needs of our society. It is calculated that the total power of the sun's radiation that is incident on the earth is 1.4×10^{17} W, which is around 5000 times the estimated primary power requirement for 2050.[5] The challenge is to develop PV technologies *via* scalable processes which are viable alternatives, both economically and in terms of efficiency, to fossil fuels. This has been achieved to a certain extent with silicon technologies. Despite having certain drawbacks, silicon has remained the foremost PV material over the past 50 years as the industry benefited from the advances made in the semiconductor industry. Commercially available silicon devices generally use

monocrystalline or multicrystalline silicon in a single-junction cell, where different regions are doped with either a *p*- or an *n*-type material, and operate at an efficiency of about 20%.[6] The silicon is responsible for both light absorption and charge transport and there is charge separation by the electric field created at the *p*-*n* junction. However the manufacturing costs involved for these first generation technologies have been a hindrance to their widespread implementation.[6, 7] Roughly half their cost is ascribed to the relatively thick layer (200-250 μm)[6] of high purity silicon used, required partly for mechanical reasons but also for effective sunlight absorption, which increases the weight of the cell as well as the cost.[6,8] Production of these devices is energy intensive, using high temperatures and vacuum. For these reasons there have been significant efforts dedicated to finding alternative photovoltaic devices. The current record research-cell efficiencies for all types of photovoltaic cells are collated for comparison by the National Renewable Energy Laboratory (NREL)[9] (Figure 1). NREL is the U.S. Department of Energy's main laboratory for renewable energy and energy efficiency research and development.

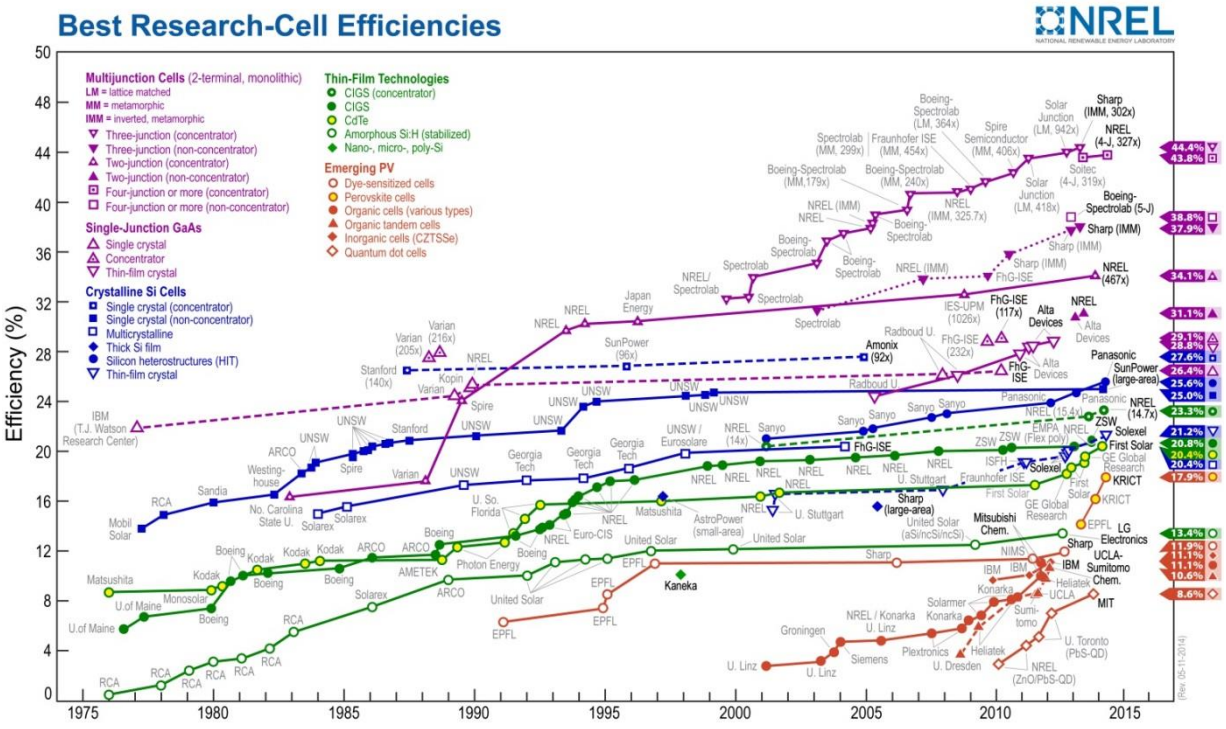

Figure 1 – Research Cell Efficiency Records, National Renewable Energy Laboratory (31/05/2014). Diagram reproduced from reference 9.

Of growing interest and importance are second generation technologies known as thin-film solar cells.[5] They are cheaper to produce than first generation devices since a thinner layer of active material is sufficient for strong light absorption (typically 1-10μm thick).[6] The cells are generally constructed by sequentially depositing layers of the semiconductors onto a substrate, such as conductive glass or plastic, *via* either chemical or electrochemical methods. The current leading materials are the II-VI semiconductor cadmium telluride (CdTe) (where II-VI refers to group in the periodic table), amorphous silicon and chalcogenide alloys such as copper indium gallium diselenide (CIGS). Laboratory efficiencies of CdTe and CIGS have now reached 19.6% and 20.4%, with these records held by the research institutes General Electric Global Research and the Swiss Federal Laboratories for Materials Science and Technology (EMPA) respectively. Despite the increasing efficiencies of these thin-film devices, material availability (such as the abundance of cadmium and tellurium), as well as the toxicity of these elements, is a key concern and likely limitation of the technology.[10] Alternatives in the field of inorganic photovoltaics include copper zinc tin sulphide (CZTS), which is similar to CIGS but with replacement of the rarer metals with more abundant ones.[5]

Third generation technologies include all those not directly related to a single *p-n* junction. For example, multi-junction cells, polymer/organic photovoltaics, quantum dot solar cells and dye-sensitized solar cells (DSCs). Multijunction solar cells are the most efficient photovoltaic structure, however their complexity of design means they are too expensive for routine applications and projects. They function by stacking together semiconductor materials with different, complementary, bandgaps so that each layer absorbs a particular region of the spectrum, hence capturing as many photons as possible. A very recent breakthrough has come in the form of perovskite solar cells. Efficiencies have rapidly progressed beyond 10% in the past couple of years[11-13] and the record efficiency for this device, certified by NREL, is a 17.9% cell from the Korean Research Institute of Chemical Technologies (KRICT). A cross-section of a perovskite cell is shown in Figure 2(a).

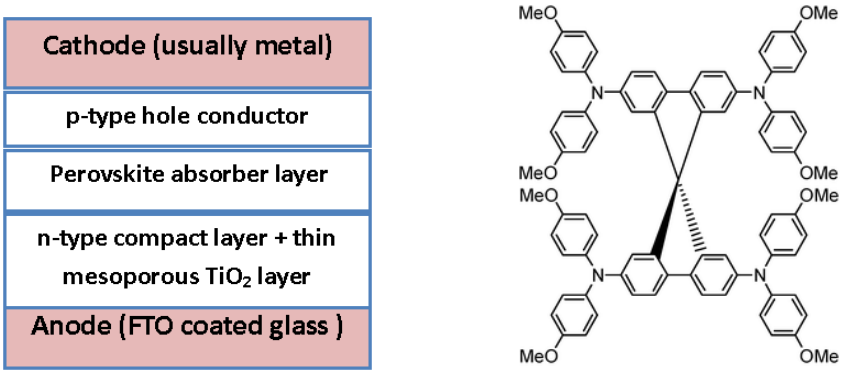

Figure 2 – (a) structure of a perovskite solar cell (diagram redrawn based on reference 14) and (b) spiro-OMeTAD (diagram reproduced from reference 15)

The *n*-type layer is usually TiO_2 and the *p*-type hole transporting material is generally spiro-OMeTAD.[14] Spiro-OMeTAD is an organic hole-conducting polymer,[15] 2,2',7,7'-tetrakis-(*N*,*N*-dip- methoxyphenylamine)-9,9'-spirobithuorene Figure 2(b). On top of the hole conducting layer, a metal electrode (usually silver) is deposited. The most popular perovskite absorber layer at present is methylammonium lead iodide ($CH_3NH_3PbI_3$), often doped with another halide ($CH_3NH_3PbI_{3-x}Cl_x$). The rapid advancement of this technology has stimulated a great amount of interest, which will likely result in a steady increase in device optimisation and cell efficiencies. However there is still a lot of work to be done on the stability of these cells and at present their mechanism of action is poorly understood.

These perovskite solar cells evolved from dye-sensitized solar cells, a well-established technology which anchors a strongly light absorbing dye onto a wide bandgap semiconductor between two conducting glass electrodes. The highest certified DSC efficiency is 11.9% ± 0.4,[16] from the company Sharp.[17] Certified solar cell efficiency tables are published by Green *et al* every six months in the journal "Progress in Photovoltaics". The cells must have been independently measured by a recognised test centre and must have a minimum area of 1 cm^2 for a 1-sun cell, where 1-sun describes the light intensity incident on the cell (this will be explained in more detail in Chapter 2). Although DSC efficiencies have tended to plateau since the initial concept was realised, a great deal of work has been done on understanding the technology and its mode of operation. The devices work well under low-light conditions and the angle of incident light is not critical, meaning they are well suited for integration into windows and building materials. DSCs offer a low-cost route to renewable energy and the technology has been scaled up to

commercial level by companies including Dyesol,[18] Solaronix[19] and G24i/GCell.[20] In addition to dye solar cell modules, innovative products such as solar powered bags and keyboards are on the market. An important industrial collaboration has also arisen by the partnership of Tata Steel and Dyesol as they seek to develop a manufacturing process that can produce roofing panels with an integrated dye sensitized photovoltaic function.[21] The remainder of this chapter will introduce and explain the concept of DSCs, discuss dye development and present a review of copper(I) dyes from the literature.

1.2. History and structure of the dye-sensitized solar cell (DSC)

The first dye-sensitized photovoltaic device was reported by Desilvestro *et al* in 1985, with an efficiency of 1.5 % with a tris(2,2'-bipyridyl-4,4'-dicarboxylate) ruthenium(II) dichloride dye. A few years later O'Regan and Grätzel reported a device with a higher TiO_2 roughness factor and thus a much improved efficiency of 7.1%[22] From this point on an entire field of research developed, as improvements in understanding, cell efficiency and scalability are sought. An excellent review of the progress of dye-sensitized solar cells was published by Hagfeldt and Boschloo in 2010.[23]

DSCs are low-cost devices whose functionality can be likened to photosynthesis. They separate the light absorption and charge transport processes, both of which are performed by silicon in first generation photovoltaic technologies, by using a photosensitizing dye adsorbed onto the surface of a wide band gap semiconductor (Figure 3).

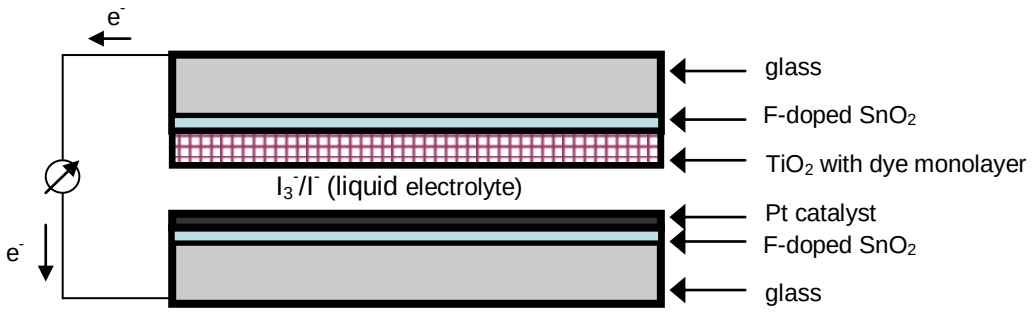

Figure 3 - a cross section of a typical DSC

The cell comprises two glass electrodes coated with a fluorine-doped tin oxide (FTO) conductive substrate. Onto one of these electrodes the semiconductor (usually TiO_2) is annealed at ~500°C and, following overnight immersion in a dye solution, the dye is

adsorbed (Figure 4). Dyes attach to the semiconductor surface *via* suitable functional groups, usually carboxylic acids, although the exact nature of the binding mode has been debated. It is now generally accepted that a combination of binding mechanisms occurs, with one report showing that approximately two thirds of surface binding is *via* an ester linkage and one third is through chelating and bridging modes.[24] Onto the second electrode a layer of platinum is deposited, which catalyses the reduction of triiodide to iodide. The electrodes are sealed together with a thermoplastic melt and an electrolyte (most commonly the I_3^-/I^- couple) completes the cell (Figure 4).

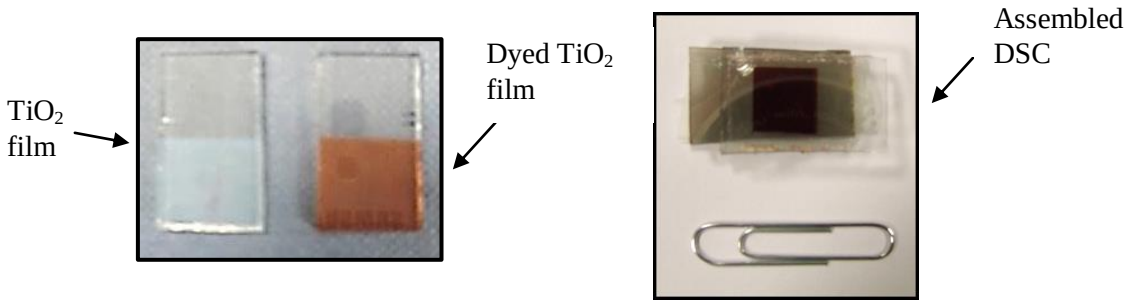

Figure 4 – an undyed and dyed TiO_2 film; a 1 cm^2 assembled DSC

1.2.1. Operating principles and electron transfer processes in the DSC

The components described above have been optimised to function together as efficiently and effectively as possible; maximising the photocurrent, photovoltage and power from the cell whilst minimising energy losses.

Key performance indicators of DSCs are the short-circuit current density (J_{SC}), the open-circuit photovoltage (V_{OC}), the solar-to-power conversion efficiency of the cell (η) and the incident photon-to-current efficiency (IPCE). The IPCE is defined as the number of electrons generated by light in the external circuit divided by the number of incident photons, at a particular wavelength. A high IPCE at a given wavelength means that almost every photon absorbed by the dye in this region is leading to an electron in the external circuit. Hence a high IPCE over a broad spectral range generally indicates a high efficiency cell. An important factor in improving the efficiency of DSCs is understanding and optimising the interfacial interactions between the dye, the semiconductor and the electrolyte.

The operating principle of the DSC is shown in Figure 5 and the equations associated with the electron transfer processes are given below. When light hits the cell it is absorbed by the dye leading to promotion of an electron to the excited state **(*excitation*)**. The electron is injected **(*CI*)** into the conduction band of the semiconductor on, what is generally accepted as, a femtosecond timescale. [25, 26] However more recent studies have found electron injection to be slower in complete DSCs.[27] The electron then diffuses to the electrode surface, before travelling through the external load to the counter electrode. On their own, wide band gap semiconductors such as TiO_2 are almost insensitive to visible light, since absorption mainly only occurs in the UV part of the spectrum.

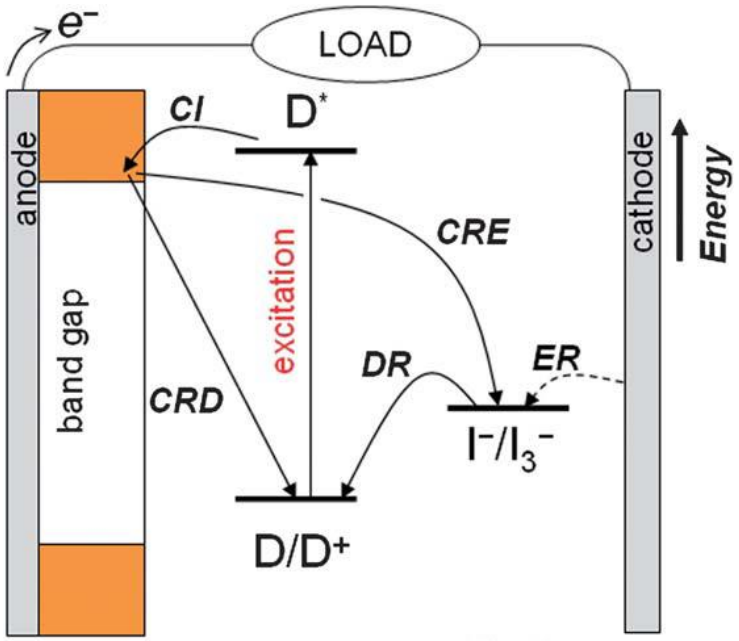

Figure 5 – energetic diagram describing the operation of a DSC with essential and detrimental processes marked (reproduced from reference 28) CI = charge injection, CRD = charge recombination with the dye, DR = dye regeneration, CRE = charge recombination with the electrolyte, ER = electrolyte regeneration

However sensitization with a dye means that electrons provided from the dye can be transported through the metal oxide, allowing effective harvesting of visible light. The oxidised dye is returned to its ground state through reduction by the I^- in the electrolyte **(*DR*)** and the I^- is regenerated by reduction of the I_3^- at the counter electrode **(*ER*)**. Charge

collection at the FTO glass working electrode and at the counter electrode also need to be efficient.

(excitation)	$D + h\nu \longrightarrow D^*$
(CI)	$D^* \longrightarrow D^+ + e^-$ (TiO_2)
(DR)	$D^+ + 3/2\ I^- \longrightarrow D + 1/2\ I_3^-$
(ER)	$I_3^- + 2e^- \longrightarrow 3I^-$

There are also undesirable loss mechanisms which reduce the efficiency of the cell. These include recombination of the injected electron with the oxidised dye before the dye is regenerated ***(CRD)*** and recombination of the injected electron with the electrolyte at the TiO_2 surface ***(CRE)***. A further loss mechanism may be decay of the dye's excited state before electron injection into the TiO_2 conduction band occurs, or inefficient light harvesting by the dye.

Fortunately, using techniques such as transient absorption spectroscopy it has been shown that electron injection from the excited state occurs on timescales much faster than excited state decay and recombination of the injected electron with the dye cation.[29,30] In the case of the most commonly studied Ru(II) polypyridyl complexes, photoexcitation of the dye results in a metal-to-ligand-charge-transfer (MLCT) involving promotion of an electron from metal t_{2g} orbitals to a π^* orbital located on a 2,2'-bipyridine (bipy) ligand. Significant overlap of the titanium 3d orbitals and the ligand π^* orbitals gives very efficient electron transfer. Physical separation of the charges within the dye cell seems to have an influence on the electron transfer kinetics, specifically on the recombination reaction between the injected electron and the oxidised dye. Following electron injection, the remaining cationic charge is predominantly situated on the metal centre but can also be distributed over ancillary ligands. Studies have shown that this charge separation significantly hinders the recombination reaction between the oxidised dye and the injected electron.[31]

1.2.2. DSC components: semiconductor

A wide bandgap semiconductor is used as a mesoporous (a material containing pores with diameters between 2 and 50 nm)[32] scaffold for the dye and as the electron transport material. On their own, metal oxides such at TiO_2 and ZnO are insensitive to visible light and would therefore not be much use in a solar cell. However, they can be sensitized with a dye, which will perform the light absorption role and inject an electron from the dye's excited state into the conduction band of the semiconductor. The best efficiencies are obtained when TiO_2 is used.[23] The fact that TiO_2 is non-toxic and cheap are additional advantages. It is commonly used as a white pigment in paint, suncream and toothpaste.[23] The three crystal structures of TiO_2 are rutile, brookite and anatase.[33] Although rutile is the most thermodynamically stable form, anatase is used for DSC applications since it has the largest bandgap (3.2 eV).[23] Efforts are ongoing to optimise the morphology of the metal oxide films. Typically nanoparticle films are used however there is interest in nanorod and nanotube structures due to the anticipated improvement, in both speed and directionality, of electron transport they would provide.[34]

Assembly of the TiO_2 film typically begins with deposition of a compact blocking layer; usually by spray pyrolysis from a solution of diisopropoxytitanium bis(acetylacetonate) in isopropanol. This blocking layer is required to prevent/reduce back reaction of electrons collected at the FTO substrate with I_3^- in the electrolyte.[35] The mesoporous layer of TiO_2 is then applied as a paste by doctor blading or screen printing. Primary particle size is ~20 nm and porosity is introduced into the film by sintering at ~500°C. The porosity of this TiO_2 layer is usually 50-60 % and its high surface area is a key aspect of its functionality in a DSC, enabling high concentrations of dye to be adsorbed. To optimise the DSC, a scattering TiO_2 layer is sometimes applied on top. This consists of larger particles (~400 nm) and assists with effective light absorption by reflecting light back into the cell. A further optimisation of this semiconductor layer is to carry out a $TiCl_4$ treatment, which deposits a layer of highly pure TiO_2 on the surface.[36]

Other metal oxides have been tried as the semiconductor, such as ZnO and SnO_2. ZnO has a very similar bandgap and conduction band edge to TiO_2 and also faster electron transport.[23, 37] However it is chemically less stable than TiO_2 and dissolves under acidic and basic conditions.[23] When used with traditional dyes such as N719, the carboxylic acid groups dissolve the ZnO and the resulting Zn^{2+} cations complex to the dye ligands, forming inactive dye molecules.[23, 38] Therefore choice of dye is important when using ZnO and it

would be better to choose a dye without acidic anchoring groups. SnO_2 has also been investigated and with a conduction band edge about 0.5 eV lower than that of TiO_2,[23] it can be useful in combination with dyes that have a low-lying lowest unoccupied molecular orbital (LUMO).[39] Since the position of the conduction band edge affects the photovoltage of the cell, photovoltages generated by SnO_2 cells are therefore lower than with TiO_2, meaning its application in DSCs is limited.

1.2.3. DSC components: electrolyte

The use of the I_3^-/I^- couple in a liquid electrolyte is still common practice; however there is interest in replacing all aspects of this system. The I_3^-/I^- couple has been optimised for use with the standard ruthenium(II) dyes. It has a suitable redox potential and the two species are physically small enough to enable rapid mass transport (in a low viscosity solvent such as acetonitrile). These features contribute to rapid dye regeneration. Furthermore, the recombination kinetics between electrons in TiO_2 and I_3^- are favourably slow.

To understand why the kinetics should be so favourable for DSC application, it is necessary to consider the complex series of reactions taking place at the TiO_2/dye/electrolyte interface. The dye and electrolyte regeneration equations in section 1.2.1 (labelled **DR** and **ER**) are an overall summary but do not describe the full sequence of events. An excellent analysis is provided in an account by Boschloo and Hagfeldt.[40] The key point is that the I_3^-/I^- redox process is overall a two electron process. However, a number of one electron reactions take place within the iodide-iodine system, some of which are important in the DSC and some of which are not. After excitation and charge injection, the oxidised dye is regenerated *via* reduction by I^-, which results in the formation of diiodide radicals ($I_2^{-\bullet}$).[40] These diiodide radicals then disproportionate into I_3^- and I^-. So, following charge injection, the dye regeneration step is:

(DR) $D^+ + I^- \longrightarrow (D \text{ --- } I)$ *(a dye-iodide complex)*

$(D \text{ --- } I) + I^- \longrightarrow D + I_2^{-\bullet}$

$2I_2^{-\bullet} \longrightarrow I_3^- + I^-$

This process has ensured that the I_3^-/I^- couple has remained the first choice of redox mediator over the past two decades. However the redox potential of the I_3^-/I^- couple is actually a lot higher in energy than necessary for dye regeneration. With a driving force of ~0.75V (versus the normal hydrogen electrode, NHE), there is a large energy loss here which could be reduced by using a redox species with a more positive redox potential. This would lead to a gain in the V_{OC} and improved overall cell efficiency. Additional disadvantages to using the I_3^-/I^- couple are its corrosive nature and its light-absorbing ability. The latter means it may undergo photochemical reactions which could reduce DSC efficiency. Alternative redox species include bromide and pseudohalides, although their similarity to the iodine species means they have the same associated problems. Recently success with cobalt(II/III) complexes has been reported, most notably from Yella and co-workers[41] who reported a record DSC efficiency of 12.3% in a cell co-sensitised with a zinc porphyrin and an organic dye (cell area <1 cm^2 therefore not certified for inclusion in the Progress in Photovoltaics chart).

This breakthrough showed that it is possible for the I_3^-/I^- couple to be replaced. Before this paper, it had appeared that one-electron outer sphere redox couples may not be viable as alternatives to I_3^-/I^- due to faster electron recombination kinetics. However with careful dye and device design this problem can be overcome. In the case of Yella *et al.*, long-chain alkoxy groups were grafted onto a D-π-A zinc porphyrin dye**,** YD2-*o*-C8 (Figure 6(a)), which was used as a co-sensitizer with the organic dye Y123 (Figure 6(b)), in conjunction with a cobalt (II/III) tris(bipy) based electrolyte. The group reported that the thickness and porosity of the TiO_2 film were very important for DSC performance. The pore size of the TiO_2 paste was increased and the film thickness was reduced relative to those used in I_3^-/I^- electrolyte devices. These adjustments reduced the mass transport limitations and high recombination rates which had hindered cobalt (II/III) based DSCs previously.

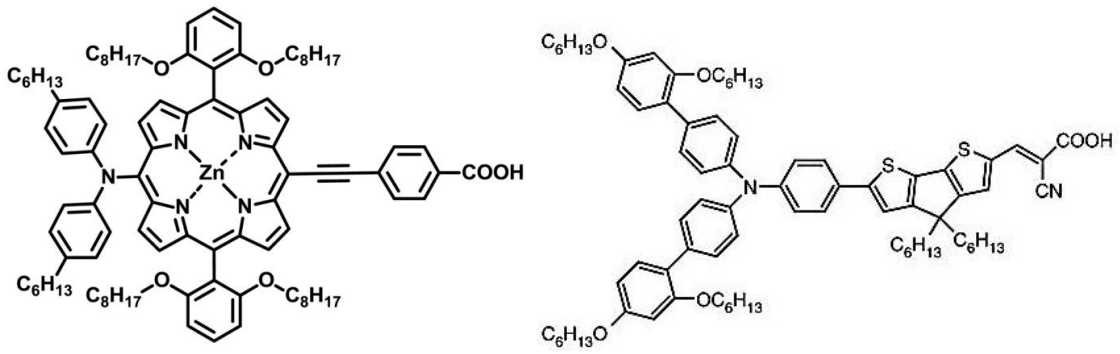

(a) **(b)**

Figure 6 – co-sensitizing dyes used by Yella (a) YD2-o-C8 and (b) Y123 (diagrams reproduced from references 41 and 61)

In addition to considering the active redox species, there is also research centred on the electrolyte medium. The use of volatile organic solvents such as acetonitrile is less than ideal for long term stability and they are also toxic. Aqueous dye cells with various redox mediators are being investigated[42-44] as a less volatile alternative, particularly since water is known to enter the cell anyway (to the detriment of cell performance) so to be able to produce cells that work well in this kind of environment is appealing. A recent paper by Xiang and colleagues reported a record aqueous DSC efficiency of 5.1%, using a hydrophobic dye and a cobalt(II/III) tris(bipy) based water electrolyte.[45] Polyethylene glycol was used as an additive to reduce phase separation between the dye and the electrolyte.

Other alternatives to volatile liquid electrolytes are ionic liquid electrolytes[46] and solid state electrolytes.[47] Ionic liquid systems, generally containing an imidazolium iodide, are a low-volatility option; however the viscosity hinders mass transport. In solid state hole-conductors, such as the polymers PEDOT and Spiro-OMeTAD, hole transfer occurs directly from the oxidised dye to the HOMO of the hole conductor and from there progresses to the counter electrode *via* a "hole-hopping" mechanism.[23] Problems with solid state hole conductors are generally related to pore filling. For a DSC to function effectively, the dye molecules must all be in contact with the TiO_2 and the hole conductor. To minimise this problem it is reported that the TiO_2 film thicknesses must be ~2 μm;[48] however using such thin films limits light absorption. The development of strongly absorbing donor: π-bridge:

acceptor (D-π-A) organic dyes has significantly improved the performance of these devices, with efficiencies of ~7% achieved.[49]

1.2.4. DSC components: the dye

Designing dyes has been at the forefront of DSC research for the past two decades and there are certain criteria which need to be fulfilled.[50] The development of dyes is discussed in more detail for the rest of this chapter, however the general requirements are:

- The dye must absorb as much visible light as possible and efficiently inject electrons into the conduction band of the semiconductor.
- A high molar extinction coefficient over the whole absorption spectrum is desirable to absorb as much of the incident light as possible.
- Appropriate functional groups for attachment to the semiconductor surface are required, usually carboxylic or phosphonic acids.
- There also needs to be suitable matching of the energy levels within the system; the LUMO of the dye must be higher in energy than the TiO_2 conduction band edge and the energy of the highest occupied molecular orbital (HOMO) needs to be appropriate for efficient regeneration of the dye by the electrolyte.
- Long term stability in contact with the electrolyte and over a lifetime equating to approximately 20 years is also desirable.

1.3 Classical design of dyes

Traditionally, the most widely investigated and successful dyes (in terms of efficiency and long-term stability) are Ru(II) polypyridyl complexes[51] with the general formula $RuL_2(X)_2$ where L represents 2,2'-bipyridyl-4,4'-dicarboxylic acid and X is typically Cl, Br, I, CN, and SCN.[31] Most commonly, π-donating isothiocyanates (NCS^-) are used as the ancillary ligands. These destabilise the t_{2g} orbitals on ruthenium, raising the HOMO energy of the complex and leading to a red-shifted absorption.[50] This is desirable because one of the main challenges with dye synthesis has been designing dyes which can harvest light at longer wavelengths. During the early 1990s extensive research into Ru(II) photosensitizers was carried out and three typical examples are shown in Figure 7.

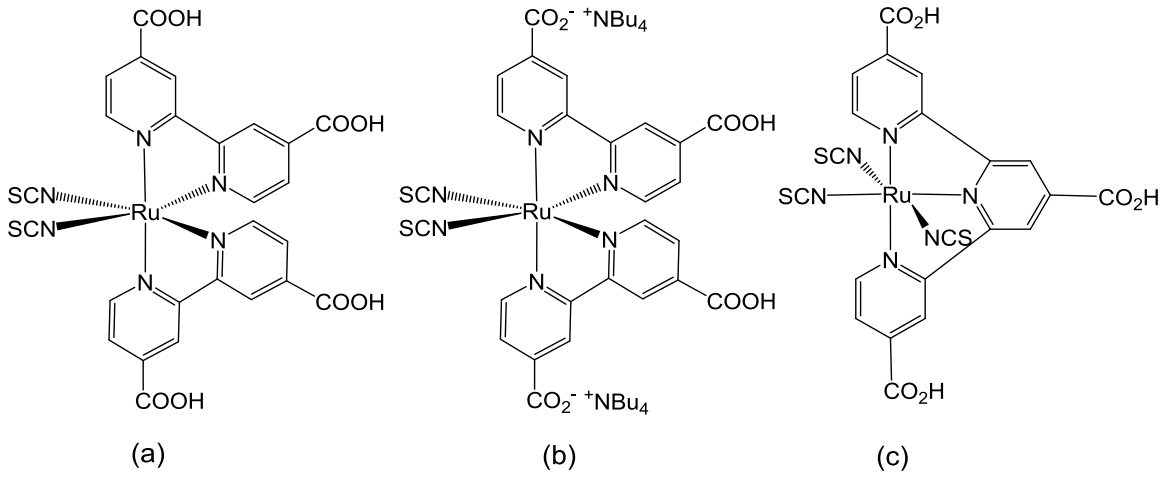

Figure 7 - structures of (a) N3 (redrawn from reference 52), (b) N719 (redrawn from reference 53) and (c) the "black dye" (redrawn from reference 54)

Visible light absorption is good due to a metal-to-ligand charge transfer (MLCT) and the use of bipyridine or terpyridine ligands means substituents can be added to tune the HOMO and LUMO energy levels of the dye. Although various metal complexes have been tried in DSCs, ruthenium complexes have proved the most successful due to appropriate ground and excited state energy levels, a broad absorption spectrum, good stability and a relatively long lived excited state lifetime.[23, 51] In 1993 Grätzel *et al* published work on N3, which was the first dye to achieve a solar-to-power conversion efficiency of over 10 % and has an incident photon-to-current efficiency (IPCE) of over 80 % between the wavelengths 480 nm to 600 nm.[52] The doubly deprotonated analogue of N3, N719, was investigated by Nazeeruddin[53] and co-workers and was found to have an improved cell efficiency over that of N3.This can be rationalised by considering the state of protonation in the complex. Where the dye is fully protonated (N3), these protons are transferred to the TiO_2 surface upon adsorption.[50] This leads to higher photocurrents due to enhanced electron injection, but a lower open circuit photovoltage since the conduction band edge is positively shifted. The opposite effect is achieved when the complex is fully deprotonated; therefore N719 is a compromise of the two in order to obtain an optimal photocurrent and photovoltage.[50, 51]

From the early work with ruthenium complexes it was highlighted that extending the absorption range of the dyes into the near-IR region was desirable. This was achieved in 1997 by Grätzel and colleagues with the development of the "black dye", which showed absorption across the whole visible spectrum, up to 920 nm, and a solar-to-power efficiency

of 10.4 %.[54] This dye has an impressive J_{SC} value of 20 mA cm^{-2} and a V_{OC} of 720 mV. From the IPCE diagrams of N3 and the "black dye" (Figure 8) it can be seen that the "black dye" absorbs further into the lower energy end of the spectrum and absorption onset is approximately 100 nm sooner than in N3. This shift was attributed to a decrease in energy of the π* orbital of the terpyridine ligand and an increase in energy of the t_{2g} metal orbital.

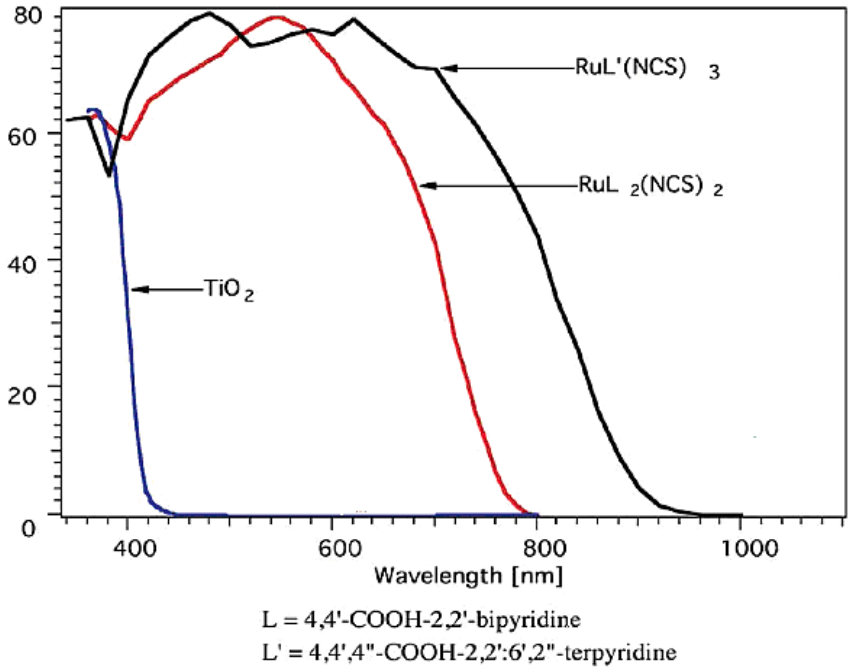

Figure 8 - IPCE diagrams for N3 (red line) and the "black dye" (black line) (reproduced from reference 55)

These three classical dyes are the most commonly studied ruthenium sensitizers and usually provide the standard for DSC comparisons and experiments. Using these as a guide, a wide range of ruthenium polypyridyl complexes have been engineered over the years and tested in cells, each with its own combination of electron donating or withdrawing ligands to tune the MLCT transition. Tuning can be achieved by introducing a ligand with a low energy π* molecular orbital and/or destabilising the metal t_{2g} orbital so that it is raised to a higher energy, closer to the ligand π* orbitals. Both methods reduce the energy gap between the HOMO and LUMO, resulting in a lower energy MLCT transition. Care must be taken to ensure that the LUMO is not so negatively shifted that electron injection into the TiO_2 conduction band is hindered. Similarly, the position of the HOMO must remain at a lower

energy than the redox potential of the active electrolyte species, to ensure dye regeneration. During the first few years of DSCs, dye optimisation was carried out according to this strategy. This approach is still relevant today but in recent years a much broader and more varied range of dyes have been systematically produced.

1.4 Modern developments in dye engineering

Since the initial breakthroughs in efficiency experienced during the early years of DSC development, a plateau of 10-11 % was reached and new strategies were needed to improve on this. Since hundreds of potential sensitizers have been synthesised and tested over the past two decades it is not feasible to cover them all here. Notable developments will be discussed and examples given of some of the best-performing sensitizers developed recently (Figure 9), on topics including heteroleptic complexes and metal-free sensitizers.

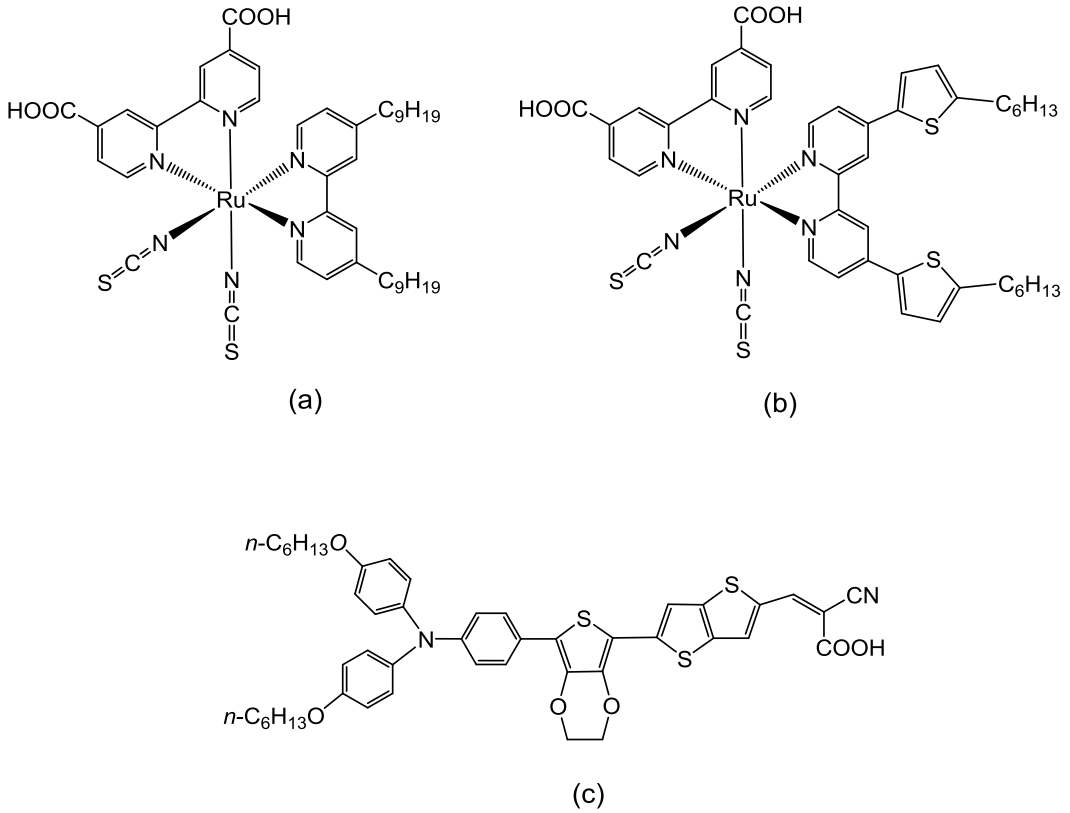

Figure 9 - (a) Z907 (redrawn from reference 56) (b) C101 (redrawn from reference 57) and (c) C217 (redrawn from reference 63)

Heteroleptic complexes have proved interesting, where one bipy ligand with attachment groups is retained and the second bipy ligand is functionalised to impart some other property to the complex. For example, Grätzel and co-workers developed Z907 (Figure 9(a)) which features two hydrophobic alkyl chains on one of the bipy ligands.[56] Hydrophobic chains improve the stability of the cells towards water, the presence of which can cause hydrolysis of the bond between the semiconductor and the carboxylic acids on the dye, causing desorption of the dye. Such structures also seem to reduce the dark current recombination reaction i.e. reduction of I_3^- by conduction band electrons, perhaps due to the long alkyl chains preventing the I_3^- from reaching the TiO_2 surface.[50]

Heteroaromatics, such as thiophene substituents, can be used to tune the energy levels of the complex. A red-shift in the MLCT absorption band can be induced since thiophene groups introduce more conjugation into the system, reducing the energy gap between the HOMO and LUMO energy levels. A particularly effective sensitizer is C101 (Figure 9(b)), which incorporates alkyl thiophene units and was the first dye to improve upon the performance of N3 with a very impressive power conversion efficiency of 11.9 % (area = 0.28 cm^2).[57] Whilst organic dyes can be claimed as being a sustainable alternative to ruthenium based dyes since no expensive metal is used, their disadvantages are often overlooked. Organic dyes generally do have higher molar extinction coefficients than metal complexes, but their absorption bands in the visible region are usually narrower[58] (typically $\Delta\lambda \sim 100$-250 nm compared to $\Delta\lambda \sim 350$ nm in the broader absorption bands of metal complexes).[59] It is also noted that organic dyes can suffer from increased recombination reactions, compared to the ruthenium complex N719, when I^-/I_3^- is used as the redox species.[60] Finally, in order to obtain the highest efficiencies, organic dyes (and porphyrins and phthalocyanines) need to be very carefully designed on a molecular level, which usually necessitates multi-step syntheses. For example, the DSC with 12.3 % efficiency prepared by Yella, with a cobalt(II/III) electrolyte, used a mixture of a porphyrin dye and the organic dye Y123 (see Figure 6).[41] The porphyrin dye is the product of an 8 step synthesis and Y123 requires a 9 step synthesis.[61] Purification of these dyes is also non-trivial.

Hundreds of organic sensitizers have been tested in DSCs, generally adopting the structure of donor: π-bridge: acceptor (D-π-A).[62] As the dye absorbs light an intramolecular charge transfer from the donor unit, through the π conducting bridge, to the acceptor group occurs, from where an electron can be injected into the semiconductor. This design means that the HOMO and LUMO are spatially separated, with the HOMO mostly located on the donor

component and the LUMO lying around the acceptor moiety. The organic dyes that have been studied include coumarins, indolines and carbazoles. One high efficiency (9.8%) example is dye C217 (Figure 9 (c)). In this case the triarylamine group is the electron donor and a cyanoacrylate group is employed as the acceptor.[63] One concern with regards to the application of organic dyes in DSCs is their interaction with the iodide/triiodide electrolyte. Through studying the literature and performing a study with ruthenium phthalocyanines, O'Regan and co-workers found that more dark current was generated using organic DSCs than compared to N719 and propose that this problem exists in varying degrees for most other organic dyes and needs to be given more attention.[64]

1.5 Towards sustainable dyes: alternatives to ruthenium

The focus of this project is synthesising alternative dyes to those that contain ruthenium metal. Although ruthenium polypyridyl complexes have been the standard for the past two decades, the abundance and cost of the metal cannot be ignored. At the 3rd International Conference on Hybrid and Organic Photovoltaics in May 2011, a presentation by the company Dyesol stated that for single digit kilogram production of N719 the metal makes up 47% of the total manufacturing cost.[65] This is due to the relative scarcity of ruthenium in the earth's crust, at only 0.001 mg/kg.[66] More sustainable alternatives include copper, which has a much higher abundance of 60 mg/kg.[66] The remainder of this chapter will provide an overview of the properties of copper(I) complexes as alternatives to ruthenium(II) complexes and also present a general literature review of copper(I) DSCs.

1.5.1 The use of copper(I) versus ruthenium(II) in DSCs

A detailed review of the photochemistry and photophysics of copper(I) complexes was recently provided by Armaroli and colleagues.[67] Being a group 11 metal, complexes of copper(I) have a full, d^{10}, electron count. For this reason, copper(I) complexes generally have a relatively long-lived MLCT excited state since there are no empty metal centred energy levels *via* which undesirable deactivation of the excited state can occur. To fulfil the 18-electron rule of transition metal complexes,[68] copper(I) can only form four bonds. In order to minimise electrostatic repulsions between the ligands, a tetrahedral geometry is generally adopted. A consideration of this geometry explains the nature of the splitting of the five *d*-orbitals. The d_{xy}, d_{xz}, and d_{yz} orbitals are pointing directly toward the ligands therefore they are higher in energy than the $d_{x^2-y^2}$ and d_{z^2} orbitals (Figure 10).

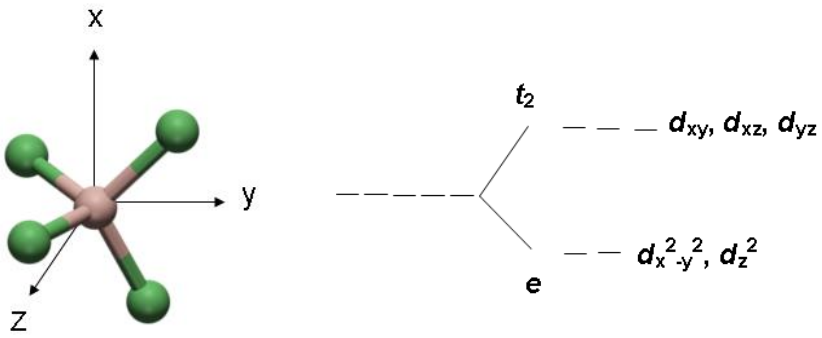

Figure 10 – geometry and orbital splitting of a tetrahedral complex (redrawn from reference 69)

To appreciate the role of the dye in a DSC a consideration of electronic transitions is very important.[70-72] The most important transition for DSC application is the MLCT, which takes place in the visible region of the spectrum from a metal t_{2g}/t_2 orbital (for ruthenium/copper respectively) to a ligand-centred π^* orbital. The 2,2'-bipyridine ligand is very suitable for DSC use due to its relatively low-energy empty π^* orbital. Ligand centred transitions from a π to a π^* orbital take place at higher energies, absorbing in the UV region of the spectrum. With its filled electron shell, metal centred *d-d* transitions are not possible in copper(I) complexes. Upon absorption of a photon, an electron is promoted from the ground electronic state to an electronically excited state. From this point, several processes are possible, as shown in the Jablonski diagram in Figure 11. These can be radiative, where the transition involves the emission of a photon, or non-radiative, where the excitation energy is transformed into vibrational or rotational energy. Vibrational relaxation occurs when the electron moves from a higher to a lower vibrational state, within the same electronic level. It is also possible for the electron to move from a vibrational state in a higher electronic excited state to a lower excited state, which is called an internal conversion. Both of these processes can happen on a very fast timescale (10^{-14}-10^{-11} seconds),[72] immediately following photon absorption, and generally precede another transition. For example, following vibrational decay to the ground vibrational level of the excited state a radiative transition directly back to the singlet ground state can occur. This is called fluorescence and involves the emission of a photon at a longer wavelength than the exciting photon.

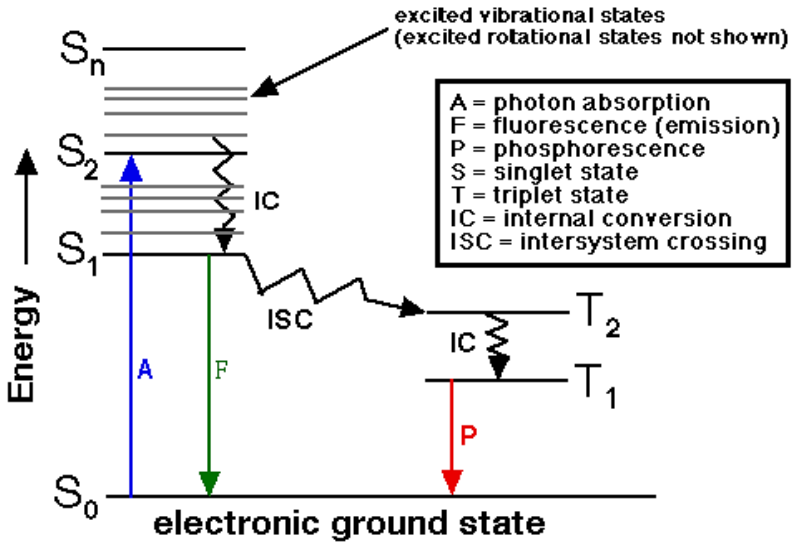

Figure 11 – a Jablonski diagram showing the possible energetic pathways of an electron within a molecule following light absorption. (Diagram reproduced from reference 73)

Alternatively, an intersystem crossing between an excited singlet and an excited triplet state can take place. This involves a change of spin therefore it is technically forbidden according to electron transition rules, and hence it is a comparatively slow process (10^{-8}-10^{-3} seconds).[72] From this point a radiative transition back to the singlet ground state can occur, which is known as phosphorescence. This happens on a slower timescale than fluorescence. A competing, non-emitting route of deactivation of the excited state can also occur, for example, a quenching process. Quenching occurs either by an electron transfer or an energy transfer to another molecule (e.g. of the dye, or oxygen).

The processes outlined in the Jablonski diagram affect the excited state lifetime of these metal complexes, which has an important bearing on their suitability for DSC application. Meyer and co-workers, in particular, have spent many years studying the excited-state properties of copper(I) complexes.[74, 75] Unlike ruthenium(II) complexes, copper(I) dyes undergo a Jahn-Teller structural rearrangement (whereby a system removes the degeneracy from electronic states with unequal electron occupation to reach a lower overall energy)[76] upon oxidation to d^9 copper(II). This involves a flattening of the excited state so that its geometry is closer to square planar. This distortion facilitates nucleophilic coordination, e.g. by solvent molecules, in the axial positions of the complex. Formation of such an exciplex/excimer is unfavourable as the species will generally undergo a non-radiative

deactivation.[77] Dye regeneration is also slowed due to increased reorganisation energy. A consequence of this effect is that copper(I) complexes have singlet state (^{1}MLCT) lifetimes and intersystem crossing rates which are dependent on the geometrical distortion of the copper centre and the nature of the solvent.[74, 78]

With the standard ruthenium(II) dyes, N3 and N719, there has been a large amount of research on which electronic state electron injection into the TiO_2 occurs from. Studies have been conducted both on single dyed films in solvent and on assembled DSCs with comparable results.[79, 80] It has been shown that there are two electron injection processes. On assembled DSCs, Teuscher and co-workers[80] found with pump-probe spectroscopy that electron injection occurred mainly on a sub 100 femtosecond timescale, attributed to injection from the ^{1}MLCT. This was then followed by a slower injection component (26.9 picoseconds) which was attributed to injection from the triplet states (^{3}MLCT) of dye aggregates or loosely bound dye molecules.

The electron injection dynamics of copper(I) complexes on a TiO_2 surface has not yet been an extensively studied. One report from Huang *et al* studied electron injection from copper(I) bis-coordinated to two 2,9-diphenyl-1,10-phenanthroline ligands to TiO_2 nanoparticles.[78] The 2,9-disubstituted-1,10-phenanthroline ligand is a suitable choice for such studies since it shields the copper(I) centre from unwanted coordination by other molecules by being less flexible than its 2,2'-bipyridine counterpart. As stated by the authors, an understanding of the factors which affect DSC device efficiency with copper(I) dyes (such as excited state lifetime and charge recombination profile) will assist in their optimisation. Huang aimed to establish whether electron injection into the TiO_2 conduction band was predominantly from the higher energy, but relatively short-lived, ^{1}MLCT or from the lower energy, but more persistent, ^{3}MLCT state.[78] The lifetimes of both the ^{1}MLCT and ^{3}MLCT states, and the rate of intersystem crossing (ISC) for this complex, were measured. Firstly it was verified that electron injection into the TiO_2 was occurring from a MLCT using electron paramagnetic resonance (EPR) and optical transient absorption spectroscopy. The rate constants for electron transfer into the TiO_2 conduction band from the ^{1}MLCT and the ^{3}MLCT were evaluated and compared to the intersystem crossing (ISC) time constant. Secondly, it was established that charge injection from the singlet state occurs much more rapidly (on a timescale of <12 ps) compared to from the triplet state, which is in the order of 1000 ps. Finally, the ISC process was found to be slower than electron injection from the ^{1}MLCT, with a time constant of 13.7 ps. So it was concluded that an ultrafast electron

injection from the ^{1}MLCT took place in the case of this particular copper(I) complex, rather than ISC and subsequent injection from ^{3}MLCT. It was noted that the steric bulk of the ligands played an important part in prolonging the intersystem crossing time, which otherwise may have made injection from the lower energy ^{3}MLCT more competitive. Although the effectiveness of these electron transfer processes are likely to differ between complexes, this paper provides a valuable insight into how important ligand choice and structural rearrangement are when considering copper(I) dyes as sensitizers for DSCs. The publication also emphasised that efficient electron injection into a semiconductor from a copper(I) complex happens in an analogous manner to ruthenium(II) complexes.

In addition to the optical transition properties discussed so far, copper(I) complexes offer similar electrochemical properties to ruthenium(II) complexes, with a reversible Cu(I/II) couple. They are also more straightforward to synthesise since the metal/ligand complexation reaction generally proceeds at room temperature, whereas preparation of ruthenium(II) complexes usually requires a high temperature reaction in DMF and significant purification efforts.[57] A notable difference is the expected greater lability of d^{10} copper(I) complexes, meaning ligand exchange is faster compared to the low spin d^{6} ruthenium(II) complexes.

1.5.2 The development of copper(I) dyes for DSC application

When this PhD commenced, there were few examples in the literature of copper(I) based DSCs. Our interest in this area stemmed from work reported by Edwin Constable's research group, first published as a communication[81] in 2008, followed the next year by a full paper in Dalton Transactions.[82] The work described a copper(I) centre coordinated to two 2,2'-bipyridine ligands functionalised with carboxylic acids in the 4- and 4'-positions (with or without alkenyl spacers) and methyl/phenyl groups in the 6- and 6'-positions (examples are compounds **1** and **2**, Figure 12).

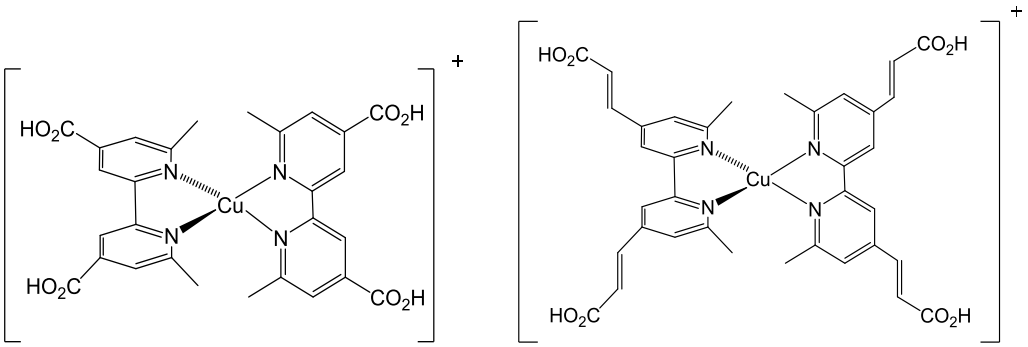

Figure 12 – Cations of the copper(I) complexes from the Constable group with efficiencies of 1.9% for compound 1 and 2.3% for compound 2 (redrawn from reference 81)

However this was not the first time copper(I) dyes had been trialled. The first reported copper(I) sensitizer used in a DSC was a 1,10-phenanthroline complex (**3**, Figure 13), investigated by Alonso-Vante in 1994.[83] Although a cell efficiency was not given, the authors acknowledged that it was low. The V_{OC} was reasonable at 600 mV however the J_{SC} was weak at only 0.6 mA. A more successful dye was reported by Sakaki in 2002 (**4**, Figure 13).[84] The group synthesised a 4,4',6,6'-tetramethyl-2,2'-bipyridine-5,5'-dicarboxylic acid complex, $[Cu(tmdcbpy)_2]^+$, and achieved a J_{SC} of 2.9 mA cm^{-2} and a V_{OC} of 630 mV. The improved photocurrent was attributed to the better positioned carboxylic acid groups. With the 1,10-phenanthroline work by Alonso-Vante the carboxylic acids are on the phenyl substituent rather than being directly attached to the 1,10-phenanthroline structure, therefore electron injection into the TiO_2 was considered unfavourable. In Sakaki's 2,2'-bipyridine ligand, the carboxylic acids were placed at the 5,5' positions and an improved cell performance over that of Alonso-Vante's complex was observed.

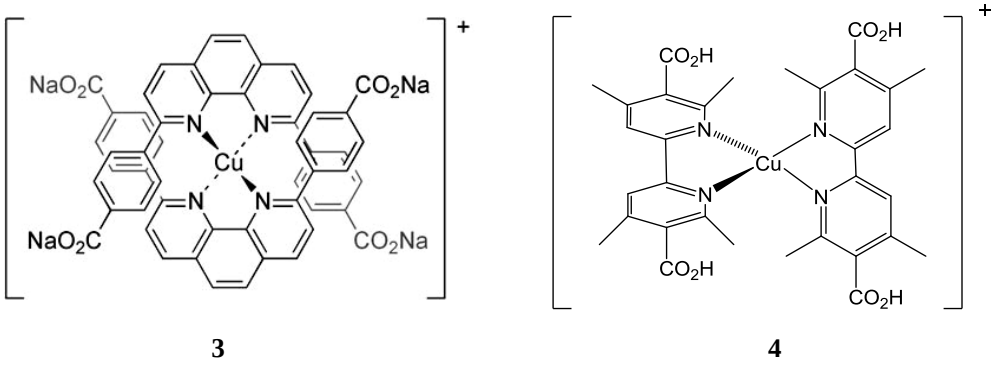

Figure 13 – Cations of the copper(I) dyes tested by Alonso-Vante (3) and Sakaki (4) (redrawn from references 83 and 84)

There was then no reported progress with copper(I) dyes until Constable's report in 2008.[81, 82] Overall solar-to-power conversion efficiencies of **1** and **2** (Figure 12) were 1.9 % and 2.3 %, for DSCs with an active area of 0.2 cm^2. The reported open-circuit photovoltages for both compounds were ~560 mV and the short-circuit photocurrents were 5.25 mA cm^{-2} and 5.90 mA cm^{-2} respectively. These DSC parameters are clearly lower than those of the top-performing ruthenium dyes, however they were the most promising application of copper(I) dyes in DSCs reported up until this point. From Figure 12 it can be seen that **1** and **2** differ in the extent of conjugation in the system. An increase in conjugation means an increase in the number of π molecular orbitals. A transition from the highest energy bonding π orbital (or metal located orbital in this case) to the lowest energy antibonding π* orbital therefore requires a smaller energy input, i.e. absorption of light at longer wavelengths.

The improved performance of these copper(I) dyes compared to the earlier ones is credited to a more strategic structural design. Studies with ruthenium(II) polypyridyl compounds generally found that electronic communication between the carboxylic acids groups and the semiconductor is optimal when the carboxylic groups are in the 4- and 4'-positions on the bipy ligand. Specific to copper(I) species, Constable found that for effective dyes it was necessary to employ some sterically bulky groups at the 6- and 6'-positions of bipy. This prevented an unfavourable structural rearrangement, from tetrahedral to square planar, upon oxidation of the copper centre. The effect of substituents on the stability, geometry distortion and excited state lifetime of copper(I) phenanthroline compounds had already been noted by McMillan and co-workers.[85-87] As discussed in section 1.5.1, geometry changes are undesirable because they can slow electron transfer processes and facilitate non-radiative decay of the excited state.

Since the reporting of **1** and **2**, there has been a steady stream of publications from the Constable group [88-94] and others [78, 95-101], particularly in the past two years. The Constable group followed their initial publications with series of "sticky" copper(I) complexes in 2010, however these were not as successful as 2,2'-bipyridine systems.[88] The structure used interesting carboxylic acid functionalized *N*-phenylpyridin-2-ylmethanimine ligands with both carboxylic acid groups expected to bind at the TiO_2 surface (Figure 14), but the overall cell efficiencies were only ≤0.23%.

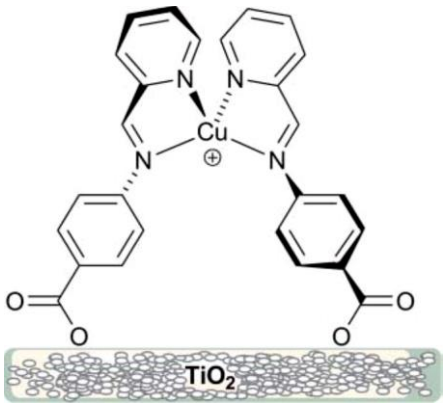

Figure 14 - a "sticky" copper(I) complex with proposed binding to the TiO_2 surface shown. Diagram reproduced from reference 88.

This poor performance was explained though density functional theory (DFT) experiments, which found that the LUMO of the complex was mostly located on the pyridine rings. Directionality is important when considering dyes for DSCs. To enable efficient electron injection the LUMO ideally needs to be situated in the direction of the TiO_2, which in this case it is not. Computing the positions of the HOMO and LUMO can be a valuable indication of whether a complex is likely to suitable for DSCs. This is one reason why theoretical investigations have become increasingly practiced and useful in DSC research.

The first computational analysis in the context of copper(I) DSCs was conducted by Lu *et al.* in 2011,[98] who concluded that copper(I) bipyridyl dyes show similar optical properties to their ruthenium(II) counterparts and should be a viable alternative. Two of the first dyes studied experimentally by Constable (**1** and **2**, Figure 12) were studied computationally by Lu, as were the 4,4'-methyl esters of these complexes. The effect of introducing heteroaromatic groups such as furan or thiophene onto one of the bipy ligands was also modelled. The exercise was useful because it allowed comparison between experimental data from Constable's work, such as bond lengths and angles, with the theoretical data. Molecular geometries, electronic structures and optical absorption spectra were predicted in the gas phase and in acetonitrile (MeCN) solution. The predicted DSC properties were seen to improve when structural optimisations, such as extending the conjugation of the system, were applied. A second wholly theoretical report was published by Baldenebro-Lopez *et al.* in 2013.[96] This set of calculations studied five homoleptic copper(I) complexes with 6,6'-bisphenyl-2,2'-bipyridine ligands. The ligands were functionalised in 4,4'-positions with either an ester/COOH group, an alkenyl ester/COOH group or a phenyl spacer with a

COOH group. Their findings agreed with those of Lu *et al*. It has also become commonplace for groups to make concurrent computational and experimental assessments of copper(I) dyes. DFT and time dependent DFT (TD-DFT) studies are useful for calculating the optimised geometry, the key molecular orbital positions (both spatial and energetic) and simulating the UV/Vis spectrum of a dye.

A more recent development by the Constable group has been the *in situ* synthesis of heteroleptic copper(I) dyes on the TiO_2 surface.[89] These complexes consist of one anchoring ligand and a second, non-anchoring, ligand. Functionalisation of a non-anchoring bipy ligand with a heteroaromatic or a bulky diphenylamino substituent have produced impressive DSC performances, for which a top efficiency of 3.8 % has been reported.[92] The group's ligand exchange strategy has enabled the screening of a large range of ligand combinations in DSCs. It involves initially binding an anchoring ligand (generally 6,6'-dimethyl-2,2'-bipyridine with carboxylic or phosphonic acid binding groups) to the TiO_2 film, then immersing the film in a solution of a homoleptic copper(I) complex. The TiO_2 film becomes coloured as the homoleptic copper complex in solution exchanges one of its ligands for an anchoring ligand, resulting in the heteroleptic species. This strategy is a powerful tool since it renders isolation of the heteroleptic complexes unnecessary. Synthesis of heteroleptic copper(I) dyes is known to be difficult due to the lability of d^{10} copper(I), resulting in the eventual formation of a mixture of the homoleptic and heteroleptic complexes in solution.[99]

Using this stepwise assembly approach, the group has made significant advancements in the field of copper(I) dyes.[89-93] Combining the anchoring ligands in Figure 15 with the functionalised ancillary ligands in Figure 16 and Figure 17 has enabled testing of a whole series of heteroleptic complex DSCs. The highest DSC efficiencies achieved for complexes with sets of ligands **9** and **10** (η = 1.20-1.51%) were when the phosphonic acid ligand **6** was employed as the anchor.[89] In these experiments, the ancillary ligand was actually found to have little influence relative to the choice of anchoring ligand.

The group built on this work by further developing the choice of ancillary ligand. Ligand **11** (Figure 16) with its extended π-conjugation, improved DSC performance.[90] A top efficiency of η = 2.35% was obtained with the complex $[Cu(\mathbf{11})(\mathbf{6})]^+$. The group rationalised this impressive outcome using TD-DFT calculations, which predominantly located the LUMO over the anchoring ligand (as desired for rapid electron injection) and found the character of

the HOMO to be dominated by ligand **11**. Presumably this greater spatial separation of the charges hinders the back migration of an injected electron from the TiO_2 to the oxidised dye and is therefore responsible for the dye's improved performance compared to using compounds from **9** or **10** as the ancillary ligand.

This train of thought was further pursued with the grafting of first and second generation hole-transporting triphenylamino dendrons (compounds **12** and **13**) onto a 6,6'-dimethyl-2,2'-bipyridine backbone.[92] Heteroleptic complexes were prepared on the surface as described previously using anchoring ligands **5, 6** or **7** and improvements in J_{SC} and η were observed when ligand **12** was replaced with the more conjugated **13**. Cells were tested 1 day after cell assembly and then a few days afterwards. There were increases in J_{SC} and η with time which the authors attribute to some "reorganisation and/or aggregation of dye molecules on the surface".[92] A high efficiency of 2.61% was achieved with [Cu(**13**)(**6**)]$^+$ six days after the cell was sealed. The homoleptic dendritic complexes were prepared initially without any steric constraints; ^{1}H NMR, mass spectrometry and UV/Vis data confirmed the formation of a [Cu(L)$_2$] complex. Although the phosphonic acid anchoring ligands again performed the best, ligand **7** also delivered comparably favourable results. It was noted by the authors that ligand **7**, which contains phenyl spacer units between bipy and the carboxylic acid groups, was an improvement over ligand **5**. A final point was the effect of the solvent in the dye bath. This work was conducted using CH_2Cl_2 as the dye bath solvent. With [Cu(**12**)(**6**)], a top DSC efficiency of 2.15% was obtained 3 days after cell sealing. However when the dye bath solvent was changed from CH_2Cl_2 to MeCN, an efficiency of 3.77% with [Cu(**12**)(**6**)], tested after 8 days, resulted. Apart from changing to MeCN in the dye bath, all other conditions were the same. The group are conducting further work into why this should have had such a significant impact.

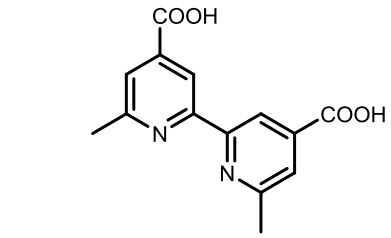

5

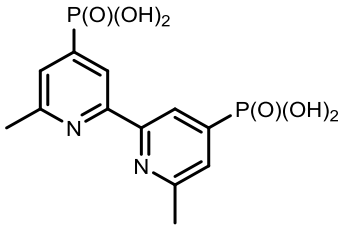

6

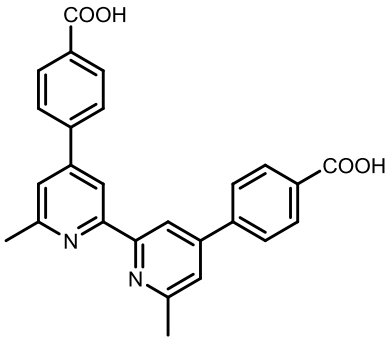

7

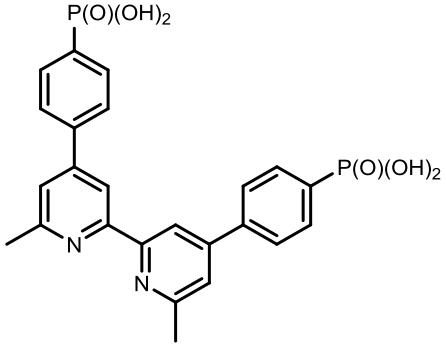

8

Figure 15 – compounds 5-8, anchoring ligands used by the Constable group

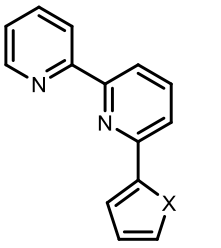

X = O, S, NMe or Se

9

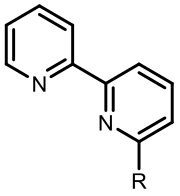

R = Ph or Me

10

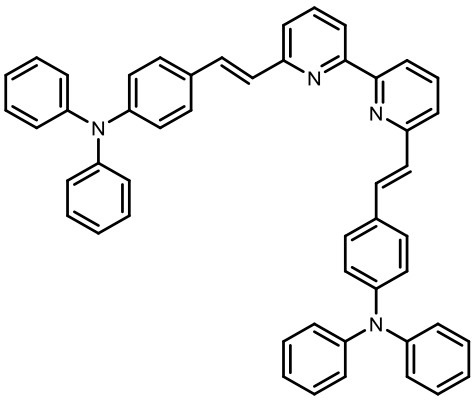

11

Figure 16 – compounds 9-14, ancillary ligands used by the Constable group (continued on next page)

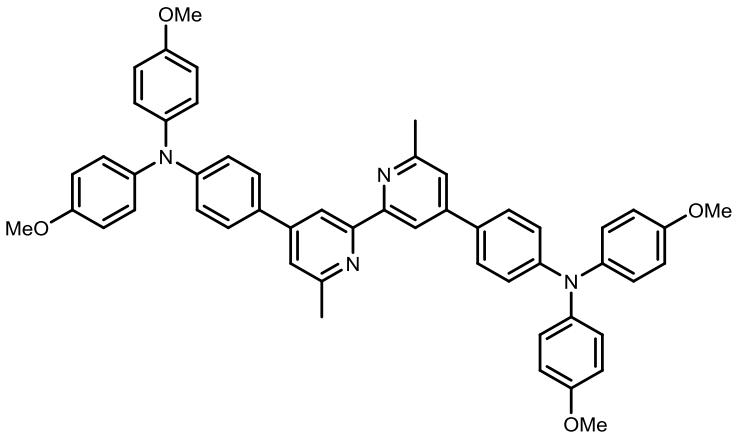

12

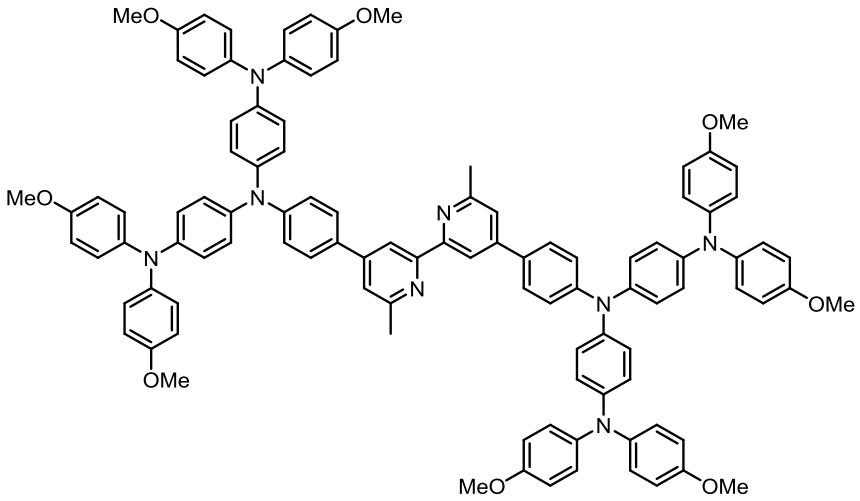

13

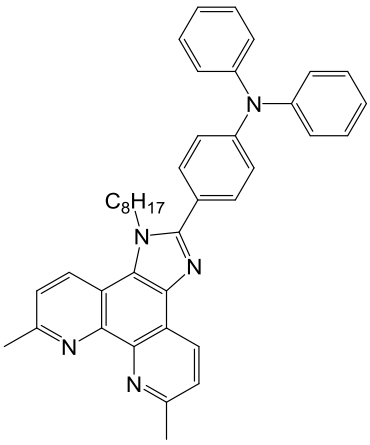

14

Figure 17 – compounds 9-14, ancillary ligands used by the Constable group (continued from previous page)

The *in situ* approach for preparing heteroleptic copper(I) species has also been employed by Hewat *et al*.[101] Copper(I) complexes with dipyrromethene (known as dipyrrin) ligands were synthesised. The group's ligand choice stemmed from the known properties of the boron-dipyrromethene series of dyes, which are highly fluorescent, readily soluble and have a relatively long-lived excited state. The dipyrrin ligands synthesised are shown in Figure 18.

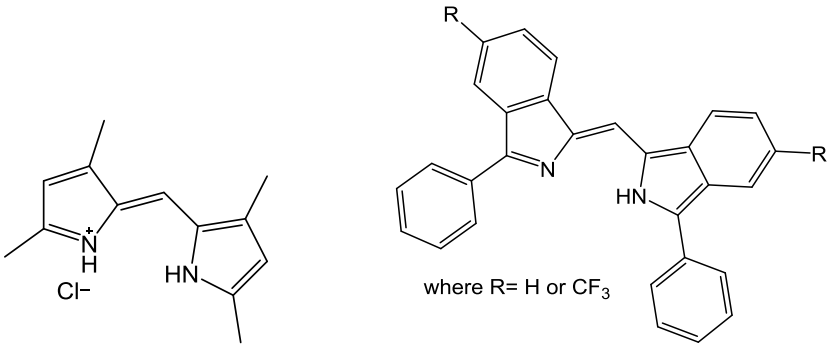

15 **16**

Figure 18 – ligands used to create copper(I) dipyrrin complexes by Hewat and co-workers (redrawn from reference 101)

For DSC application, the anchoring ligand was 4,4′-dicarboxy-6,6′-dimethyl-2,2'-bipyridine (**5,** Figure 15). However, for stability reasons, the spectroscopic and electrochemical properties of the heteroleptic complexes were assessed where ligand **5** contained a methyl group or an ethyl ester in the 4- and 4'-positions instead. Observations regarding the stability of the dyes were made. This is an important point for dye application in DSCs, particularly with heteroleptic complexes where ligand exchange in solution can occur readily to produce a mixture of products. Indeed after 7 and then 17 days it was noted by ^{1}H NMR spectroscopy that the complexes were breaking down in solution. Stability did increase however on moving from ligand **15** to the bulkier variants of **16**. Complexes with the carboxylic acid anchoring group in place were not isolated and instead synthesis was on the TiO_2 surface according to Constable's method.[89] The best DSC efficiencies were between 0.13 and 0.41 %. These rather low values were attributed to the low oxidation potentials of the complexes as determined by electrochemistry, meaning dye regeneration by the I_3^-/I^- couple may have been hindered. Some improvement was observed when the

electron-withdrawing CF_3 groups were introduced into the dipyrrin structure, due to a positive shift in the oxidation potential of the complex. The increase in conjugation on moving from **15** to **16** also led to improvements in the electronic absorption spectrum and DSC efficiencies.

Prior to this, the Robertson group had also published work[100] of a copper(I) dye using one 4,4'-dicarboxy-2,2'-bipyridine ligand (or similar variants of) and one large, geometrically rigid ligand (**17**, Figure 19). The bulky co-ligand negates the need to functionalise the bipy ligand in the 6- and 6'-positions, simplifying the ligand synthesis process. The inflexible ligand of choice was bis{2-(diphenylphosphanyl)phenyl} ether (POP).[100] Crystal structures confirmed that the POP ligand stabilised the copper(I) state as desired with the complex shown to adopt a distorted tetrahedral structure. Although the DSC efficiencies with **17** were low (≤ 0.05 %), the exercise proved that stable heteroleptic complexes could be made, which are synthetically simpler than the 4-,4'- and 6-,6'-substituted analogues. However the POP ligand was not a particularly good sensitizer and exhibited poor light harvesting.

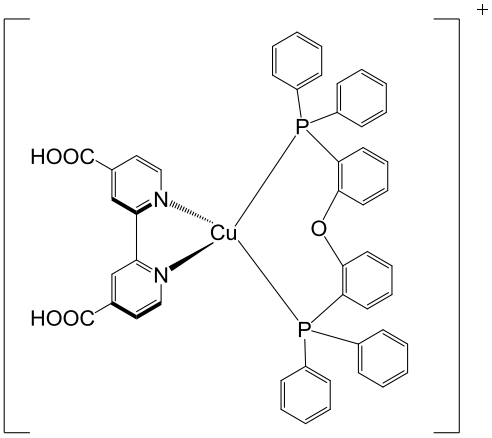

17

Figure 19 – cation of the copper(I) complex from the Robertson group (redrawn from reference 100)

In the same way, Sandroni and co-workers have also recently been synthesising heteroleptic copper(I) complexes for DSC application but with a better light harvesting ancillary ligand.[99] They have successfully assembled stable dyes *via* the HETPHEN strategy. HETPHEN stands for "HETeroleptic PHENanthroline" and this strategy was established by Schmittel *et al* in 1997.[102] It is a means of carefully designing copper(I) complexes which

are stable to the labile ligand exchange reactions that typically make heteroleptic copper(I) complexes difficult to prepare. In other words, an ancillary ligand is selected, which offers sufficient steric bulk to make forming the homoleptic arrangement unfavourable. In this case a 2,9-diaryl phenanthroline ligand is coupled with an anchoring 2,2'-biquinoline-4,4'-dicarboxylic acid. Two complexes were prepared (**18** and **19,** Figure 20); one with a 2,9-dimesityl-1,10'-phenanthroline and a second that was further functionalised with electron donating groups.[99] They demonstrated stable, reversible electrochemistry and exhibited broad electronic absorption spectra with peak absorption between 500 and 600 nm; however their molar extinction coefficients were noted as low. Solar-to-power-conversion efficiencies were also fairly low, at ≤0.71% (dyed area of 0.25 cm^2). Using the measured oxidation potential data, the authors calculated the driving force for electron injection (ΔG_{inj}) and concluded that these low values were responsible for the moderate DSC performances. The 2,2'-biquinoline-4,4'-dicarboxylic acid ligand will be considered in greater detail in Chapter 5.

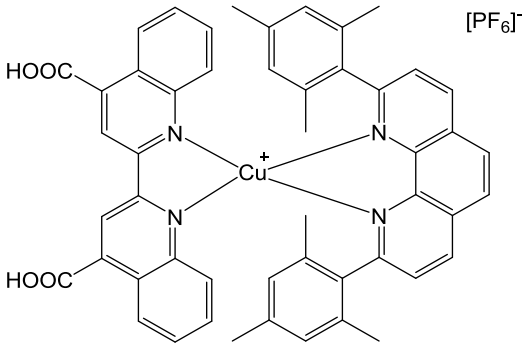

18

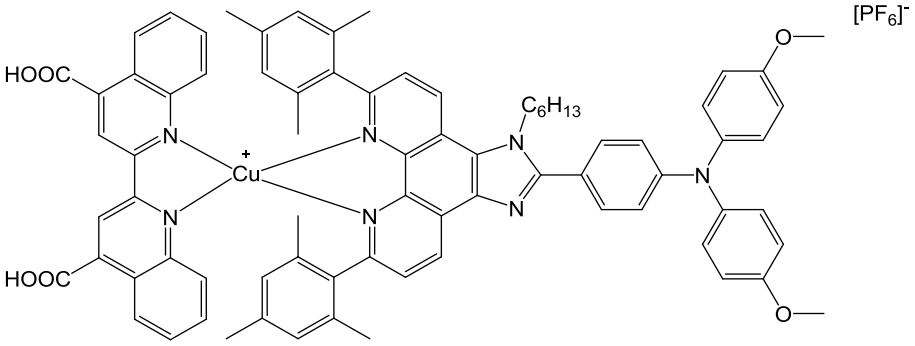

19

Figure 20 – Two heteroleptic complexes synthesised by Sandroni and co-workers (redrawn from reference 99)

In addition to the work by Sandroni and colleagues, copper(I) complexes bound to 2,9-disubstituted-1,10-phenanthroline ligands have been explored to various extents by Constable,[93] Ashbrook[97] and Huang.[78] Constable and Ashbrook have both assembled heteroleptic complexes on TiO_2 *via* the *in situ* ligand exchange strategy and used these photoanodes in cells with a cobalt(II/III) mediator. Constable's communication optimised the cell environment and DSC devices for copper(I) dyes with a cobalt mediator and concluded that comparable efficiencies to those obtained with the I_3^-/I^- couple were possible.[93] TiO_2 film thickness and a $TiCl_4$ post-treatment were both found to be influential towards DSC functionality with a cobalt(II/III) electrolyte. Employing ligands **8** (Figure 15) and **14** (Figure 17) in a copper(I) complex, efficiencies between 0.22% and 2.02% were obtained. The highest efficiency was achieved with a screen-printed 4 layer thickness (12-15 μm) of TiO_2 and 110 h of dipping dye time, with a post-treatment of 60 mM aqueous $TiCl_4$.

A more detailed physical study of copper(I) cells with a cobalt(II/III) mediator was carried out by Ashbrook.[97] The group utilised the same *in situ* stepwise assembly approach to construct heteroleptic 2,9-dimethyl-1,10-phenanthroline complexes and used them in conjunction with $Co(DTB)_3^{2+/3+}$ (where DTB = 4,4'-di-*tert*-butyl-2,2'-bipyridine). Using 2,9-dimethyl-1,10-phenanthroline-5,6-diol as their ligand starting point, the 5,6-diol provided a handle for functionalisation with either anchoring groups or electron donating groups. As one 1,10-phenanthroline ligand was functionalised to coordinate to the TiO_2 surface, the ancillary ligand was modified with an electron donor group (Figure 21).

Rather than focussing principally on DSC device optimisation, Ashbrook used a range of techniques to assess the impact of appending the 2,9-dimethyl-1,10-phenanthroline with the electron donating 10-alkylated 2,4,6,8-tetramethylphenothiazine (TMPTZ). This acts as a secondary electron donor; being rapidly oxidised by the copper(II) species following initial light absorption and electron injection (see Figure 21). The $TMPTZ^+$ is then reduced by the cobalt (II/III) mediator. Variations of these 2,9-dimethyl-1,10-phenanthroline copper(I) complexes, with and without the TMPTZ electron donating group, were studied *via* solution cyclic voltammetry, transient absorption spectroscopy, open-circuit voltage decay and transient current measurements.

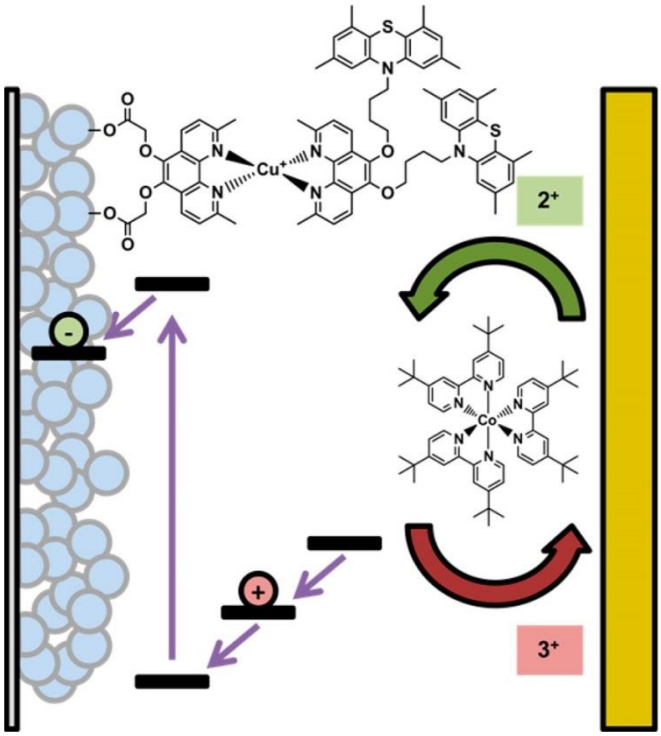

Figure 21 – diagram reproduced from reference 97 showing the functionalisation of the 1,10-phenanthroline ligands and the role of the secondary electron donor

The effect of the solvent environment and electrolyte additives on the copper(II) form of the dye was studied. Where TMPTZ was missing from the ligand, coordination to copper(II) of a solvent molecule or the additive 4-*tert*-butylpyridine was observed through cyclic voltammetry and was found to slow dye regeneration through the formation of adducts. However where TMPTZ was present on the ligand this process was prevented since the copper(II) centre was too rapidly reduced for adducts to form.

This introductory chapter has outlined the wider context to this research, described the dye-sensitized solar cell technology and reviewed progress by other groups with copper(I) dyes as an alternative to ruthenium(II) complexes. The importance of structural control through ligand choice for enhanced stability of the copper(I) complexes has also been highlighted, and will be a recurring point of discussion throughout this thesis.

1.6 References

1. E. Bequerel, *C. R. Acad. Sci.*, 1839, **9**, 145-149.
2. http://unfccc.int/kyoto_protocol/items/2830.php.
3. https://www.gov.uk/government/policies/reducing-the-uk-s-greenhouse-gas-emissions-by-80-by-2050, 06/08/2013.
4. http://ec.europa.eu/energy/renewables/index_en.htm, 06/08/2013.
5. L. M. Peter, *Philos. Trans. R. Soc. A-Math. Phys. Eng. Sci.*, 2011, **369**, 1840-1856.
6. D. M. Bagnall and M. Boreland, *Energ. Policy*, 2008, **36**, 4390-4396.
7. L. El Chaar, L. A. Lamont and N. El Zein, *Renew. Sust. Energ. Rev.*, 2011, **15**, 2165-2175.
8. J. Nelson, *The Physics of Solar Cells*, Imperial College Press, 2003.
9. http://www.nrel.gov/ncpv/, National Renewable Energy Laboratory, Golden, Colorado, 07/08/2013.
10. H. X. Wang, *Int. J. Photoenergy*, 2011.
11. J. H. Heo, S. H. Im, J. H. Noh, T. N. Mandal, C.-S. Lim, J. A. Chang, Y. H. Lee, H.-j. Kim, A. Sarkar, M. K. Nazeeruddin, M. Graetzel and S. I. Seok, *Nat. Photonics*, 2013, **7**, 487-492.
12. M. M. Lee, J. Teuscher, T. Miyasaka, T. N. Murakami and H. J. Snaith, *Science*, 2012, **338**, 643-647.
13. M. Liu, M. B. Johnston and H. J. Snaith, *Nature*, 2013, **501**, 395–398.
14. P. Qin, S. Tanaka, S. Ito, N. Tetreault, K. Manabe, H. Nishino, M. K. Nazeeruddin and M. Gratzel, *Nature communications*, 2014, **5**, 3834-3834.
15. C.-Y. Hsu, Y.-C. Chen, R. Y.-Y. Lin, K.-C. Ho and J. T. Lin, *Phys. Chem. Chem. Phys.*, 2012, **14**, 14099-14109.
16. M. A. Green, K. Emery, Y. Hishikawa, W. Warta and E. D. Dunlop, *Prog. Photovoltaics*, 2013, **21**, 827-837.
17. R. Komiya, A. Fukui, N. Murofushi, N. Koide, R. Yamanaka and H. Katayama, in *Technical Digest, 21st International Photovoltaic Science and Engineering Conference* Fukuoka, 2011.
18. http://www.dyesol.com.
19. http://www.solaronix.com/.
20. http://gcell.com/.
21. http://www.dyesol.com/partners/current-projects/tata-steel, 01/08/2011.
22. B. O' Regan and M. Grätzel, *Nature*, 1991, **353**, 737-740.
23. A. Hagfeldt, G. Boschloo, L. Sun, L. Kloo and H. Pettersson, *Chem. Rev.*, 2010, **110**, 6595-6663.
24. Y. X. Weng, L. Li, Y. Liu, L. Wang and G. Z. Yang, *J. Phys. Chem. B*, 2003, **107**, 4356-4363.
25. J. B. Asbury, R. J. Ellingson, H. N. Ghosh, S. Ferrere, A. J. Nozik and T. Lian, *J. Phys. Chem. B*, 1999, **103**, 3110-3119.
26. G. Benkö, J. Kallioinen, J. E. I. Korppi-Tommola, A. P. Yartsev and V. Sundström, *J. Am. Chem. Soc.*, 2001, **124**, 489-493.
27. S. E. Koops, B. C. O'Regan, P. R. F. Barnes and J. R. Durrant, *J. Am. Chem. Soc.*, 2009, **131**, 4808-4818.
28. N. Martsinovich and A. Troisi, *Energ. Environ. Sci.*, 2011, **4**, 4473-4495.
29. S. A. Haque, Y. Tachibana, D. R. Klug and J. R. Durrant, *J. Phys. Chem. B*, 1998, **102**, 1745-1749.
30. Y. Tachibana, M. K. Nazeeruddin, M. Grätzel, D. R. Klug and J. R. Durrant, *Chem. Phys.*, 2002, **285**, 127-132.
31. N. Robertson, *Angew. Chem.-Int. Edit.*, 2006, **45**, 2338-2345.

32. J. Rouquerol, D. Avnir, C. W. Fairbridge, D. H. Everett, J. H. Haynes, N. Pernicone, J. D. F. Ramsay, K. S. W. Sing and K. K. Unger, *Pure and Applied Chemistry*, 1994, **66**, 1739-1758.
33. P. W. Atkins, T. Overton, J. Rourke, M. Weller and F. Armstrong, *Inorganic Chemistry*, Fourth edn., Oxford University Press, 2006, Chapter 6.
34. P. Roy, S. Berger and P. Schmuki, *Angew. Chem.-Int. Edit.*, 2011, **50**, 2904-2939.
35. P. J. Cameron and L. M. Peter, *J. Phys. Chem. B*, 2003, **107**, 14394-14400.
36. S.-W. Lee, K.-S. Ahn, K. Zhu, N. R. Neale and A. J. Frank, *J. Phys. Chem. C*, 2012, **116**, 21285-21290.
37. C. Bauer, G. Boschloo, E. Mukhtar and A. Hagfeldt, *J. Phys. Chem. B*, 2001, **105**, 5585-5588.
38. K. Keis, E. Magnusson, H. Lindstrom, S. E. Lindquist and A. Hagfeldt, *Sol. Energ. Mat. Sol. Cells*, 2002, **73**, 51-58.
39. S. Ferrere, A. Zaban and B. A. Gregg, *J. Phys. Chem. B*, 1997, **101**, 4490-4493.
40. G. Boschloo and A. Hagfeldt, *Accounts Chem. Res.*, 2009, **42**, 1819-1826.
41. A. Yella, H.-W. Lee, H. N. Tsao, C. Yi, A. K. Chandiran, M. K. Nazeeruddin, E. W.-G. Diau, C.-Y. Yeh, S. M. Zakeeruddin and M. Grätzel, *Science*, 2011, **334**, 629-634.
42. T. Daeneke, Y. Uemura, N. W. Duffy, A. J. Mozer, N. Koumura, U. Bach and L. Spiccia, *Adv. Mater.*, 2012, **24**, 1222-1225.
43. C. H. Law, S. C. Pathirana, X. O. Li, A. Y. Anderson, P. R. F. Barnes, A. Listorti, T. H. Ghaddar and B. C. O'Regan, *Adv. Mater.*, 2010, **22**, 4505-4509.
44. T. A. G. Risbridger, F. A. Castro and P. J. Cameron, *J. Phys. Chem. C*, 2012, **116**, 22253-22260.
45. W. Xiang, F. Huang, Y.-B. Cheng, U. Bach and L. Spiccia, *Energy Environ. Sci.*, 2013, **6**, 121-127.
46. M. Gorlov and L. Kloo, *Dalton Trans.*, 2008, 2655-2666.
47. D. Li, D. Qin, M. Deng, Y. Luo and Q. Meng, *Energ. Environ. Sci.*, 2009, **2**, 283-291.
48. B. E. Hardin, H. J. Snaith and M. D. McGehee, *Nat. Photonics*, 2012, **6**, 162-169.
49. J. Burschka, A. Dualeh, F. Kessler, E. Baranoff, N. L. Cevey-Ha, C. Y. Yi, M. K. Nazeeruddin and M. Gratzel, *J. Am. Chem. Soc.*, 2011, **133**, 18042-18045.
50. M. K. Nazeeruddin and M. Grätzel, *Comprehensive Coordination Chemistry II*, Elsevier, **2004** , Chap. 9.16, p. 719.
51. M. K. Nazeeruddin, E. Baranoff and M. Grätzel, *Sol. Energy*, 2011, **85**, 1172-1178.
52. M. K. Nazeeruddin, A. Kay, I. Rodicio, R. Humphry-Baker, E. Muller, P. Liska, N. Vlachopoulos and M. Grätzel, *J. Am. Chem. Soc.*, 1993, **115**, 6382-6390.
53. M. K. Nazeeruddin, S. M. Zakeeruddin, R. Humphry-Baker, M. Jirousek, P. Liska, N. Vlachopoulos, V. Shklover, C. H. Fischer and M. Grätzel, *Inorg. Chem.*, 1999, **38**, 6298-6305.
54. M. K. Nazeeruddin, P. Pechy and M. Grätzel, *Chem. Commun.*, 1997, 1705-1706.
55. M. Grätzel, *Accounts Chem. Res.*, 2009, **42**, 1788-1798.
56. P. Wang, S. M. Zakeeruddin, J. E. Moser, M. K. Nazeeruddin, T. Sekiguchi and M. Grätzel, *Nat. Mater.*, 2003, **2**, 402-407.
57. Y. M. Cao, Y. Bai, Q. J. Yu, Y. M. Cheng, S. Liu, D. Shi, F. F. Gao and P. Wang, *J. Phys. Chem. C*, 2009, **113**, 6290-6297.
58. Y. Chen, Z. Zeng, C. Li, W. Wang, X. Wang and B. Zhang, *New J. Chem.*, 2005, **29**, 773-776.
59. B. E. Hardin, H. J. Snaith and M. D. McGehee, *Nature Photonics*, 2012, **6**, 162-169.
60. B. C. O'Regan, I. López-Duarte, M. V. Martínez-Díaz, A. Forneli, J. Albero, A. Morandeira, E. Palomares, T. Torres and J. R. Durrant, *J. Am. Chem. Soc.*, 2008, **130**, 2906-2907.

61. H. N. Tsao , C. Yi , T. Moehl, J.-H. Yum, S. M. Zakeeruddin, M. K. Nazeeruddin and M. Grätzel, *ChemSusChem*, 2011, **4**, 591-594.
62. A. Mishra, M. K. R. Fischer and P. Baeuerle, *Angew. Chem.-Int. Edit.*, 2009, **48**, 2474-2499.
63. G. L. Zhang, H. Bala, Y. M. Cheng, D. Shi, X. J. Lv, Q. J. Yu and P. Wang, *Chem. Commun.*, 2009, 2198-2200.
64. B. C. O'Regan, I. Lopez-Duarte, M. V. Martinez-Diaz, A. Forneli, J. Albero, A. Morandeira, E. Palomares, T. Torres and J. R. Durrant, *J. Am. Chem. Soc.*, 2008, **130**, 2906-2907.
65. Dyesol, in *3rd International Conference on Hybrid and Organic Photovoltaics*, Valencia, Spain, 2011.
66. D. R. Lide, *CRC Handbook of Chemistry and Physics*, 85th edn., CRC Press, 2004.
67. N. Armaroli, G. Accorsi, F. Cardinali and A. Listorti, in *Photochemistry and Photophysics of Coordination Compounds I*, eds. V. Balzani and S. Campagna, Springer Berlin Heidelberg, 2007, vol. 280, pp. 69-115.
68. W. B. Jensen, *J. Chem. Educ.*, 2005, **82**, 28-28.
69. P. W. Atkins, T. Overton, J. Rourke, M. Weller and F. Armstrong, *Inorganic Chemistry*, Fourth edn., Oxford University Press, 2006.
70. P. W. Atkins, T. Overton, J. Rourke, M. Weller and F. Armstrong, *Inorganic Chemistry*, Fourth edn., Oxford University Press, 2006, Chapter 17.
71. P. W. Atkins, *Physical Chemistry*, Sixth edn., Oxford University Press, 1998, Chapter 17.
72. http://chemwiki.ucdavis.edu/Physical_Chemistry/Spectroscopy/Electronic_Spectroscopy/Jablonski_diagram, 20/2/2014.
73. http://www.shsu.edu/chm_tgc/chemilumdir/JABLONSKI.html.
74. D. V. Scaltrito, D. W. Thompson, J. A. O'Callaghan and G. J. Meyer, *Coord. Chem. Rev.*, 2000, **208**, 243-266.
75. M. Ruthkosky, C. A. Kelly, F. N. Castellano and G. J. Meyer, *Coord. Chem. Rev.*, 1998, **171**, 309-322.
76. H. A. Jahn and E. Teller, *Proc. R. Soc. London, Ser. A* 1937, **161**, 220-235.
77. M. D. Perez, P. I. Djurovich, A. Hassan, G. Y. Cheng, T. J. Stewart, K. Aznavour, R. Bau and M. E. Thompson, *Chem. Commun.*, 2009, 4215-4217.
78. J. Huang, O. Buyukcakir, M. W. Mara, A. Coskun, N. M. Dimitrijevic, G. Barin, O. Kokhan, A. B. Stickrath, R. Ruppert, D. M. Tiede, J. F. Stoddart, J.-P. Sauvage and L. X. Chen, *Angew. Chem.-Int. Edit.*, 2012, **51**, 12711-12715.
79. J. Kallioinen, G. Benko, V. Sundstrom, J. E. I. Korppi-Tommola and A. P. Yartsev, *J. Phys. Chem. B*, 2002, **106**, 4396-4404.
80. J. Teuscher, J.-D. Decoppet, A. Punzi, S. M. Zakeeruddin, J.-E. Moser and M. Graetzel, *J. Phys. Chem. Lett.*, 2012, **3**, 3786-3790.
81. T. Bessho, E. C. Constable, M. Grätzel, A. H. Redondo, C. E. Housecroft, W. Kylberg, M. K. Nazeeruddin, M. Neuburger and S. Schaffner, *Chem. Commun.*, 2008, 3717-3719.
82. E. C. Constable, A. H. Redondo, C. E. Housecroft, M. Neuburger and S. Schaffner, *Dalton Trans.*, 2009, 6634-6644.
83. N. Alonso-Vante, J. F. Nierengarten and J. P. Sauvage, *J. Chem. Soc.-Dalton Trans.*, 1994, 1649-1654.
84. S. Sakaki, T. Kuroki and T. Hamada, *J. Chem. Soc.-Dalton Trans.*, 2002, 840-842.
85. M. K. Eggleston, D. R. McMillin, K. S. Koenig and A. J. Pallenberg, *Inorg. Chem.*, 1997, **36**, 172-176.
86. R. M. Everly, R. Ziessel, J. Suffert and D. R. McMillin, *Inorg. Chem.*, 1991, **30**, 559-561.

87. C. T. Cunningham, K. L. H. Cunningham, J. F. Michalec and D. R. McMillin, *Inorg. Chem.*, 1999, **38**, 4388-4392.
88. B. Bozic-Weber, E. C. Constable, C. E. Housecroft, M. Neuburger and J. R. Price, *Dalton Trans.*, 2010, **39**, 3585-3594.
89. B. Bozic-Weber, E. C. Constable, C. E. Housecroft, P. Kopecky, M. Neuburger and J. A. Zampese, *Dalton Trans.*, 2011, **40**, 12584-12594.
90. B. Bozic-Weber, V. Chaurin, E. C. Constable, C. E. Housecroft, M. Meuwly, M. Neuburger, J. A. Rudd, E. Schoenhofer and L. Siegfried, *Dalton Trans.*, 2012, **41**, 14157-14169.
91. B. Bozic-Weber, S. Y. Brauchli, E. C. Constable, S. O. Furer, C. E. Housecroft, F. J. Malzner, I. A. Wright and J. A. Zampese, *Dalton Trans.*, 2013, **42**, 12293-12308.
92. B. Bozic-Weber, S. Y. Brauchli, E. C. Constable, S. O. Fuerer, C. E. Housecroft and I. A. Wright, *Phys. Chem. Chem. Phys.*, 2013, **15**, 4500-4504.
93. B. Bozic-Weber, E. C. Constable, S. O. Furer, C. E. Housecroft, L. J. Troxler and J. A. Zampese, *Chem. Commun.*, 2013, **49**, 7222-7224.
94. B. Bozic-Weber, E. C. Constable and C. E. Housecroft, *Coord. Chem. Rev.*, 2013, **257**, 3089-3106.
95. J. Baldenebro-Lopez, J. Castorena-Gonzalez, N. Flores-Holguin, J. Almaral-Sanchez and D. Glossman-Mitnik, *Int. J. Mol. Sci.*, 2012, **13**, 16005-16019.
96. J. Baldenebro-Lopez, N. Flores-Holguin, J. Castorena-Gonzalez and D. Glossman-Mitnik, *J. Photochem. Photobiol., A*, 2013, **267**, 1-5.
97. L. N. Ashbrook and C. M. Elliott, *J. Phys. Chem. C*, 2013, **117**, 3853-3864.
98. X. Q. Lu, S. X. Wei, C. M. L. Wu, S. R. Li and W. Y. Guo, *J. Phys. Chem. C*, 2011, **115**, 3753-3761.
99. M. Sandroni, M. Kayanuma, A. Planchat, N. Szuwarski, E. Blart, Y. Pellegrin, C. Daniel, M. Boujtita and F. Odobel, *Dalton Trans.*, 2013, **42**, 10818-10827.
100. C. L. Linfoot, P. Richardson, T. E. Hewat, O. Moudam, M. M. Forde, A. Collins, F. White and N. Robertson, *Dalton Trans.*, 2010, **39**, 8945-8956.
101. T. E. Hewat, L. J. Yellowlees and N. Robertson, *Dalton Trans.*, 2014, **43**, 4127-4136.
102. M. Schmittel, U. Lüning, M. Meder, A. Ganz, C. Michel and M. Herderich, *Heterocycl. Commun.*, 1997, **3**, 493–498.

Chapter 2 - Theory

2. Theory

This chapter describes the theory behind some of the techniques and measurements used in this research in the context of their application for dye sensitized solar cell (DSC) analysis.

2.1. Calculating DSC efficiency

In Chapter 1 the basic operating principals of a DSC were explained. To measure the performance of a DSC, cells are connected as shown in Figure 22, illuminated at a light intensity equivalent to 1 sun and a current-voltage (*I-V*) curve measured with a potentiostat. The term "1 sun" refers to a standard set of light intensity conditions for solar cell measurements, which is generally at "AM 1.5". AM is an air mass coefficient which defines the path length of the light through the earth's atmosphere and angle of incidence relative to the equator. 1 sun corresponds to a solar intensity of 1000 W m^{-2}.[1]

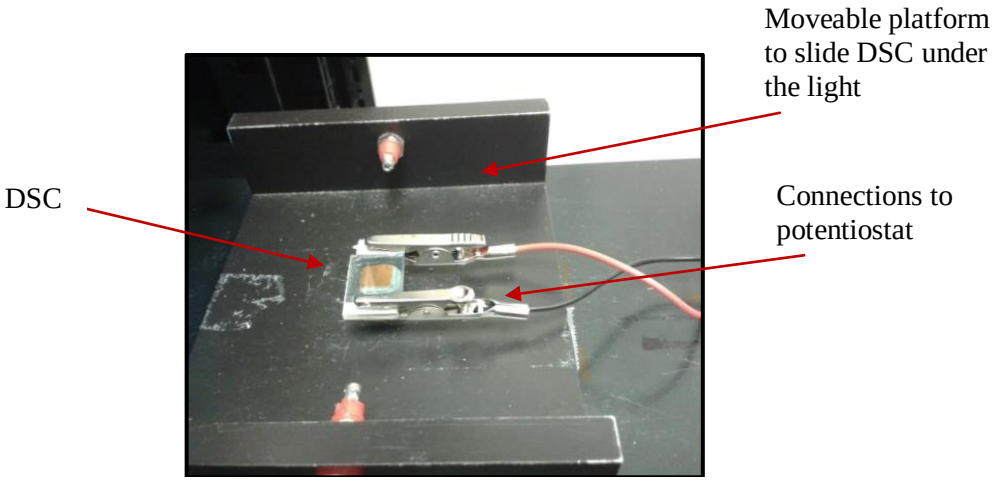

Figure 22 – setup for measuring the efficiency of DSCs

To calculate the solar-to-power conversion efficiency (η) of a DSC, four key parameters are recorded, or calculated, from the *I-V* curve. These are the short-circuit photocurrent (J_{SC}), the open-circuit photovoltage (V_{OC}), the maximum power point (P_{max}) and the fill factor (*FF*), as labelled in Figure 23.

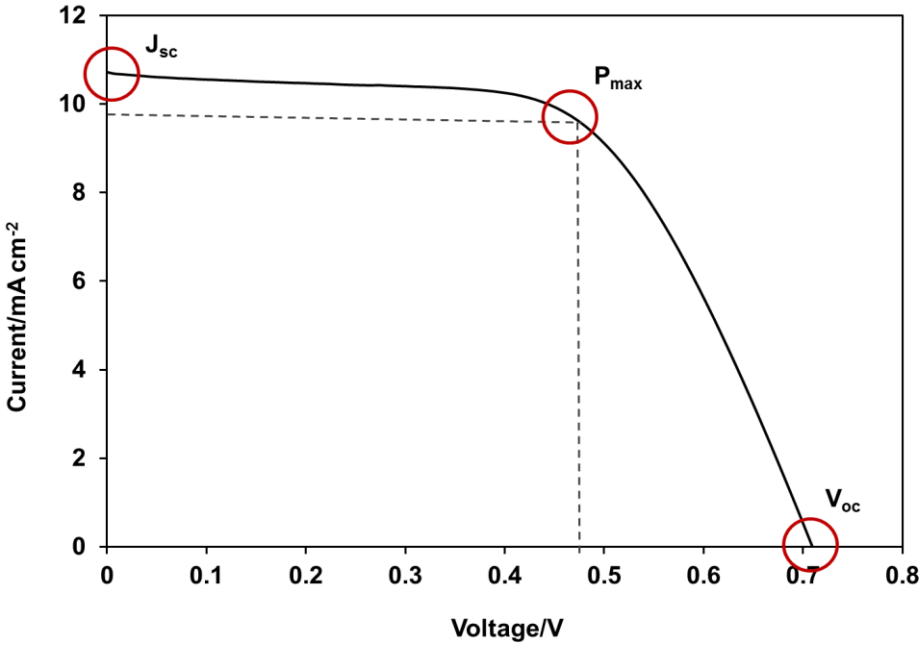

Figure 23 – *I-V* curve with key parameters marked

P_{max} is the product of the photocurrent and photovoltage measured where the power output of the cell is at its maximum. The fill factor, which is a value between 0 and 1, is the ratio of the maximum power from the solar cell to the product of V_{OC} and J_{SC} as shown in Equation 1. It can be interpreted as the "squareness" of the *I-V* curve, as marked by the dotted line in Figure 23. A low fill factor can be indicative of high resistance within the DSC.

$$FF = \left(\frac{P_{\max}}{V_{OC} J_{SC}} \right)$$

Equation 1

These values are used together with the total solar power incident on the cell (P_{in}) to calculate η (Equation 2).

$$\eta = \left(\frac{J_{SC} V_{OC} FF}{P_{in}} \right) * 100$$

Equation 2

It is useful to consider how these values arise in relation to operation of a DSC. The photovoltage arises as the difference between the Fermi energy level (E_f) in the semiconductor and the potential of the redox species in the electrolyte (Figure 24). The Fermi level is defined as the point where the probability of finding an electron is 0.5 and it may exist either in an occupied band or in a band gap. In a semiconductor such as TiO_2, E_f is close enough to the conduction band (E_{cb}) energy to be thermally populated with electrons.[2] In the dark, E_f and the electrolyte redox potential are equal. However, upon illumination electrons are injected into the TiO_2 conduction band and E_f is raised, causing the splitting shown in Figure 24. E_{cb} and E_f are very sensitive to the conditions at the TiO_2 surface. Their positions can be shifted positively or negatively through changes in the pH of the surrounding environment, e.g. through the presence of certain additives in the electrolyte.

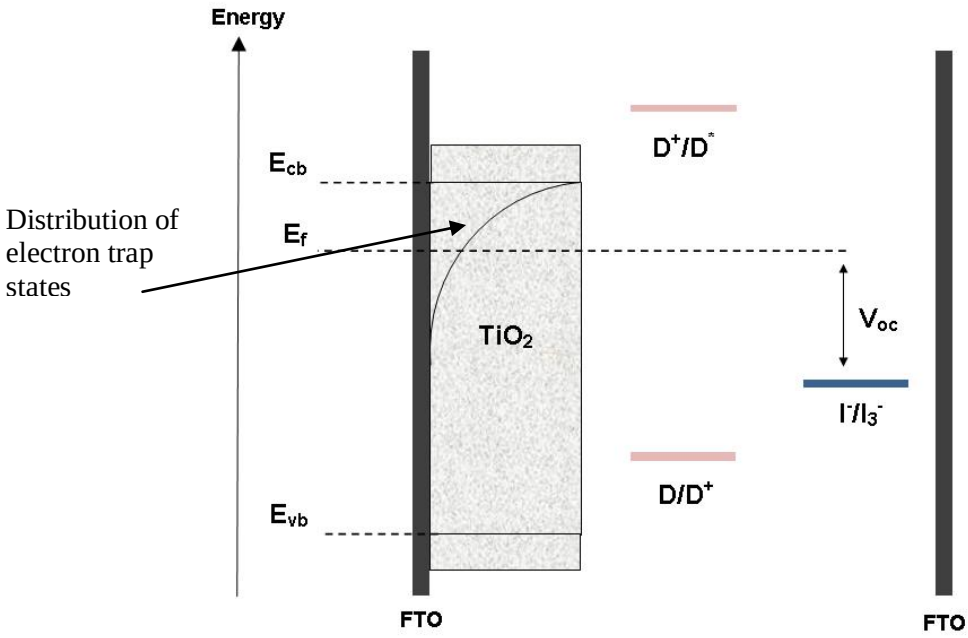

Figure 24 – energy level diagram of a DSC, where E_f, E_{vb} and E_{cb} are the Fermi energy level, the valence band energy and the conduction band energy of the semiconductor respectively. D/D^+ and D^+/D^* are the ground and excited state energies of the dye (redrawn from reference 3)

The amount of current generated is dictated by a combination of factors:

- The light harvesting efficiency, which depends on the dye absorption properties and surface coverage.

- Electron injection efficiency, which depends on appropriate energy level matching between D^+/D^* and E_{cb}.
- Charge collection efficiency, which depends on competition from a recombination reaction between the injected electrons and the oxidised species in the electrolyte.

2.2. Incident Photon to Current Efficiency Measurements (IPCE)

IPCE measurements calculate the ratio of electrons which result in the external circuit to the number of photons incident on the cell, as a function of wavelength. This is also known as the external quantum efficiency (EQE). A high IPCE at a particular wavelength means that almost every photon absorbed by the dye in this region is leading to an electron in the external circuit, i.e. a high IPCE over a broad wavelength range generally indicates a high efficiency cell. To calculate the IPCE, Equation 3 is used.[1]

$$IPCE(\%) = \left(\frac{1250 * J_{SC}}{wavelength * photonflux} \right)$$

Equation 3

Equation 3 combines the value of *hc* (1250) in eV nm (where *h* is Plank's constant; 6.626×10^{-34} J s and *c* is the speed of light; 3.00×10^{8} m s^{-1}), J_{SC} is the photocurrent density (mA cm^{-2}), wavelength (nm) and photon flux (W m^{-2}). The IPCE spectrum will generally look similar to the electronic absorption spectrum of a dye.

2.3. Cyclic Voltammetry (CV)

Electrochemistry studies electron transfer reactions at an electrode surface.[4] Cyclic voltammetry is an example of an electrochemical experiment which can be used to probe the oxidation and reduction processes which the dye undergoes, both in solution and on the surface on a TiO_2 film. CV is used in this thesis to estimate the HOMO energy level, and then to use this value in conjunction with UV/Vis data to estimate the LUMO. CV is also useful for probing reaction mechanisms, for example where there are electrochemical/chemical steps. Therefore the technique is also used in this thesis for probing the regeneration of the dye by iodide. In order to make the best use of the CV

technique and to understand the results obtained from a CV experiment, a consideration of the background operating principals and theory is essential.

CV is typically carried out in a three-electrode system; consisting of a working electrode (WE), counter electrode (CE) and a reference electrode (RE) (Figure 25). Current passes between the working and the counter electrode and the change in potential is measured between the working and the reference electrode. The counter electrode is typically an inert material such as platinum and should have a large surface area to ensure efficient electron transfer. The reference electrode has a fixed potential drop across the electrode and electrolyte interface, which allows measurement and control of the working electrode/electrolyte potential drop.

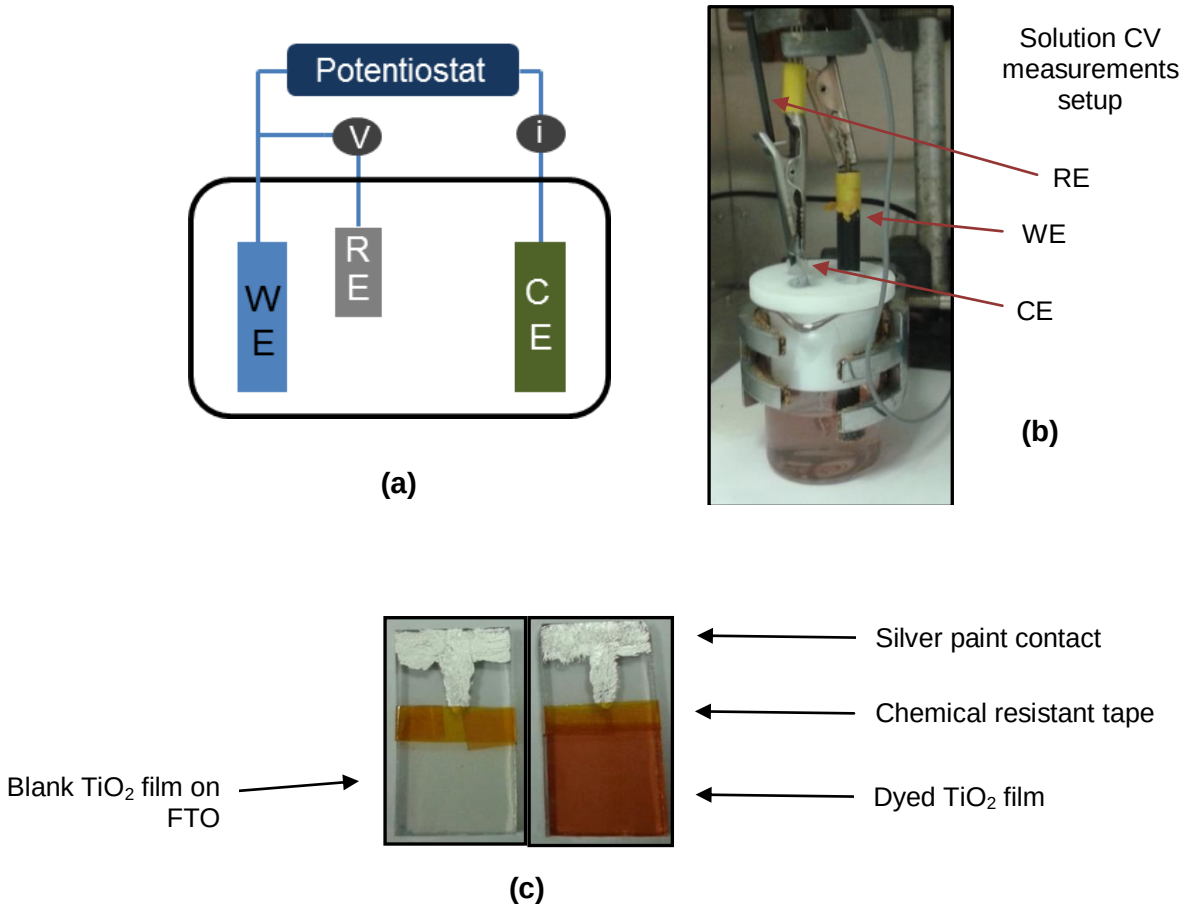

Figure 25 – (a) schematic of an electrochemical cell; (b) setup for solution CV experiments; (c) working electrode design for surface CV experiments

In CV, an applied potential is swept from a starting point to a defined second potential and then back again. This is in contrast to linear sweep voltammetry which scans in only one direction. CV is performed on a static solution (i.e. unstirred) and reactions occur as the species of interest either gains or loses an electron at the working electrode surface. The two principle factors which govern a CV reaction are the rate at which the species of interest reaches the electrode surface (mass transport) and the rate of electron transfer between the reactant molecule and the electrode (kinetic effects) (Figure 26).

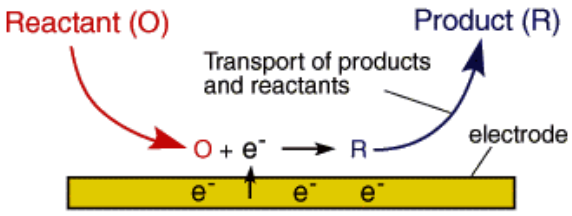

Figure 26 – diagram showing how reactions occur in an electrochemical experiment (reproduced from reference 5)

Mass transport encompasses diffusion, convection and migration processes.[4] In terms of cyclic voltammetry, diffusion is the main contributing effect. Convection is avoided through using a stationary solution, although there will always be a small amount of natural convection. Migration effects arise from the influence of the electric field at the electrode/solution interface on ions, inducing their movement to or from the electrode. This leads to changes in the electric field and hence an overall variation in the migratory flux. These variations in the system make data interpretation difficult; therefore it is preferable to eliminate migratory effects. This is achieved by using a high-concentration background electrolyte (e.g. 0.1 M aqueous KNO_3), which helps to maintain electrical neutrality across the bulk solution by causing a potential drop at the electrode surface. To further understand the role of the background electrolyte it is necessary to consider the nature of the electrode/solution interface (Figure 27).

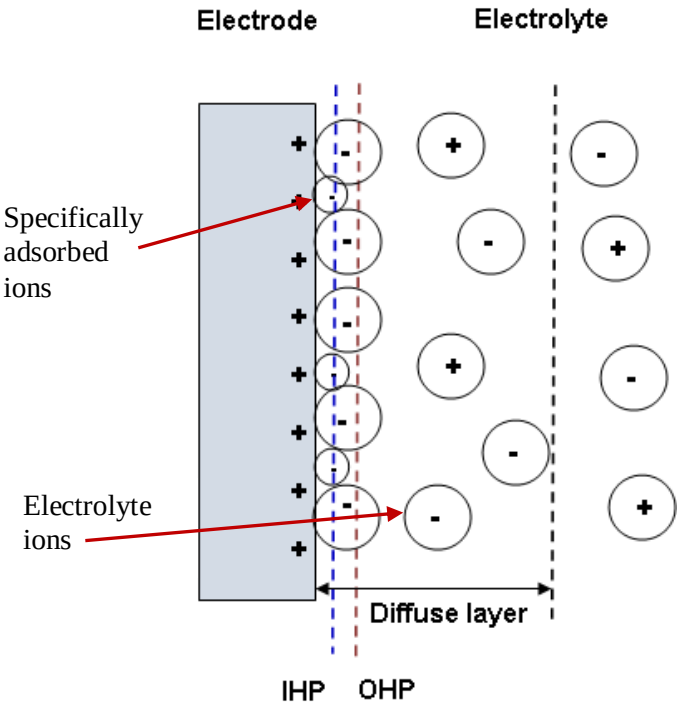

Figure 27 – diagram of the electrical double layer, with the Inner (IHP) and Outer Helmholtz (OHP) planes marked (redrawn from reference 4)

An electrode will always have a very slight charge at its surface, due to an excess or deficiency of electrons. This induces an equal but opposite response of the ions in solution. However these ions can only approach the electrode surface to a distance defined by their solvation shells, i.e. there is layer of solvent molecules between the ions and the electrode.

This electrode/electrolyte interface is termed the Helmholtz electrical double layer and describes the separation of these two layers of charge. The Outer Helmholtz Plane (OHP) is shown in Figure 27 and it marks the minimum distance of approach of solvated ions to the electrode surface. Over this distance there will be a potential drop. Extensions of this simple model include the identification of the Inner Helmholtz Plane (IHP), which marks the centrepoint of specifically adsorbed ions in direct contact with the electrode surface i.e. if some ions were present within the monolayer of solvent molecules. Modifications were also made by Gouy and Chapman, Stern and Grahame, who concluded that the potential drop actually took place over a thicker diffuse layer than initially thought.[4, 6, 7] In order to allow the reactant molecules to get sufficiently close to the electrode surface, the distance of this potential drop should be minimised. The background electrolyte collapses the electrical double layer to help achieve this. The electrolyte also increases the conductivity of the solution and maintains a constant ionic strength in solution during the experiment. Choice

of electrolyte is an important part of CV experiment planning. For example, many dyes studied for DSCs are insoluble in water therefore conducting a solution based CV experiment in an aqueous background electrolyte would cause the dye to precipitate during the experiment and interfere with reliable measurements.

Once these migratory effects have been eliminated the main factor to consider is diffusion, which is the movement of ions along a concentration gradient. The rate of diffusion at any point can be defined through Fick's first law of diffusion (Equation 4), where j is the diffusional flux (moles of material diffusing through a unit area in one second) for a species B; D_B is a diffusion coefficient (in units of distance per unit time) and x is the position.

$$j = -D_B\left(\frac{\delta[B]}{\delta x}\right)$$

Equation 4

A consideration of diffusion is required to understand the shape of a cyclic voltammogram. As the potential is swept to increasingly positive values, electrons begin to be transferred from the HOMO of the electroactive species to the electrode, which results in an oxidative current flowing and an increasing rate constant. This current will increase as long as the reactant species, *B*, at the electrode surface can be replaced rapidly enough by diffusion of fresh material from the bulk solution. A "diffusion layer" builds up over time in which species *B* has been depleted. The response of the system after the peak current has been reached is thus due to diffusion limitation, since reactant species need to travel further to reach the electrode.

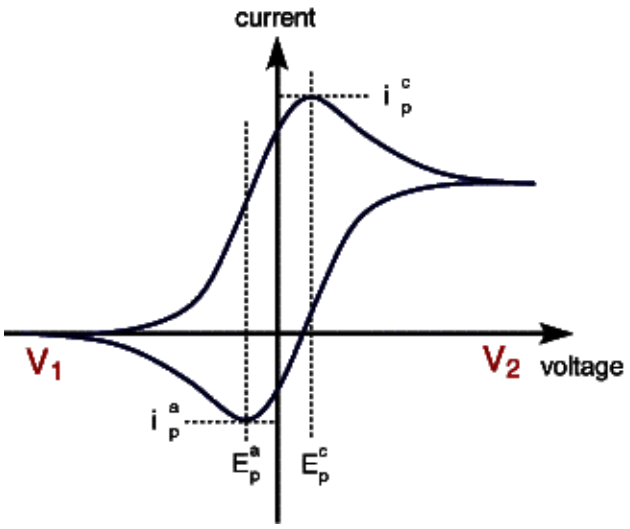

Figure 28 – typical form of a reversible cyclic voltammogram, where i_p^c is the peak cathodic current, i_p^a is the peak anodic current, E_p^a is the peak anodic potential and E_p^c is the peak cathodic potential (reproduced from reference 8)

The Nernst equation relates the concentrations of the oxidised and reduced species to the equilibrium potential at the electrode.[6]

$$E = E^0 + \left(\frac{RT}{nF}\right)\ln\left(\frac{a_O}{a_R}\right)$$

Equation 5

E is the equilibrium potential of the electrode, E^0 is the standard electrode potential, a_O and a_R are the activity coefficients of the oxidised and reduced species, F is the Faraday constant (96,485 C mol^{-1}), R is the ideal gas constant (8.314 J K^{-1} mol^{-1}), T is the temperature (K) and n is the number of electrons transferred in the reaction. However, it is usually more convenient to replace the activities with concentrations and assume the activity coefficients are unity. This can be done by using the measured cell potential, known as the formal electrode potential $E^{0'}$, which modifies Equation 5 to Equation 6, where [O] and [R] are the concentrations of oxidised and reduced species respectively:

$$E = E^{0'} + \left(\frac{RT}{nF}\right)\ln\frac{[O]}{[R]}$$

Equation 6

Under equilibrium conditions the concentrations of the oxidised and reduced species at the electrode surface are equal, therefore the equilibrium potential is equal to the formal electrode potential. A term commonly referred to in this thesis is the half wave potential, $E_{1/2}$, which is calculated from $[(E_p^a - E_p^c)/2]$ in a cyclic voltammogram. $E_{1/2}$ is related to the formal potential according to Equation 7, where D_R and D_O are the diffusion coefficients of the reduced and oxidised species respectively. When the ratio of D_R/D_O is unity, then $E_{1/2}$ is equal to $E^{0'}$.

$$E_{1/2} = E^{0'} + \left(\frac{RT}{nF}\right)\ln\left(\frac{D_R}{D_O}\right)^{1/2}$$

Equation 7

After consideration of mass transport effects, the second factor which determines reactivity at an electrode surface is the kinetic feasibility. An electron transfer process is described as reversible, irreversible or quasi-reversible. To be ideally reversible certain criteria need to be met:

- The magnitude of the two current peaks is the same
- The potential difference between the two current peaks is 59 mV for a one electron transfer process
- Peak potential separation is independent of scan rate
- The peak currents are proportional to the square root of scan rate

Irreversible electron kinetics may occur, for example, if the oxidised species is chemically unstable and reacts before it can be reduced at the electrode surface. Alternatively, a large overpotential may be required to oxidise/reduce the species, meaning the peak potential separation is much greater than 59 mV.

2.4. Electrochemical Impedance Spectroscopy (EIS)

EIS is a versatile technique from which a lot of data about electron transfer processes at the interfaces in a DSC can be obtained. A brief overview will be provided here in the context of its use in this research, however more detailed explanations of the topic are available in the literature.[9]

EIS measures the complex resistance to the flow of electrical current in a circuit. A small, oscillating sinusoidal potential (E_t, Equation 8, where E_m is the amplitude of the signal, f is the frequency and t is time) is applied to an electrochemical cell and the current response is measured.

$$E_t = E_m \sin(2\pi f t)$$

Equation 8

In a linear system the current response, I_t, will be at the same frequency as the applied potential but can be shifted in phase by a quantity, θ (Figure 29).

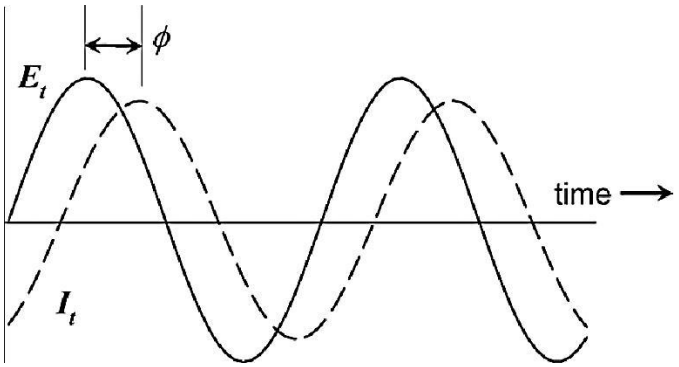

Figure 29 – the current response in a linear system (reproduced from reference 10)

I_t will have an amplitude different to I_m, where I_m is the maximum current amplitude and θ is the phase difference between the applied voltage and detected current (Equation 9).

$$I_t = \mathrm{I_m} \sin(2\pi f t + \theta)$$

Equation 9

The capacitance, *C*, can be related to the detected current through the relationship in Equation 10.

$$I_t = C\frac{dE}{dt} = C(2\pi f E_m \cos(2\pi f t))$$

Equation 10

which is equivalent to Equation 11.

$$I_t = C(2\pi f E_m \sin(2\pi f t + \frac{\pi}{2}))$$

Equation 11

It can therefore be seen that the phase difference between the current and voltage in the case of a capacitor is $\pi/2$. In a similar arrangement to Ohm's Law, the impedance of the system can be calculated from Equation 12.

$$\mathrm{Z} = \frac{E_t}{I_t}$$

Equation 12

Therefore the impedance response of a capacitor can be shown according to Equation 13.

$$\mathrm{Z} = \frac{1}{(2\pi f C)}$$

Equation 13

The impedance of a resistor is simpler. Substitution of Equation 8 and Equation 9 into Ohm's Law (Equation 14) produces
Equation 15.

$$E = IR$$

Equation 14

$$\mathrm{R} = \frac{E_m \sin(2\pi ft)}{\mathrm{I_m} \sin(2\pi ft + \theta)}$$

Equation 15

For a resistor there is no change in phase, i.e. $\theta = 0$. Therefore this cancels out to generate Equation 16, where $R=Z$.

$$\mathrm{R} = \frac{E_m}{\mathrm{I_m}} = Z$$

Equation 16

The phase difference between the current and voltage can take any value and can change with frequency. The impedance, Z, at a particular frequency can be represented as a complex number, as shown in Equation 17.

$$Z(f) = Z'\sin(2\pi ft) - Z''\cos(2\pi ft)$$

Equation 17

Z' is the "real" part, plotted on the x-axis, and –Z'' is the imaginary part, plotted on the y-axis. This produces a Nyquist plot, where each data point is an impedance measurement taken at one frequency. In order to understand the impedance response of a system, an equivalent circuit model is fitted to the data. As a frequency-based technique, EIS takes advantage of the fact that the physiochemical processes taking place in each component of a DSC are frequency dependent i.e. their separate responses to the a.c. potential modulation can be identified. A simple example of such a plot is shown in Figure 30, with the equivalent circuit shown in the inset.

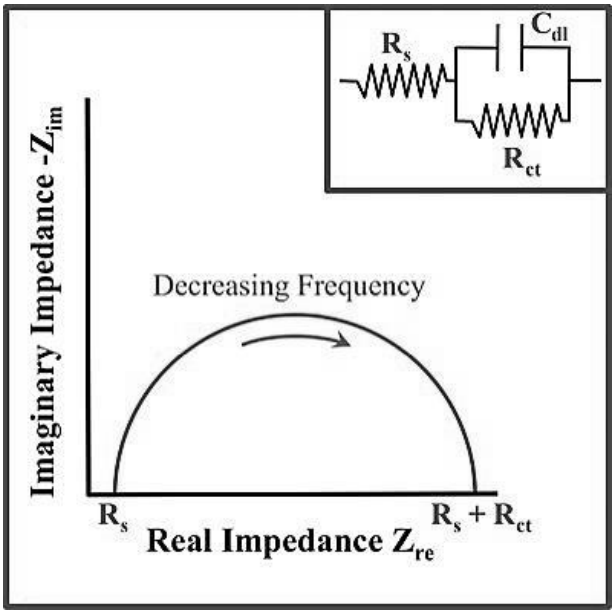

Figure 30 – an impedance plot for a parallel RC circuit (where R_{ct} = resistance to charge transfer and C_{dl} = double layer capacitance), in series with a resistor (R_s). (Reproduced from reference 11)

The characteristic semi-circle arises since the current will pass predominately through either C_{dl} or R_{ct}, depending on the frequency. At high frequencies the current passes through the capacitor, whereas at low frequencies it mainly passes through the resistor. The total impedance at low frequencies is the sum of R_s and R_{ct} whereas as high frequencies the impedance value tends towards zero. However it will be shifted along the x-axis by R_s since the current will still encounter the impedance of R_s. The typical equivalent circuit for modelling a DSC response is more complex.

A built-in extended element (DX type 11-Bisquert #2) is used to represent the mesoporous semiconductor film and models the electron diffusion and recombination processes in the TiO_2 (Figure 31).[9] It comprises a combination of simple resistance and capacitance elements and accounts for the fact that electrons need to move *via* diffusion in order to be collected at the contact point. This diffusive transport introduces the opportunity for recombination to occur at a number of points and also leads to a chemical capacitance across the film.

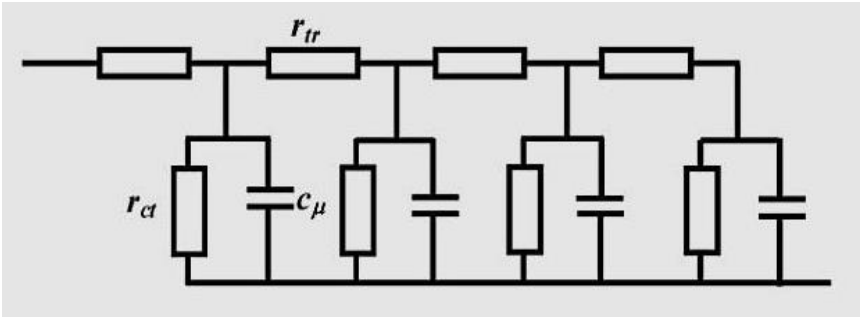

Figure 31 – the extended element used to represent the TiO_2 film impedance response (reproduced from reference 12)

The typical DSC equivalent circuit and impedance response, showing the separate physical processes in a cell, is shown in Figure 32. The small semi-circle at high frequency corresponds to processes at the counter electrode interface, C_{dl} and R_{ct}. The charge transfer processes in the TiO_2 film are represented by a straight line extending ~45° away from the x-axis and in the larger semicircle. A further element is the Warburg impedance, W, which models the diffusion of the redox species in the electrolyte and is observed at low frequencies.

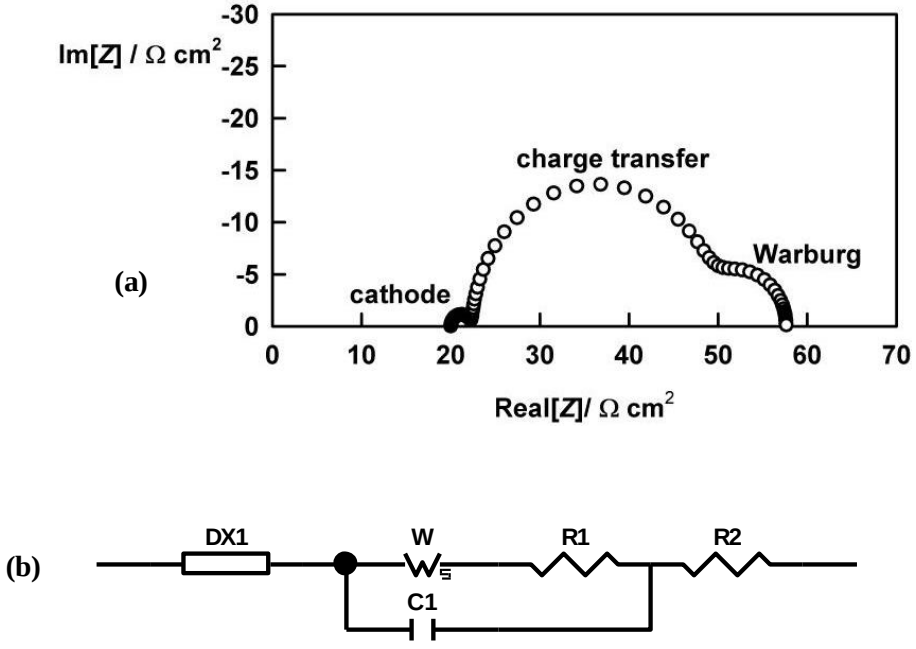

Figure 32 – (a) a typical DSC impedance plot (diagram reproduced from reference 12) and (b) an equivalent circuit

With DSCs, EIS is used to provide a measure of the electron collection efficiency versus electron recombination reactions, either with triiodide in the electrolyte or with oxidised dye molecules. This is achieved through calculation of the electron diffusion length, L_n (Equation 18), and the effective electron lifetime, τ_n (Equation 19).[9, 13] The diffusion length is the average distance an electron diffuses through the TiO_2 film before it is lost in one of the recombination processes mentioned previously. Therefore it is desirable that $L_n > L$, where L is the TiO_2 film thickness. Similarly, the effective electron lifetime is the average time an electron will remain free before it undergoes a recombination reaction. Therefore it is desirable that τ_n is greater than the time it takes for charge extraction.

$$L_n = L\left(\frac{r_{rec}}{r_{tr}}\right)^{1/2}$$

Equation 18

$$\tau_n = r_{rec}.C_\mu$$

Equation 19

The values of r_{rec} (the recombination resistance between electrons in the TiO_2 film and ions in the electrolyte), r_{tr} (the transport resistance for electrons in the TiO_2 film) and c_μ (the chemical capacitance) can all be acquired from impedance plots.

2.5. Open-Circuit Photovoltage Decay (OCVD)

An OCVD measurement allows calculation of the effective electron lifetime, τ_n, as a function of photovoltage or charge density and also provides a way of assessing how effective a blocking layer is.[14, 15] Blocking layers are used normally to prevent electrons undergoing a back reaction with triiodide ions in the electrolyte.[14] A cell is illuminated at open circuit in order to populate the TiO_2 conduction band with electrons injected from the photoexcited dye. Provided that dye regeneration occurs efficiently *via* the electrolyte, this electron injection occurs at a constant and stable rate. However the concentration of electrons in the TiO_2 substrate is also affected by the competing recombination reaction with the oxidised component of the electrolyte. The cell is illuminated for a set period of time, to obtain a steady photovoltage, and the illumination is then switched off. The

photovoltage immediately starts to decay (Figure 33) as electrons leave the TiO_2 film and undergo recombination.

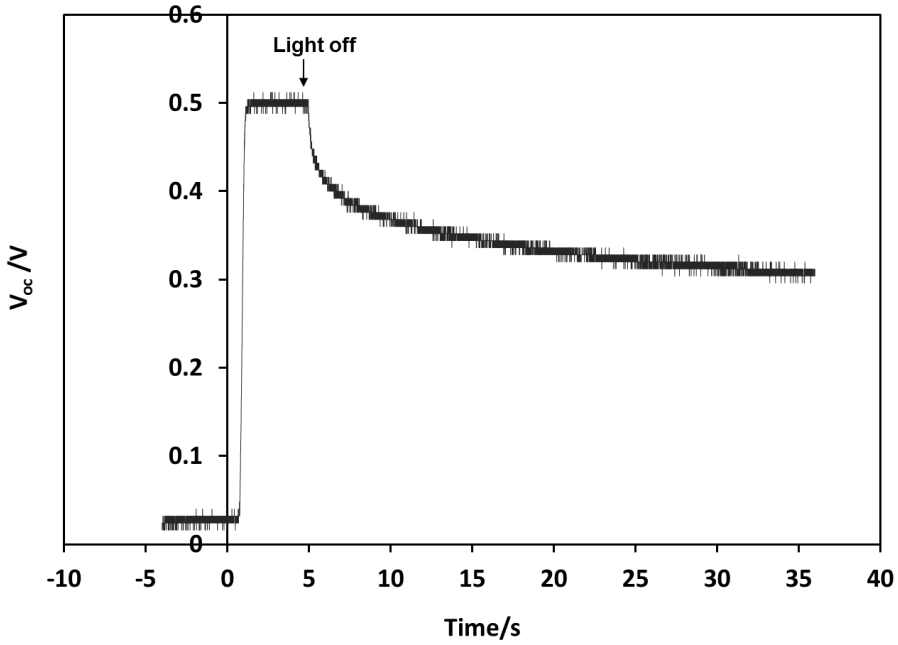

Figure 33 – DSC voltage decay with time under open circuit conditions

This decay is initially very rapid due to the high concentration of electrons in the film available for recombination, however the decay in V_{OC} slows at longer times. This slowing can be understood by considering electron transport through the TiO_2 film. Research has shown that electrons exist more predominantly in trap states in the TiO_2 film than in the conduction band.[12] Although transport to the FTO contact is driven by diffusion along a concentration gradient, trapping and detrapping processes can complicate this. Trap states are localised energy states that exist in the bandgap of the TiO_2, although the exact nature of them remains under debate.[16] It is generally accepted that transport through the TiO_2 film takes place as electrons are trapped and thermally detrapped between these states and the TiO_2 conduction band. Therefore as the density of electrons in the conduction band increases under illumination and the Fermi energy level moves up, so the density of trapped electrons increases. Once the illumination has been interrupted the Fermi-level starts to drop, which lowers the density of conduction band electrons. Therefore the electron lifetime increases, since it is inversely proportional to the concentration of conduction band electrons.[12] The recombination rate therefore decreases as the concentration of conduction band electrons decreases, hence slowing the decay in photovoltage.

From the gradient of the decay curve, τ_n can be calculated using Equation 20, where k_B is the Boltzmann constant (J K^{-1}), T is temperature (K) and q is the elementary charge (C).[13, 15]

$$\tau_n = -\frac{k_B T}{q}\left(\frac{dU_{photo}(t)}{dt}\right)^{-1}$$

Equation 20

2.6. Density Functional Theory (DFT) calculations

In DSC research, DFT and time dependent (TD) DFT measurements are used to estimate key properties of a dye, such as energy levels and electronic transitions. They are used to such effect in this thesis and the calculations were carried out by collaborators Gerko Oskam, Humberto J. Mandujano-Ramírez and Gabriel Merino at CINVESTAV IPN, Dept. Fis Aplicada, Merida 97310, Yucatan, Mexico.

DFT derives from *ab initio* molecular orbital calculations, which are ultimately based on the Schrödinger equation (Equation 21, where $\hat{H}$ is the Hamiltonian operator acting on the wavefunction, ψ, to determine the permitted energy levels, E, of a molecule).

$$\hat{H}\psi = E\psi$$

Equation 21

As it is impossible to solve the Schrödinger equation for molecules with more than one electron, certain approximations must be made. The Hamiltonian operator contains all of the energy terms of the molecule, i.e. the kinetic and potential energy terms.[17] The Born-Oppenheimer approximation is applied to the system, which assumes that nuclei are stationary since they are significantly heavier than electrons.[2] This approximation removes the energy terms related to the nuclei from $\hat{H}$.

The next step is to approximate the electron-related energies. The problem with considering a "many-body" system is that electron motion is correlated, i.e. they interact and have an effect on each other. In order to solve the Schrödinger Equation for one electron at a time, it can be assumed that each electron moves in a uniform field. This electron-electron

correlation energy typically only accounts for ~5% of the total system energy. The electron-electron exchange energy, i.e. whether the electron is spin "up" or "down" can also be modelled. Applying these two approximations together is called Hartree-Fock theory. This is one of the earliest types of *ab initio* calculation. Over time, higher levels of theory have developed which try to approximate the correlation energy (e.g. Møller-Plesset,[18] coupled cluster). DFT evolved from these traditional quantum chemistry methods as a route for approximating the electron-electron correlation energy. DFT depends only on calculating the electron density, which depends only on spatial variables, and therefore disregards electron spin. It achieves this through a set of equations known as a functional. DFT is often combined with Hartree-Fock theory to create hybrid DFT, as it is a relatively fast and accurate way of solving computational problems.

The wavefunction, ψ, locates the permitted orbital energies of electrons. The atomic radial distribution functions can be approximated using Gaussian functions, which are summed together to produce a basis set. The basis set describes the regions where electrons can be located. Since the basis set is suited for isolated atoms, other functions need to be applied in order for the basis set to work for molecular systems. These include polarisation functions and diffuse functions. The wavefunction can be calculated and recalculated through the Schrödinger equation until the lowest energy state for the molecule is found i.e. geometry optimisation.

Generally a range of functionals and basis sets will be investigated to see what best suits the system of interest. TD-DFT is an extension of DFT and uses a time-dependent electronic density rather than the "many-body" wavefunction as in DFT. It can be used to calculate excited state energies of molecules and simulate electronic absorption spectra.

2.7. References

1. M. K. Nazeeruddin and M. Grätzel, *Comprehensive Coordination Chemistry II*, Elsevier, **2004** , Chap. 9.16, p. 719.
2. P. W. Atkins, *Physical Chemistry*, Sixth edn., Oxford University Press, 1998, Chapter 14.
3. T. W. Hamann, R. A. Jensen, A. B. F. Martinson, H. Van Ryswyk and J. T. Hupp, *Energ. Environ. Sci.*, 2008, **1**, 66-78.
4. A. C. Fisher, *Electrode Dynamics*, Oxford University Press, 2005.
5. http://www.cheng.cam.ac.uk/research/groups/electrochem/JAVA/electrochemistry/ELEC/l2html/l2mt.html.
6. A. J. Bard and L. R. Faulkner, *Electrochemical Methods - Fundamentals and Applications*, Second edn., Wiley, 2001.
7. D. C. Grahame, *Chem. Rev.*, 1947, **41**, 441-501.
8. http://www.ceb.cam.ac.uk/research/groups/rg-eme/teaching-notes/linear-sweep-and-cyclic-voltametry-the-principles.
9. J. Bisquert and F. Fabregat-Santiago, *Dye-Sensitized Solar Cells*, EPFL Press, 2010, Chapter 12, p. 457.
10. H. D. ErtuğruL and Z. O. Uygun, *Impedimetric Biosensors for Label-Free and Enzymless Detection*, 2013.
11. http://www.gscsg.com/Electrochemical%20Impedance%20Spectroscopy.html.
12. A. Hagfeldt and L. Peter, *Dye-Sensitized Solar Cells*, EPFL Press, 2010, Chapter 10.
13. J. Bisquert, F. Fabregat-Santiago, I. Mora-Sero, G. Garcia-Belmonte and S. Gimenez, *J. Phys. Chem. C*, 2009, **113**, 17278-17290.
14. P. J. Cameron and L. M. Peter, *J. Phys. Chem. B*, 2003, **107**, 14394-14400.
15. A. Zaban, M. Greenshtein and J. Bisquert, *ChemPhysChem*, 2003, **4**, 859-864.
16. L. Peter, *Accounts Chem. Res.*, 2009, **42**, 1839-1847.
17. A. C. Phillips, *Introduction to Quantum Mechanics*, Wiley, 2003.
18. C. Møller and M. S. Plesset, *Phys. Rev.*, 1934, **46**, 618-622.

Chapter 3 - Experimental

3. Experimental

3.1 General procedures

All chemicals and reagents were obtained from major suppliers and used as bought, unless otherwise stated. Reactions which required the use of anhydrous, inert-atmosphere techniques were carried out under nitrogen or argon, using a high vacuum Schlenk line. NMR spectra were run on either Bruker Avance 250, 300, 400 or 500 MHz instruments at 298 K. ^{1}H and ^{13}C NMR spectra were referenced to residual solvent. ^{31}P and ^{19}F measurements were referenced to H_3PO_4 and $CFCl_3$ respectively. Mass spectra were recorded in-house with a Bruker Daltonik micrOTOF electrospray time-of-flight (ESI-TOF) mass spectrometer or submitted to the EPSRC National Mass Spectrometry Service Centre in Swansea. Elemental analyses were run in-house using an Exeter Analytical CE 440 analyzer or carried out by Stephen Boyer at London Metropolitan University. IR spectra were recorded on a Perkin-Elmer 1600 FT IR spectrometer, with absorption maxima (ν_{max}) recorded in wavenumbers (cm^{-1}) and described as strong (s), medium (m), weak (w) and broad (br). All crystallographic data were collected on a Nonius kappa CCD diffractometer with MoK α radiation, λ = 0.71073 Å. T = 150(2) K throughout and all structures were solved by direct methods and refined on F^2 data using the SHELXL-97 suite of programs. Collection and solving of crystallography data was carried out by Dr Matthew Jones. Details of the data collected are given in the appendix to this report.

3.2 Electronic absorption and emission experiments

Electronic absorption spectra were recorded on a Varian-Cary 50 Probe UV-Visible spectrophotometer. Measurements were usually run between 900 nm and 300 nm and the scan rate was 600 nm/min. Background scans were carried out for every experiment, for both solution and surface based measurements. For the UV/Vis experiments of surface-bound dye, a dyed single-layer mesoporous TiO_2 film on FTO glass was used. An undyed film prepared at the same time was used as the background.

Two setups were used for recording emission spectra. For the work in Chapter 5, spectra were measured at the University of Edinburgh using a Fluoromax 2 fluorometer controlled by the ISAMain software. They were recorded at room temperature (rt) and at 77 K with 0.1 mM solutions of the dye in degassed ethanol (EtOH) or CH_2Cl_2. All other measurements were carried out in degassed methanol (MeOH) or CH_2Cl_2 at the University of Bath using a Perkin Elmer LS 50-B Fluorescence Spectrometer and were recorded at rt.

3.3 DSC manufacture

3.3.1 Preparation of the working electrodes

Prior to use, the fluorine-doped tin oxide (FTO) glass (Hartford Glass or Sigma Aldrich, TEC 15) was cut into 7.5 x 2.5 cm strips and cleaned using the following regime:

- 15 min sonication in 5% Decon 90 solution with heating to 80°C, rinse in Milli-Q water. Repeat this step.
- 15 min sonication in Milli-Q water
- 15 min sonication in isopropanol (IPA) with heating to 80°C
- 15 min sonication in EtOH

The first step in preparing every photoanode for DSCs was depositing a compact TiO_2 blocking layer by spray pyrolysis from a 0.2 M solution of diisopropoxytitanium bis(acetylacentonate) in IPA onto the conductive side of the FTO glass. On a hot plate insulated with aluminium foil, the glass was heated to ~400 °C and the blocking layer solution was sprayed onto the surface using a hand-held atomiser. The films were deposited by spraying one short burst to the top, middle and bottom of the glass every 10 s for 2.5 min.

A layer of colloidal TiO_2 paste (Dyesol, DSL 18NR-T, average nanoparticle size 20 nm) was then deposited onto the surface using the doctor blade method. Adhesive scotch tape was used to control the film thickness and area. For the work in this thesis, two methods of TiO_2 film preparation were used. In ***method 1***, two pieces of scotch tape were placed in parallel, 1 cm apart, on the FTO glass. The paste was applied between the tapes by rolling it down using a glass rod (the doctor blading technique). The film was allowed to dry on a hot plate at ~100°C for 5 min, before a second layer of TiO_2 paste was applied in the same manner. The film was transferred to a chamber furnace (Elite Thermal Systems) while it was at rt and the temperature would generally be ramped up at ~20°C /min to 500°C, where it was held for 30 min then allowed to cool to rt. In ***method 2***, a single or double layer of scotch tape was used to carry out one paste application, *via* doctor blading, and the TiO_2 film was then rested in an EtOH atmosphere for 1 min. Following this, the film was rested in air for 3.5 h and sintered in a tube furnace (Lenton Thermal Designs) according to the following ramping sequence:

- 5°C/min to 125°C – dwell for 5 min
- 5°C/min to 325°C – dwell for 5 min
- 5°C/min to 375°C – dwell for 5 min
- 5°C/min to 450°C - dwell for 15 min
- 1°C/min to 500°C – dwell for 15 min
- Cool to rt

Where a scattering layer was used, the manufacturing process was as follows. A single layer of TiO_2 paste (Dyesol, DSL 18NR-T, average nanoparticle size 20 nm) was applied, the film was rested in an EtOH atmosphere for 1 min, and then sintered at 150°C for 20 min. A single layer of scattering TiO_2 paste (Dyesol, WER2-O Scattering Titania Paste, average nanoparticle size 150-250 nm) was then applied on top, followed by resting in an EtOH atmosphere for 1 min and sintering in the tube furnace according to the detailed ramping sequence described previously.

Where a $TiCl_4$ treatment was used post-sintering on TiO_2 films, it will be noted accordingly. An aqueous $TiCl_4$ solution was prepared to a concentration of 40 mM through careful addition of $TiCl_4$ to an ice-cooled beaker of deionised water. TiO_2 films were immersed in the $TiCl_4$ solution at 60°C for 40 min, then rinsed with water and EtOH and dried under a flow of nitrogen. The films were then sintered again at 500°C for 30 min.

Dyeing of the TiO_2 films was typically overnight unless stated otherwise. Where the dye N719 (Dyesol) was used, the dye bath was a 0.3 mM solution in a 1:1 mixture of *tert*-butanol:acetonitrile (*t*-BuOH:MeCN). Films were immersed in the dye bath while still warm to the touch, rinsed (with the same solvent as used in the dye bath) after removal and dried under a flow of nitrogen. At this point the dyed TiO_2 film was scraped to the desired area (typically 1 cm^2) using the edge of a glass microscope slide before being used in a cell. For the other dyes described in this thesis the dye bath was typically a 0.3 mM MeOH solution. Conditions will be specified where they vary from this. Where the co-adsorbate chenodeoxycholic acid was used, it was added to the dye bath at a concentration of 10 mM prior to film dyeing.

3.3.2 Preparation of the counter electrodes

For the counter electrode (CE), two holes (0.6 mm diameter) were drilled within a 1cm^2 area of an FTO plate (Hartford Glass or Sigma Aldrich, TEC 15 or TEC 7) prior to cleaning *via* the regime described in section 3.3.1. Platinum was deposited by pipetting a couple of drops of 5 mM hexachloroplatinate solution in IPA onto the glass, followed by heating at 390 °C for 15 min.

3.3.3 Electrolyte

Unless stated otherwise, the standard electrolyte recipe used was 0.03 M I_2, 0.6 M 1-propyl-3-methylimidazolium iodide, 0.1 M guanidine thiocyanate and 0.5 M *tert*-butyl pyridine (4-TBP) in MeCN and valeronitrile (85:15).

3.3.4 DSC assembly

The electrodes were sealed together with Surlyn thermoplastic (Solaronix, Meltonix 1170-25, 25 μm thickness), with heating to ~110 °C on a hot plate, while applying pressure with a hand press. Electrolyte was introduced into the cell through the drilled holes in the counter electrode and the holes were then sealed using Surlyn and a glass cover slip. To improve the contact points for cell measurement silver conductive paint was applied to the electrodes.

3.4 Photovoltaic measurements

Two solar simulators were used in the course of this research. A Müller Elektronic Optik solar simulator that used a 450 W xenon lamp as the light source and had been calibrated to 1 sun with a standard silicon solar cell (Czibula & Grundmann, type RS-OD-1). An AM 1.5 filter was used and a potentiostat recorded the *I-V* data. The second system was a TS Space Systems solar simulator with a 200 W metal halide lamp and an inbuilt AM 1.5 filter. This was calibrated against a silicon reference cell (Fraunhofer ISE, RS-OD-4) and used a Keithley 2601A Sourcemeter to record the *I-V* data.

3.5 Electrochemical experiments

3.5.1 Cyclic Voltammetry (CV)

All CV experiments were performed on a three electrode system with a μAutolab potentiostat and data was collected using either the Nova 1.5 or GPES software. For surface

studies, the working electrode (WE) was either a dyed TiO_2 film on FTO glass or a piece of clean FTO glass onto which a drop of dye solution had been deposited and the solvent allowed to evaporate. For discussion of each experiment it will be noted which type of electrode was used. No blocking layer was deposited on the FTO glass used for these electrodes. Where TiO_2 films were used, a single layer of paste was applied *via* doctor blading followed by sintering at 500°C for 30 min. Films were dyed overnight unless otherwise stated. The WE active areas were typically between 0.7 cm^2 and 1 cm^2 and were kept as constant as possible for films within experiments. For solution studies a boron doped diamond WE was used. A platinum CE and an Ag/AgCl (3 M KCl, DRIREF-2, World Precision Instruments) reference electrode (RE) completed the cell. The majority of CV experiments employed 0.1 M tetrabutylammonium hexafluorophosphate (*TBAHFP)* in MeCN as the electrolyte, although on occasion aqueous 0.1 M KNO_3 was used.

3.5.2 Electrochemical Impedance Spectroscopy (EIS)

EIS was carried out on assembled DSCs using a potentiostat (Solartron, SI 1287) and a frequency response analyser (Solartron, SI 1250). Cells were illuminated by a green light-emitting diode (LED, 530 nm) at photon fluxes of $2.66x10^{15}$ and $3.64x10^{15}$ s^{-1} cm^{-2}, as controlled by an LED driver. The DC potential was set at open circuit and an AC amplitude of 10 mV was applied. Measurements were conducted in the frequency range 65535 to 0.1 Hz. Capture and analysis of data was using the Z-Plot and Z-View software respectively.

3.6 Computational details

Computational experiments were carried out by collaborators Gerko Oskam, Humberto J. Mandujano-Ramírez and Gabriel Merino at CINVESTAV IPN, Dept. Fis Aplicada, Merida 97310, Yucatan, Mexico. All density functional theory (DFT) computations have been performed with the Gaussian 09 code[1] using the M06 functional[2] in conjunction with a LANL2DZ basis set.[3-5] Stationary points were characterized by harmonic frequency computations at the same theoretical level. Structures were also optimized including continuum solvation effects using the SMD solvent model, choosing MeOH as solvent.[6] To compute the UV-Vis transitions of the complexes studied, the time-dependent (TD) DFT approach was used at the same level. Computations were carried out to cover a spectral region down to 350 nm.

3.7 Open-Circuit Photovoltage Decay (OCVD)

OCVD experiments were conducted on assembled DSCs. A green LED (530 nm) was employed to illuminate the DSCs. The illumination period (4 s) was controlled by a waveform generator (PPR1, Hi-Tek Instruments 2791366) *via* an LED driver. The output signal was measured on an oscilloscope (Tektronix TDS 3012) *via* a high impedance buffer and recorded using the WaveStar software.

3.8 Incident Photon to Current Efficiency Measurements (IPCE)

The IPCE setup consisted of a light source (Bentham IL1 illuminator), a monochromator (Bentham TMc 300), a lock-in amplifier (Stanford Research Systems, SR830 DSP), a Femto amplifer (DLPCA-200), a lens to focus the beam onto the active area of the cell, and a PC running the Benth2008 software. Measurements were recorded of assembled DSCs, enclosed in a dark chamber, and a measurement time of 1 s was used. The IPCE setup was calibrated with a silicon photodiode (Thorlabs, SN:10102835).

3.9 Ligand and copper(I) complex synthesis

Preparation of [Cu(2,2'-biquinoline-4,4'-dicarboxylic acid)$_2$][HNEt$_3$]

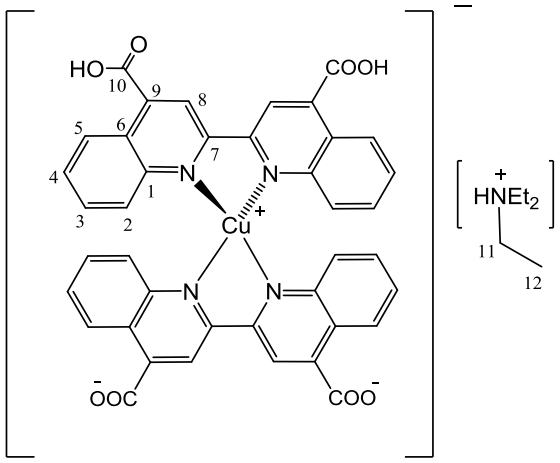

20

Under N_2, a solution of tetrakis(acetonitrile)copper(I) hexafluorophosphate, $[Cu(CH_3CN)_4][PF_6]$, (0.271 g, 0.73 mmol, 1.0 eq) in MeCN (10 mL) was added *via* cannula to a stirring solution of 2,2'-biquinoline-4,4'-dicarboxylic acid (0.50 g, 1.46 mmol, 2.0 eq) in CH_2Cl_2 (10 mL). Triethylamine (0.40 mL, 2.92 mmol, 4.0 eq) was added *via* syringe and the white slurry immediately became a clear, deep purple solution. The reaction was stirred for 16 h at rt. The solvent was removed under vacuum and the isolated purple solid purified by recrystallisation from MeOH and diethyl ether (Et_2O). A dark purple powder was isolated by filtration and dried under vacuum to yield the desired product (0.217 g, 0.26 mmol, 35 %). ^{1}H NMR (400 MHz, CD_3OD) δ_H/ppm 9.12 (s, 4H, H^8), 8.64 (d, J = 8.5 Hz, 4H, H^2), 7.80 (d, J = 8.5 Hz, 4H, H^5), 7.57 (t, J = 7.5 Hz, 4H, H^3), 7.38 (t, J = 7.5 Hz, 4H, H^4), 3.22 (q, J = 7.0, 12H, H^{11}), 1.31 (t, J = 7.0 Hz, 18H, H^{12}). ^{13}C {^{1}H} NMR (125 MHz, CD_3OD) δ_C/ppm 172.8 (C^{10}), 153.6 (C^7), 149.4 (C^6), 147.6 (C^1), 132.4 (C^4), 130.0 (C^3), 129.0 (C^5), 128.1 (C^2), 128.0 (C^9), 119.0 (C^8), 47.9 (C^{11}), 9.2 (C^{12}). ^{31}P {^{1}H} NMR (122 MHz, CD_3OD) δ_P/ppm -144.6 (PF_6). ^{19}F NMR (376 MHz, CD_3OD) δ_F/ppm -74.8 (PF_6). ν_{max} (cm^{-1}) 2980 (m), 1712 (w), 1583 (m), 1560 (m). ESI-TOF MS *m/z* calcd for $[C_{40}H_{22}CuN_4O_8]^-$, 749.0739; found, 749.0750. UV/Vis (MeOH) λ_{max} / nm (ε/dm^3 mol^{-1} cm^{-1}) 359 (55800), 564 (11700). Anal. calcd for $[C_{46}H_{38}CuN_5O_8].[PF_6C_6H_{16}N]$ (complex with co-crystallised $[PF_6][NEt_3]$): C, 56.80; H, 4.95; N, 7.64. Found: C, 57.08; H, 4.74; N, 7.30.

Preparation of 6,6'-dichloro-[2,2'-biquinoline]-4,4'-dicarboxylic acid

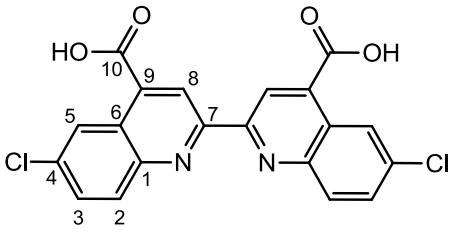

21

To a 25 % KOH solution (aq, 20 mL), 5-chloroisatin (1.50 g, 8.26 mmol, 3.13 eq) was gradually added until dissolved. This was followed by addition of acetoin (0.233 g, 2.64 mmol, 1.0 eq) and the reaction was refluxed overnight. After cooling to rt, the resulting beige slurry was filtered and the isolated solid was washed with 1 M KOH (aq) and then dissolved in H_2O. Acidification to pH 6 with 1 M HCl (aq) precipitated the pure product (0.276 g, 0.667 mmol, 25 %). ^{1}H NMR (250 MHz, CD_3OD, with a drop of 1 M NaOH) δ_H/ppm 8.85 (s, 2H, H^8), 8.53 (d, J = 2.3 Hz, 2H, H^5), 8.20 (d, J = 9.0 Hz, 2H, H^2), 7.76 (dd, J = 9.0, 2.3 Hz, 2H, H^3). ^{13}C {^{1}H} NMR (75 MHz, CD_3OD, with a drop of 1 M NaOH) δ_C/ppm 174.8 (C^{10}), 157.7 (C^7), 148.7(C^4), 148.5 (C^6), 134.6 (C^1), 133.0 (C^2), 132.0 (C^3), 127.6 (C^9), 127.1 (C^5), 119.2 (C^8). ν_{max} (cm^{-1}) 3113 (br), 2970 (s), 1702 (s), 1586 (m). HRMS (-ve ESI-TOF) *m*/*z* calculated for $[C_{20}H_{10}N_2O_4Cl_2–H]^-$, 410.9945; found, 410.9955. Mp. >300 °C.

Preparation of [Cu(6,6'-dichloro-[2,2'-biquinoline]-4,4'-dicarboxylic acid)$_2$][HNEt$_3$]

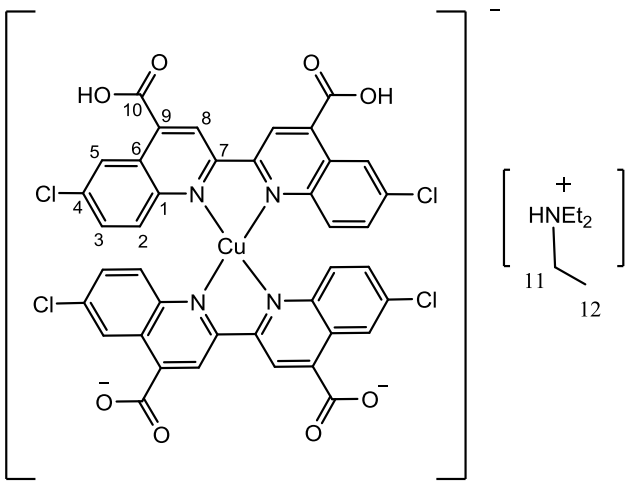

22

To a stirring slurry of 6,6'-dichloro-[2,2'-biquinoline]-4,4'-dicarboxylic acid (0.14 g, 0.34 mmol, 2.0 eq) in MeOH (10 mL) under N_2, a solution of $[Cu(CH_3CN)_4][PF_6]$ (63.1 mg, 0.17 mmol, 1.0 eq) in MeCN (3 mL) was added *via* cannula. Triethylamine (0.1 mL, 0.68 mmol, 4.0 eq) was added *via* syringe and a clear, dark purple solution resulted. The reaction was stirred at rt under N_2 for 6 h. The solvent was removed and the isolated purple solid was re-dissolved in a minimum amount of MeOH and Et_2O added until a precipitate started to appear. The flask was transferred to the freezer overnight before a dark purple powder was isolated by filtration and dried (36.4 mg, 36.7 μmol, 22 %). ^{1}H NMR (250 MHz, CD_3OD) δ_H/ppm 9.12 (s, 4H, H^8), 8.69 (d, J = 2.0 Hz, 4H, H^5), 7.72 (d, J = 9.0 Hz, 4H, H^2), 7.37 (dd, J = 2.0, 9.0 Hz, 4H, H^3), 3.22 (q, J = 7.5, 8H, H^{11}), 1.31 (t, J = 7.5 Hz, 12H, H^{12}). ^{13}C {^{1}H} NMR (75 MHz, CD_3OD) δ_C/ppm 172.4 (C^{10}), 154.0 (C^7), 149.4 (C^6), 145.9 (C^4), 135.8 (C^1), 133.0 (C^3), 130.7 (C^2), 128.8 (C^9), 127.2 (C^5), 120.3 (C^8), 47.8 (C^{11}), 9.2 (C^{12}). ^{31}P {^{1}H} NMR (122 MHz, CD_3OD) δ_P/ppm -143.9 (PF_6). ν_{max} (cm^{-1}) 3360 (br), 1603 (s), 1577 (s), 1556 (s). HRMS (-ve ESI-TOF) *m*/*z* calculated for $[C_{40}H_{20}CuN_4O_8Cl_4\text{-}2H]^-$, 886.9159; found, 886.9095. UV/Vis (MeOH) λ_{max} / nm (ε / dm^3 mol^{-1} cm^{-1}) 564 (11700). Anal. calcd for $[C_{40}H_{20}CuN_4O_8Cl_4][HNEt_3\text{-}PF_6]$: C, 48.59 ; H, 3.19; N, 6.16. Found: C, 48.15; H, 3.55; N, 6.17.

Preparation of 5-aminoisatin

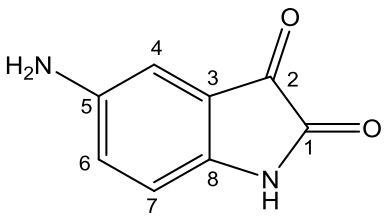

23

To a suspension of iron powder (0.250 g, 4.50 mmol, 3.0 eq) in a mixture of EtOH and H_2O (7 mL:3 mL), 5-nitroisatin (0.288 g, 1.50 mmol, 1.0 eq) was added followed by a portion of conc. $HCl_{(aq)}$ (37 %, 1.2 mL). The reaction was refluxed overnight and a dark brown solution resulted. After cooling to rt, the pH of the reaction was adjusted to 8 through addition of sat. aqueous sodium bicarbonate. The brown slurry was filtered through celite and the filtrate was extracted with ethyl acetate (EtOAc). The organic phase was washed with brine, dried over $MgSO_4$ and concentrated under vacuum. Purification by column chromatography (75:25 EtOAc:petrol ether) yielded the title compound as a dark red residue (61.9 mg, 0.38 mmol, 25 %). ^{1}H NMR (250 MHz, DMSO-d_6) δ_H/ppm 10.59 (s, 1H, NH), 6.82 (dd, *J* = 2.5, 8.3 Hz, 1H, H^6), 6.70 (d, *J* = 2.5 Hz, 1H, H^4), 6.63 (d, *J* = 8.3 Hz, 1H, H^7), 5.08 (s, 2H, NH_2). HRMS (+ve ESI-TOF) *m*/*z* calculated for $(C_8H_6N_2O_2+H)^+$, 163.0508; found, 163.0501. Data in agreement with those previously reported.[7]

Preparation of 4,4'-dicarboxy-2,2'-bipyridine

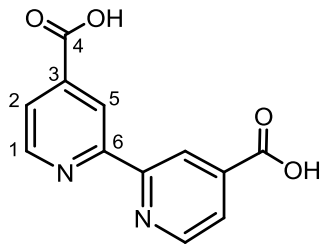

24

4,4'-dimethyl-2,2'-bipyridine (2.38 g, 12.9 mmol) was added slowly to a stirring, ice-bath cooled solution of $Na_2Cr_2O_7.2H_2O$ (8.67 g, 29.1 mmol) in conc. H_2SO_4 (25 mL). The resulting orange slurry was stirred at rt for 2 h until the reaction had turned dark green and was no longer warm. The mixture was poured into cold distilled water (400 mL) to afford a pale yellow precipitate. This was isolated by filtration and dissolved in 10 % KOH (aq, 300 mL). The product was crystallised by acidifying the solution with 10 % HCl (aq, 300 mL) until pH ~2 was reached. The precipitate was isolated *via* filtration and dried to yield the white product (3.03 g, 12.4 mmol, 96 %). ^{1}H NMR (300 MHz, DMSO-d_6) δ_H/ppm 8.92 (d, J = 5.0 Hz, 2H, H^1), 8.84 (s, 2H, H^5), 7.91 (d, J = 5.0 Hz, 2H, H^2); ^{13}C {^{1}H} NMR (75 MHz, DMSO-d_6) δ_C/ppm 166.4 (C^4), 155.9 (ArC), 151.0 (C^1), 139.9 (ArC), 123.8 (C^2), 119.9 (C^5). ν_{max} (cm^{-1}) 3114 (w), 2431 (br), 1709 (m). Data in agreement with those previously reported,[8] except that hydroxyl proton not observed in ^{1}H NMR.

Preparation of 2,2'-bipyridine-4,4'-dicarboxylic acid dimethyl ester

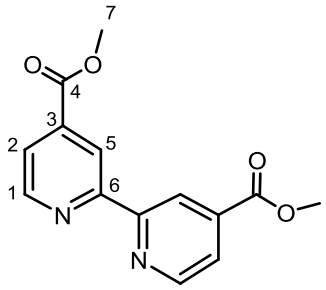

25

Conc. H_2SO_4 (12 mL) was added dropwise to a cooled, stirring solution of 4,4'-dicarboxy-2,2'-bipyridine (**24**) (5.87 g, 24.0 mmol) in MeOH (100 mL). The resulting white slurry was refluxed overnight during which time a cloudy pink solution formed. After cooling the solution was added carefully to distilled water (250 mL) resulting in a pale pink slurry. The pH of the mixture was adjusted to 8 with NaOH (aq, 25 % w/v) followed by extraction of the product into chloroform ($CHCl_3$). The organic extracts were dried over $MgSO_4$ and the solvent evaporated to yield a white crystalline product (4.12 g, 15.1 mmol, 63 %). ^{1}H NMR (300 MHz, $CDCl_3$) δ_H/ppm 8.96 (dd, *J* = 0.6, 1.5 Hz, 2H, H^5), 8.86 (dd, *J* = 0.6, 4.8 Hz, 2H, H^1), 7.90 (dd, *J* = 1.5, 4.8 Hz, 2H, H^2), 4.00 (s, 6H, H^7); ^{13}C {^{1}H} NMR (75 MHz, $CDCl_3$) δ_C/ppm 165.6 (C^4), 156.5 (C^6), 150.2 (C^1), 138.6 (C^3), 123.3 (C^2), 120.6 (C^5), 52.8 (C^7); ν_{max} (cm^{-1}) 3023 (w), 2967 (w), 1728 (s); HRMS (+ve ESI-TOF) *m/z* calculated for $(C_{14}H_{12}N_2O_4+H)^+$, 273.0875; found 273.0921. Data in agreement with those previously reported.[9]

Preparation of 2,2'-bipyridine-*N*-oxide-4,4'-dicarboxylic acid dimethyl ester

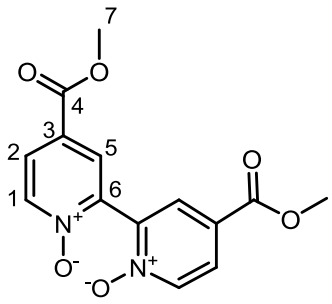

26

To a stirring white slurry of 2,2'-bipyridine-4,4'-dicarboxylic acid dimethyl ester (**25**) (4.10 g, 15.1 mmol) in acetic acid (AcOH) (25 mL), H_2O_2 (24 mL, 35 % wt in H_2O) was added slowly. This was refluxed for 4.5 h during which time it changed initially to a yellow slurry and then to a clear, yellow solution. After allowing the solution to cool for a few minutes, a further portion of H_2O_2 (12 mL, 35 % wt in H_2O) was carefully added and the solution brought back to reflux for 2.5 h. The clear, yellow solution was allowed to cool overnight, resulting in the precipitation of a cotton wool-like white solid which was filtered and washed with H_2O and MeOH. Addition of MeOH to the filtrate and overnight storage in the freezer induced a second crop of the pyridine *N*-oxide product to crystallise (3.83 g, 12.6 mmol, 86 % total yield). ^{1}H NMR (250 MHz, $CDCl_3$) δ_H/ppm 8.35 (d, J = 7.0 Hz, 2H, H^1), 8.19 (d, J = 2.5 Hz, 2H, H^5), 7.97 (dd, J = 2.5, 7.0 Hz, 2H, H^2), 3.95 (s, 6H, H^7); ^{13}C {^{1}H} NMR (75 MHz, $CDCl_3$) δ_C/ppm 163.6 (C^4), 142.2 (ArC), 140.2 (C^1), 128.7 (C^5), 126.8 (C^2), 125.7 (ArC), 52.9 (C^7); ν_{max} (cm^{-1}) 3124 (w), 3078 (w), 1719 (s); HRMS (+ve ESI-TOF) *m*/*z* calculated for $(C_{14}H_{12}N_2O_6+H)^+$, 305.0769 ; found 305.0789.

Preparation of 6,6'-dichloro-4,4'-dimethoxycarbonyl-2,2'-bipyridine

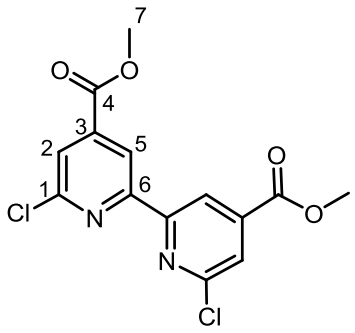

27

The reaction was performed under N_2 in a dry round bottom flask (RBF) equipped with a reflux condenser. To neat 2,2'-bipyridine-*N*-oxide-4,4'-dicarboxylic acid dimethyl ester (**26**) (0.45 g, 1.48 mmol) with stirring was added, $POCl_3$ (3.8 mL) dropwise. The white slurry was refluxed for 24 h forming a clear, light brown solution. On cooling a pale yellow precipitate formed. The solid was isolated by filtration and washed very carefully with a saturated solution of K_2CO_3 (aq). The resulting yellow solid was dried under high vacuum to afford the title compound, (0.25 g, 0.73 mmol, 49 %). ^{1}H NMR (250 MHz, $CDCl_3$) δ_H/ppm 8.85 (d, J = 1.0 Hz, 2H, H^5), 7.94 (d, J = 1.0 Hz, 2H, H^2), 4.02 (s, 6H, H^7); ^{13}C {^{1}H} NMR (75 MHz, $CDCl_3$) δ_C/ppm 164.3 (C^4), 155.5 (ArC), 152.0 (ArC), 141.5 (ArC), 124.9 (C^2), 119.5 (C^5), 53.2 (C^7); ν_{max} (cm^{-1}) 3084 (w), 1732 (s), 1551 (m), 1275 (s). HRMS (+ve ESI-TOF) m/z calculated for $(C_{14}H_{10}N_2O_4Cl_2+H)^+$, 341.0096; found 341.0096. Data in agreement with those previously reported.[10]

Preparation of 6,6'-dibromo-4,4'-dimethoxycarbonyl-2,2'-bipyridine

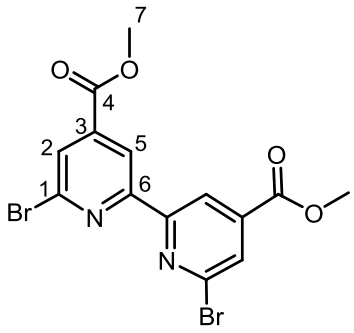

28

The reaction was performed under N_2 in a dry RBF equipped with a reflux condenser. To a refluxing, cream coloured slurry of 6,6'-dichloro-4,4'-dimethoxycarbonyl-2,2'-bipyridine (**27**) (60.0 mg, 0.18 mmol, 1.0 eq) in AcOH (2 mL), HBr (45 % in AcOH, 0.34 mL, 15.0 eq) was added by syringe and the reaction refluxed overnight. A yellow/orange slurry resulted from which a dark yellow solid was isolated after removal of the excess solvent under vacuum. This was washed with a saturated solution of sodium bicarbonate (aq, 5 mL) to yield the pure title complex as a white powder (42.0 mg, 0.098 mmol, 56 %). ^{1}H NMR (250 MHz, $CDCl_3$) δ_H/ppm 8.87 (d, J = 1.0 Hz, 2H, H^5), 8.09 (d, J = 1.0 Hz, 2H, H^2), 4.01 (s, 6H, H^7); ^{13}C {^{1}H} NMR (75 MHz, $CDCl_3$) δ_C/ppm 164.2 (C^4), 155.9 (ArC), 142.3 (ArC), 141.0 (ArC), 128.6 (C^2), 119.8 (C^5), 53.1 (C^7). ν_{max} (cm^{-1}) 3093 (w), 1730 (s), 1537 (s). HRMS (+ve ESI-TOF) *m*/*z* calculated for $(C_{14}H_{10}N_2O_4Br_2+H)^+$, 428.9086; found 428.9092. Data in agreement with those previously reported.[10]

Preparation of 6,6'-dibromo-4,4'-dicarboxy-2,2'-bipyridine

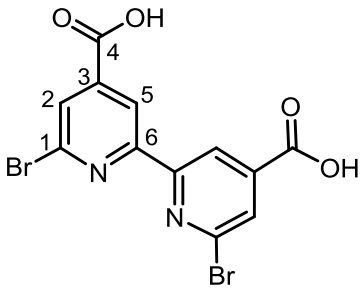

29

.

Method 1

The reaction was performed under N_2 in a dry RBF equipped with a reflux condenser. To a refluxing, cream coloured slurry of 6,6'-dichloro-4,4'-dimethoxycarbonyl-2,2'-bipyridine (**27**) (0.155 g, 0.45 mmol, 1 eq) in AcOH (2.3 mL), HBr (aq, 48 %, 0.25 mL, 5.0 eq) was added by syringe. An immediate colour change to dark orange occurred. After refluxing for 6 h an additional portion of HBr was added (aq, 0.12 mL, 2.5 eq) and the reaction was refluxed for a further 24 h. A dark orange/brown slurry resulted from which a light brown solid was isolated after removal of the excess solvent under vacuum (0.14 g, 0.36 mmol, 81 %).

Method 2

A solution of 6,6'-dibromo-4,4'-dimethoxycarbonyl-2,2'-bipyridine **(28)** (0.076 g, 0.18 mmol) in MeOH (20 mL) and 1 M NaOH (aq, 7 mL) was refluxed overnight. After cooling to rt the reaction volume was concentrated under vacuum and then acidified to ~ pH 6 with 1 M HCl (aq). A white solid precipitated which was filtered out, dried and identified as the desired product (0.050 g, 0.12 mmol, 70 %).

^{1}H NMR (250 MHz, CD_3OD) δ_H/ppm 8.82 (d, J = 0.9 Hz, 2H, H^5), 8.11 (d, J = 0.9 Hz, 2H, H^2). ^{13}C {^{1}H} NMR (75 MHz, CD_3OD) δ_C/ppm 166.6 (C^4), 157.5 (ArC), 144.1 (ArC), 143.8 (ArC), 130.1 (ArCH), 121.1 (ArCH). ν_{max} (cm^{-1}) 3420 (m, br), 3085 (w), 1700 (s), 1541 (s). HRMS (-ve ESI-TOF) *m*/*z* calculated for $(C_{12}H_6N_2O_4Br_2\text{-}H)^-$, 400.8602; found 400.8693. Mp > 300°C.

Preparation of 6,6'-dichloro-4,4'-dicarboxy-2,2'-bipyridine

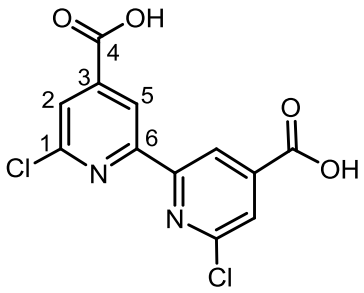

30

To a stirring, pale yellow slurry of 6,6'-dichloro-4,4'-dimethoxycarbonyl-2,2'-bipyridine (**27**) (0.10 g, 0.29 mmol) in MeOH (20 mL) was added 1 M NaOH (aq, 9 mL) and the reaction was refluxed overnight. Following cooling to rt, a cream coloured precipitate was isolated by filtration. The solid was dissolved in distilled water and the solution pH adjusted to ~6 with 1 M HCl (aq). The resulting white product was filtered and dried (67.0 mg, 0.21 mmol, 73 %). ^{1}H NMR (250 MHz, CD_3OD) δ_H/ppm 8.80 (d, J = 1.0 Hz, 2H, H^5), 7.97 (d, J = 1.0 Hz, 2H, H^2); ^{13}C {^{1}H} NMR (125 MHz, CD_3OD) δ_C/ppm 167.0 (C^4), 156.7 (ArC), 153.1 (ArC), 145.3 (C^1), 125.8 (C^2), 120.4 (C^5). ν_{max} (cm^{-1}) 3089 (w), 2857 (m, br), 1704 (s), 1551 (s), 1280 (s). HRMS (-ve ESI-TOF) *m*/*z* calculated for $(C_{12}H_6N_2O_4Cl_2\text{-}H)^-$, 310.9626; found 310.9755.

Preparation of 6,6'-bisthiophene-4,4'-dimethoxycarbonyl-2,2'-bipyridine

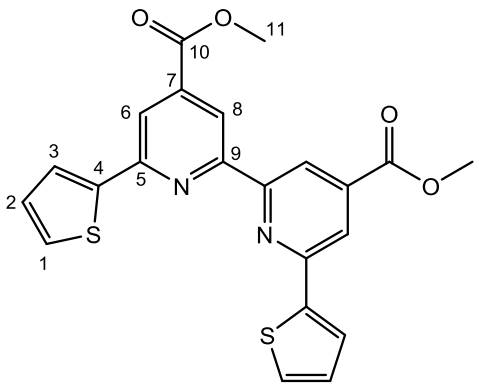

31

2-thienylboronic acid (18.2 mg, 0.14 mmol, 3.0 eq), K_3PO_4 (40.3 mg, 0.19 mmol, 4.0 eq), palladium(II) acetate, $Pd_3(OOCCH_3)_6$, (1.30 mg, 1.90 µmol, 4 mol %) and 2-dicyclohexylphosphino-2′,6′-dimethoxybiphenyl ligand (SPhos) (1.90 mg, 4.74 µmol, 10 mol %) were weighed into a microwave reaction tube, evacuated, and then the vessel filled with argon. To 6,6'-dibromo-4,4'-dimethoxycarbonyl-2,2'-bipyridine (**28**) (20.4 mg, 47.4 µmol, 1 eq), in a RBF under argon, a solvent mix of degassed dioxane and water (2 mL:0.4 mL) was added. This solution was added *via* syringe to the microwave tube and the reaction was heated in a microwave reactor at 100°C for a total time of 3 h. A black palladium solid was filtered out and washed with EtOAc. The washings were combined with the clear, yellow filtrate and concentrated under vacuum. This crude residue was purified by column chromatography (graduated eluent mix from 10:90 EtOAc:petrol ether to 25:75 EtOAc:petrol ether) to isolate the desired product (no yield calculated due to small quantity obtained). ^{1}H NMR (250 MHz, $CDCl_3$) δ_H/ppm 8.91 (s, 2H, H^{bipy}), 8.25 (s, 2H, H^{bipy}), 7.79 (d, J = 3.0 Hz, 2H, H^{thio}), 7.48 (d, J = 5.0 Hz, 2H, H^{thio}), 7.18 (dd, J = 5.0 Hz, 3.0 Hz, 2H, H^2); ^{13}C {^{1}H} NMR (125 MHz, $CDCl_3$) δ_C/ppm 165.9 (C^{10}), 156.0, 153.2, 144.3, 128.7, 128.4, 125.8, 118.6, 53.1 (C^{11}). HRMS (+ve ESI-TOF) m/z calculated for $(C_{22}H_{16}N_2O_4S_2+Na)^+$, 459.0449; found 459.0461.

Preparation of 6,6'-bisthiophene-4,4'-dicarboxy-2,2'-bipyridine

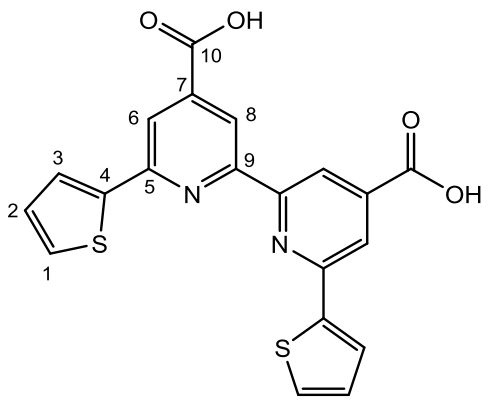

32

6,6’-dibromo-4,4’-dicarboxy-2,2’-bipyridine (**29**) (20.0 mg, 49.8 µmol, 1.0 eq), 2-thienylboronic acid (19.1 mg, 0.15 mmol, 3.0 eq), K_3PO_4 (42.2 mg, 0.20 mmol, 4.0 eq), $Pd_3(OOCCH_3)_6$ (1.30 mg, 1.99 µmol 4 mol %) and SPhos (2.0 mg, 4.98 µmol, 10 mol %) were weighed into a microwave reaction tube, evacuated, and then the vessel filled with argon. A solvent mix of degassed EtOH and water (2 mL:0.4 mL) was added and the tube was heated in a microwave reactor at 100°C for 20 min. A black palladium solid was filtered out to obtain a clear, yellow liquid. Although column chromatography was carried out twice on the crude mixture, isolation of the pure product was not achieved. However some crystallisation of the product occurred when the reaction volume was left slowly to evaporate at rt (no yield calculated or ^{13}C NMR data due to small quantity obtained). ^1H NMR (250 MHz, CD_3OD) δ_H/ppm 8.89 (d, J = 1.0 Hz, 2H, H^{bipy}), 8.24 (d, J = 1.3 Hz, 2H, H^{bipy}), 7.84 (dd, J = 3.8, 1.0 Hz, 2H, H^{thio}), 7.52 (dd, J = 5.0, 1.0 Hz, 2H, H^{thio}), 7.17 (dd, J = 5.0, 3.8 Hz, 2H, H^2). HRMS (-ve ESI-TOF) m/z calculated for $(C_{20}H_{12}N_2O_4S_2\text{-}H)^-$, 407.0160; found 407.0172.

Preparation of [Cu(6,6'-dichloro-4,4'-dicarboxy-2,2'-bipyridine)$_2$][PF$_6$]

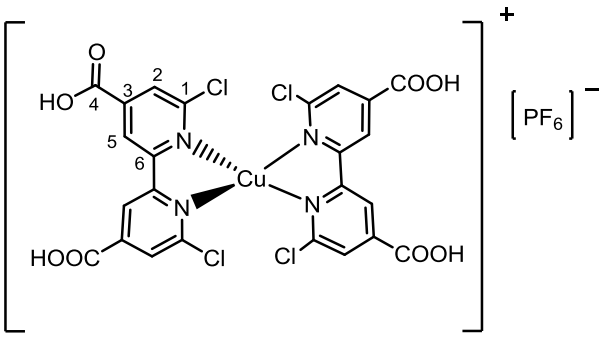

33

Under an atmosphere of N_2, a solution of $[Cu(CH_3CN)_4][PF_6]$ (11.0 mg, 0.029 mmol, 1.0 eq) in MeCN (2 mL) was added *via* cannula to a stirring, cream-coloured slurry of 6,6'-dichloro-4,4'-dicarboxy-2,2'-bipyridine (**30**) (18.0 mg, 0.058 mmol, 2.0 eq) in MeOH (2 mL). An immediate colour change to an orange, cloudy solution occurred. The reaction was stirred overnight under N_2 at rt. The pale coloured solid was removed by filtration and the red/orange solution was retained. Removal of the solvent isolated a light red/brown solid (21 mg, 0.025 mmol, 88 %). ^{1}H NMR (500 MHz, CD_3OD) δ_H/ppm 8.92 (s, H^5), 8.17 (s, H^2). ν_{max} (cm^{-1}) 3640 (w), 3341 (s, br), 3099 (w), 1736 (m), 1626 (s), 1543 (s), 1231 (m), 833 (s). Anal. calcd for $[C_{24}H_{12}Cl_4CuN_4O_8PF_6]$, C, 34.53; H, 1.45; N, 6.71. Found: C, 33.0; H, 2.22; N, 5.52.

Preparation of [Cu(6,6'-dibromo-4,4'-dicarboxy-2,2'-bipyridine)$_2$][PF$_6$]

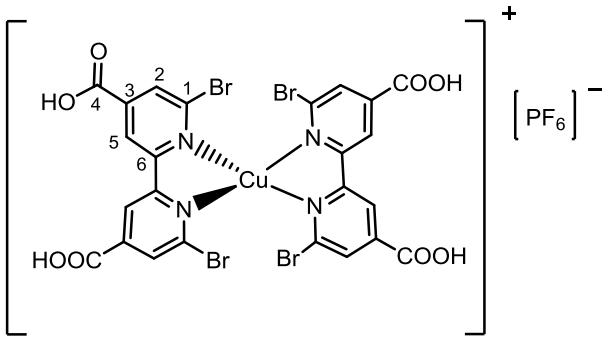

34

Under an atmosphere of N_2, a solution of [Cu(CH$_3$CN)$_4$][PF$_6$] (23.0 mg, 0.062 mmol, 1.0 eq) in MeCN (3 mL) was added *via* cannula to a stirring cream-coloured slurry of 6,6'-dibromo-4,4'-dicarboxy-2,2'-bipyridine (**29**) (0.050 g, 0.12 mmol, 2 eq) in MeOH (3 mL). An immediate colour change to a dark orange/red slurry occurred. The reaction was stirred under N_2 at rt overnight. A pale coloured solid was removed by filtration and the dark red/purple solution was retained. Removal of this solvent isolated a dark purple/red solid, which was washed with Et_2O and dried to afford the title compound, (18 mg, 0.018 mmol, 29 %). ^{1}H NMR (500 MHz, CD_3OD) δ_H 8.90 (4H, s, H^5), 8.24 (4H, s, H^2); ^{13}C {^{1}H} NMR (125 MHz, CD_3OD) δ_C/ppm 169.2 (C^4), 154.0, 142.9, 131.4, 122.4. ν_{max} (cm^{-1}) 3400 (m, br), 3094 (w), 1732 (s), 1538 (s), 1366 (s), 1220 (s). HRMS (+ve MALDI); *m*/*z* calculated for $(C_{24}H_{12}N_4O_8CuBr_4\text{-}PF_6)^+$, 866.6641; found 866.7. Anal. calcd for [$C_{24}H_{12}Br_4CuN_4O_8PF_6$], C, 28.47; H, 1.19; N, 5.53. Found: C, 28.20; H, 1.55; N, 5.55.

Preparation of 1,6-di(thiophen-2-yl)hexa-1,5-diene-3,4-dione

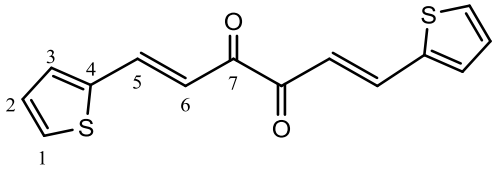

35

To a stirring solution of 2,3-butanedione (1.3 mL, 15.0 mmol, 1.0 eq) in MeOH (20 mL), 2-thiophenecarboxaldehyde (5.6 mL, 60.0 mmol, 4.0 eq) was added, followed by piperidine (0.30 mL, 3.0 mmol, 0.2 eq) and acetic acid (0.17 mL, 3.0 mmol, 0.20 eq). The reaction was refluxed overnight resulting in the precipitation of a dark orange solid. The flask was transferred to the freezer to induce maximum product precipitation. The solid was then isolated by filtration, washed with ice-cold MeOH and dried to yield the title compound as a bright orange powder (0.937 g, 3.42 mmol, 23 %). ^{1}H NMR (250 MHz, $CDCl_3$) δ_H/ppm 7.98 (d, *J* = 16.0 Hz, 2H, H^5), 7.50 (d, *J* = 5.0 Hz, 2H, H^1), 7.42 (d, *J* = 3.5 Hz, 2H, H^3), 7.26 (d, *J* = 16.0 Hz, 2H, H^6), 7.11 (dd, *J* = 5.0, 3.5 Hz, 2H, H^2). ^{13}C {^{1}H} NMR (62.5 MHz, $CDCl_3$) δ_C/ppm 188.3 (C^7), 140.3 (C^4), 139.8 (C^5), 133.2 (C^3), 130.6 (C^1), 128.6 (C^2), 118.4 (C^6). ν_{max} (cm^{-1}) 3090 (m), 1668 (s), 1579 (m), 1510 (m). HRMS (+ve ESI-TOF) *m*/*z* calculated for $(C_{14}H_{10}O_2S_2+Na)^+$, 297.0020; found 297.0026. Mp. 167-169 °C. Data in agreement with those previously reported.[11]

Preparation of 6,6'-dimethyl-4,4'-di(thiophen-2-yl)-2,2'-bipyridine

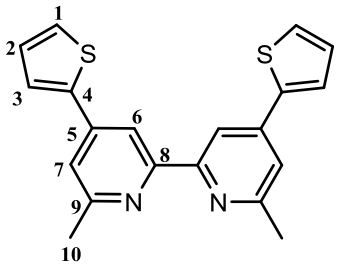

36

To a portion of 1,6-di(thiophen-2-yl)hexa-1,5-diene-3,4-dione **(35)** (4.14 g, 15.1 mmol, 1.0 eq) stirring in MeOH (130 mL), *N*-acetonylpyridinium chloride (5.18 g, 30.2 mmol, 2.0 eq) and ammonium acetate (7.32 g, 95.0 mmol, 6.3 eq) were added sequentially. The reaction was refluxed overnight and, after cooling to rt, an off-white precipitate was isolated by filtration and washed with ice-cold MeOH to yield the pure title compound (2.39 g, 6.85 mmol, 45 %). ^{1}H NMR (250 MHz, $CDCl_3$) δ_H/ppm 8.47 (d, J = 1.5 Hz, 2H, H^6), 7.66 (dd, J = 3.5, 1.0 Hz, 2H, H^3), 7.42 (dd, J = 5.0, 1.0 Hz, 2H, H^1), 7.39 (d, J = 1.5 Hz, 2H, H^7), 7.15 (dd, J = 5.0, 3.5 Hz, 2H, H^2), 2.70 (s, 6H, H^{10}). ^{13}C NMR {^{1}H} (75 MHz, $CDCl_3$) δ_C/ppm 158.7 (C^9), 156.4 (C^8), 142.6 (C^4), 141.9 (C^5), 128.3 (C^2), 126.8 (C^1), 125.5 (C^3), 119.5 (C^7), 115.0 (C^6), 24.7 (C^{10}). ν_{max} (cm^{-1}) 3071 (w), 1590 (s), 1548 (s). HRMS (+ve ESI-TOF) *m*/*z* calculated for $(C_{20}H_{16}N_2S_2 + H)^+$, 349.0828; found, 349.0968. Decomposed at temp >235 °C.

Preparation of 6,6'-dimethyl-4,4'-di(5,5'-bromothiophen-2-yl)-2,2'-bipyridine

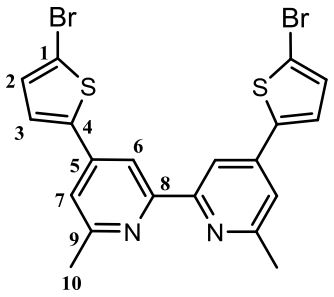

37

To a stirring, pale coloured slurry of 6,6'-dimethyl-4,4'-di(thiophen-2-yl)-2,2'-bipyridine (**36**) (1.40 g, 4.0 mmol, 1.0 eq) in dry CH_2Cl_2 (180 mL) was added bromine (1.20 mL, 24.1 mmol, 6.0 eq) *via* syringe. An immediate colour change to a dark red slurry was observed. The reaction was stirred at rt under argon for 4 h before a solution of $Na_2S_2O_3$ (~180 mL, 10% aq) was added. After vigorous stirring for 10 min, the resulting beige slurry was filtered and the isolated solid dried, yielding the desired product as a beige coloured powder (1.35 g, 2.67 mmol, 66 %). ^{1}H NMR (300 MHz, $CDCl_3$) δ_H/ppm 8.42 (d, *J* = 1.0 Hz, 2H, H^6), 7.43 (d, *J* = 4.0 Hz, 2H, H^2), 7.27 (d, *J* = 1.5 Hz, 2H, H^7), 7.11 (d, *J* = 4.0 Hz, 2H, H^3), 2.70 (s, 6H, H^{10}). ^{13}C {^{1}H} NMR (75 MHz, $CDCl_3$) δ_C/ppm 158.7 (C^9), 154.9 (C^8), 142.7 (C^4), 142.6 (C^1), 131.6 (C^3), 126.8 (C^2), 119.7 (C^7), 115.4 (C^6), 114.9 (C^5), 24.4 (C^{10}). ν_{max} (cm^{-1}) 3064 (w), 3034 (w), 1586 (m), 1545 (m). HRMS (+ve ESI-TOF) *m*/*z* calculated for $(C_{20}H_{14}Br_2N_2S_2 + H)^+$, 504.9043; found, 504.9027. Decomposed at temp >220 °C.

Preparation of 6,6'-dimethyl-5,5'-[2,2'-bipyridin-4,4'-diyl]-bis[thiophene-2-methanoate]

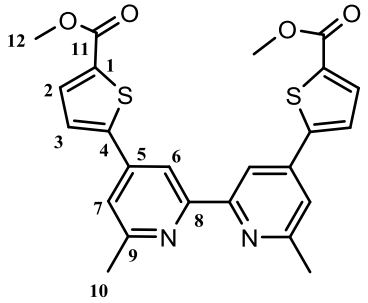

38

To 4,4'-bis(5-bromothiophen-2-yl)-6,6'-dimethyl-2,2'-bipyridine (**37**) (0.30 g, 0.59 mmol, 1.0 eq) stirring under N_2 in THF at -78 °C, *n*-BuLi (1.48 M in hexane, 0.82 mL, 1.2 mmol, 2.05 eq) was added slowly resulting in formation of a dark red solution. Methyl chloroformate was then added (0.18 mL, 2.4 mmol, 4.0 eq) and the reaction was allowed to warm to rt, resulting in a light brown, clear solution which continued to stir overnight. Following gradual addition of the reaction mixture to water, the product was extracted into EtOAc and dried over $MgSO_4$. Removal of the solvent from the organic layer gave the crude product, which was purified by chromatography (90:10 hexane-NEt_3 followed by 100% EtOAc) to yield the pure title compound as a beige powder (0.16 g, 0.34 mmol, 58 %). ^{1}H NMR (300 MHz, $CDCl_3$) δ_H/ppm 8.52 (s, 2H, H^6), 7.82 (d, J = 4.0 Hz, 2H, H^2), 7.61 (d, J = 4.0 Hz, 2H, H^3), 7.40 (d, J = 1.0 Hz, 2H, H^7), 3.93 (s, 6H, H^{12}), 2.71 (s, 6H, H^{10}). ^{13}C {^{1}H} NMR (125 MHz, $CDCl_3$) δ_C/ppm 162.4 (C^{11}), 159.0 (C^9), 156.3 (C^8), 148.3 (C^4), 141.6 (C^5), 134.3 (C^2), 133.9 (C^1), 125.8 (C^3), 119.8 (C^7), 115.1 (C^6), 52.4 (C^{12}), 24.7 (C^{10}). ν_{max} (cm^{-1}) 2951 (w), 2924 (w), 2853 (w), 1708 (s), 1591 (s). HRMS (+ve ESI-TOF) *m*/*z* calculated for $(C_{24}H_{20}N_2O_4S_2 + H)^+$, 465.0937; found, 465.0955.

Preparation of 6,6'-dimethyl-5,5'-[2,2'-bipyridin-4,4'-diyl]-bis[thiophene-2-carboxylic acid]

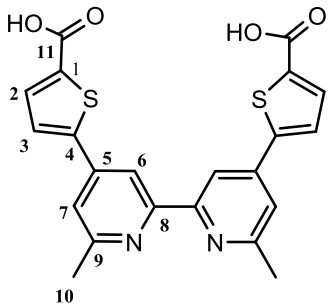

39

To a stirring solution of 6,6'-dimethyl-5,5'-[2,2'-bipyridin-4,4'-diyl]-bis[thiophene-2-methanoate] (**38**) (40.0 mg, 0.086 mmol) in THF (3 mL) and MeOH (2.0 mL), a portion of 1 M NaOH (3.0 mL, aq) was added and the reaction refluxed overnight. After cooling the reaction volume was reduced under vacuum and then acidified to pH 6 with 1 M HCl (aq), causing the precipitation of an off-white solid. This was isolated by filtration, dried and identified as the desired product (21.0 mg, 0.048 mmol, 56 %). ^{1}H NMR (300 MHz, CD_3OD with a drop of 1 M NaOH) δ_H/ppm 8.31 (d, *J* = 1.0 Hz, 2H, H^6), 7.71 (d, *J* = 4.0 Hz, 2H, H^3), 7.63 (d, *J* = 1.5 Hz, 2H, H^7), 7.61 (d, *J* = 4.0 Hz, 2H, H^2), 2.69 (s, 6H, H^{10}). ^{13}C {^{1}H} NMR (75 MHz, CD_3OD with a drop of 1 M NaOH) δ_C/ppm 169.9 (C^{11}), 161.1 (C^9), 157.9 (C^8), 146.7 (C^5), 145.4 (C^1), 145.0 (C^4), 132.6 (C^2), 127.9 (C^3), 121.3 (C^7), 116.8 (C^6), 24.8 (C^{10}). ν_{max} (cm^{-1}) 2923 (w), 1688 (s), 1592 (s). HRMS (+ve ESI-TOF) *m*/*z* calculated for $(C_{22}H_{16}N_2O_4S_2 + H)^+$, 437.0630; found, 437.0599. Decomposed at temp >190 °C.

Preparation of [Cu(6,6'-dimethyl-4,4'-di(thiophen-2-yl)-2,2'-bipyridine)$_2$][PF$_6$]

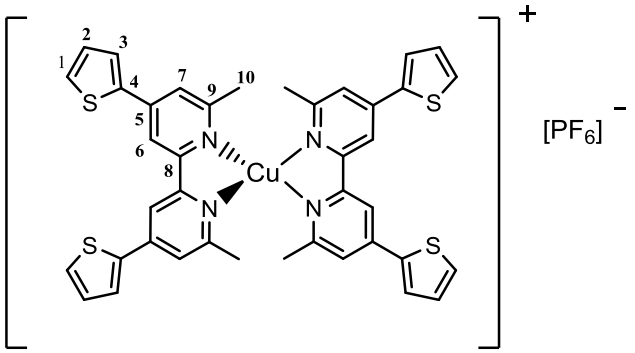

40

The reaction was performed under N_2. To a clear, light brown solution of 6,6'-dimethyl-4,4'-di(thiophen-2-yl)-2,2'-bipyridine (**36**) (0.05 g, 0.14 mmol, 2.0 eq) stirring in CH_2Cl_2 (10 mL), a portion of $[Cu(CH_3CN)_4][PF_6]$ (27.0 mg, 0.071 mmol, 1.0 eq) in MeCN (5.0 mL) was added *via* cannula. A dark red, clear solution immediately resulted which was stirred overnight. The reaction volume was then reduced under vacuum and Et_2O was added until a solid began to precipitate. The flask was transferred to the freezer overnight and then the mixture filtered to isolate a dark red powder. This was washed with diethyl ether, dried and identified as the desired product (23.0 mg, 0.025 mmol, 35%). ^{1}H NMR (250 MHz, DMSO-d_6) δ_H/ppm 8.93 (s, 4H, H^6), 8.23 (d, J = 3.0 Hz, 4H, H^{thio}), 7.91 (d, J = 5.0 Hz, 4H, H^{thio}), 7.88 (s, 4H, H^7), 7.36 (t, J = 5.0 Hz, 4H, H^2), 2.27 (s, 12H, H^{10}). ^{13}C {^{1}H} NMR (75 MHz, DMSO-d_6) δ_C/ppm 157.7, 152.2, 143.2, 139.9, 130.2, 129.5, 128.9, 122.0, 116.2, 24.9 (C^{10}). HRMS (+ve ESI-TOF) *m/z* calculated for $(C_{40}H_{32}N_4S_4Cu)^+$, 759.0800; found, 759.0925. UV/Vis (acetone) λ_{max} / nm (ε / dm^3 mol^{-1} cm^{-1}) 495 (17,540).

Preparation of [Cu(6,6'-dimethyl-5,5'-[2,2'-bipyridin-4,4'-diyl]-bis[thiophene-2-methanoate)$_2$][PF$_6$]

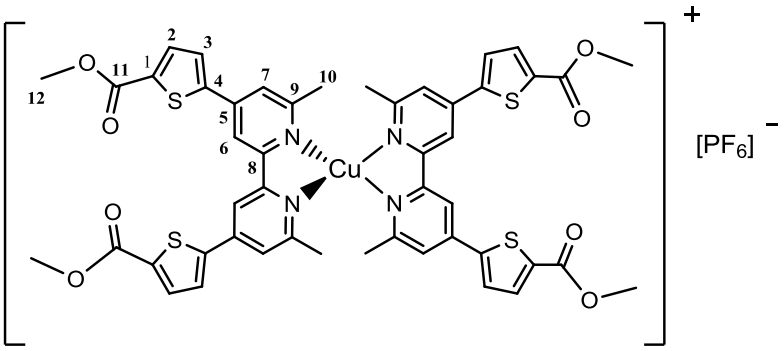

41

The reaction was performed under N_2. To a stirring solution of 6,6'-dimethyl-5,5'-[2,2'-bipyridin-4,4'-diyl]-bis[thiophene-2-methanoate] (**38**) (10.0 mg, 21.5 µmol, 2.0 eq) in CH_2Cl_2 (2.0 mL), a portion of $[Cu(CH_3CN)_4][PF_6]$ (4.0 mg, 10.8 µmol, 1.0 eq) in MeCN (2.0 mL) was added *via* cannula. A dark red clear solution formed immediately which was stirred for 4 h. Et_2O was added until a dark precipitate started to appear. The flask was stored in the freezer overnight, after which a dark red solid was isolated by filtration, dried and identified as the desired complex (7.0 mg, 6.2 µmol, 57%). ^{1}H NMR (250 MHz, acetone-d_6) δ_H/ppm 9.07 (s, 4H, H^6), 8.09 (d, J = 4.0 Hz, 4H, H^3), 8.07 (d, J = 1.0 Hz, 4H, H^7), 7.93 (d, J = 4.0 Hz, 4H, H^2), 3.94 (s, 12H, H^{12}), 2.45 (s, 12H, H^{10}). ^{13}C {^{1}H} NMR (125 MHz, acetone-d_6) δ_C/ppm 162.6 (C^{11}), 159.3 (C^9), 153.5 (C^8), 147.0 (C^5), 143.5 (C^4), 136.5 (C^1), 135.5 (C^2), 129.1 (C^3), 123.5 (C^7), 117.7 (C^6), 53.0 (C^{12}), 25.4 (C^{10}). ^{31}P {^{1}H} NMR (122 MHz, acetone-d_6) δ_P/ppm -143.4 (PF_6). ν_{max} (cm^{-1}) 2957 (w), 1714 (s), 1609 (s). HRMS (+ve ESI-TOF) *m*/*z* calculated for $(C_{48}H_{40}N_4O_8S_4Cu)^+$, 991.1020; found, 991.0986. UV/Vis (acetonitrile) λ_{max} / nm (ε / dm^3 mol^{-1} cm^{-1}) 314 (78,600), 514 (10,500). Mp. >220 °C.

Preparation of [Cu(6,6'-dimethyl-5,5'-[2,2'-bipyridin-4,4'-diyl]-bis[thiophene-2-carboxylic acid])$_2$][PF$_6$]

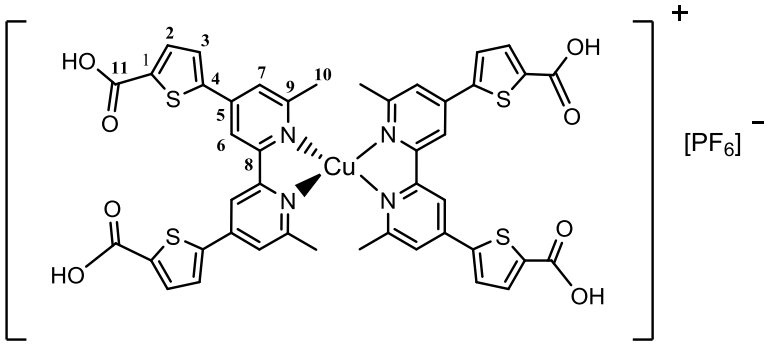

42

The reaction was performed under N_2. To a stirring solution of (6,6'-dimethyl-[2,2'-bipyridine]-4,4'-diyl)bis(thiophene-2-carboxylic acid) (**39**) (57.7 mg, 0.13 mmol, 2.0 eq) in degassed MeOH (15 mL), a quantity of 1 M NaOH (aq, 0.6 mL) was added. To this, a portion of [Cu(CH_3CN)$_4$][PF_6] (24.6 mg, 0.066 mmol, 1.0 eq) in MeCN (3.0 mL) was added *via* cannula and a dark red coloured, clear solution formed immediately and was left stirring under N_2 overnight. The solvent volume was reduced under vacuum and then acidified to pH 4 with 1 M HCl (aq), which precipitated a dark red solid. This was isolated by filtration and washed with Et_2O to give the desired product (29.9 mg, 27.6 µmol, 42 %). ^{1}H NMR (400 MHz, CD_3OD) δ_H/ppm 8.79 (s, 4H, H^6), 7.97 (d, *J* = 4.0 Hz, 4H, H^3), 7.85 (s, 4H, H^7), 7.64 (d, *J* = 4.0 Hz, 4H, H^2), 2.34 (s, 12H, H^{10}). ^{13}C {^{1}H} NMR (125 MHz, CD_3OD) δ_C/ppm 159.1 (C^9), 153.8 (C^8), 145.3 (C$^{1/4}$), 143.7 (C^5), 132.3 (C^2), 128.9 (C^3), 122.9 (C^7), 116.9 (C^6), 25.2 (C^{10}). ^{31}P {^{1}H} NMR (162 MHz, CD_3OD) δ_P/ppm -144.5 (PF_6). ν_{max} (cm^{-1}) 2956 (w), 1693 (s), 1607 (s). UV/Vis (MeOH) λ_{max} / nm (ε / dm^3 mol^{-1} cm^{-1}) 316 (50,000), 506 (9030). Mp. >220 °C.

Preparation of 1,6-di(2-furyl)hexa-1,5-diene-3,4-dione

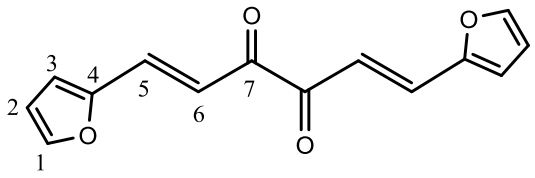

43

To a stirring solution of 2,3-butanedione (1.97 mL, 22.5 mmol, 1.0 eq) in MeOH (30 mL), 2-furaldehyde (7.46 mL, 90.0 mmol, 4.0 eq) was added, followed by portions of piperidine (0.44 mL, 4.5 mmol, 0.2 eq) and acetic acid (0.26 mL, 4.5 mmol, 0.2 eq). The reaction was refluxed overnight resulting in the precipitation of a dark orange solid. The flask was transferred to the freezer overnight to induce maximum product precipitation. The solid was isolated by filtration, washed with ice-cold MeOH and dried to yield the title compound as a bright orange powder (2.66 g, 10.9 mmol, 49 %). ^{1}H NMR (250 MHz, $CDCl_3$) δ_H/ppm 7.61 (d, J = 16.0 Hz, 2H, H^{alk}), 7.57 (d, J = 2.0 Hz, 2H, H^{furan}), 7.31 (d, J = 16.0 Hz, 2H, H^{alk}), 6.80 (d, J = 3.5 Hz, 2H, H^{furan}), 6.53 (dd, J = 3.5, 2.0 Hz, 2H, H^{2}). ^{13}C {^{1}H} NMR (75 MHz, $CDCl_3$) δ_C/ppm 188.6 (C^{7}), 151.5, 146.0, 133.0, 117.7, 117.3, 113.0. ν_{max} (cm^{-1}) 3125 (w), 1664 (s), 1587 (s), 1545 (s). HRMS (+ve ESI-TOF) *m/z* calculated for $(C_{14}H_{10}O_4+H)^+$, 243.0657; found, 243.0660. Data in agreement with those previously reported.[12]

Preparation of 4,4'-di(2-furyl)-6,6'-dimethyl-2,2'-bipyridine

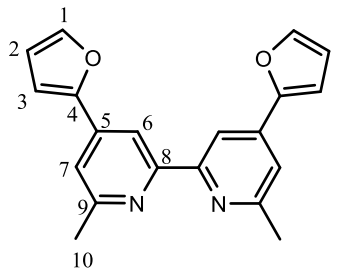

44

To a portion of 1,6-di(2-furyl)hexa-1,5-diene-3,4-dione (**43**) (2.16 g, 8.91 mmol, 1.0 eq) stirring in MeOH, *N*-acetonylpyridinium chloride (3.06 g, 17.8 mmol, 2.0 eq) and ammonium acetate (4.33 g, 56.1 mmol, 6.3 eq) were added sequentially. The reaction was refluxed overnight and, after cooling to room temperature, an off-white precipitate was isolated by filtration and washed with ice-cold MeOH to yield the title compound. The filtrate was reduced in volume under vacuum and transferred to the freezer to obtain a second crop of product (1.37 g, 4.34 mmol, 49 % total yield). ^{1}H NMR (250 MHz, $CDCl_3$) δ_H/ppm 8.46 (s, 2H, H^6), 7.56 (d, J = 1.5 Hz, 2H, H^{furan}), 7.46 (d, J = 1.0 Hz, 2H, H^7), 7.00 (d, J = 3.5 Hz, 2H, H^{furan}), 6.54 (dd, J = 3.5, 2.0 Hz, 2H, H^2), 2.70 (s, 6H, H^{10}). ^{13}C {^{1}H} NMR (75 MHz, $CDCl_3$) δ_C/ppm 158.5, 156.2, 151.9, 143.5, 138.7, 117.2, 113.0, 112.1, 108.8, 24.8 (C^{10}). HRMS (+ve ESI-TOF) m/z calculated for $(C_{20}H_{16}N_2O_2+H)^+$, 317.1290; found, 317.1291. Data in agreement with those previously reported.[12]

Preparation of 6,6'-Dimethyl-2,2'-bipyridine-4,4'-dicarboxylic acid

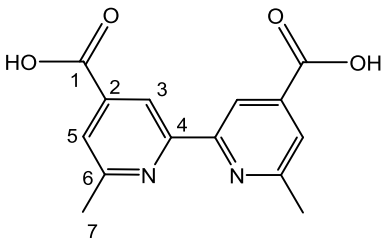

45

To a stirring, warm (~35°C), solution of 4,4'-di(2-furyl)-6,6'-dimethyl-2,2'-bipyridine (**44**) (0.20 g, 0.63 mmol) in *t*-BuOH/H_2O (29 mL:6 mL), $KMnO_4$ (1.30 g, 8.22 mmol) was added. The reaction was refluxed overnight and a clear solution with a black precipitate resulted. The solid was removed by filtration and the filtrate volume was concentrated under vacuum. The pH was adjusted to 2 with 1 M HCl (aq), resulting in the precipitation of a white solid. This was filtered, dried and identified as the title complex (0.086 g, 0.32 mmol, 50 %). ^{1}H NMR (250 MHz, DMSO-d_6) δ_H/ppm 8.64 (s, 2H, H^3), 7.77 (s, 2H, H^5), 2.67 (s, 6H, H^7). ^{13}C {^{1}H} NMR (125 MHz, DMSO-d_6) δ_C/ppm 166.7 (C^1), 159.5, 155.3, 123.1, 117.1, 24.4 (C^7). HRMS (-ve ESI-TOF) *m*/*z* calculated for $(C_{14}H_{12}N_2O_4\text{-}H)^-$, 271.0719; found, 271.0741. Data in agreement with those previously reported,[12, 13] except that C^2 not observed.

Preparation of [Cu(6,6'-dimethyl-2,2'-bipyridine-4,4'-dicarboxylic acid)$_2$][Cl]

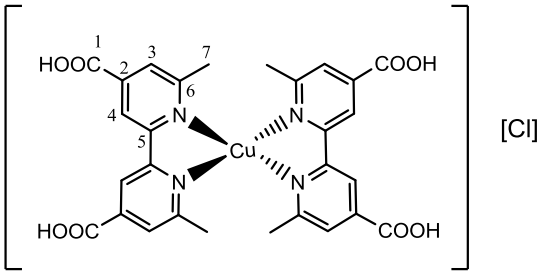

1

To a solution of 6,6'-dimethyl-2,2'-bipyridine-4,4'-dicarboxylic acid (**45**) (0.090g, 0.33 mmol) stirring in H_2O (3 mL) at 70°C, 15 drops of 1 M NaOH (aq) was added. This was followed by addition of a solution of $CuSO_4{\cdot}5H_2O$ (0.042 g, 0.17 mmol) in H_2O (2 mL) and a further 20 drops of 1 M NaOH (aq). The reaction vessel was evacuated and put under a nitrogen atmosphere before a solution of ascorbic acid (0.044 g, 0.25 mmol) in H_2O (0.3 mL) was added *via* cannula transfer. An immediate colour change to dark red was observed and the solution continued to stir for 1 h before cooling to rt. The reaction was acidified to pH 2 with 1 M HCl (aq) and a dark red solid precipitated. This was filtered, washed with Et_2O and dried (0.075 g, 0.12 mmol, 69 %). The complex was purified through a Sephadex (LH-20) gel filtration column (eluent MeOH). ^{1}H NMR (500 MHz, CD_3OD) δ_H/ppm 8.90 (s, 4H, H^4), 8.13 (s, 4H, H^3), 2.34 (s, 12H, H^7). ^{13}C {^{1}H} NMR (125 MHz, D_2O with a drop of 1 M NaOH) δ_C/ppm 172.6 (C^1), 158.1, 152.1, 145.7, 124.6, 118.3, 24.2 (C^7). ν_{max} (cm^{-1}) 3000 (w), 2798 (w), 2540 (w), 1717 (s), 1563 (s). HRMS (+ve ESI-TOF) *m/z* calculated for $(C_{28}H_{24}N_4O_8Cu)^+$, 607.0885; found, 607.0940. Data in agreement with those previously reported.[12]

3.10 References

1. M. J. Frisch, G. W. Trucks, H. B. Schlegel, G. E. Scuseria, M. A. Robb, J. R. Cheeseman, G. Scalmani, V. Barone, B. Mennucci, G. A. Petersson, H. Nakatsuji, M. Caricato, X. Li, H. P. Hratchian, A. F. Izmaylov, J. Bloino, G. Zheng, J. L. Sonnenberg, M. Hada, M. Ehara, K. Toyota, R. Fukuda, J. Hasegawa, M. Ishida, T. Nakajima, Y. Honda, O. Kitao, H. Nakai, T. Vreven, J. A. Montgomery, J. E. Peralta, F. Ogliaro, M. Bearpark, J. J. Heyd, E. Brothers, K. N. Kudin, V. N. Staroverov, R. Kobayashi, J. Normand, K. Raghavachari, A. Rendell, J. C. Burant, S. S. Iyengar, J. Tomasi, M. Cossi, N. Rega, J. M. Millam, M. Klene, J. E. Knox, J. B. Cross, V. Bakken, C. Adamo, J. Jaramillo, R. Gomperts, R. E. Stratmann, O. Yazyev, A. J. Austin, R. Cammi, C. Pomelli, J. W. Ochterski, R. L. Martin, K. Morokuma, V. G. Zakrzewski, G. A. Voth, P. Salvador, J. J. Dannenberg, S. Dapprich, A. D. Daniels, Farkas, J. B. Foresman, J. V. Ortiz, J. Cioslowski and D. J. Fox, Wallingford CT, 2009.
2. Y. Zhao and D. G. Truhlar, *Theor. Chem. Acc.*, 2008, **120**, 215-241.
3. W. R. Wadt and P. J. Hay, *J. Chem. Phys.*, 1985, **82**, 284-298.
4. P. J. Hay and W. R. Wadt, *J. Chem. Phys.*, 1985, **82**, 299-310.
5. P. J. Hay and W. R. Wadt, *J. Chem. Phys.*, 1985, **82**, 270-283.
6. A. V. Marenich, C. J. Cramer and D. G. Truhlar, *J. Phys. Chem. B*, 2009, **113**, 6378-6396.
7. A. Beauchard, Y. Ferandin, S. Frere, O. Lozach, M. Blairvacq, L. Meijer, V. Thiery and T. Besson, *Bioorg. Med. Chem.*, 2006, **14**, 6434-6443.
8. T. M. Postma, W. R. J. D. Galloway, F. B. L. Cougnon, G. D. Pantoş, J. E. Stokes and D. R. Spring, *Synlett*, 2013, **24**, 765-769.
9. T. Prakasam, M. Lusi, M. Elhabiri, C. Platas-Iglesias, J.-C. Olsen, Z. Asfari, S. Cianférani-Sanglier, F. Debaene, L. J. Charbonnière and A. Trabolsi, *Angew. Chem.-Int. Edit.*, 2013, **52**, 9956-9960.
10. C. Barolo, M. K. Nazeeruddin, S. Fantacci, D. Di Censo, P. Comte, P. Liska, G. Viscardi, P. Quagliotto, F. De Angelis, S. Ito and M. Grätzel, *Inorg. Chem.*, 2006, **45**, 4642-4653.
11. Y.-F. Sun, L. Zhong, X.-M. Hou, S.-Y. Ma, W.-Z. Duan and R.-T. Wu, *Color. Technol.*, 2012, **128**, 331-339.
12. E. C. Constable, A. H. Redondo, C. E. Housecroft, M. Neuburger and S. Schaffner, *Dalton Trans.*, 2009, 6634-6644.
13. V. M. Mukkala and J. J. Kankare, *Helv. Chim. Acta*, 1992, **75**, 1578-1592.

Chapter 4 - Synthesis and study of a model copper(I) dye; [Cu(6,6'-dimethyl-2,2'-bipyridine-4,4'-dicarboxylic acid)$_2$][Cl], (1)

4. Synthesis and study of a model copper(I) dye; [Cu(6,6'-dimethyl-2,2'-bipyridine-4,4'-dicarboxylic acid)$_2$][Cl], (1)

4.1. Introduction

In the work of Constable and colleagues which re-introduced copper(I) dyes to the dye-sensitized solar cell (DSC) community, [Cu(6,6'-dimethyl-2,2'-bipyridine-4,4'-dicarboxylic acid)$_2$][Cl] was synthesised and reported.[1, 2] The characterisation and crystallographic data for the complex and its preceding ligands were thoroughly described and the paper set the course for a number of other publications on copper(I) DSCs over the subsequent years. Synthesis of this dye (complex **1**, Figure 34) was reproduced here in order to carry out further analysis of its properties. In addition, it was suggested to us in a personal communication that stability of the dye and of its DSC devices was problematic. Therefore the aims of this investigation were to obtain a greater understanding of the dye, of its stability in a DSC and of its electrochemical behaviour. The results would also be useful it as a starting point for developing new dyes. This chapter will describe the synthesis and some studies carried out with the complex **1**. Further work to study this dye with a cobalt$^{2+/3+}$ mediator in DSC devices will be covered in Chapter 5.

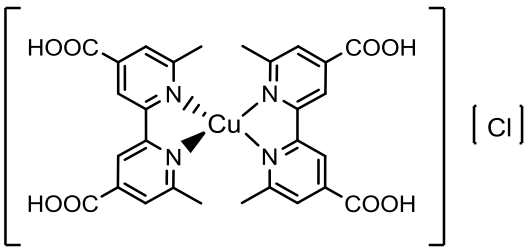

Figure 34 - [Cu(6,6'-dimethyl-2,2'-bipyridine-4,4'-dicarboxylic acid)$_2$][Cl], complex 1

4.2. Synthesis of complex 1

Synthesis of complex **1** was *via* a 4-step process from furfural and 2,3'-butanedione (Scheme 1), as described in the literature.[2] Characterisation data obtained for the ligands (**43**-**45**) and the copper(I) complex matched that in the literature,[2-4] apart from the elemental analysis obtained for the metal complex. Constable's paper reports CHN data for the tetrahydrated copper(I) complex, however the analysis on complex **1** returned lower quantities of the organic components than fitted this structure. Formation of some copper^{II} oxide following exposure to air is not ruled out.

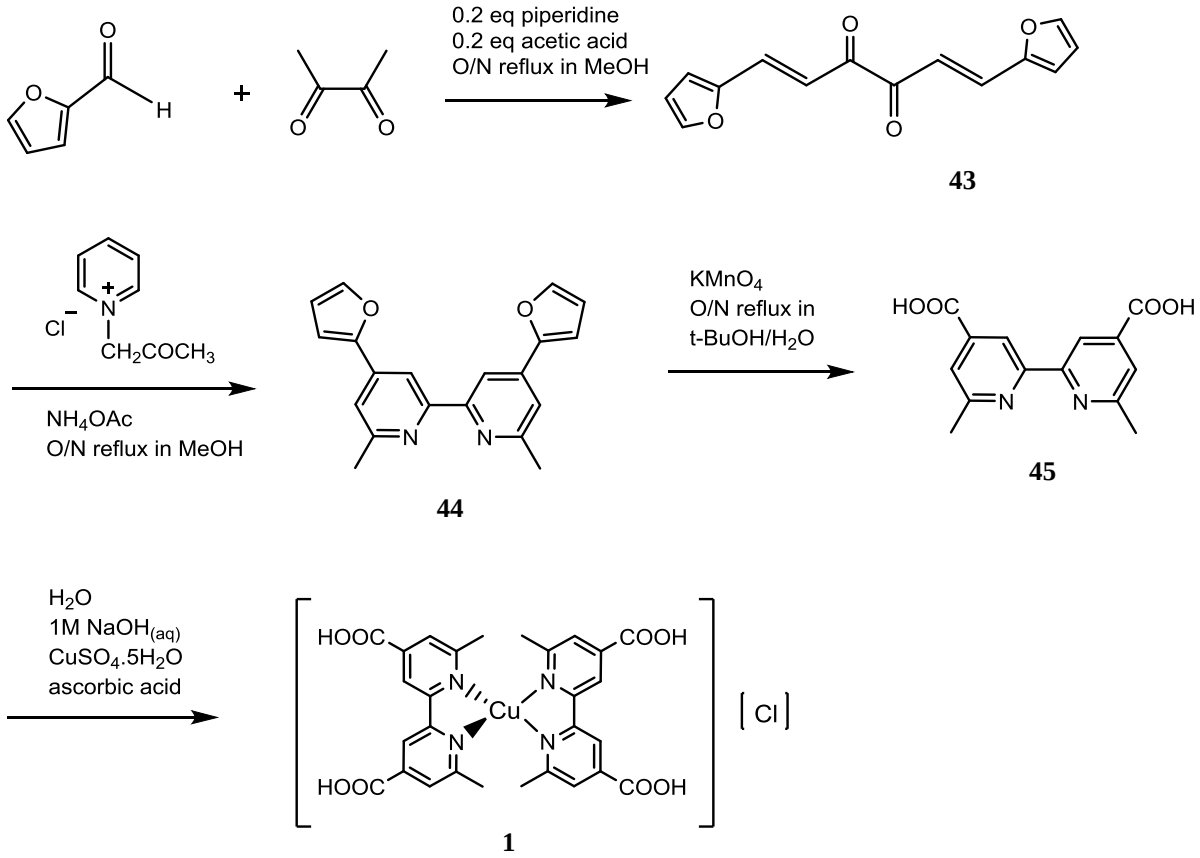

Scheme 1 – synthetic route towards [Cu(6,6'-dimethyl-2,2'-bipyridine-4,4'-dicarboxylic acid)$_2$][Cl], complex 1

4.3. Dye adsorption behaviour

Some studies of dye uptake on the TiO_2 films were carried out over a range of dye times. Films were dyed from a 0.3 mM solution of complex **1** in MeOH and absorption spectra recorded (Figure 35). The adsorption isotherm shows typical behaviour for dye uptake on a TiO_2 film (Figure 36).[5-8] Dye uptake is fastest initially and then slows to an eventual plateau as the sites available for binding become fewer. The kinetics for this process do not strictly follow Langmuir Adsorption Isotherm behaviour, since the TiO_2 surface is a highly porous network of particles rather than a flat surface. It is noted that there is also a shift in $\lambda_{(max)}$ from 480 to 494 nm with increasing dye time, which is often associated with aggregation of the dye on the TiO_2 surface.[9-11]

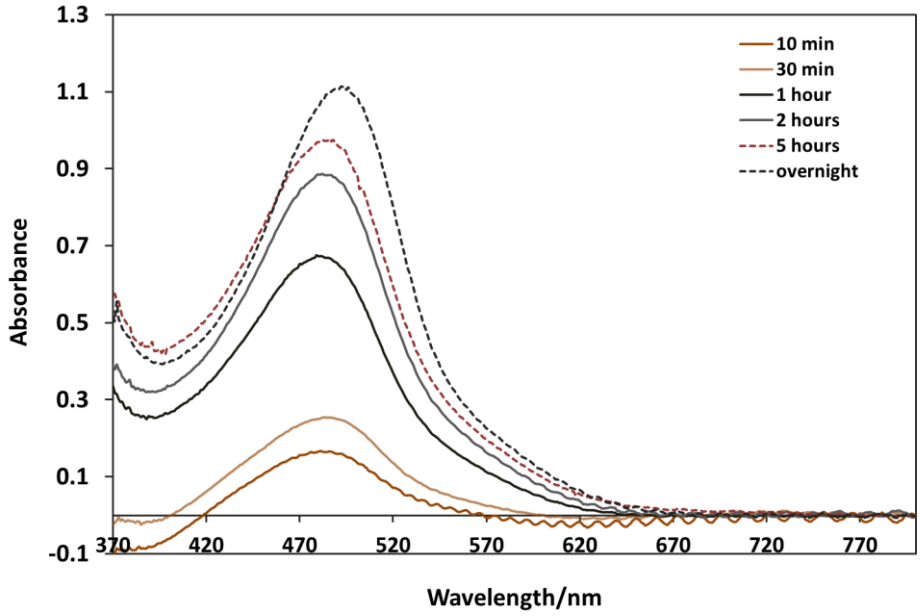

Figure 35 - UV/Vis spectra of complex 1 on a TiO_2 surface, dyed for increasing periods of time; 10 min (-), 30 min (-), 1 hour (-), 2 hours (-), 5 hours (---) and overnight (---)

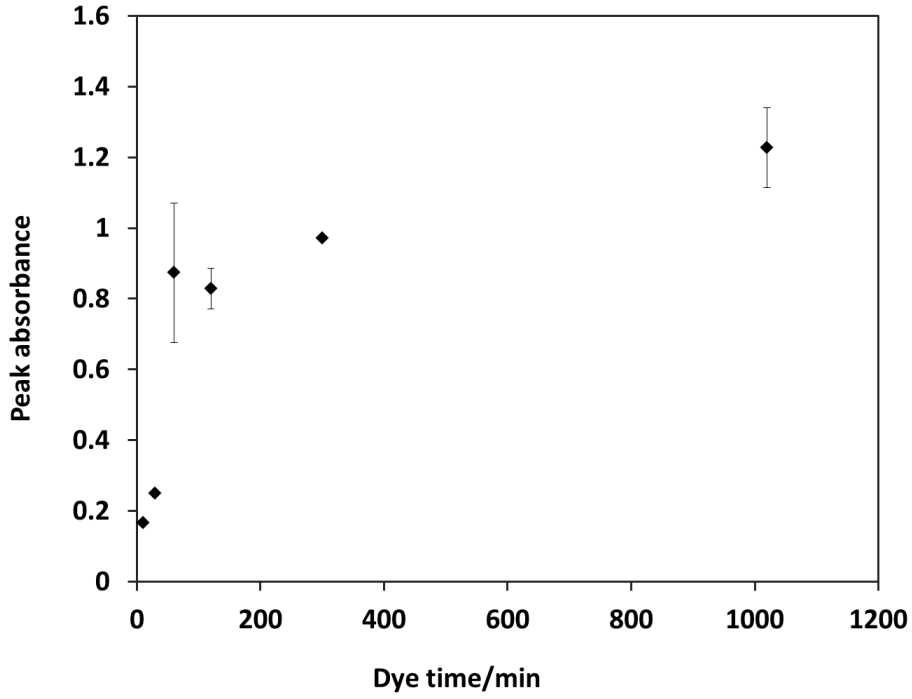

Figure 36 - adsorption isotherm for complex 1 on a TiO_2 surface, at 480 nm (error bars show one standard deviation, n=2. All points have error bars, some are just very small)

4.4. DSC device experiments

DSCs were constructed with complex **1** to compare how efficiency varied with dye time and in the presence of air. The TiO_2 films were prepared *via* ***method 1*** (see Chapter 3.3.1). Cells were filled using the same electrolyte formula as detailed in Constable's paper; 0.5 M LiI, 0.05 M I_2, 0.5 M 1-methylbenzimidazole and 0.6 M 1-butyl-3-methylimidazolium iodide in 3-methoxypropionitrile.[2] Over the range of cells assembled, a top overall solar-power-to-conversion efficiency of 0.44 % was measured for a 0.8 cm^2 cell after a TiO_2 dye time of 4 hours from a 0.3 mM solution in MeOH. No additional treatments (e.g. scattering layer or $TiCl_4$) were used, analogous to the literature report. The cell reported with this dye in the literature[2] was 0.45 cm^2 and had a η value of 0.41 %.[2] Therefore we exceeded the literature reported result with complex **1** and did so with a larger cell area.

The effects of increasing film dye time on DSCs with complex **1** were studied over the course of three experiments/batches of cells. The results of experiment 1 are shown in Figure 37 and Table 1. The data shown are for the best performing cells in this experiment, where a minimum of two cells were prepared each time. These cells all had dyed areas of ~0.8 cm^2 and were dyed from 0.3 mM solutions in MeOH.

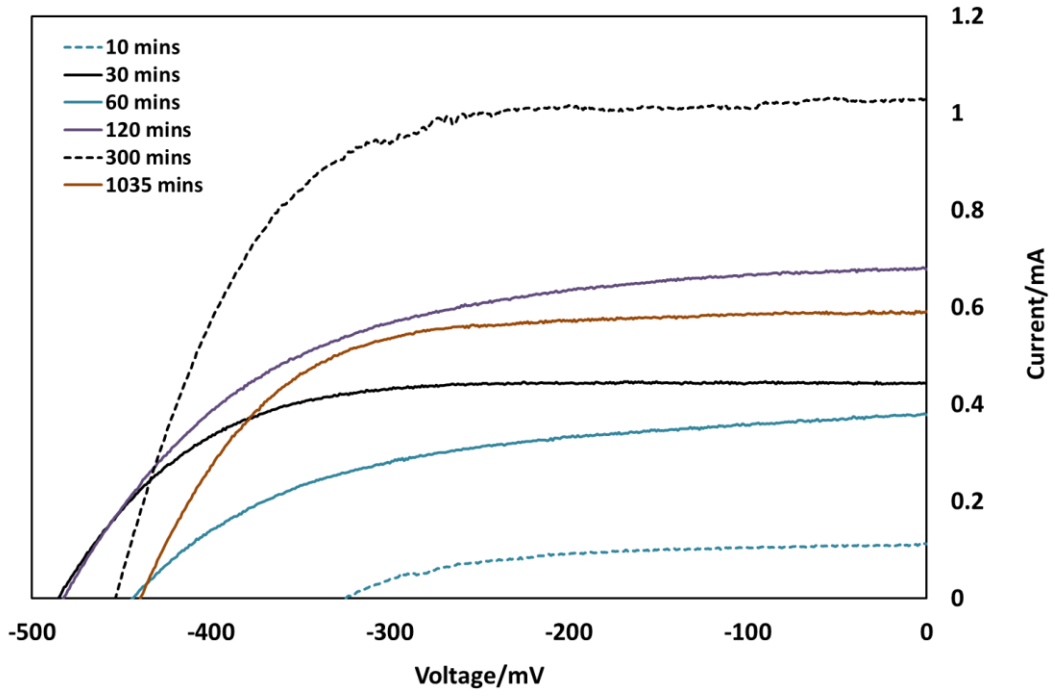

Figure 37 – *I-V* curves for DSCs prepared with TiO_2 films dyed for increasing periods of time. Dye times shown on graph. Data for these cells is in Table 1.

Table 1 - cell parameters for DSCs constructed with complex 1 at increasing dye times

TiO_2 film dye time (min)	J_{SC} (mA)	V_{OC} (mV)	*FF*	η (%)
10	0.121	325	0.49	0.03
30	0.453	485	0.65	0.18
60	0.407	444	0.47	0.10
120	0.694	482	0.53	0.24
300	1.050	453	0.63	0.37
1035	0.611	439	0.62	0.19

A further two batches of cells were prepared in this way and the average data are presented in Figure 38. Each data point represents a minimum of two and a maximum of 8 DSCs. Although the errors are fairly large, a general trend can still be identified. It can be seen that η generally increases with increasing dye time; however there was an observed decrease when TiO_2 films were dyed overnight. Cells constructed after films were dyed for 10 minutes performed the most poorly, attributed to low dye uptake in such a short period of time. After overnight dyeing, η decreased relative to a film dye time of 5 hours. For comparison, DSCs were also constructed with N719 after dyeing for 30 minutes, 2 hours and overnight. Cell efficiencies increased with dye time and, in contrast to complex **1**, were highest in the cells where films were dyed overnight.

A decrease in cell parameters is likely due to aggregation of dye on the TiO_2 surface, or else some degradation of dye, with prolonged time in the dye bath. Aggregation was suggested from the UV/Vis measurements discussed in section 4.3, and occurs when multiple layers of the dye adhere to the TiO_2 surface. Ideally only a monolayer would attach, ensuring efficient electronic communication between the dye molecules and the TiO_2. However there can be a build-up of dye molecules, *via* intermolecular interactions such as hydrogen bonding and π-π stacking, which are not directly bound to the TiO_2 surface. These unbound dye layers could still contribute to light absorption but electrons might not be injected into the circuit, i.e. contribute to the photocurrent, since the dye molecules are not electronically coupled to the TiO_2. In addition, aggregates of dye also provide a route for quenching of the excited state.[9, 10] Therefore, aggregation of dye is undesirable in DSCs.

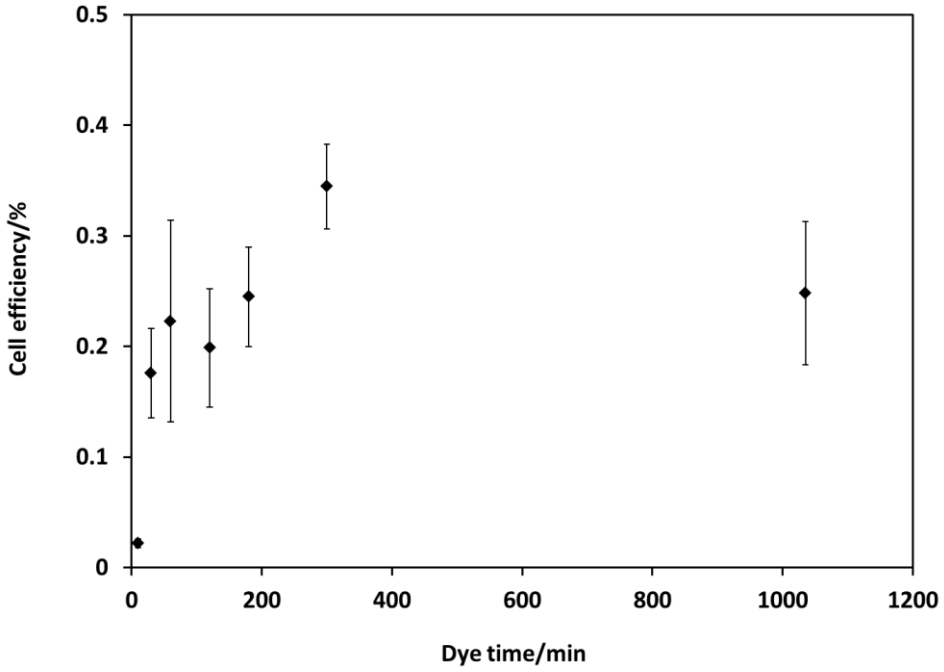

Figure 38 – TiO_2 film dye time versus DSC efficiency (error bars show one standard deviation, n=2 to 8. All points have error bars, some are just very small)

Choice of dye bath solvent may also be a contributing factor to aggregation. Recently, Ozawa and co-workers conducted a study into choice of dye bath solvent and its effect on DSC performance with the black dye.[12] The work identified that lower short-circuit photocurrents and overall cell efficiencies were recorded when MeOH was used as the dye bath solvent, even though there was more dye adsorbed on the surface. Photo- and electrochemical measurements of the black dye in solution and anchored on a TiO_2 surface found the dye was aggregating on the TiO_2 surface.

An alternative reason for the decrease in cell efficiency for a longer dye time is degradation of the dye/DSC. As mentioned previously, it was indicated to us that complex **1** was limited by instability. One week after assembly brown spots appeared on the dye's surface in 40 % of the DSCs, suggesting instability of the dye in contact with the electrolyte. Rendondo *et al* suggests that long-term stability of copper(I) DSCs with an I^-/I_3^- electrolyte is questionable due to slow reaction of the dye with the electrolyte to form copper(I) iodide.[13] Application of complex **1** with a cobalt$^{2+/3+}$ mediator is considered in Chapter 5.

Reaction of the dye with oxygen may also be a factor; therefore construction of some DSCs to minimise contact with oxygen was carried out. Without access to a "clean room" or glove box setup for fabrication, the assembly process was modified as follows from the standard procedure; the TiO_2 films were prepared under a N_2 umbrella and the dye baths were degassed with N_2 prior to film dyeing. As well as reducing time in contact with oxygen, the use of an N_2 umbrella for TiO_2 film manufacture will have reduced the presence of contaminants, such as dust, in the films. Three dye times were investigated; 2 hours, 5 hours and 18 hours. The results were varied, with the two hour dye time DSCs recording the highest efficiencies (Figure 39 and Table 2). Cells from a 5 hour dye time gave considerably poorer results than its DSC counterparts in air. However it was noted that poorer cell sealing meant the quality of cell was lower in this case. In general, using degassed dye baths and the nitrogen umbrella for preparation did not improve the DSC performance with complex **1**. Overnight dyeing in this experiment resulted in virtually the same cell output as observed for cells assembled by the standard route, with consistently lower cell parameters compared to those with films dyed for times between 2 and 5 hours. A more rigorous air-free experiment would need to be conducted in order to further study the effect of oxygen (or lack of) on dye degradation.

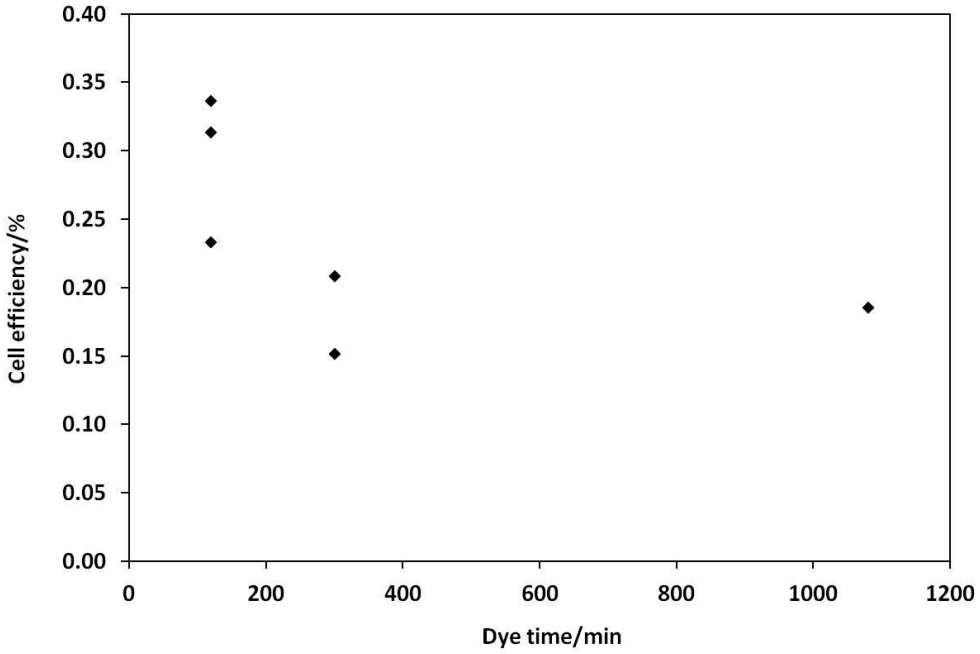

Figure 39 –TiO_2 film dye time versus DSC efficiency for cells prepared with complex 1 under N_2. Data for these cells is in Table 2.

Table 2 – DSCs constructed under a N_2 environment. Data for immediate measurement of *I-V* curves and retesting a week later

	Immediate testing				Testing after 1 week			
Dye time (min)	J_{SC} (mA)	V_{OC} (mV)	*FF*	η (%)	J_{SC} (mA)	V_{OC} (mV)	*FF*	η (%)
120	1.07	480	0.61	0.31	0.77	480	0.55	0.20
120	1.22	460	0.60	0.34	1.35	500	0.51	0.34
120	0.84	460	0.60	0.23	0.72	470	0.51	0.17
300	0.70	470	0.64	0.21	0.83	480	0.57	0.23
300	0.58	470	0.56	0.15	0.58	460	0.33	0.09
1080	0.72	440	0.59	0.19	1.03	460	0.43	0.20

DSCs in Figure 39 were retested a week later and these data are also shown in Table 2. It can be seen that half of the cells recorded the same, or higher, efficiencies. In these cases the improvements were acquired through an increased J_{SC}. The limited number of cells in this batch means the effect was not studied in more depth here. However it will be considered in greater detail in Chapter 7.

4.5. Cyclic voltammetry studies of complex 1

Cyclic voltammetry of complex **1** was carried out using a dyed TiO_2 film as the working electrode (WE). As TiO_2 is an insulator under the conditions used in the CV, electron transfer to and from adsorbed dye molecules occurs *via* dye molecules in contact with bare FTO at the base of the pores. Observation of dye electrochemistry therefore indicates dye coverage throughout the porous TiO_2 network to the FTO contact.

The WEs were prepared as described in Chapter 3.5.1 and films were dyed from a 0.3 mM solution of complex **1** in MeOH. A platinum counter electrode (CE) and an Ag/AgCl reference electrode (RE, 3 M KCl) completed the cell. The background electrolyte was 0.1 M tetrabutylammonium hexafluorophosphate (TBAHFP) in MeCN. Once background scans had been recorded with a blank TiO_2 film, the WE was switched for a dyed film and scans were run until the potential window of activity was identified. The system was studied at scan rates increasing from 10 mV/s to 5 V/s. A complex set of results was obtained which varied with scan rate. At scan rates <100 mV/s a reversible oxidation and reduction were

visible, with a peak reduction potential (E_p^{red}) and peak oxidation potential (E_p^{ox}) of +0.29 V and +0.68 V respectively (Figure 40 (a)). This peak separation increased with scan rate.

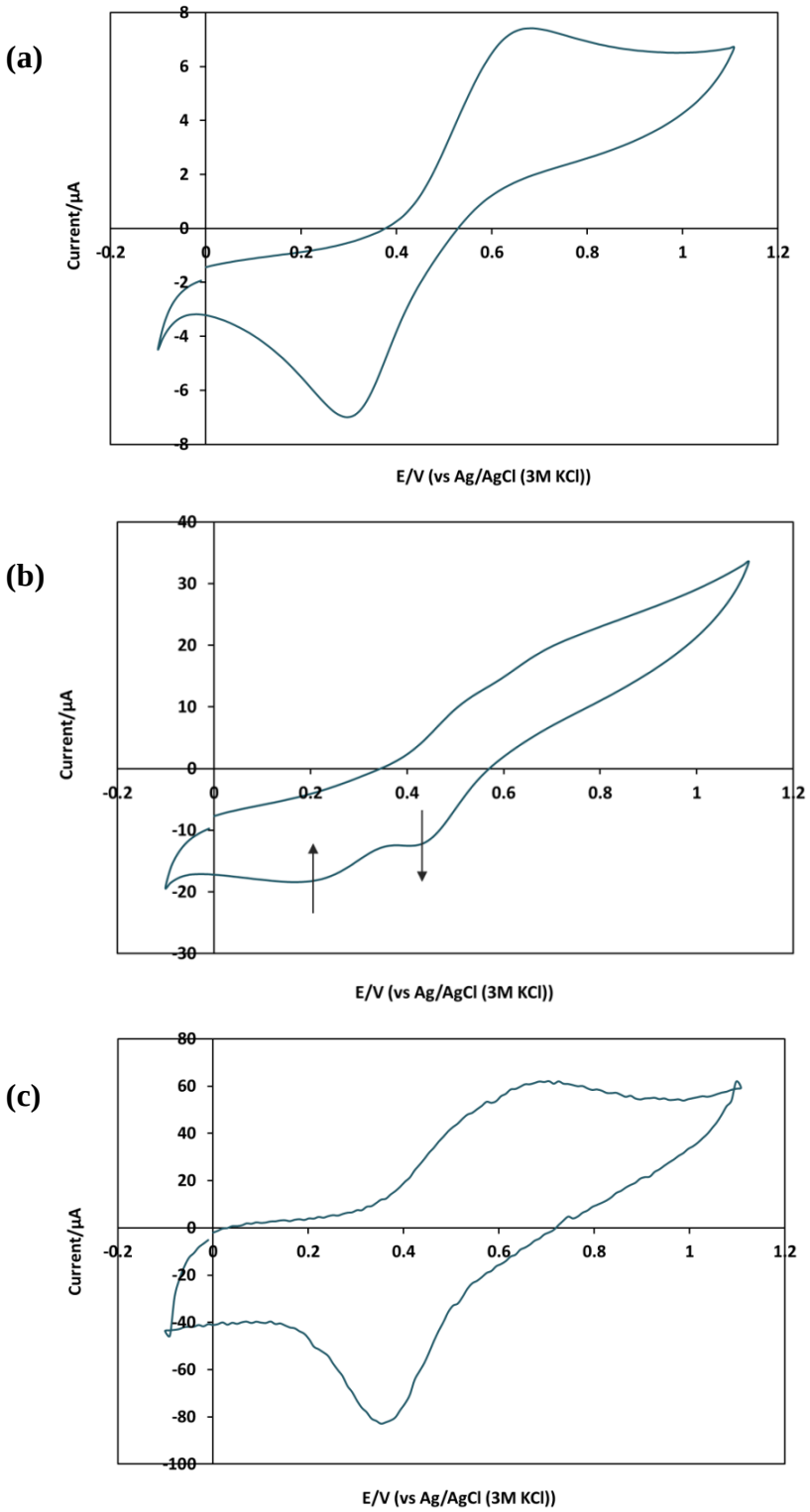

Figure 40 – a CV of complex 1 adsorbed to a TiO_2 film at a scan rate of (a) 10 mV/s; (b) 500 mV/s and (c) 5 V/s

In addition, at scan rates ≥250 mV/s a second reduction peak appeared at +0.42 V. This peak increased in magnitude with scan rate whilst the reduction peak at +0.29 V decreased (Figure 40 (b)). At the fastest scan rates, the second reduction peak dominates and the reduction which was initially present at +0.29 V has disappeared (Figure 40 (c)). A second oxidation peak, albeit broad, is also apparent at the intermediate scan rates at around +0.52 V (Figure 40 (b)). Although these observations are complicated to rationalise, one possible explanation is an ECE mechanism according to Figure 41 (where E represents an electrochemical step and C represents a chemical step).

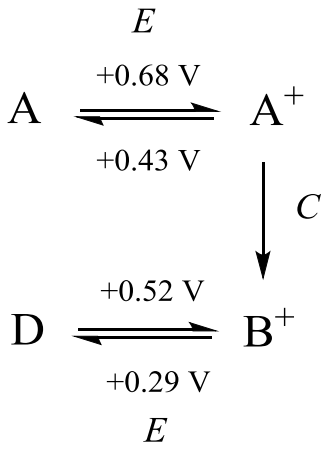

Figure 41 – proposed reaction mechanism for complex 1 on a TiO_2 surface

This mechanism would explain the observations at different scan rates as follows. At very slow scan rates oxidation of the dye (A) occurs at E_p^{ox} = +0.68 V, which is followed by a chemical conversion of A^+ to B^+, before electrochemical reduction of A^+ can take place. The reduction present at very slow scan rates is therefore attributed to reduction of this chemically generated species B^+ to D. At intermediate scan rates the timescale for electrochemical reduction of A^+ becomes more competitive; therefore this is observed at +0.43 V. At the fastest scan rates this is the only reduction process observed, implying the chemical step of A^+ through to B^+ has been switched off. The second oxidation peak is presumably due to oxidation of D back to B^+. This double peak is only observed at the intermediate scan rates however with similar oxidative potentials and broad peaks, it is possible that the second oxidation is masked at slow scans rates.

Once a scan rate of 5 V/s had been reached, further slow scans were run (from 25 mV/s to 250 mV/s) to check whether an irreversible change had affected the films during the fast scans. However the system responded the same way as initially observed. This variation in behaviour with scan rate implies some instability on the TiO_2 surface. Possibilities for the chemical step include reaction of the oxidised dye with a solvent molecule or oxygen, or loss of a ligand.

Regeneration of the dye with LiI was also studied. The reduction of the excited state of complex **1** by iodide can be probed using cyclic voltammetry. A dyed TiO_2 film was again used as the WE and the other conditions were kept the same. Through adding an increasing concentration of LiI to the experiment (from 0 M to 0.87 mM in a solution of 0.1 M TBAHFP in MeCN) an EC' mechanism was observed (Figure 42) where E refers to an electrode step and C' is a catalytic chemical process.

E: $D - e^- \longrightarrow D^+$

C': $D^+ + 3/2\ I^- \longrightarrow D + 1/2\ I_3^-$

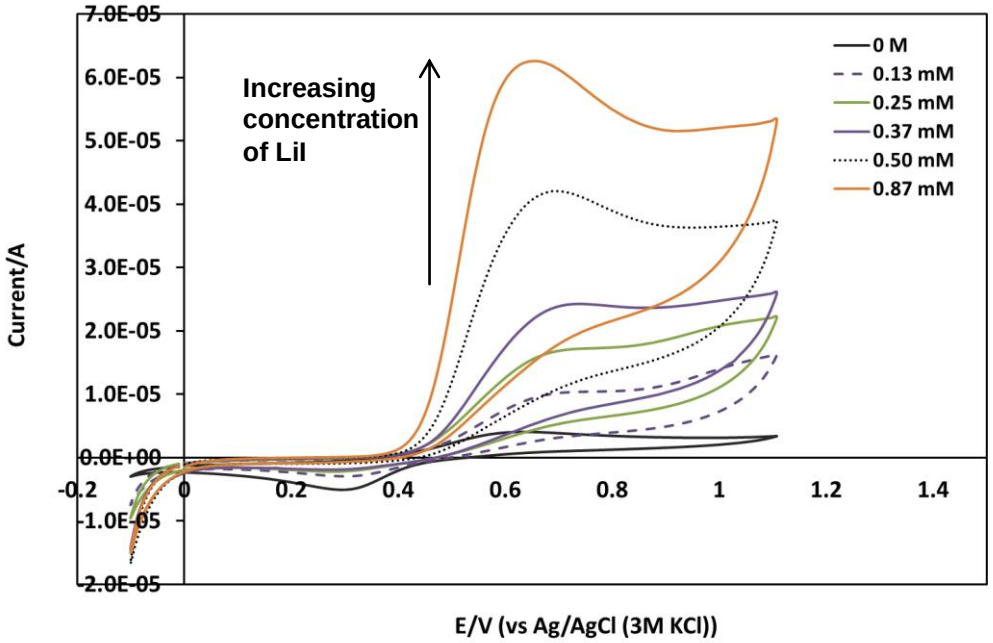

Figure 42 – CVs showing the current response after adding increasing concentrations of LiI at a scan rate of 10 mV/s; 0 M (-), 0.13 mM (--), 0.25 mM (-), 0.37 mM (-), 0.50 mM (···) and 0.87 mM (-)

A large increase in the oxidative current was observed with increasing concentration of iodide. This is due to the dye's ground state being regenerated in the catalytic chemical step, then rapidly re-oxidised at the anode. The reduction peak initially decreases then disappears completely as iodide is chemically reducing the oxidised species rather than the electron transfer occurring at the electrode. This response suggests that under the conditions of the electrochemical experiment at least, regeneration of the dye by the redox mediator is occurring. Regeneration of the dye in an assembled DSC will also be subject to other influences, such as the other electrolyte components. The experiment was repeated at scan rates of 0.5 V/s and 1.5 V/s with the same response observed.

4.6. Conclusions

[Cu(6,6'-dimethyl-2,2'-bipyridine-4,4'-dicarboxylic acid)$_2$][Cl], complex **1**, and its preceding ligands were prepared according to literature methods and characterised. Varying the immersion time of TiO_2 films in methanolic solutions of complex **1** produced the expected trend in dye uptake with increased dye time. There was also an observed shift in the visible region absorbance maxima to longer wavelengths as the dye time was increased, which is often associated with dye aggregation on the TiO_2 surface.

DSCs were constructed for a range of TiO_2 film dye times, from 10 minutes to 17 hours. Cell efficiencies achieved were higher than, or comparable to, those reported in the literature for this complex. A top efficiency of 0.44 % was obtained for a 0.8 cm^2 dyed area cell. DSC efficiencies were generally found to increase with dye time from 10 minutes up to 5 hours. Where the TiO_2 film was dyed overnight, cell parameters were consistently lower than those dyed for between 2 and 5 hours. Therefore an optimum dye time for this complex is around 5 hours, although a range of measurements between 5 and 17 hours should ideally be carried out. The decline in performance following overnight dyeing was not noted with N719. It is likely due either to dye aggregation on the surface or a degradation of the dye. Aggregation is suggested from the UV/Vis experiments. Degradation could be due to time spent in air, in contact with solvent or in contact with electrolyte components. Instability in air is implied from the elemental analysis, which showed too low quantities of C, H and N. There were also two redox processes taking place on the TiO_2 films studied by cyclic voltammetry. The reversible system observed at very slow scan rates disappeared at faster scan rates, as a second reduction peak (at a more positive potential) started to dominate the scan.

The presence of oxygen in the DSC assembly process was reduced by dyeing films from a degassed dye solution and using a nitrogen umbrella for film preparation. No significant improvement was noted. Overnight dyeing still produced a lower efficiency cell relative to those dyed for 2 and 5 hours. The cells in this experiment were retested a week later and improvements, or an equal response, were observed in half of the batch. Improvements in η were due to an increase in J_{SC}, which will be considered further in Chapter 7.

Regeneration of complex **1** with LiI was found to occur effectively, as determined *via* cyclic voltammetry. The electrochemically oxidised dye molecules are chemically reduced by

iodide, resulting in an observed decrease in the reduction peak in CV and an increase in the oxidative current.

In conclusion, the dark red-coloured complex **1** is suitable for DSC application and produces reasonable solar-to-power conversion efficiencies. However there is scope for improvement. It exhibits a narrow visible region absorption band at $\lambda_{(max)}$ 480 nm. Therefore, as acknowledged in the literature,[14, 15] addition of more chromophoric groups would be beneficial in order to broaden the light harvesting of the dye. In addition, the stability of complex **1** is unclear. Shorter dye times are preferable and an alternative redox mediator to the iodide/triiodide couple would possibly be an improvement.

4.7. References

1. T. Bessho, E. C. Constable, M. Grätzel, A. H. Redondo, C. E. Housecroft, W. Kylberg, M. K. Nazeeruddin, M. Neuburger and S. Schaffner, *Chem. Commun.*, 2008, 3717-3719.
2. E. C. Constable, A. H. Redondo, C. E. Housecroft, M. Neuburger and S. Schaffner, *Dalton Trans.*, 2009, 6634-6644.
3. V. M. Mukkala and J. J. Kankare, *Helv. Chim. Acta*, 1992, **75**, 1578-1592.
4. P. Karrer, C. Cochand and N. Neuss, *Helv. Chim. Acta*, 1946, **29**, 1836-1841.
5. E. Dell'Orto, L. Raimondo, A. Sassella and A. Abbotto, *J. Mater. Chem.*, 2012, **22**, 11364-11369.
6. M. Durr, A. Schmid, M. Obermaier, A. Yasuda and G. Nelles, *J. Phys. Chem. A*, 2005, **109**, 3967-3970.
7. P. J. Holliman, B. V. Velasco, I. Butler, M. Wijdekop and D. A. Worsley, *Int. J. Photoenergy*, 2008, Article ID 827605.
8. A. Fillinger and B. A. Parkinson, *J. Electrochem. Soc.*, 1999, **146**, 4559-4564.
9. S. Agrawal, M. Pastore, G. Marotta, M. A. Reddy, M. Chandrasekharam and F. De Angelis, *J. Phys. Chem. C*, 2013, **117**, 9613-9622.
10. Z.-S. Wang, Y. Cui, Y. Dan-oh, C. Kasada, A. Shinpo and K. Hara, *J. Phys. Chem. C*, 2007, **111**, 7224-7230.
11. J. Bujdák and N. Iyi, *J. Phys. Chem. B*, 2005, **109**, 4608-4615.
12. H. Ozawa, M. Awa, T. Ono and H. Arakawa, *Chem. Asian J.*, 2012, **7**, 156-162.
13. A. H. Rendondo, E. C. Constable and C. E. Housecroft, *Chimia*, 2009, **63**, 205-207.
14. B. Bozic-Weber, S. Y. Brauchli, E. C. Constable, S. O. Furer, C. E. Housecroft, F. J. Malzner, I. A. Wright and J. A. Zampese, *Dalton Trans.*, 2013, **42**, 12293-12308.
15. X. Q. Lu, S. X. Wei, C. M. L. Wu, S. R. Li and W. Y. Guo, *J. Phys. Chem. C*, 2011, **115**, 3753-3761.

Chapter 5 - Application and analysis of a copper(I) 2,2'-biquinoline-4,4'-dicarboxylic acid dye (20) in a DSC

5. Application and analysis of a copper(I) 2,2'-biquinoline-4,4'-dicarboxylic acid dye (20) in a DSC

5.1 Introduction and theory

This chapter follows on from work started in an MRes project at the University of Bath and which was published in 2013.[1,2] Synthesis of more sustainable dyes for use in DSCs by replacing ruthenium with copper metal is the title objective of this thesis, however, it is also important that the choice of ligand agrees as far as possible with this objective. To that end, the synthesis and study of a homoleptic copper(I) dye with the commercially available 2,2'-biquinoline-4,4'-dicarboxylic acid (dcbiq) ligand (or bicinchoninic acid, BCA, Figure 43) was carried out. Following on from the conclusions reached in Chapter 4, the 2,2'-biquinoline ligand was also chosen due to its higher level of conjugation relative to the typically used 2,2'-bipyridine (bipy) ligand. Therefore its complexes should absorb more visible light at longer wavelengths. Furthermore, as described in Chapter 1.5.2, employing bulky ligands such as dcbiq constrains the copper(I) metal centre within a rigid environment to prevent geometry changes between the copper(I) and (II) oxidation states.

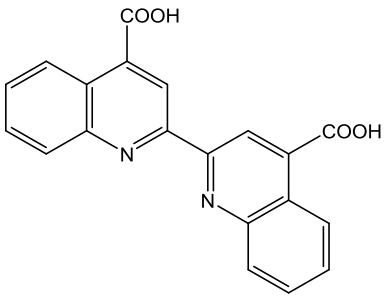

Figure 43 – 2,2'-biquinoline-4,4'-dicarboxylic acid (dcbiq)

$[Cu(dcbiq)_2]^+$ is a known complex and is most commonly used in the BCA assay, which measures protein concentration in a solution.[3, 4] In terms of use of the dcbiq ligand in dyes for DSC application, ruthenium(II) biquinoline complexes, both heteroleptic[5, 6] and homoleptic[7] have been trialled, although their DSC properties and performance were poorer than for other ruthenium sensitizers. Incident photon-to-current efficiencies (IPCEs) for the heteroleptic ruthenium complexes were low (≤ 10%). Homoleptic sensitizers of the type *cis*-$Ru(dcbiq)_2(NCS)_2$ also produced low IPCE values and overall cell efficiencies were <0.4%. These findings have been attributed to inefficient electron injection into the TiO_2 conduction band due to a low-lying π* orbital on the dcbiq ligand. Sandroni and co-workers recently reported the synthesis of heteroleptic copper(I) complexes which employed an

anchoring dcbiq ligand and sterically bulky variants of the 1,10-phenanthroline ligand[8] (Figure 44, complexes **18** and **19**). Synthesis of these dyes *via* the HETPHEN strategy ("HETeroleptic PHENanthroline") involves choosing a chelating ligand which is so bulky as to make formation of the homoleptic species highly unfavourable. Similarities between these species and the homoleptic complex presented in this chapter will be noted later.

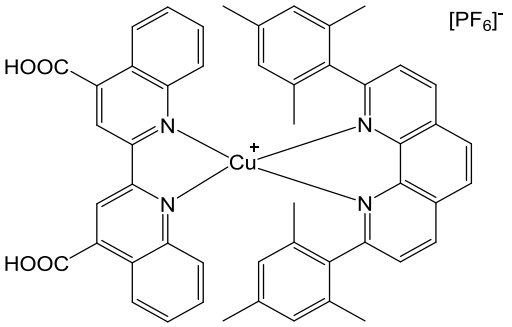

18

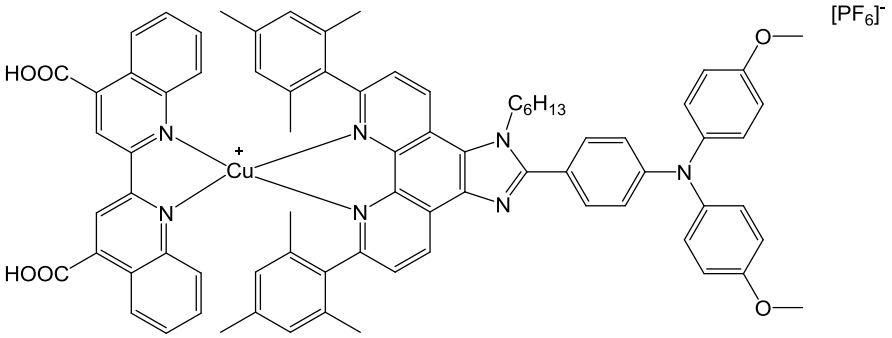

19

Figure 44 - Two heteroleptic complexes synthesised by Sandroni and co-workers with 2,2'-biquinoline-4,4'-dicarboxylic acid[8]

Although it is commonly reported in the literature[7, 9, 10] that dcbiq has a too low-lying π^* orbital to enable electron injection from its metal complexes into the TiO_2 conduction band, computational analysis of a copper(I) 2,2'-biquinoline-4,4'-dicarboxylic acid complex by us, and others,[11] suggests that the energetic position of the lowest unoccupied molecular orbital (LUMO) should be adequate for electron injection. To the best of our knowledge the practical application of this dye in DSCs has not previously been reported.

5.2 Synthesis and structure of complex 20

The complex (**20**, Figure 45) was synthesised under N_2 using two equivalents of the commercially available 2,2'-biquinoline-4,4'-dicarboxylic acid and one equivalent of $[Cu(MeCN)_4][PF_6]$. Solubility of the ligand in common organic solvents was poor; therefore four equivalents of NEt_3 were added to the reaction mixture, resulting in the formation of a clear, deep purple solution (Figure 45).

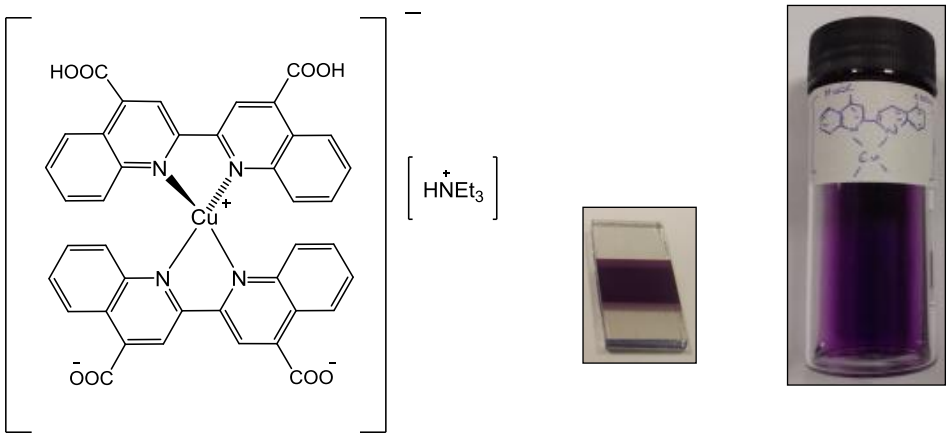

20

Figure 45 – structure of [Cu(2,2'-biquinoline-4,4'-dicarboxylic acid)$_2$]$^-$ [HNEt$_3$]$^+$ (complex 20); the dye in methanol and a dyed TiO_2 film

The dark purple solid obtained following recrystallisation from MeOH and Et_2O was identified as the desired complex. Full structural assignment was possible using 2D ^{1}H and ^{13}C {^{1}H} NMR experiments. Crystals of suitable quality for X-ray diffraction were grown from slow evaporation of a MeOH solution of the dye. From analysis of the C-O and C=O bond distances in the crystal structure (Figure 46), it is implied that in its solid-state form the complex exists with one biquinoline ligand being fully deprotonated and the other fully protonated. This results in a copper(I) 2,2'-biquinoline-4,4'-dicarboxylic acid anion, which is charge balanced with a $[HNEt_3]^+$ counterion. In support of this, negative mode ESI-MS showed a peak at *m/z* 749.0750, corresponding to the molecular anion shown in Figure 45, $[M]^-$. This crystal was higher quality than those obtained previously, which enabled the identification of the quaternary amine cation. The crystal structure of the copper(I) anion indicates that the ligands are close to being orthogonal, in a pseudo-tetrahedral geometry, with an angle between the two biquinoline planes of 75.29°. For the similar complex,

[Cu(4,4',6,6'-tetramethyl-2,2'-bipyridine)$_2$][BF_4], synthesised by the Robertson group, the angle between the planes of the two bipyridyls is 72.18°.[12] Furthermore, for their homoleptic bipyridyl complexes, the Constable group reported least squares planes angles of 81.11° and 84.49°.[13] Therefore complex **20** exhibits an analogous geometry to these previously reported structures. Key bond lengths and angles for complex **20** are collected in Table 3 and they are also within the range of similar Cu(I) complexes reported in the literature.[13-15] The arrangement of molecules of complex **20** in the unit cell (Figure 46 (b)) shows some π-π stacking between biquinoline rings in adjacent molecules with distances between overlapping biquinoline rings ranging between 3.4 and 3.8 Å, as well as hydrogen bonding between the carboxylic acid groups.

Table 3 – key bond lengths and bond angles of complex 20

[Cu(2,2'-biquinoline-4,4'-dicarboxylic acid)$_2$]$^-$ (Complex 20)	
Bond/Angle	**Bond length (Å) /Angle (°)**
Cu(1)-N(1)	2.015(4)
Cu(1)-N(2)	2.003(4)
Cu(1)-(N3)	2.002(4)
Cu(1)-N(4)	2.022(4)
N(1)-Cu(1)-N(2)	81.10(15)
N(1)-Cu-N(3)	132.33(16)
N(1)-Cu-N(4)	115.23(15)

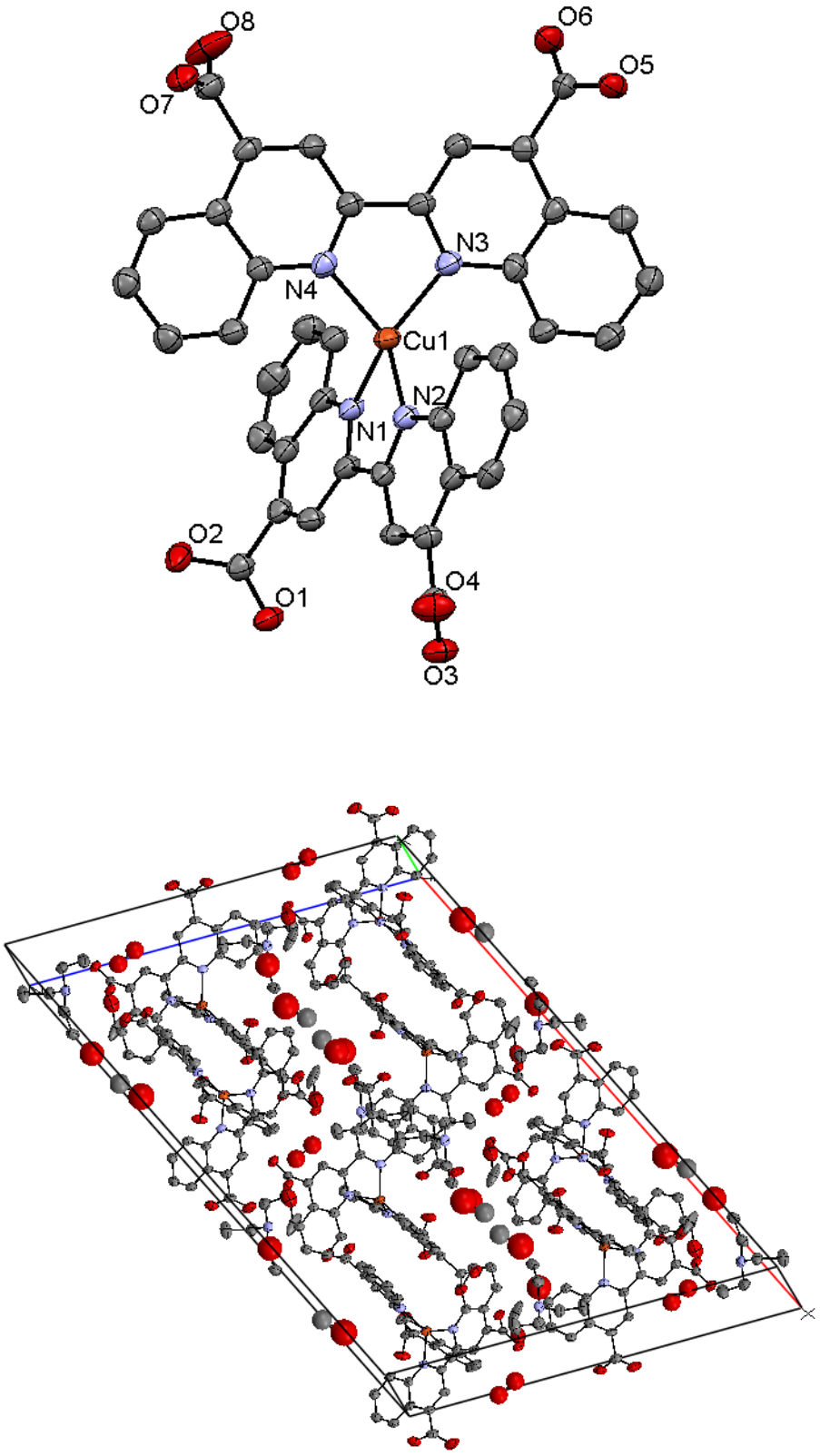

Figure 46 – (a) crystal structure of the [Cu(2,2'-biquinoline-4,4'-dicarboxylic acid)$_2$]$^-$ anion. All hydrogen atoms have been removed for clarity, as have solvent of crystallisation and the [HNEt$_3$]$^+$ counterion; (b) crystal packing structure of complex 20

There was no evidence of the $[PF_6]^-$ ion in the unit cell however its presence was noted in $^{31}P\{^1H\}$ and ^{19}F NMR spectra of the dye and also implied in the elemental analysis results. Given the ratios in ^1H NMR of the triethylamine protons to those on the copper(I) anion, it was concluded that whilst one equivalent of triethylamine was charge balancing the copper(I) 2,2'-biquinoline-4,4'-dicarboxylic acid anion, a second equivalent was co-crystallising with the $[PF_6]^-$ anion. The elemental analysis matched for this arrangement. Its ease of synthesis, cheap starting materials and excellent dyeing of TiO_2 films suggested that this dye could be a promising sensitizer.

5.3 UV/Vis spectroscopy studies

It was highlighted[1] that the electronic absorption spectrum for complex **20** (Figure 47) demonstrates that the increased conjugation of the 2,2'-biquinoline ligand induces a so-called "red shift" in absorbance compared to its 2,2'-bipyridine analogue (complex **1**, Figure 47). As described in Chapter 4, complex **1** was synthesised from furfural and 2,3'-butanedione[13] and will be used in this chapter for comparisons to complex **20**.

The peak absorptions at 360 nm for complex **20** and 326 nm for complex **1** are attributed to a ligand based $\pi \rightarrow \pi^*$ transition. Bands at 564 nm for complex **20** and 491 nm for complex **1** are attributed to a metal-to-ligand charge transfer (MLCT). It is clear from the red-shifted position of the absorption maxima that the energies of both the $\pi \rightarrow \pi^*$ transition and the MLCT in complex **20** are reduced relative to those in complex **1**. As discussed previously, this can either be due to an increase in energy of the highest occupied molecular orbital (HOMO) or a lowering of the LUMO orbital. Using UV/Vis data in conjunction with cyclic voltammetry (CV) experiments enables an estimation of the HOMO and LUMO energy levels, which will be discussed later.

The molar extinction coefficient, ε, is larger for complex **20** (11,700 $M^{-1}cm^{-1}$ in MeOH at $\lambda_{(max)}$ 564 nm) than recorded for complex **1** (6800 $M^{-1}cm^{-1}$ at $\lambda_{(max)}$ 491 nm); as one would expect with the enhanced conjugation in the structure. In addition, it is similar to the benchmark ruthenium(II) complex N3, which has a ε of 14,200 $M^{-1}cm^{-1}$ at 534 nm.[16] As expected, there are also several similarities between complex **20** and the heteroleptic copper(I) biquinoline sensitizers reported by Sandroni *et al* (Figure 44). The shapes of the UV/Vis spectra are very similar, with all three showing a clear absorption tail extending to

~700 nm and a maximum visible region absorbance of ~560 nm. The molar extinction coefficients of complexes **18** and **19** for this transition are noted as ~5000 M^{-1} cm^{-1}.

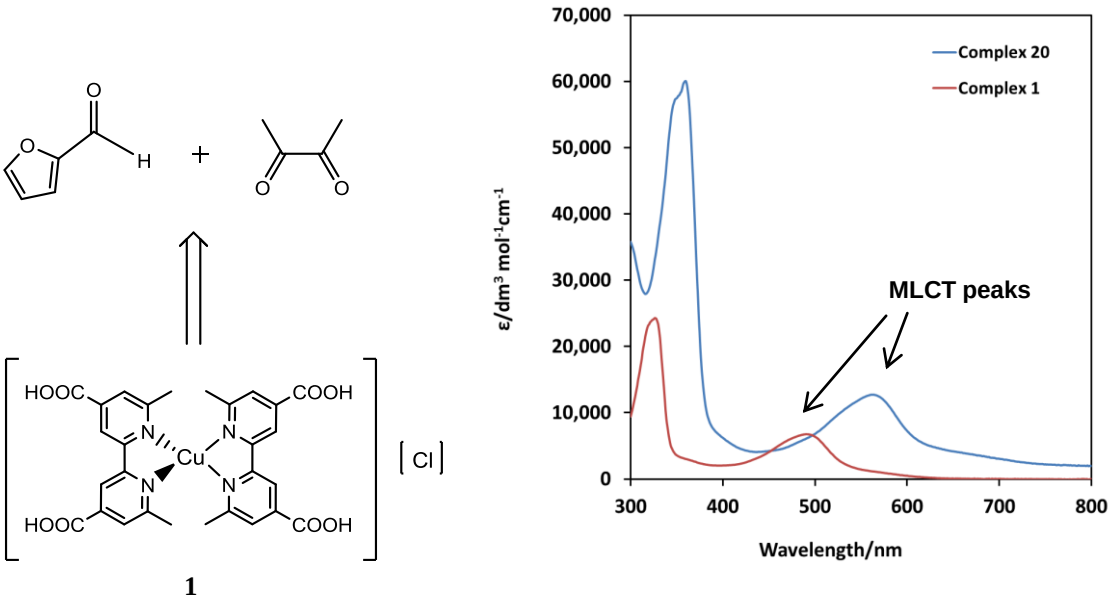

Figure 47 – structure of [Cu(6,6'-dimethyl-2,2'-bipy-4,4'-dicarboxylic acid)][Cl] (complex 1) and UV/Vis spectra of complexes 20 and 1 compared (in MeOH)

UV/Vis spectra of complex **20** anchored to a TiO_2 surface were recorded for films dyed for increasing periods of time (Figure 48). The increase in absorbance with dye time was analogous to that observed for complex **1** in Chapter 4.3, although without the shift in $\lambda_{(max)}$ with increasing dye time. There was, however, a shift in $\lambda_{(max)}$ for the surface bound **20** to a slightly higher energy relative to that measured in solution (552 nm compared to 564 nm). Sandroni *et al* observed the same behaviour for the heteroleptic copper(I) biquinoline complexes[8] and attributed the response to the variation in protonation between the dcbiq ligand on the surface (fully deprotonated) and in solution. This effect is also noted elsewhere.[17] In addition, it is noted that this difference between solution and surface UV/Vis measurements can also originate from dye aggregation on the film or solvatochromatism in solution.[18]

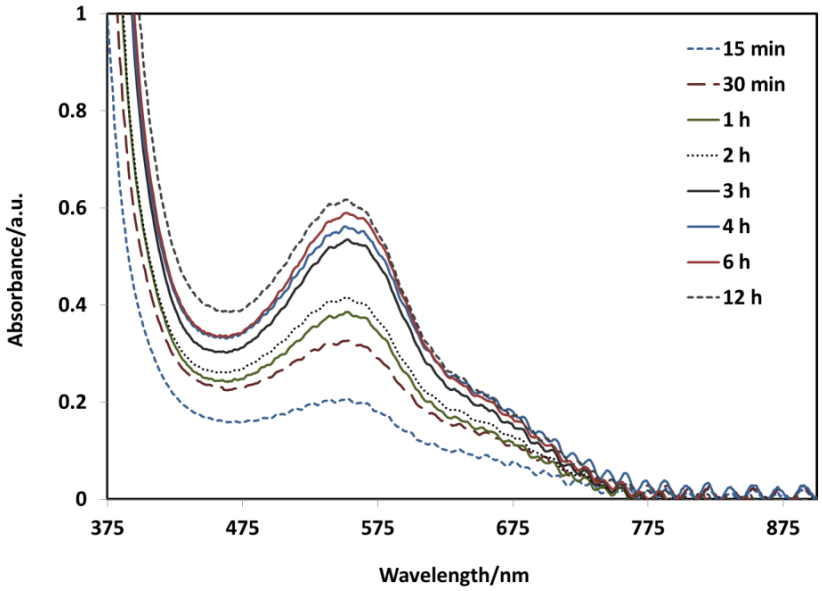

Figure 48 - UV/Vis spectra of complex 20 adsorbed on TiO_2 films at increasing dye times; 15 min (- - -), 30 min (- - -), 1 hour (-), 2 hours (⋯), 3 hours (-), 4 hours (-), 6 hours (-), 12 hours (--)

5.4 Dye uptake and its effect on DSC performance

To calculate the amount of complex **20** adsorbed on the TiO_2 films, the dye was then desorbed from the same films (those from Figure 48) by immersion in 1 M KOH (aq.) for 40 minutes. The dye complex decomposed under the basic conditions used for desorption, resulting in colourless KOH (aq.) solutions. Therefore the dye coverage was calculated from the amount of dcbiq ligand in solution, using the absorbance at 332 nm, (ε = 26,100 $M^{-1}cm^{-1}$). The calibration measurements, made using solutions of dye in 1 M KOH (aq.), were also colourless. The dye uptake curve is shown in Figure 49. After overnight dyeing, the surface coverage was found to be $\approx 10 \times 10^{-8}$ mol cm^{-2} of geometric film area. This figure is comparable to reported data for the analogous ruthenium biquinoline complex[7] and the typical ruthenium dyes N3[16] and N719.[16, 19, 20] In these measurements TiO_2 film thicknesses were typically between 9 and 10 microns, measured by reflectometry.

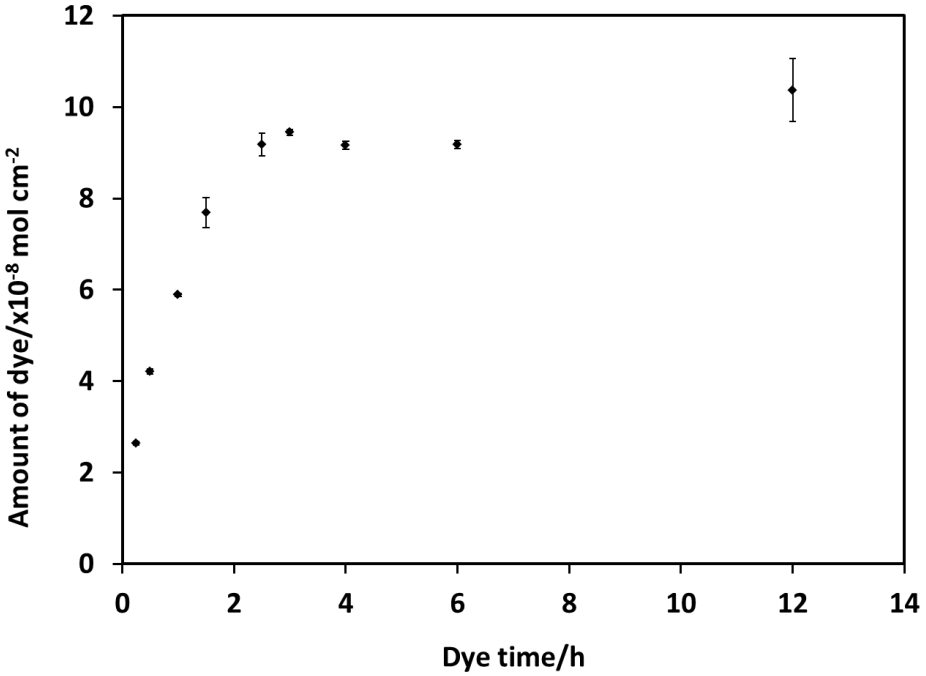

Figure 49 - Amount of complex 20 adsorbed on TiO_2 films with increasing dye time (n=2, error bars show one standard deviation. All points have error bars, some are just very small), measured by UV/Vis, following dye desorption from the films into 1M KOH (aq.)

DSCs constructed with complex **20** had overall solar-to-power conversion efficiencies far lower than desired (η typically $\leq$ 0.1%).[1] Therefore the effect of TiO_2 film dye time on DSCs assembled with complex **20** was also studied (Figure 50 and Figure 51). The TiO_2 films were prepared *via* ***method 1*** (see Chapter 3.3.1) and the standard electrolyte recipe was used. Films were dyed from 0.53 mM solutions of **20** in MeOH and all cells had a dyed area of 1 cm^2. As observed with complex **1**, DSCs made from films dyed with complex **20** for longer periods of time showed a lower overall solar-to-power conversion efficiency. A V_{OC} loss of 100 mV was observed between the shortest and longest dye times (Figure 50) and a decrease in η of ~20% (Figure 51). There was initially an increase in η on going from 30 minutes to 2 hours dye time; however this was followed by a decrease for the 5 hour and overnight DSCs. For comparison, an N719 cell dyed overnight from the same batch of films had the following characteristics; J_{SC} = 9.96 mA cm^{-2}, V_{OC} = 0.720 V, η = 3.35 %. The decrease in overall cell efficiency was due to a loss of photovoltage rather than current, and a reduced V_{OC} suggests an increase in the recombination reaction, which can be a consequence of aggregated systems.[21] Therefore it was concluded from this experiment that shorter dye times (~2 hours) appear preferable for DSCs with complex **20**, as was the case with complex **1**, although overall its performance in DSCs was mediocre.

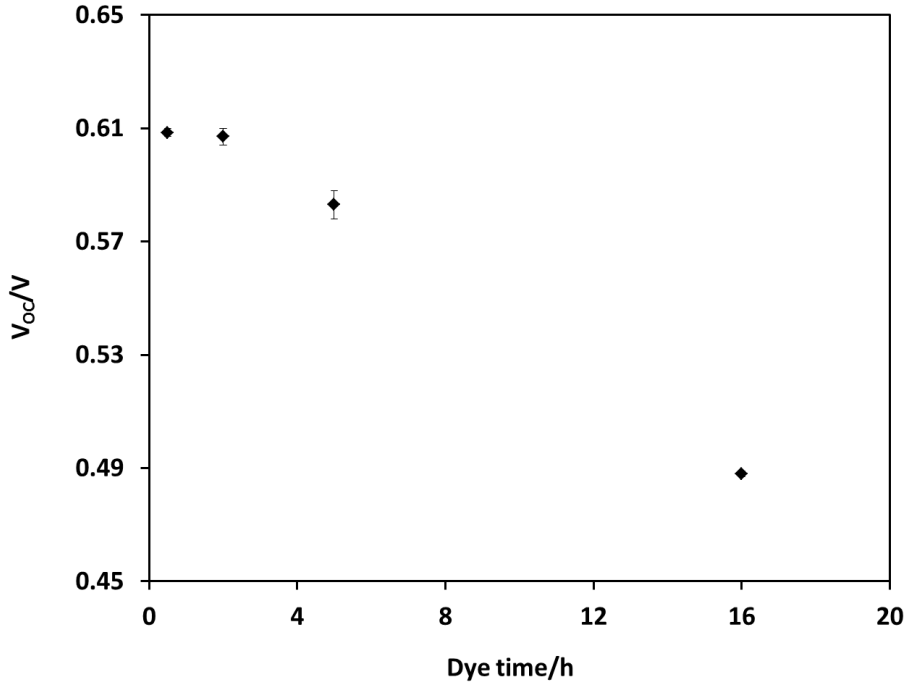

Figure 50 - variation in V_{OC} with TiO_2 film dye time (n=2, error bars show one standard deviation. All points have error bars, some are just very small). Note the x-axis scale is between 0.45 V and 0.65 V

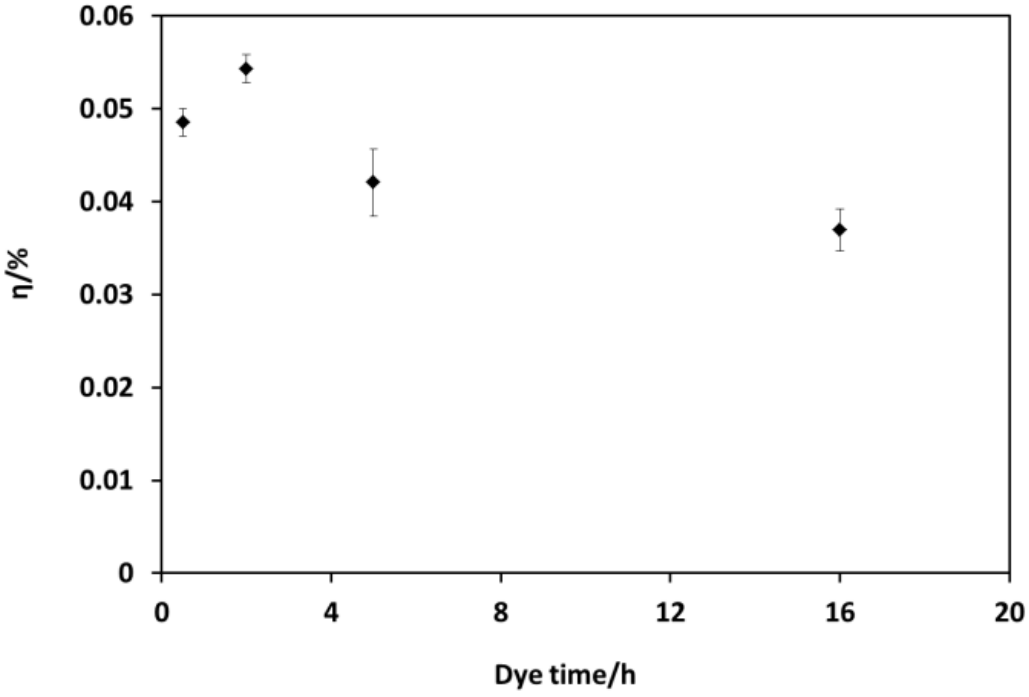

Figure 51 - variation in η with TiO_2 film dye time (n=2, error bars show one standard deviation)

5.5 Emission spectroscopy experiments

Emission spectroscopy can provide information about the excited state of the dye molecule. Generally, if emission is observed it is an indication that the excited state lifetime is sufficient for injection into the TiO_2 conduction band. However, as described in Chapter 1.5.1, fluorescence and phosphorescence are not the only means of deactivating an excited state. The electron can be lost in a non-radiative decay process, or through some type of quenching mechanism with other dye molecules or oxygen. Therefore all solutions in these experiments were degassed beforehand to reduce the chance of quenching by oxygen.

Emission spectroscopy measurements of a 0.1 mM solution of complex **20** in EtOH produced a broad emission peak at 400 nm following excitation at 320 nm, attributed to fluorescence from the ligand-based π^* excited state (Figure 52). When cooled to 77 K, three peaks at 500, 536 and 584 nm became resolved following a 330 nm excitation, interpreted as phosphorescence from the same state (Figure 53). Excitation acquisitions confirmed the wavelengths responsible for these emission spectra. Excitation over a large range of wavelengths in the visible region of the spectrum was tried, but no emission was observed at either temperature.

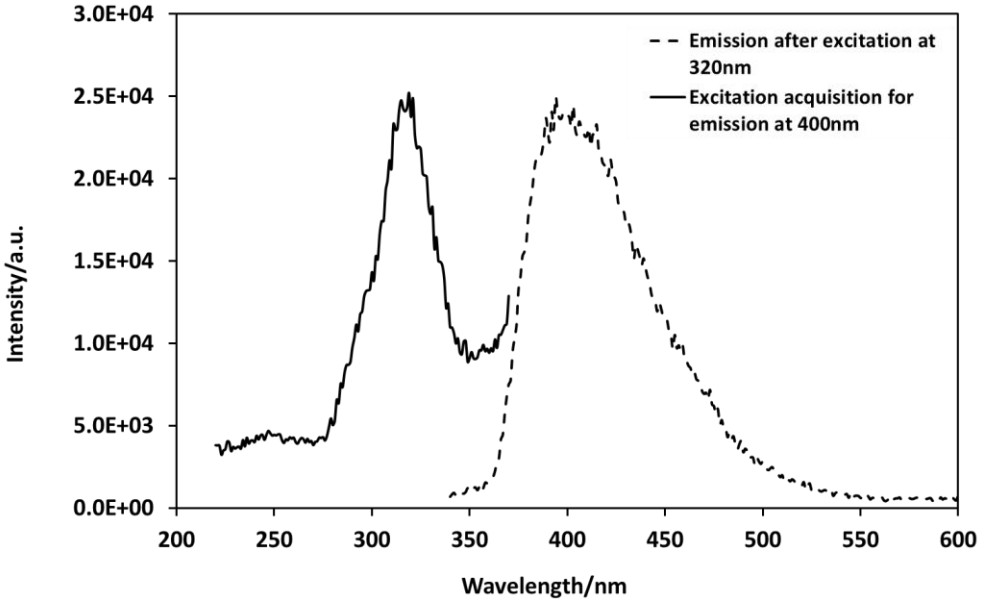

Figure 52 – excitation and emission spectra of complex 20 in EtOH at room temperature, following excitation at 320 nm

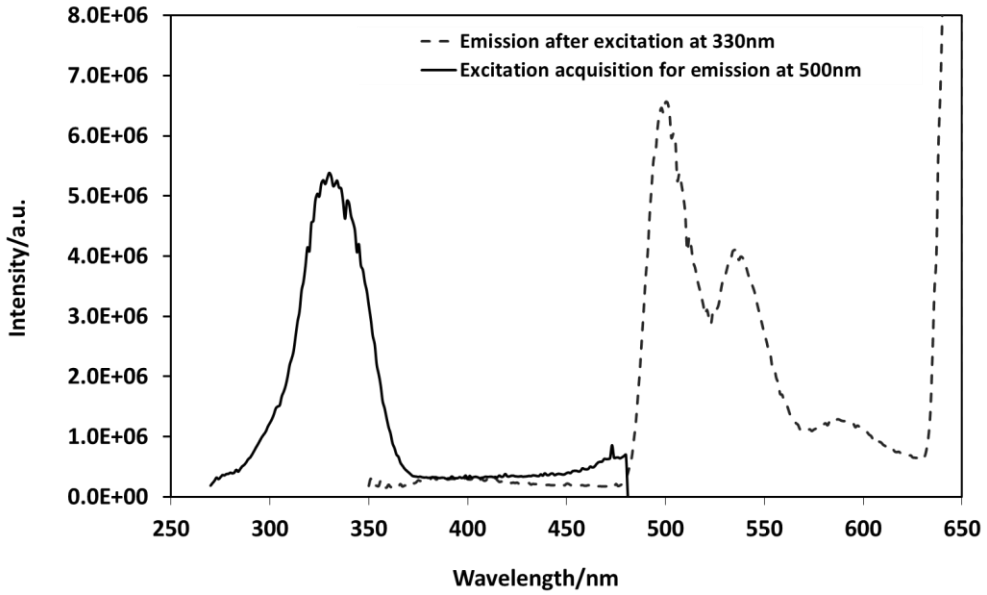

Figure 53 - excitation and emission spectra of complex 20 in EtOH at 77 K following excitation at 330 nm

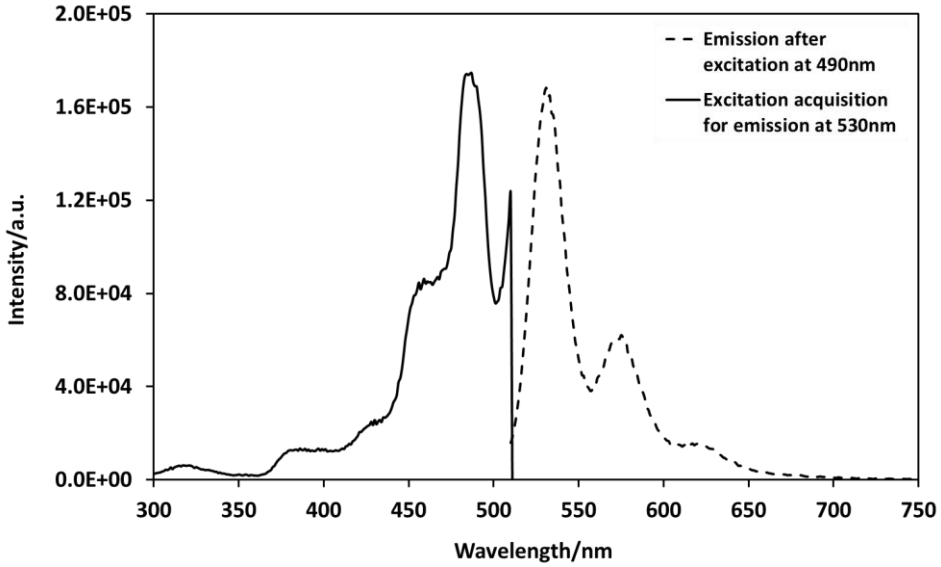

Figure 54 - excitation and emission spectra of complex 20 in CH_2Cl_2 at room temperature following excitation at 490 nm

When the solvent was changed to the weakly-coordinating CH_2Cl_2, fluorescence was observed at room temperature following excitation at 490 nm (Figure 54) and at 520 nm (Figure 55). It is difficult to determine whether this is emission from a ligand-based π* state or the MLCT state, as the excitation wavelengths are midway between those expected for

either state, with respect to the observed electronic absorption spectrum (which was carried out in CH_2Cl_2 for direct comparison).

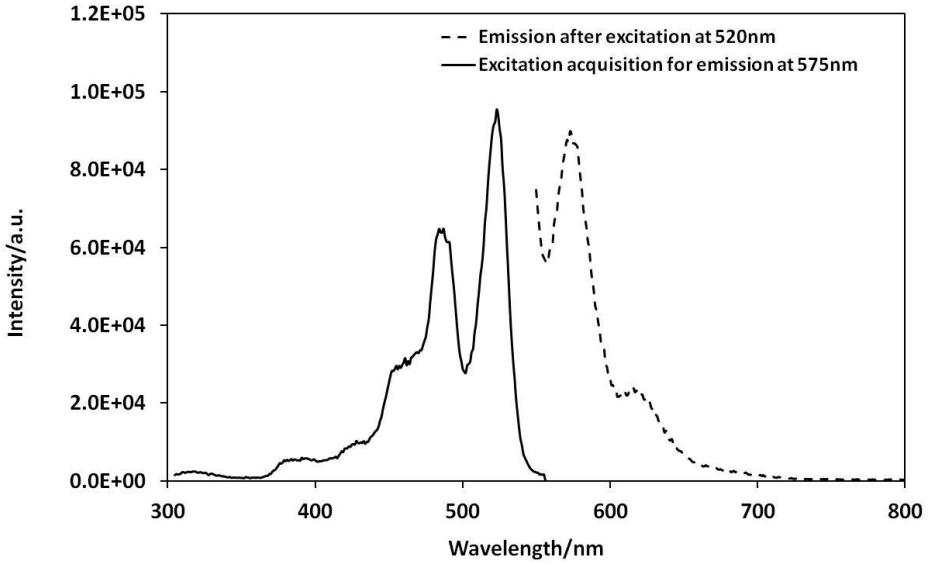

Figure 55 - excitation and emission spectra of complex 20 in CH_2Cl_2 at room temperature following excitation at 520 nm

There was also an emission peak at 385 nm following excitation at 320 nm (not shown), which agreed with the fluorescence observed at this wavelength in the EtOH experiments. The emission scan following excitation at this wavelength was run to 620 nm and there were no peaks at 530 nm and 575 nm, indicating that these emissions were not due to the 320 nm excitation. No emission was observed in CH_2Cl_2 at 77 K, however a high level of background noise from the frozen sample may have been responsible for this.

The luminescent properties of ruthenium(II) polypyridine complexes are well known, for example in N3[16] and the black dye.[22] However, as mentioned earlier, decay *via* a competing pathway can inhibit the radiative processes. Arakawa reports observation of emission for analogous ruthenium(II) biquinoline compounds at 77 K in an ethanol-methanol (4:1) mix.[7] However, difficulties in obtaining luminescence data for heteroleptic copper(I) biquinoline complexes were reported by Sandroni *et al*, who reasoned that the lack of emission was either due to a quenching mechanism from a flattening of the complex, or else a non-radiative vibrational deactivation.[8] Such explanations may similarly be applicable in the case of the homoleptic species.

5.6 Cyclic voltammetry of complex 20 and experimental estimation of energy levels

It was shown that a reversible copper (I) to (II) redox cycle occurred in solution and when the dye was anchored onto a dyed TiO_2 film,[1] with a greater peak-to-peak potential separation (ΔE_p) in the solution electrochemistry than in the surface measurements. This suggested a larger reorganisation energy in solution than when the dye was constrained on the surface, which can be linked to geometry switching between tetrahedral copper(I) and square planar copper(II) species occurring more easily in solution.

A CV of a TiO_2 film, dyed with complex **20** from a 3 mM solution in MeOH overnight, at a scan rate of 0.1 V/s, is shown in Figure 56. WEs were prepared as described in Chapter 3.5.1. The TiO_2 background signal has been subtracted. An Ag/AgCl RE was used along with a platinum CE and the electrolyte was 0.1 M TBAHFP in MeCN.

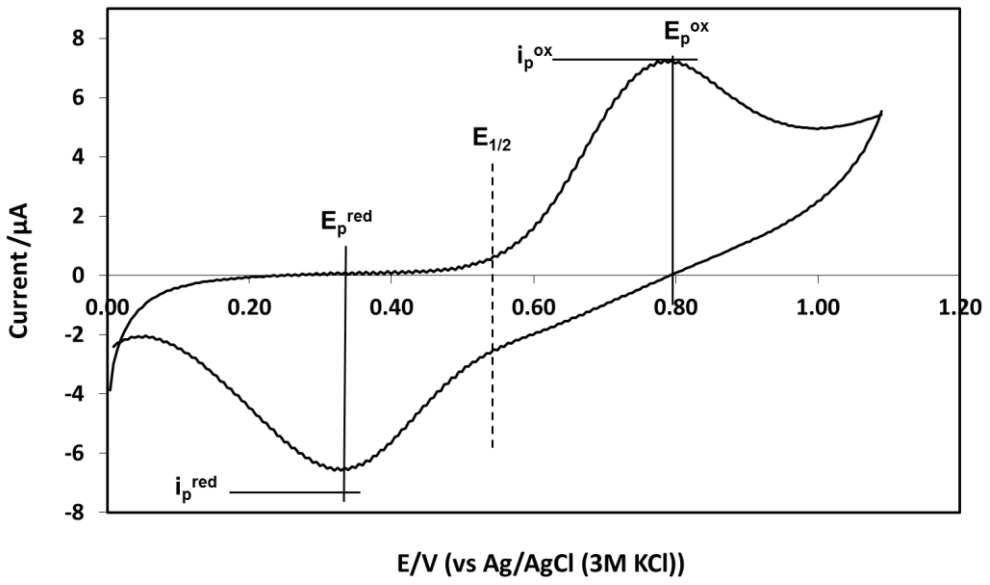

Figure 56 - a CV of complex 20 adsorbed on a TiO_2 film at a scan rate of 0.1 V/s

It can be seen that the peak oxidative current, i_p^{ox}, is 7.3 µA and the peak reductive current, i_p^{red}, is -6.6 µA. The peak oxidation potential, E_p^{ox}, is +0.78 V and the peak reduction potential, E_p^{red}, is +0.33 V versus Ag/AgCl (3M KCl). Vatsadze *et al.* reported the electrochemistry of the similar complex $[CuL_2][Cl]$ where L = di-*n*-hexyl 2,2´-biquinoline-4,4´-dicarboxylate.[23] The Cu(I) to (II) oxidation occurred at E_p^{ox} = +0.74 V versus Ag/AgCl

(sat. KCl), which is in good agreement with our findings. For the same complex, but with a $[BF_4]^-$ counterion, the group reported E_p^{ox} = +0.75 V and E_p^{red} = +0.36 V (vs Ag/AgCl/KCl)[24] which also implies that the counterion has little effect on the dye energy levels.

CV data can be used to estimate the HOMO and LUMO energy levels of the dye. The half wave potential, $E_{1/2}$, is the mid-point between E_p^{ox} and E_p^{red} and is closely related to the HOMO level of the dye, given that the onset of the oxidative wave indicates electrons are starting to be removed from the ground state. For complex **20**, $E_{1/2}$ is +0.56 V versus Ag/AgCl (3M KCl) (or +0.77 V versus the normal hydrogen electrode, NHE, where the reduction potential of the Ag/AgCl reference electrode (3M KCl) is 0.210 V versus NHE), which can be taken as an estimate of the HOMO level. Versus vacuum, the energetic position of the HOMO for complex **20** can be estimated as; HOMO = [(-4.5) - (0.210 + $E_{1/2}$)] = -5.27 eV, where the energy level of the NHE is located 4.5 eV below the zero vacuum energy level.[25]

On initial inspection, this value should be adequate for dye regeneration given that the standard potential of the I^-/I_3^- redox couple is -4.85 eV versus vacuum,[26] resulting in a driving force for regeneration of 0.42 eV. For comparison, the potentials of the HOMOs for N3 and N719 are -5.6 eV[26] and -5.5 eV[27] respectively versus vacuum. Therefore the driving force for regeneration with these dyes is higher than for complex **20**.

Reduction of the excited state of complex **20** by iodide was further probed using CV by adding an increasing quantity of LiI. The experiment was carried out in the same way as described in Chapter 4.5 and an analogous response was observed (Figure 57), indicating that dye regeneration is taking place under these electrochemical conditions.

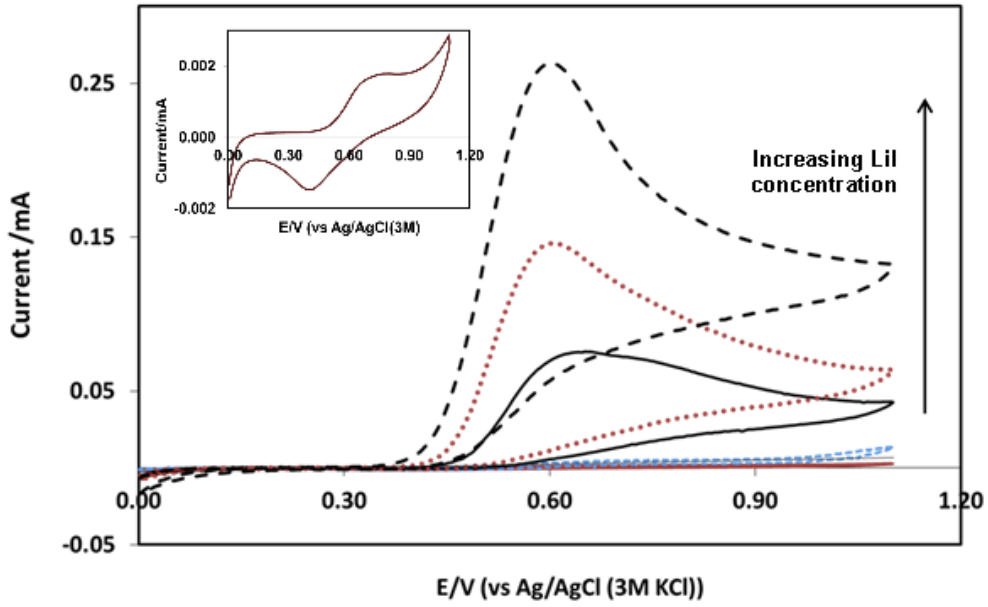

Figure 57 - CV of complex 20 immobilised on a TiO_2 film at a scan rate of 0.01 V/s with increasing concentrations of LiI; 3.39 mM (- - -), 2.78 mM (···), 1.55 mM (—), 0.31 mM (- - -), 0 mM (—). The inset shows a zoomed in view of the CV with 0 mM LiI (vs Ag/AgCl, 0.1 M TBAHFP in MeCN electrolyte)

Injection of electrons from the excited state of the dye into the TiO_2 conduction band is another key process reliant on energy level position. The electrochemically obtained value for the HOMO can be added to the absorption onset value for the MLCT from the UV/Vis spectrum (i.e. the optical band gap) to estimate the energetic position of the LUMO. The absorption onset is difficult to quote accurately for complex **20** given the broad shoulder prior to the main absorbance peak. In describing the heteroleptic complexes **18** and **19**, Sandroni *et al* state that "*the absorption onset lies around 750 nm*".[8] Therefore if a similarly conservative estimate of onset is taken to be at 760 nm, this corresponds to an optical band gap of 1.63 eV and therefore a LUMO energy of -3.64 eV (a potential of -0.86 V vs NHE). However due to the broad shoulder this estimation is fairly crude and therefore we reason it is appropriate to quote a range (marked in Figure 58) for λ_{onset} and the LUMO. A λ_{onset} range of 760 nm to 635 nm corresponds to an optical band gap between 1.95 and 1.63 eV. Therefore the LUMO is estimated at between -3.64 and -3.32 eV, which is appropriately higher in energy than the conduction band edge of TiO_2 (anatase) at -4.0 eV.[26] However DSCs with complex **20** record very low currents, which strongly suggest electron injection is not from this energy level; or else the electrons are being lost by some mechanism before they can be collected at the FTO substrate.

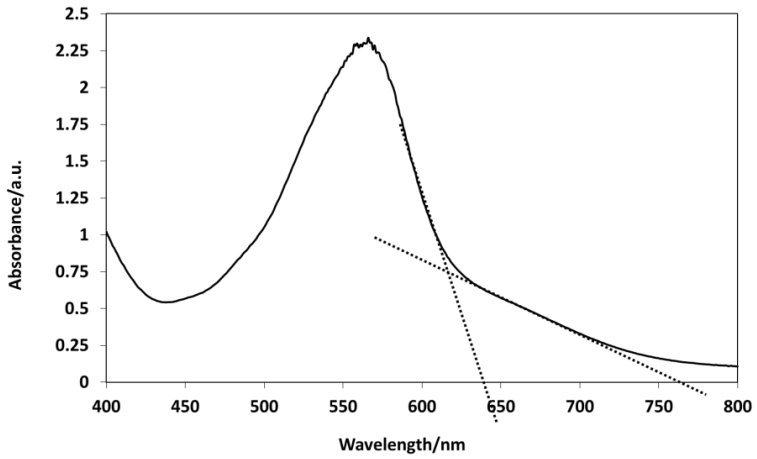

Figure 58 - UV/Vis MLCT band for complex 20 with absorption onset marked

An estimation of the first electronic excited state can be made by adding the zero-zero transition energy ($E^{0\text{-}0}$), obtained from emission spectroscopy, to $E_{1/2}$. $E^{0\text{-}0}$ is the energy for an electronic transition occurring between the lowest vibrational states in the ground and excited electronic states, which is the same in the absorption and emission spectra. The emission data for the excitation wavelength closest to the absorption maxima was used and an $E^{0\text{-}0}$ value of 2.30 eV is obtained (marked in Figure 59). Addition to $E_{1/2}$ results in an excited state energy of -2.86 eV versus vacuum. If electron injection is occurring from this state then there would be more than sufficient driving force for injection into the TiO_2 conduction band. However, given the ambiguity in the emission data, we are cautious in this conclusion.

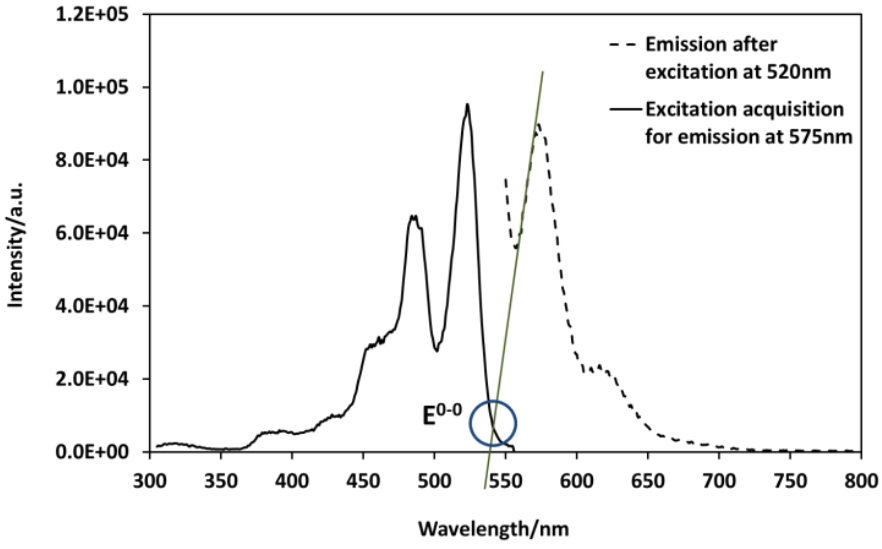

Figure 59 – emission spectrum for complex 20, with $E^{0\text{-}0}$ marked

5.7 Computational analysis of complex 20

A possible reason for the poor cell performance of **20** is inefficient electron injection into the semiconductor conduction band. This is based on studies by other groups done with an analogous ruthenium(II) biquinoline sensitizer[7] and additional literature which describes the low-lying nature of the ligand LUMO.[9, 10] However, it has also been shown previously in this chapter that calculations based on the experimental results suggest the energy levels of **20** should be adequate for electron injection into TiO_2 and for dye regeneration. Therefore a complementary computational assessment was carried out by collaborators at CINVESTAV-IPN, Mérida, México.

A combination of DFT and TD-DFT experiments can predict the electronic absorption spectrum, analyse the character of the highest occupied molecular orbitals (HOMOs) and lowest unoccupied molecular orbitals (LUMOs), and provide the energies of these orbitals. The calculations used the M06 functional and the LANL2DZ basis set. Solvent effects for methanol were modelled using the continuum solvation model, SMD. The counter ion was not included in the calculations, however other copper(I) computational work has indicated that the effect of the counter ion on the molecular energy levels is negligible therefore this should not be an issue.[11, 28]

Electron injection occurs most efficiently when the LUMO of the dye is located on the pathway to the semiconductor and, as visible in Figure 60, there is a significant contribution to the LUMO from the carboxylic acid groups in the case of complex **20**. The HOMO and HOMO-1 are mainly metal centred. The computations indicate that the most stable structure of the complex **20** anion shows a slight deviation from C_2 symmetry, with the protons located on different ligands. There was a slight discrepancy here with the experimental crystallographic data, which found the protons were located on the same ligand. However, the structures are energetically very similar (the energy difference including the zero-point energy correction, is only 1.1 kcal/mol), thus the locations of the protons in the solid state may be influenced by forces such as intermolecular hydrogen bonding.

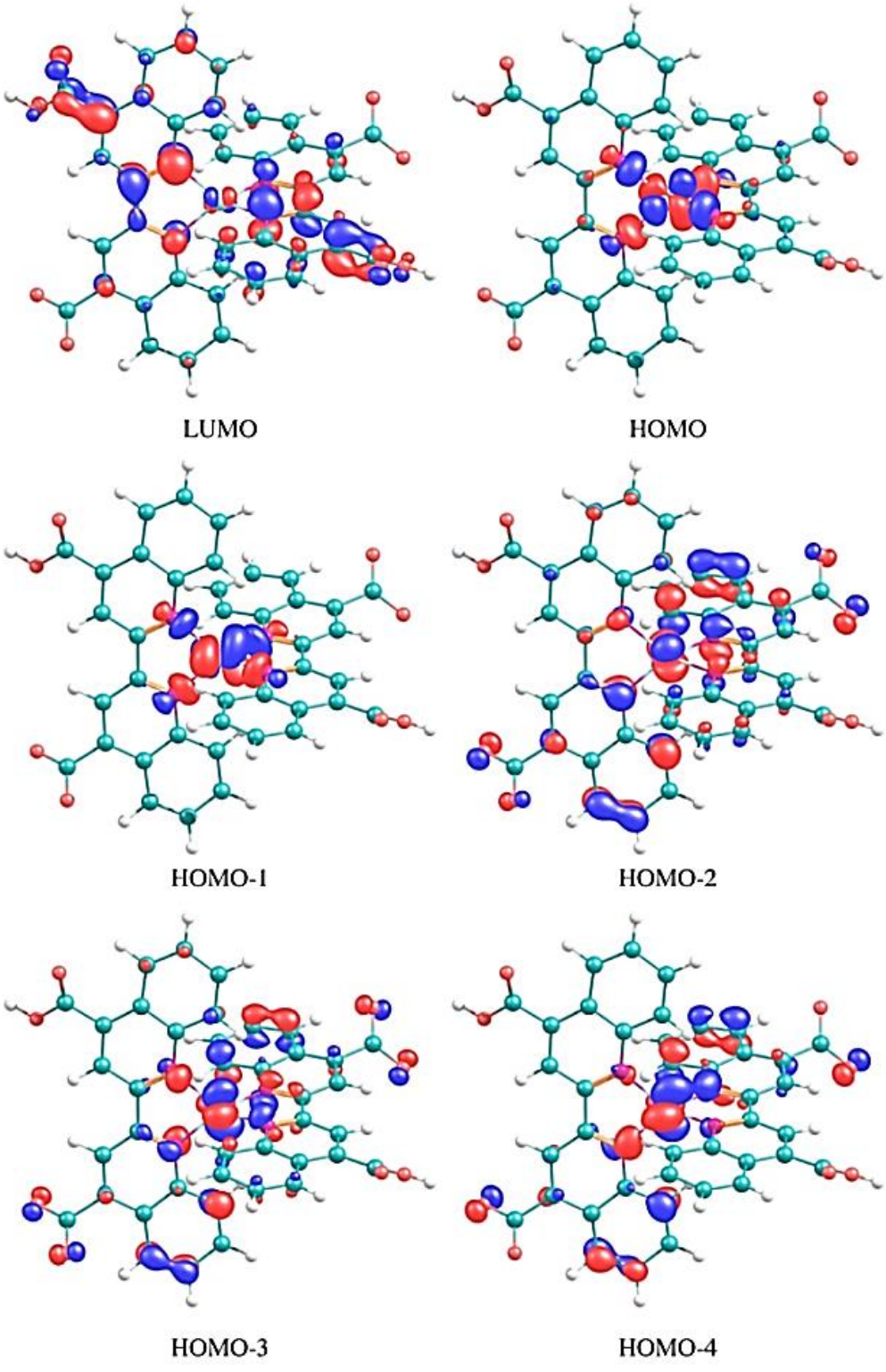

Figure 60 – molecular orbital plots for the five highest occupied and lowest unoccupied orbitals of the complex 20 anion

An analysis of the highest occupied and the lowest unoccupied molecular orbitals of complex **20** is presented in Table 4. From Figure 60 and Table 4 it can be seen that the largest contributions to the highest occupied orbitals are the antibonding combinations of the nitrogen lone pairs with a significant contribution from the copper metal t_2 orbitals (ranging from 22% to 63%). There are two main optical transition bands found by computational analysis. These have maximum absorption wavelengths at 563 nm and 361 nm, which is in excellent agreement with the experimentally obtained values of 564 nm and 360 nm. The energies and oscillator strengths for these, and other significant, transitions are presented in Table 5. The lower energy band involves multiple MLCT transitions, mainly excitations from the HOMO and HOMO-1, corresponding to one-electron excitations from t_2-π^*/t_2-π to π^*-ligand levels. The UV region absorption band involves transitions mainly from HOMO-5 and HOMO-9 to the lowest unoccupied π^* orbitals localized on the ligand.

Computed energies for the HOMO, LUMO and band gap are -5.78, -2.81 and 2.97 eV respectively. For comparison, the experimentally found values for the HOMO and first excited state are in fairly good agreement at -5.27 eV and -2.86 eV. The experimentally calculated LUMO is slightly lower in energy than the computed value. However due to the slow tail off in absorbance towards the low energy region of the spectrum, an absorption onset range (760 to 635 nm) was taken to calculate a LUMO between -3.64 and -3.32 eV. When considering the range of values, the position of the LUMO is more comparable to the computed value. Both the experimental and computational values are, however, still more positive than the conduction band edge of TiO_2 (positioned at -4.0 eV versus vacuum[29]) as required for electron injection. As mentioned previously, the HOMO energy levels for N3 and N719 are -5.6 eV and -5.5 eV therefore the values for complex **20** are comparable to this.

In terms of dye regeneration, the more conservative HOMO energy value is the experimentally obtained -5.27 eV, as this produces the lowest dye regeneration driving force (0.42 eV). This driving force is reduced when considering the formation of the diiodide radical as being actually responsible for dye regeneration, since the standard potential of the $I_2^{\bullet-}/I^-$ couple is lower in energy than that of I^-/I_3^-.[26] A study by Clifford and colleagues[30] found that regeneration of a ruthenium sensitizer, $Ru(dcbpy)_2Cl_2$, with a driving force of 0.46 eV, exhibited slow regeneration by iodide. Similar regeneration issues have also been observed for some organic dyes, as noted by Hagfeldt *et al* in their recent review.[31] The results suggest that the HOMO level needs to be energetically lower than the

potential of I^-/I_3^- by about 0.5 eV to ensure rapid dye ground state regeneration. The driving force for regeneration of complex **20** is close to this value and the sensitizer was regenerated under electrochemical conditions, however the process may not be as efficient as with the typical ruthenium dyes.

It is worth noting that the computational assessment was based on crystallographic data and the geometry of the structure was optimised. For the experimental work it is necessary to combine data from studies done on the surface (CV) and in solution (electronic absorption/emission spectroscopy). Aside from possible surface/solution measurement differences there could also be solvent effects since the UV/Vis/emission work was carried out in MeOH/CH_2Cl_2 whereas the CV used MeCN. In addition, slight differences between the optical and electrochemical bandgaps may exist.

In conclusion, computational analysis supported and generally reproduced the experimental findings and provided the composition of the main optical transitions for complex **20**.

Table 4 - Energies and Composition of the Higher Occupied and Lower Unoccupied Molecular Orbitals of the complex 20 anion

MO	occ	E(eV)	Cu (% contribution)
LUMO+5	0	-1.23	
LUMO+4	0	-1.24	
LUMO+3	0	-1.86	
LUMO+2	0	-1.89	
LUMO+1	0	-2.73	
LUMO	0	-2.81	
HOMO	2	-5.78	58 (d_{xy})
HOMO-1	2	-6.11	63 (d_{xz})
HOMO-2	2	-6.68	22 (d_{yz})
HOMO-3	2	-6.76	35 (d_z2, d_x^2-$_y^2$)
HOMO-4	2	-6.86	43 (d_{yz})
HOMO-5	2	-7.02	
HOMO-6	2	-7.03	

Table 5 - Wavelength, oscillator strength and composition of the most important optical transitions of the complex 20 anion

λ (nm)	f	Composition
692	0.036	HOMO-1 → LUMO+1 (18%) HOMO → LUMO (79%)
563	0.163	HOMO-1 → LUMO+1 (79%)
419	0.041	HOMO → LUMO+2 (81%)
375	0.038	HOMO-4 → LUMO (41%)
368	0.023	HOMO-4 → LUMO+1 (45%) HOMO-5 → LUMO +1 (10%)
361	0.114	HOMO-5 → LUMO (40%) HOMO-9 → LUMO (29%)
359	0.057	HOMO-8 → LUMO (11%) HOMO-6 → LUMO (44%)
355	0.082	HOMO-12 → LUMO (46%)
350	0.039	HOMO-8 → LUMO+1 (19%) HOMO-7 → LUMO (40%)

5.8 Studying electron behaviour in DSCs with complex 20

There are a number of techniques that can be used to probe the electron transfer processes in a DSC. These allow interactions in the cell to be monitored in a real time manner, under normal operating conditions, and can aid in rationalising DSC performance problems. On DSCs containing complex **20**, open circuit photovoltage decay (OCVD) experiments were carried out. Such measurements record the photovoltage decay of a cell as a function of time after a set period of illumination, as described in Chapters 2.5 and 3.7. Figure 61 shows the decay curves for a DSC with complex **20** and an N719 cell, prepared on the same day under the same conditions. The standard iodide/triiodide electrolyte was used and both dye baths were at a concentration of 0.3 mM (in MeOH and 50:50 *t*-BuOH:MeCN for complex **20** and N719 respectively).

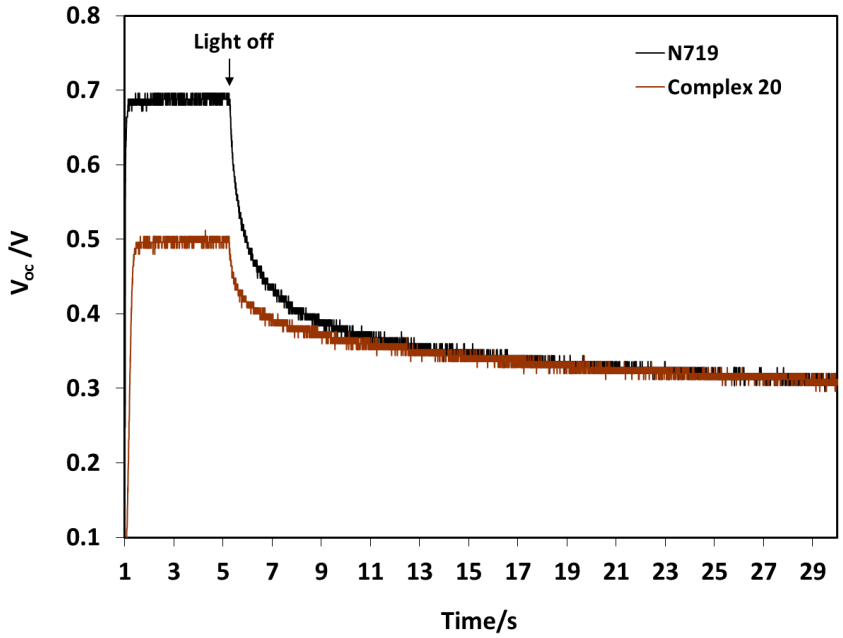

Figure 61 - OCVD plots for DSCs with N719 (—) and complex 20 (—)

The initial rapid decay in photovoltage is a typical response. It has been shown[32] that a compact blocking layer is most influential over the slow component of the photovoltage decay. Therefore in this case it can be seen that the blocking layer is effective for both dyes. If this were not the case then a far more rapid decay of photovoltage to zero would be observed. The shape of both decay curves is the same, bar the difference in initial photovoltage, indicating the specific metal/ligand nature of the dye is not affecting this process.

The effective electron lifetime, τ_n, can be calculated from the decay curves using equation 20 (Chapter 2.5). Figure 62 shows τ_n for N719 and complex **20** plotted against V_{OC}. Since the rate of the back reaction with triiodide increases with the number of free electrons in the TiO_2 film,[33,34] it is often commonplace for τ_n to be reported versus the charge density in the TiO_2 film. The electron density could not be measured in this case due to equipment problems however it is reasonable to assume a similar charge distribution for both cells. The cells were constructed from the same TiO_2 film under identical conditions. The same electrolyte was used and the state of protonation is the same for both N719 and complex **20**, with two of the carboxylic acid groups being deprotonated, meaning that the position of the TiO_2 conduction band should not be significantly different between the cells.

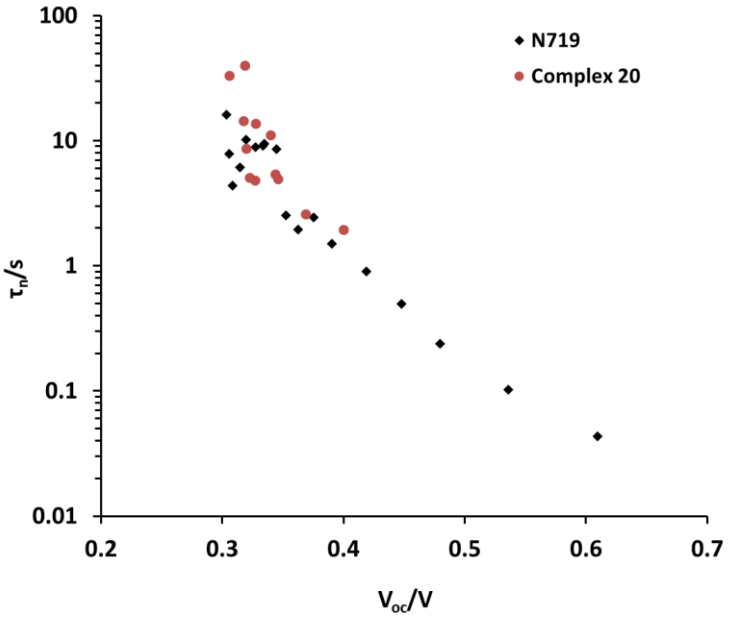

Figure 62 – electron lifetime for DSCs with N719 (···) and complex 20 (···) as a function of photovoltage

It can be seen from Figure 62 that τ_n in both cells is very similar, with an anticipated trend of lower electron lifetimes (i.e. a higher rate of recombination reaction) at higher photovoltages. There is a higher concentration of charges in the TiO_2 film at higher photovoltages therefore there are more free electrons to undergo reaction with triiodide. As the quasi-Fermi energy and concentration of charges decreases, the rate of recombination slows and prolongs the electron lifetime. This experiment shows that recombination behaviour is analogous in both cells and the dye does not seem to have an influence.

The photocurrent response at different light intensities was also investigated to probe why DSC efficiencies with complex **20** were so low. This was carried out by illuminating the DSC with a green LED (530 nm) and using filters to modify the light intensity. The photon flux can be plotted against the short circuit photocurrent to determine if the current is limited in some way (Figure 63). Although a linear increase of photocurrent with light intensity was expected, at higher photon fluxes it can be seen that the current increase slows down towards a plateau. With such low currents (μA) it is difficult to reliably draw conclusions. However it is known that the current obtained from a DSC is a consequence of three key factors;[35] the light harvesting ability of the dye, which is determined by the molar extinction coefficient of the dye and the dye loading on the semiconductor surface; the injection efficiency, which depends on appropriate energy level matching; and the electron

collection efficiency at the FTO substrate, which is determined by the rate of reaction between electrons in the film and triiodide/oxidised dye.

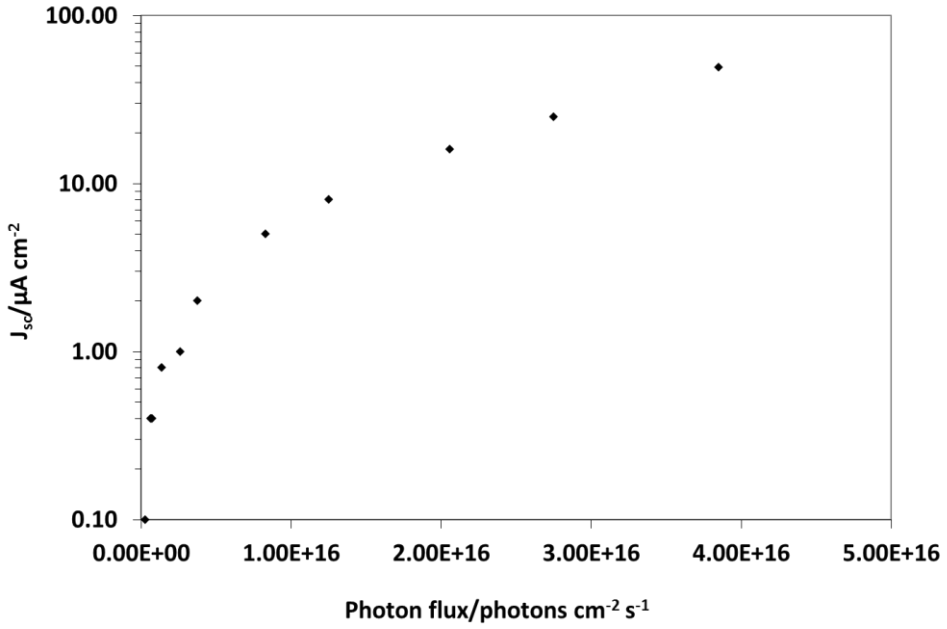

Figure 63 - studying J_{SC} for a complex 20 DSC at different light intensities

The type of response seen in Figure 63 usually indicates some type of limitation on the current, either of an electron transfer process or diffusion. However at these low light intensities diffusion limitation is very unlikely. Possible kinetic limitations include electron injection and slow dye regeneration by iodide.

Meyer and colleagues presented a poster at the Gordon Research Conference on Photochemistry in 2011 detailing work with a homoleptic copper(I) biquinoline dye.[36] The group found from transient absorption spectroscopy that electron injection was occurring from the biquinoline dye into the TiO_2 semiconductor. They concluded that there was a ligand trapping mechanism taking place which was preventing the injected electrons from being collected at the glass substrate. This was a postulation based on work they published[37] in 2002 with $[Ru(bpy)_2(deebq)][PF_6]_2$ (where bpy is 2,2'-bipyridine and deebq is 4,4'-diethylester- 2,2'-biquinoline). Following rapid electron injection from upper excited states, the group speculated that there was transport of the electron through the TiO_2 before it was trapped by a dye molecule in its ground state. If this mechanism is occurring here it would

provide an explanation for why the estimated energy levels of complex **20**, which suggest electron injection should be viable, are at variance with very low observed photocurrents. Dye regeneration by iodide is a further possible kinetic limitation and the possibility of the overpotential being too small for efficient regeneration was discussed in Chapter 5.7. Although under electrochemical conditions the dye's ground state is regenerated by iodide, in a working cell environment (where there are more variables) this may not be the case.

From the experiments in this section more information on DSCs constructed with complex **20** was obtained. The studies confirmed that the blocking layer for the cells is effective and that τ_n is comparable to N719. However, the efficiency of electron injection and dye regeneration are still questionable. Low DSC efficiencies may be due to a combination of the two factors.

5.9 Use of a $Co^{2+/3+}$ electrolyte with complexes 20 and 1

Previously,[1] time was spent trying to optimise the DSC environment for complex **20** when it was found that η values were typically no greater than 0.1 %. The IPCE spectrum showed an external quantum efficiency (EQE) of no greater than 1% between the key wavelengths of 450 to 650 nm. Therefore it appeared as if electron injection into the TiO_2 conduction band, or else charge collection efficiency, was a problem. One attempt at improvement was varying the composition of the electrolyte; more specifically, the concentration of 4-*tert*-butylpyridine (4-TBP). 4-TBP is known to increase the V_{OC} due to both a negative shift of the TiO_2 conduction band edge and by reducing the recombination reaction.[38] Cells were constructed with 0 M, 0.3 M and 0.5 M 4-TBP in the standard I_3^-/I^- electrolyte. The V_{OC} increased with increasing concentration of 4-TBP, as expected. A higher J_{SC} was obtained in the absence of 4-TBP, assumed to be due to an increase in electron injection hence suggesting injection was an issue. However the losses and gains balanced out so that there was no overall improvement in η.

Recently, cobalt based mediators have found success in DSCs.[39, 40] Relevant to this work, copper(I) DSCs with a cobalt electrolyte have also reported favourable results.[41, 42] A $Co^{2+/3+}$ couple offers advantages such as a more positive redox potential versus NHE compared to I^-/I_3^-, meaning there is a smaller energy loss in the dye regeneration step and hence a gain in the V_{OC}.[43] The cobalt species is less light absorbing than I^-/I_3^-, less volatile and may also offer better long term stability for copper(I) DSCs.[41] As mentioned earlier, it

is suggested that there is a reaction over time between copper(I) dyes and an iodide electrolyte in the cell, forming copper(I) iodide.[44]

Early breakthroughs with a cobalt based mediator, namely from Nusbaumer[45] and Sapp,[46] used the standard ruthenium dyes N719 and N3 respectively. Sapp and colleagues reported N3 DSCs with efficiencies 80% as high as their control I^-/I_3^- electrolyte cells.[46] Recent success with optimised cobalt electrolyte DSC systems from groups such as Feldt[40] and Yella[39] has been achieved using organic dyes designed specifically for use with cobalt mediators in conjunction with careful control of the semiconductor film properties. However the $Co^{2+/3+}$ redox couple displays slightly faster recombination kinetics than I_3^-/I^-, therefore electron transfer to the oxidised mediator is still fast enough to hinder efficient cell output.[43, 47] Therefore in these recent papers the research groups employed a strategy of designing dyes with steric properties to block the approach of Co^{3+}, hence reducing the back reaction. A further challenge associated with using $Co^{2+/3+}$ mediators is mass transport limitation due to the larger size of $Co^{2+/3+}$, relative to I^-/I_3^-.[43, 48, 49]

Although it is acknowledged that neither complex **20** nor **1** are ideally suited structurally for application with a cobalt redox couple, a set of initial studies were carried out on a non-optimised system to see what effect a direct switching from I^-/I_3^- would have. Firstly, complex **20** was paired with a cobalt mediator and the cell data compared to that for N719 cells constructed under the same conditions (Table 6). The TiO_2 films were prepared with a double layer thickness (~14 μm) *via* ***method 2*** (see Chapter 3.3.1) and the dyed cell areas were $1cm^2$. The cobalt electrolyte consisted of 0.2 M $Co(bpy)_3(PF_6)_2$, 0.05 M $Co(bpy)_3(PF_6)_3$, 0.1 M $LiClO_4$ and 0.2 M 4-TBP in MeCN.

Although the three control cells prepared with the standard I^-/I_3^- electrolyte were not of the highest standard either, it is clear from Table 6 that simply directly replacing this electrolyte with the cobalt based one was detrimental to both dyes. There were losses in both the photocurrent and photovoltage which is most likely due to a higher recombination reaction between electrons in the TiO_2 and the Co^{3+} compared to with I_3^-. However it is interesting to note that the decline in η was of a very similar magnitude between the two dyes. Moving from an iodide to a cobalt electrolyte brings about a loss in efficiency of 88 % for N719 and 86 % for complex **20**. The fact that the cell efficiencies decrease by a similar amount suggests that the reason for complex **20**'s poor DSC performance is not dye regeneration. With its more positive redox potential relative to I^-/I_3^-, $Co^{2+/3+}$ would be expected to have

even less of a driving force for regeneration of complex **20** if this was a limitation in DSCs with I^-/I_3^-. However its DSC decline is comparable to that of N719.

Table 6 – cell parameters for DSCs constructed with I^-/I_3^- and $Co^{2+/3+}$ electrolytes, for complex 20 and N719

Cell no.	Electrolyte	V_{OC} (mV)	J_{SC} (mA)	*FF*	η (%)
N719	I^-/I_3^-	631	7.08	57.5	2.57
N719	$Co^{2+/3+}$	542	0.8	72.8	0.31
complex **20**_cell1	I^-/I_3^-	449	0.15	66.7	0.045
complex **20**_cell 2	I^-/I_3^-	457	0.13	68.8	0.040
complex **20**_cell 3	$Co^{2+/3+}$	421	0.029	45.8	0.006
complex **20**_cell 4	$Co^{2+/3+}$	410	0.032	48.2	0.006

Moving on from this, the same cobalt electrolyte was tried with complex **1** (Table 7). In this case, some modifications were made. All cells had a dyed area of 1 cm^2 and were prepared with a single layer of TiO_2 paste (~6.5 μm). A scattering layer was applied and some of the cells were treated with $TiCl_4$, according to Chapter 3.3.1. A scattering layer is useful for improving light harvesting, since light can be reflected back into the cell. For TiO_2 films used with the cobalt electrolyte, dye baths also contained 10 mM chenodeoxycholic acid as a coadsorbate. Coadsorbates can offer many improvements to a DSC,[50, 51] one such being suppression of the recombination reaction.

Table 7 – cell parameters for DSCs constructed with I^-/I_3^- and $Co^{2+/3+}$ electrolytes for complex 1

Cell no.	$TiCl_4$?	Electrolyte	V_{OC} (mV)	J_{SC} (mA)	*FF*	η (%)
complex **1**_cell 1	Y	I^-/I_3^-	543	0.92	69.6	0.35
complex **1**_cell 2	Y	I^-/I_3^-	502	0.53	69.7	0.19
complex **1**_cell 3	Y	I^-/I_3^-	542	1.01	65.9	0.36
complex **1**_cell 4	N	I^-/I_3^-	499	0.47	68.4	0.16
complex **1**_cell 5	N	I^-/I_3^-	492	0.41	72.2	0.15
complex **1**_cell 6	Y	$Co^{2+/3+}$	504	0.17	61.1	0.052
complex **1**_cell 7	Y	$Co^{2+/3+}$	519	0.14	52.6	0.038
complex **1**_cell 8	Y	$Co^{2+/3+}$	505	0.16	56.7	0.046
complex **1**_cell 9	N	$Co^{2+/3+}$	484	0.056	50.4	0.014
complex **1**_cell 10	N	$Co^{2+/3+}$	488	0.068	50.4	0.017

It can be seen in Table 7 that the cobalt based cells were still outperformed by the iodide cells. The $TiCl_4$ treatment significantly improves cells relative to those without the treatment. The lower photocurrent with the cobalt based cells may be due in part to the competitive binding of chenodeoxycholic acid on the TiO_2 surface with complex **1**. As observed in DSCs with complex **20**, lower photovoltages suggest that the recombination reaction is still higher in cells with the cobalt electrolyte than with iodide. For the most part, the fill factor is also ~20% lower in DSCs with cobalt than with iodide. This may be due to an increase in series resistance due to the larger size of $Co^{2+/3+}$, relative to I^-/I_3^-. The difference in magnitude of η between the cobalt and iodide cells in the experiments with complex **20** and **1** is very similar (a factor of ~10 lower with cobalt). Therefore the use of coadsorbates with a single TiO_2 layer did not seem to afford any improvement to the DSCs. The $TiCl_4$ treatment resulted in a definite improvement in DSC photocurrent and photovoltage relative to cells prepared with the same electrolyte but without the treatment. Treating with an aqueous solution of $TiCl_4$ deposits a very thin layer of ultrapure TiO_2 on

the surface. This procedure increases the roughness of the mesoporous TiO_2 layer, leading to increased dye adsorption. Other advantages noted in the literature include an increased electron diffusion length and lifetime.[52, 53]

5.10 Further work: functionalising the 2,2'-biquinoline-4,4'-dicarboxylic acid ligand

Functionalisation of the ligand framework with electron withdrawing or donating groups was mentioned in Chapter 1.3, but will be considered here in the context of the dcbiq ligand. The HOMO and LUMO energy levels in a dye are influenced by the nature of the substituents in the ligand framework. In general, electron-withdrawing groups (EWGs) will lead to a decrease in molecular orbital energy levels and electron-donating groups (EDGs) will lead to an increase. In terms of the HOMO energy, EDGs attached to the metal are transferring electron density onto the metal centre, causing a destabilisation of the *d*-orbitals and therefore raising the energy of the HOMO. As expected, EWGs will have a comparatively stabilising effect and shift the HOMO in the opposite direction. The LUMO of complexes of the type discussed here is typically located over the electron-poor 2,2'-bipyridine/biquinoline ligand and attached carboxylic acid anchoring groups. Incorporating EWGs into this backbone will make the 2,2'-bipyridine/biquinoline ligand an even better π-acceptor, i.e. lowering the LUMO energy level, whilst incorporating EDGs which can push electron density onto the 2,2'-bipyridine/biquinoline ligand should serve to increase the energetic position of the LUMO. This shift could be favourable for ligands such as 2,2'-biquinoline where the LUMO is potentially too low for efficient injection into the TiO_2 conduction band, or where a low-lying π* orbital on the ligand may be trapping electrons.

Substituents can have an electronic effect in one of two ways; through resonance or induction. Both of these effects can be either electron donating or withdrawing. Resonance effects occur through π-bonds as part of a delocalised system of π-electrons. In an aromatic system such as 2,2'-bipyridine/biquinoline, atoms attached to the ring which have a lone pair can donate these electrons into the system and thus increase its electron density. Resonance effects are electron withdrawing where the substituent attached to the ring has an electronegative atom, which removes delocalised electron density from the aromatic ring. Induction occurs through σ-bonds and the electronegativity of the atoms involved determines whether it is a positive or negative inductive effect. With this rationale in mind, the functionalisation of dcbiq with EDGs was considered. Searching the literature found

that synthesis of 2,2'-biquinoline-4,4'-dicarboxylic acid, and variants of it, could be achieved in just one step *via* the Pfitzinger reaction.[54,55] A procedure from Vatsadze *et al* was followed,[23] which couples isatin compounds with acetoin in the presence of a strong base *via* a condensation reaction (
Scheme 2).

There were a number of options for EDGs, for example alkyl groups, amines, methoxy groups and halides. Ease of integration into the 2,2'-biquinoline ligand was also a consideration in terms of available starting materials. Halides are electron withdrawing through induction but also electron donating *via* their lone pair. 5-chloroisatin is a commercially available and cheap (£13.80/25g, Sigma Aldrich) starting material therefore this was chosen as the starting point, generating the 6,6'-dichloro-[2,2'-biquinoline]-4,4'-dicarboxylic acid ligand, **21**. Once **21** had been obtained, two equivalents of it were reacted with $[Cu(CH_3CN)_4][PF_6]$ in the presence of triethylamine to afford the dark purple copper(I) complex, **22**, which was characterised and fully assigned through ^{1}H and ^{13}C $\{^{1}H\}$ NMR experiments.

Analysis indicates that the copper(I) complex formed in the same way as complex **20**. ESI mass spectrometry found the molecular ion at m/z 886.9095 which matches for a structure where two of the carboxylic acid groups are deprotonated, as observed in complex **20**. This would result in a copper(I) anion, which was expected to be charge balanced by a protonated triethylamine cation. ^{1}H NMR analysis showed triplet and quartet chemical shifts at 3.22 and 1.31 ppm, consistent with protonated, rather than free, triethylamine. From integration of the spectrum it was calculated that there were 1.3 equivalents of NEt_3 for every copper(I) anion. It is expected that the 0.3 remaining equivalents are crystallising with $[PF_6]^-$, as occurred with complex **20**. The presence of the $[PF_6]^-$ group in the batch of dye was confirmed through ^{31}P $\{^{1}H\}$ NMR.

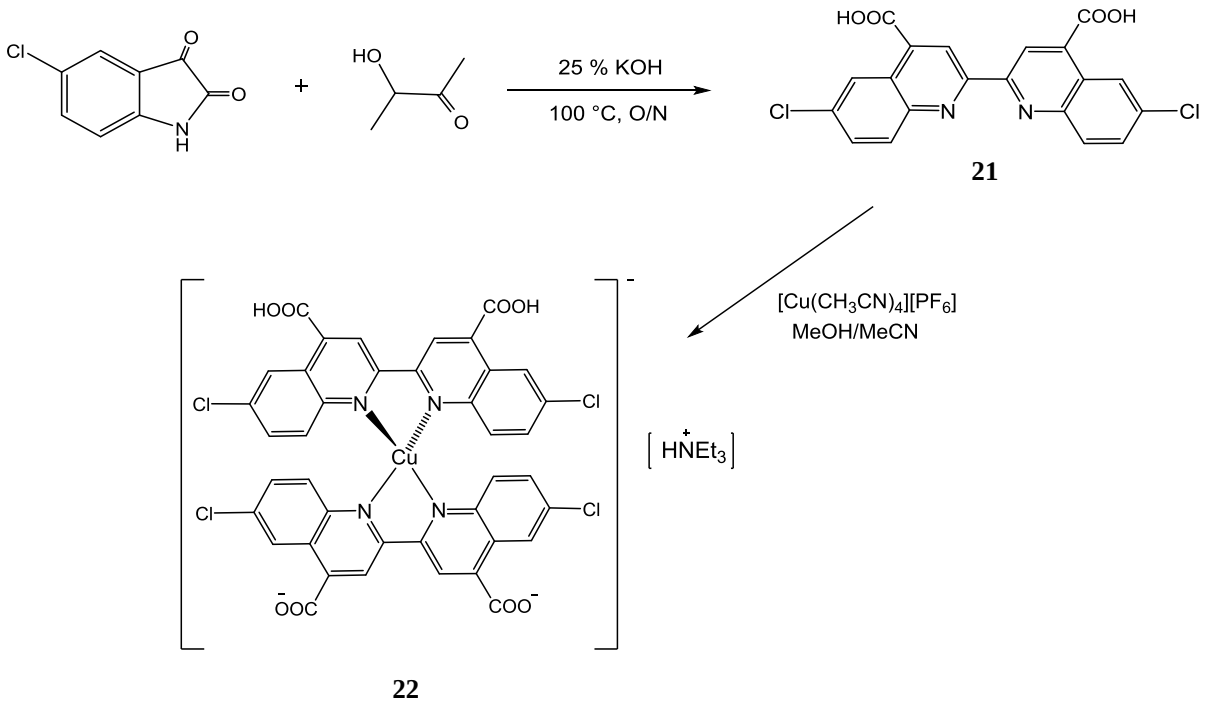

Scheme 2 – synthesis towards a (bis)chloro-functionalised 2,2'-biquinoline ligand, 21, and copper(I) complex, 22

The electronic absorption spectrum of complex **22** is shown in Figure 64 and compared to that of compound **20**. The $\lambda_{(max)}$ for the MLCT is at 555 nm in MeOH, with $\varepsilon = 6540\ M^{-1}\ cm^{-1}$. For complex **20** this transition occurs at a $\lambda_{(max)}$ of 564 nm and $\varepsilon = 11{,}700\ M^{-1}\ cm^{-1}$ in MeOH. There is a slight shift in absorption maxima towards the higher energy end of the spectrum when the chloride substituents are present. This is most likely due to an increase in energy of the π^* orbitals on the 2,2'-biquinoline ligand, induced by electron donation into the system by the chlorides. The molar extinction coefficient of complex **22** is just over half that of complex **20**.

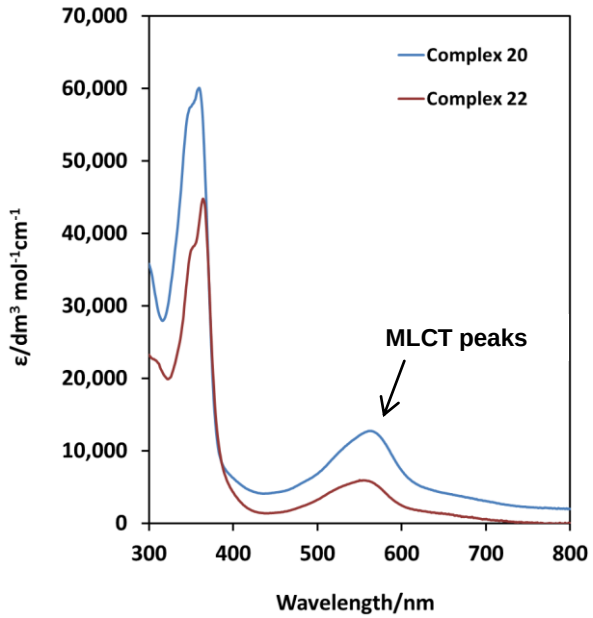

Figure 64 – UV/Vis spectrum of the chloride functionalised complex 22, compared to complex 20

DSCs were constructed with complex **22**, however the dye was not as stable as **20** to heating during the assembly process. During cell sealing on the hot plate, the dyed TiO_2 films quickly changed colour from dark purple to a dark yellow. Cells were assembled with two films which had undergone this discolouration and a further two cells were sealed at a lower temperature where no discolouration occurred. The cell parameters are given in Table 8. The discolouration of the films affected the photocurrent obtained and consequently led to lower overall cell efficiencies. From this preliminary study, complex **22** did not offer improved DSCs relative to complex **20**. Optimising the cell environment in such ways as modifying the electrolyte, including a scattering layer and a $TiCl_4$ treatment may lead to higher efficiencies being achieved, however a more substantial difference may be observed by incorporating more strongly electron donating substituents.

Table 8 – cell parameters for DSCs with complex 22

Dye	V_{OC} (mV)	J_{SC} (mA)	FF (%)	η (%)
22 (discoloured)	557	0.117	65.1	0.042
22 (discoloured)	559	0.114	63.3	0.040
22	581	0.142	66.8	0.055
22	568	0.148	67.1	0.056
N719	721	8.466	62.0	3.78

Attention was therefore directed towards one of the most strongly electron donating groups; the $–NH_2$ group. 5-aminoisatin (**23**) was not commercially available but could be prepared through the reduction of 5-nitroisatin (Scheme 3). One route for this is the Bechamp reduction, which employs iron powder and concentrated HCl. A route described by Romagnoli *et al* was followed[56] to obtain the title compound as a red residue following purification by column chromatography. Characterisation data for it matched those reported in the literature.[57] The Pfitzinger reaction was then carried out with **23** however characterisation of the dark red solid obtained from the reaction was severely limited by solubility. ^1H NMRs were run in DMSO-d_6 and NaOD/D_2O as well as tried in the common organic solvents, but an NMR could not be obtained. Therefore synthesis of the corresponding copper(I) complex was not completed.

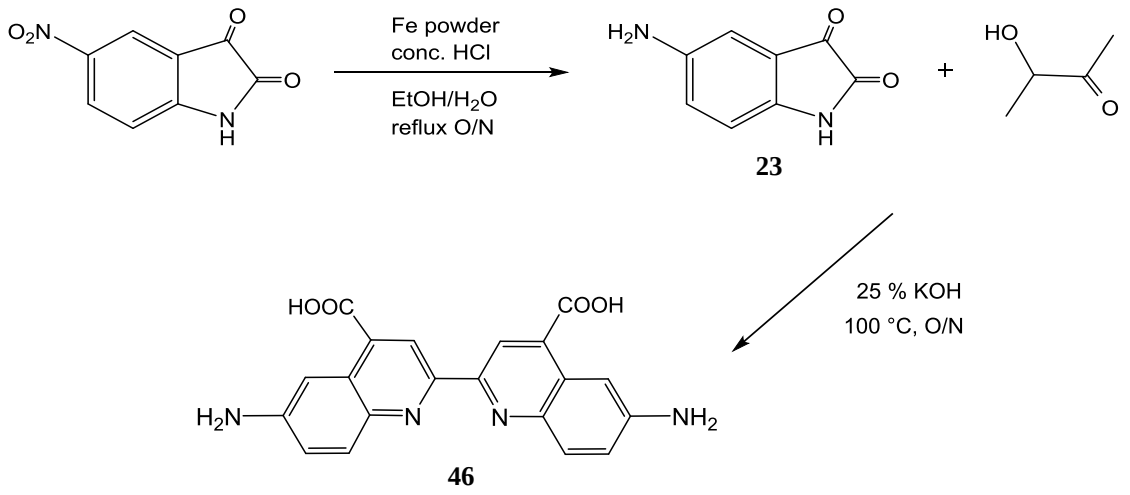

Scheme 3 - synthesis towards a (bis)amino-functionalised 2,2'-biquinoline ligand, 46

5.11 Conclusions

This chapter has considered the suitability of a homoleptic copper(I) 2,2'-biquinoline-4,4'-dicarboxylic acid dye for DSCs. The anionic structure of the copper(I) fragment and the nature of the cation has been elucidated through X-ray crystallography, NMR experiments and elemental analysis. Properties such as $\lambda_{(max)}$ in the electronic absorption spectrum and the molar extinction coefficient were found to be superior to the copper(I) 2,2'-bipyridine-4,4'-dicarboxylic acid analogue (complex **1**), due to increased conjugation in the ligand. DSCs were constructed with TiO_2 films dyed for increasing periods of time with complex **20** and cells following 2 hours of dyeing outperformed those dyed overnight. The loading of complex **20** on the TiO_2 surface was also calculated through a desorption experiment and uptake was found to be comparable to the typical ruthenium dyes.

A preliminary comparison of complexes **20** and **1** in DSCs with the I^-/I_3^- redox couple and a $Co^{2+/3+}$ electrolyte was made, to see whether this was an optimisation route worth pursuing. Although the key cell parameters (V_{OC}, J_{SC}, fill factor and η) of both dyes, and N719, decreased with the cobalt electrolyte, this can be rationalised as follows. DSC conditions with a $Co^{2+/3+}$ mediator typically need to be more carefully designed than with the I^-/I_3^- couple, for example through choice of dye, semiconductor surface and thickness. Through techniques such as intensity modulated photocurrent and photovoltage spectroscopy (IMPS/IMVS), Peter and colleagues calculated the electron diffusion length in DSCs with the $Co^{2+/3+}$ redox couple to be a lot shorter than in those with the I^-/I_3^- couple.[47] This has implications for the TiO_2 film thickness; indeed it was concluded that in cells with film thicknesses greater than 5 μm there will be a significant loss of electrons unless some mechanism for blocking the redox mediator is incorporated. This could be a surface treatment of the TiO_2, using co-adsorbates or designing a dye with functionalities which would hinder the approach of Co^{3+}. It is acknowledged that the structure of complex **20** is not optimal for use with the $Co^{2+/3+}$ redox couple, therefore further work would have to be carried out using thinner TiO_2 films and some surface passivation or use of co-adsorbates. In the case of the work with complex **1**, addition of the coadsorbate chenodeoxycholic acid and use of thinner TiO_2 films did not result in DSCs which were competitive with I^-/I_3^-. However it is likely that the range of semiconductor modifications and dye design strategies discussed in this chapter would need to be implemented together in order to be successful.

The energies of the HOMO, LUMO and first excited state have been estimated experimentally and through computational analysis for complex **20** with good agreement

between the results. The position of the HOMO is lower in energy than the standard I^-/I_3^- potential, as required for dye regeneration, albeit with a lower driving force than for the typical ruthenium dyes. Efficient dye regeneration was observed under electrochemical conditions, *via* a cyclic voltammetry experiment probing catalytic dye regeneration with LiI. However it is acknowledged that under assembled DSC conditions the situation may be different. The energetic positions of the LUMO and first excited state indicate electron injection should be able to take place effectively, although loss of electrons from the semiconductor film *via* a ligand trapping mechanism as observed by Meyer[37] cannot be ruled out. Alternatively, the dye's excited state may just rapidly decay non-radiatively, as supposed by Sandroni and colleagues with regards to the heteroleptic copper(I) biquinoline complexes.[8] A further possibility is that following initial electron excitation, intersystem crossing occurs from the ^{1}MLCT state to the lower-lying ^{3}MLCT, which may be too low in energy for the electron to be injected into the TiO_2 conduction band. That the low photocurrents and DSC efficiencies are due to a combination of these scenarios is also a possibility.

In DSCs with the I^-/I_3^- electrolyte, the recombination reaction is on a similar timescale to that with N719 and the effective electron lifetimes are very similar according to OCVD measurements. This suggests that an increased rate of recombination relative to N719 is not the reason for poor DSC performances. There is some suggestion of current limitation through measurements recorded at different light intensities; however the currents measured were very low. Since diffusion limitation at the low light intensities used in the experiment is very unlikely, some kinetic effect must be the responsible factor. Slow dye regeneration and/or inefficient electron injection can again be speculated as reasons for this.

Given that overall solar-to-power conversion efficiencies with complex **20** are so low, it is not particularly viable for application in DSCs. However in the final part of the chapter functionalisation of the 2,2'-biquinoline-4,4'-dicarboxylic acid ligand was introduced as future work. Using a (bis)chloride-substituted biquinoline complex did not have a great enough influence over the energy levels to improve the DSC performance. The more strongly electron donating amino group was introduced later on however problems with the ligand solubility meant that complexation to copper(I) was not carried out. Further pursuit of this functionalisation strategy is not ruled out, if suitable conditions for working with ligand **46** could be found.

5.12 References

1. K. Wills, S. E. Lewis, M. D. Jones and P. J. Cameron, MRes in Sustainable Chemical Technologies, University of Bath, 2010.
2. K. A. Wills, H. J. Mandujano-Ramirez, G. Merino, D. Mattia, T. Hewat, N. Robertson, G. Oskam, M. D. Jones, S. E. Lewis and P. J. Cameron, *RSC Adv.*, 2013, 23361-23369.
3. P. K. Smith, R. I. Krohn, G. T. Hermanson, A. K. Mallia, F. H. Gartner, M. D. Provenzano, E. K. Fujimoto, N. M. Goeke, B. J. Olson and D. C. Klenk, *Anal. Biochem.*, 1985, **150**, 76-85.
4. R. D. Braun, K. J. Wiechelman and A. A. Gallo, *Anal. Chim. Acta*, 1989, **221**, 223-238.
5. M. K. Nazeeruddin, E. Muller, R. Humphry-Baker, N. Vlachopoulos and M. Gratzel, *Journal of the Chemical Society-Dalton Transactions*, 1997, 4571-4578.
6. S. Ruile, O. Kohle, P. Pechy and M. Grätzel, *Inorg. Chim. Acta*, 1997, **261**, 129-140.
7. A. Islam, H. Sugihara, L. P. Singh, K. Hara, R. Katoh, Y. Nagawa, M. Yanagida, Y. Takahashi, S. Murata and H. Arakawa, *Inorg. Chim. Acta*, 2001, **322**, 7-16.
8. M. Sandroni, M. Kayanuma, A. Planchat, N. Szuwarski, E. Blart, Y. Pellegrin, C. Daniel, M. Boujtita and F. Odobel, *Dalton Trans.*, 2013, **42**, 10818-10827.
9. B. Machura and R. Kruszynski, *Polyhedron*, 2007, **26**, 3336-3342.
10. M. K. Nazeeruddin, E. Muller, R. Humphry-Baker, N. Vlachopoulos and M. Grätzel, *J. Chem. Soc.-Dalton Trans.*, 1997, 4571-4578.
11. J. Baldenebro-Lopez, J. Castorena-Gonzalez, N. Flores-Holguin, J. Almaral-Sanchez and D. Glossman-Mitnik, *Int. J. Mol. Sci.*, 2012, **13**, 16005-16019.
12. C. L. Linfoot, P. Richardson, T. E. Hewat, O. Moudam, M. M. Forde, A. Collins, F. White and N. Robertson, *Dalton Trans.*, 2010, **39**, 8945-8956.
13. E. C. Constable, A. H. Redondo, C. E. Housecroft, M. Neuburger and S. Schaffner, *Dalton Trans.*, 2009, 6634-6644.
14. B. Bozic-Weber, E. C. Constable, C. E. Housecroft, P. Kopecky, M. Neuburger and J. A. Zampese, *Dalton Trans.*, 2011, **40**, 12584-12594.
15. B. Bozic-Weber, V. Chaurin, E. C. Constable, C. E. Housecroft, M. Meuwly, M. Neuburger, J. A. Rudd, E. Schoenhofer and L. Siegfried, *Dalton Trans.*, 2012, **41**, 14157-14169.
16. M. K. Nazeeruddin, A. Kay, I. Rodicio, R. Humphry-Baker, E. Muller, P. Liska, N. Vlachopoulos and M. Grätzel, *J. Am. Chem. Soc.*, 1993, **115**, 6382-6390.
17. Z.-S. Wang, Y. Cui, Y. Dan-oh, C. Kasada, A. Shinpo and K. Hara, *J. Phys. Chem. C*, 2007, **111**, 7224-7230.
18. S. Agrawal, M. Pastore, G. Marotta, M. A. Reddy, M. Chandrasekharam and F. De Angelis, *J. Phys. Chem. C*, 2013, **117**, 9613-9622.
19. E. Dell'Orto, L. Raimondo, A. Sassella and A. Abbotto, *J. Mater. Chem.*, 2012, **22**, 11364-11369.
20. A. Peic, D. Staff, T. Risbridger, B. Menges, L. M. Peter, A. B. Walker and P. J. Cameron, *J. Phys. Chem. C*, 2011, **115**, 613-619.
21. J. R. Mann, M. K. Gannon, T. C. Fitzgibbons, M. R. Detty and D. F. Watson, *J. Phys. Chem. C*, 2008, **112**, 13057-13061.
22. M. K. Nazeeruddin, P. Pechy and M. Grätzel, *Chem. Commun.*, 1997, 1705-1706.
23. S. Z. Vatsadze, A. V. Dolganov, A. V. Yakimanskii, M. Y. Goikhman, I. V. Podeshvo, K. A. Lyssenko, A. L. Maksimov and T. V. Magdesieva, *Russ. Chem. Bull.*, 2010, **59**, 724-732.
24. T. V. Magdesieva, A. V. Dolganov, P. M. Polestchuk, A. V. Yakimanskii, M. Y. Goikhman, I. V. Podeshvo and V. V. Kudryavtsev, *Russ. Chem. Bull.*, 2007, **56**, 1380-1389.

25. F. Brovelli, B. L. Rivas, J. C. Bernede, M. A. del Valle, F. R. Diaz and Y. Berredjem, *Polym. Bull.*, 2007, **58**, 521-527.
26. G. Boschloo and A. Hagfeldt, *Accounts Chem. Res.*, 2009, **42**, 1819-1826.
27. M. Grätzel, *Accounts Chem. Res.*, 2009, **42**, 1788-1798.
28. X. Q. Lu, S. X. Wei, C. M. L. Wu, S. R. Li and W. Y. Guo, *J. Phys. Chem. C*, 2011, **115**, 3753-3761.
29. M. Grätzel, *Nature*, 2001, **414**, 338-344.
30. J. N. Clifford, E. Palomares, M. K. Nazeeruddin, M. Gratzel and J. R. Durrant, *J. Phys. Chem. C*, 2007, **111**, 6561-6567.
31. A. Hagfeldt, G. Boschloo, L. Sun, L. Kloo and H. Pettersson, *Chem. Rev.*, 2010, **110**, 6595-6663.
32. P. J. Cameron and L. M. Peter, *J. Phys. Chem. B*, 2003, **107**, 14394-14400.
33. L. M. Peter, *Phys. Chem. Chem. Phys.*, 2007, **9**, 2630-2642.
34. A. Hagfeldt and L. Peter, *Dye-Sensitized Solar Cells*, EPFL Press, 2010, Chapter 10.
35. T. W. Hamann, R. A. Jensen, A. B. F. Martinson, H. Van Ryswyk and J. T. Hupp, *Energ. Environ. Sci.*, 2008, **1**, 66-78.
36. A. Taheri and G. J. Meyer, in *Gordon Research Conference on Photochemistry*, Easton, Massachusetts, 2011.
37. P. G. Hoertz, D. W. Thompson, L. A. Friedman and G. J. Meyer, *J. Am. Chem. Soc.*, 2002, **124**, 9690-9691.
38. G. Boschloo, L. Haggman and A. Hagfeldt, *J. Phys. Chem. B*, 2006, **110**, 13144-13150.
39. A. Yella, H.-W. Lee, H. N. Tsao, C. Yi, A. K. Chandiran, M. K. Nazeeruddin, E. W.-G. Diau, C.-Y. Yeh, S. M. Zakeeruddin and M. Grätzel, *Science*, 2011, **334**, 629-634.
40. S. M. Feldt, E. A. Gibson, E. Gabrielsson, L. Sun, G. Boschloo and A. Hagfeldt, *J. Am. Chem. Soc.*, 2010, **132**, 16714-16724.
41. B. Bozic-Weber, E. C. Constable, S. O. Furer, C. E. Housecroft, L. J. Troxler and J. A. Zampese, *Chem. Commun.*, 2013, **49**, 7222-7224.
42. L. N. Ashbrook and C. M. Elliott, *J. Phys. Chem. C*, 2013, **117**, 3853-3864.
43. T. W. Hamann, *Dalton Trans.*, 2012, **41**, 3111-3115.
44. A. H. Rendondo, E. C. Constable and C. E. Housecroft, *Chimia*, 2009, **63**, 205-207.
45. H. Nusbaumer, J. E. Moser, S. M. Zakeeruddin, M. K. Nazeeruddin and M. Gratzel, *J. Phys. Chem. B*, 2001, **105**, 10461-10464.
46. S. A. Sapp, C. M. Elliott, C. Contado, S. Caramori and C. A. Bignozzi, *J. Am. Chem. Soc.*, 2002, **124**, 11215-11222.
47. H. X. Wang, P. G. Nicholson, L. Peter, S. M. Zakeeruddin and M. Gratzel, *J. Phys. Chem. C*, 2010, **114**, 14300-14306.
48. J. Cong, Y. Hao, L. Sun and L. Kloo, *Adv. Energy Mater.*, 2014, DOI: 10.1002/aenm.201301273.
49. B. M. Klahr and T. W. Hamann, *J. Phys. Chem. C*, 2009, **113**, 14040-14045.
50. X. Ren, Q. Feng, G. Zhou, C.-H. Huang and Z.-S. Wang, *J. Phys. Chem. C*, 2010, **114**, 7190-7195.
51. A. C. Khazraji, S. Hotchandani, S. Das and P. V. Kamat, *J. Phys. Chem. B*, 1999, **103**, 4693-4700.
52. H. Choi, C. Nahm, J. Kim, J. Moon, S. Nam, D.-R. Jung and B. Park, *Curr. Appl. Phys.*, 2012, **12**, 737-741.
53. P. Wang, S. M. Zakeeruddin, P. Comte, R. Charvet, R. Humphry-Baker and M. Grätzel, *J. Phys. Chem. B*, 2003, **107**, 14336-14341.
54. M. G. A. Shvekhgeimer, *Chem. Heterocycl. Compd.* , 2004, **40**, 257-294.
55. W. Pfitzinger, *J. Prakt. Chem.*, 1886, **33**, 100.

56. R. Romagnoli, P. G. Baraldi, O. Cruz-Lopez, D. Preti, J. Bermejo and F. Estevez, *ChemMedChem*, 2009, **4**, 1668-1676.
57. A. Beauchard, Y. Ferandin, S. Frere, O. Lozach, M. Blairvacq, L. Meijer, V. Thiery and T. Besson, *Bioorg. Med. Chem.*, 2006, **14**, 6434-6443.

Chapter 6 - Synthesis of copper(I) dyes with heteroaromatic-functionalised 2,2’-bipyridine ligands

6. Synthesis of copper(I) dyes with heteroaromatic- functionalised 2,2'-bipyridine ligands

6.1. Introduction and theory

Following the detailed investigations completed with the copper(I) complex of 2,2'-biquinoline-4,4'-dicarboxylic acid ligand (Chapter 5, complex **20**) and the copper(I) (6,6'-dimethyl-2,2'-bipyridine-4,4'-dicarboxylic acid)$_2$ complex (Chapter 4, complex **1**) the focus shifted back to the 2,2'-bipyridine (bipy) framework, but with a functionalization strategy. From the extensive amount of work documented regarding the improvement of dyes, certain functional groups have been shown to impart favourable properties on the dye molecule for application in DSCs, for example, the five-membered heteroaromatic rings; pyrrole, furan and thiophene (Figure 65). [1]

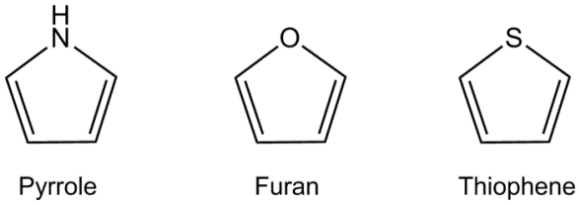

Figure 65 – electron rich five-membered heteroaromatic rings

The aromaticity of these planar ring systems is established according to Hückel's rule, which states that a complex is aromatic when the number of its π-electrons equals 4n+2, where n is zero or a positive integer. In the case of thiophene, there is one electron associated with each carbon in the ring and two from sulphur, therefore n=1. All five atoms are sp^2 hybridised and the formation of the π-electron cloud is through overlap between a 2p-orbital on each carbon atom and a 3p-orbital on sulphur. This creates three pairs of delocalized π-electrons in the system, two of which are typically shown in the structure and the third pair is shown on the sulphur atom. Sulphur has a second pair of non-bonding electrons which are not involved in the delocalised system. This delocalised cloud of six electrons over five atoms confers extra stability to the cyclic systems through resonance and results in an electron-rich system; a factor which can be exploited for dye synthesis. These five-membered systems are not as aromatic as benzene due to the electronegativity of the heteroatoms involved, which reduces the involvement of the lone pair in the delocalisation. An order of aromaticity (also stability) according to resonance energy is as follows: benzene > thiophene > pyrrole > furan. The stability of benzene is due to the delocalised electron density being distributed over more carbon atoms.

Extending the absorption range of dyes is a key area for improvement in DSCs. There is a widely acknowledged mismatch between a typical sensitizer absorption spectrum and the solar radiation spectrum, which can be addressed by designing dyes which absorb light at longer wavelengths, i.e. by causing a so-called "red shift" in the spectrum.[2-4]

The metal-to-ligand charge transfer (MLCT) is the electronic transition responsible for visible light absorption; therefore it is a vital feature of metal-based dyes. The introduction of electron donating heteroaromatic groups, either in the ancillary or the anchoring ligand, increases the π-conjugation in the ligand system. This is known to induce desirable bathochromic (a change of absorbance position to a longer wavelength), and also hyperchromic (an increase in intensity of an absorbance peak), shifts in the MLCT band in the UV/Vis spectrum. This improvement to the optical properties is most valuable in terms of light harvesting by the dye, which can lead to increases in the photocurrent and the solar-to-power conversion efficiencies of DSCs. Improving the molar extinction coefficient and light absorbing properties of a dye means that thinner TiO_2 films may also be used. Thinner films reduce the likelihood of a recombination reaction between the injected electron and either the I_3^- in the electrolyte or the oxidised form of the dye.[4]

As well as having the greatest aromatic character of the heteroaromatics discussed, a further advantage of thiophene rings is their synthetic versatility. There are many well-established, reliable and relatively straightforward procedures in organic chemistry for functionalisation of the ring. In particular, the 2- and 5- positions are highly susceptible to electrophilic attack and also lithiation, which can allow insertion of a range of additional moieties, including aldehydes and halides. S_EAr reactivity of the thiophene ring is most common at the 2- and 5- positions (as opposed to the 3- and 4- positions), due to the stability of the carbocation intermediate species. When substitution at the 2- position takes place there are three resonance forms of the corresponding dearomatised cationic intermediate. If reaction occurred at the 3- position, only two resonance forms may be invoked for the corresponding intermediate, which is less stable (Figure 66). In addition, it is noted in the literature that thiophene-containing chromophores usually have enhanced photo- and thermal stability.[1]

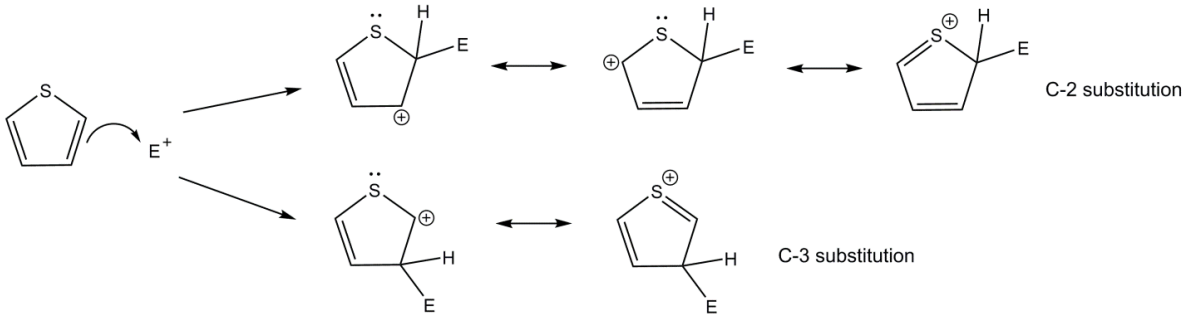

Figure 66 – relative reactivity of thiophene towards electrophilic aromatic substitution at the 2- and 3- positions

There is significant precedent in the literature for employing such heteroaromatics in the ligand framework of dyes for DSCs. A recent review compared a number of ruthenium(II) dyes with thienyl moieties to the standard N3 or N719 dyes.[1] It was highlighted that all the complexes reviewed demonstrated both a bathochromic and hyperchromic shift in the absorption spectrum relative to N3 or N719. The largest shift was for a homoleptic ruthenium(II) complex where the thiophene ring was incorporated between the bipy ligand and the anchoring carboxylic acid groups. It was found that this particular arrangement of the ligand components lowered the LUMO energy of the sensitizer. Synthesis of the ligand, and the corresponding ruthenium(II) complex (referred to as BTC-1, Figure 67), was reported by Mishra and colleagues in 2009.[5]

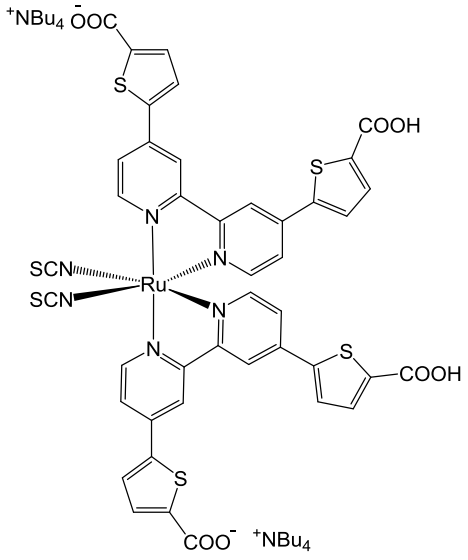

Figure 67 – structure of BTC-1, reported by Mishra *et al.*[5]

DSCs with a higher overall efficiency relative to N719 (6.1% compared to 4.8%, constructed under the same conditions) were achieved with BTC-1. In the UV/Vis spectrum the lowest energy MLCT was observed at 563 nm, which was 28 nm further towards the lower energy end of the spectrum compared to N719. This was attributed to the extended π-conjugation in the system relative to N719 and a higher energy HOMO level. An increase of 72% in the molar extinction coefficient was also observed for this transition relative to the analogous transition in N719.[5] The HOMO and LUMO energy levels were experimentally determined for both BTC-1 and N719. As exhibited through the shift in the absorption spectrum, the band gap for BTC-1 was reduced compared to that of N719. It should be noted that the performance of the BTC-1 dye only exceeded that of N719 when thin films (3.3 or 5.5 μm) of TiO_2 were used. In cells consisting of a 7 μm film plus 5 μm scattering layer their performances were very similar.

In terms of copper(I) dyes, the incorporation of heteroaromatics has not yet been fully explored. The Constable group included heteroaromatic groups in the ancillary ligand of a range of heteroleptic complexes, in the form $[CuL_2][PF_6]$ where L is 2,2'-bipyridine substituted in the 6-position with groups such as furan, thiophene or N-methylpyrrole.[6] The heteroleptic species was generated *in situ* by a ligand exchange method between the homoleptic complex and a TiO_2 film already treated with a TiO_2 coordinating ligand, namely a 2,2'-bipyridine ligand with carboxylic or phosphonic acid groups (Figure 68). The ligands, homoleptic and heteroleptic copper(I) complexes were characterised and compared in detail using NMR spectroscopy and X-ray crystallography. Incorporation of the heteroleptic complexes into DSCs found there was actually little variation between the thiophene, furan and N-methylpyrrole groups. The choice of binding group was found to be far more influential in this study, with the phosphonate anchoring groups achieving the highest efficiencies. This is an interesting, and thoroughly characterised, series of structures, however the emphasis of the work was on exploring the ligand exchange strategy and the key message concerned the influence of the binding group rather than a detailed study of the heteroaromatic substituents. Therefore there is still much work to be done along this route of functionalisation.

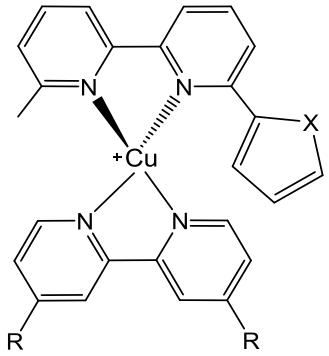

Figure 68 – structure of a series of copper(I) complexes from Constable and colleagues[6] where X = O, S or NMe and R = CO_2H or $PO(OH)_2$

A computational assessment of the use of heteroaromatics in copper(I) dyes was published by Lu *et al.* in 2011.[7] The group's calculations indicated overall that copper(I) polypyridyl complexes were viable alternatives to ruthenium(II) sensitizers, and specifically that enhancing the π-conjugation by introducing heteroaromatic groups into the ancillary ligands resulted in a positive shift of both the HOMO and LUMO energy levels in the dye; an increase in oscillator strength and a red shift in the electronic absorption spectrum.

The work in this chapter describes the synthesis of functionalised 2,2'-bipyridine-4,4'-dicarboxylic acid ligands and the subsequent copper(I) complexes. 2,2'-bipyridine-4,4'-dicarboxylic acid is an established ligand system for DSCs and has already proven successful when coordinated to copper(I), therefore the scope for improvement with it was assessed. Conscious of the fact that steric bulk at the 6- and 6'-positions would be necessary; this was seen as an obvious target for functionalisation. Methyl and phenyl groups had already been reported at these positions; therefore substitution with halides was considered (Ligands **30** and **29**, Figure 70). Not only would the steric effects be of interest, in terms of providing the rigidity necessary to prevent geometric switching between the copper(I) and (II) oxidation states, but their differing electronegativities may also have an impact on the electron density in the aromatic system. There has been no study of halides within the ligand framework for copper(I) dyes, although a paper by Zampese and co-workers[8] described the study of homo- and heteroleptic complexes using a 4,4'-di-(4-bromophenyl)-6,6'-dialkyl-2,2'-bipyridine ancillary ligand (Figure 69). However, this study was primarily focussed on varying the 6- and 6'-substituents for increasingly long alkyl chains, or a phenyl ring, and the bromine atoms were present simply as a point for further derivatisation in the molecule.

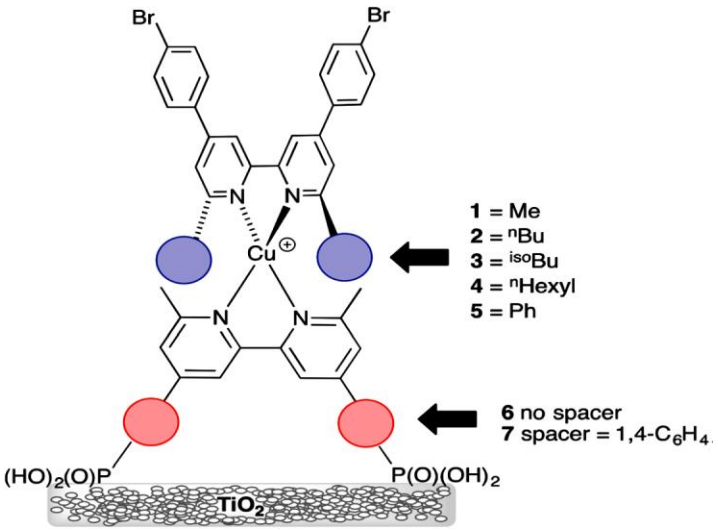

Figure 69 – a schematic of the heteroleptic dyes studied with bromide substituents in the ligand framework (diagram reproduced from reference 8)

If installation of halides in the 6- and 6'-positions was successful, the ultimate aim was to use the brominated ligand in such cross-coupling reactions as the Suzuki–Miyaura reaction,[9] replacing the bromides with functional groups such as thiophene rings (Ligand **32**, Figure 70). At that time, there was no published work on copper(I) dyes with thiophene rings in the ligand framework.

In a related project, the incorporation of thiophene groups in the 4- and 4'- positions of the 2,2'-bipyridine ligand, i.e. between bipy and the anchoring carboxylic acid groups, was considered. Interest in the target molecule (**39**, Figure 70) stemmed from the work reported by Mishra,[5] which had shown promise in ruthenium(II) complexes. However, methyl groups would be introduced at the 6- and 6'-positions to provide the geometric stability necessary for a copper(I) based dye. A DFT analysis of this structure (Chapter 7.3) indicated that the LUMO and LUMO+1 orbitals would be mainly distributed over the thiophene rings and the carboxylic acid groups, which would be important for efficient electron injection into the TiO_2 conduction band. Therefore it was indicated that the 4- and 4'-positioning of the thiophene groups would be electronically more appropriate than a 6- and 6'-positioning.

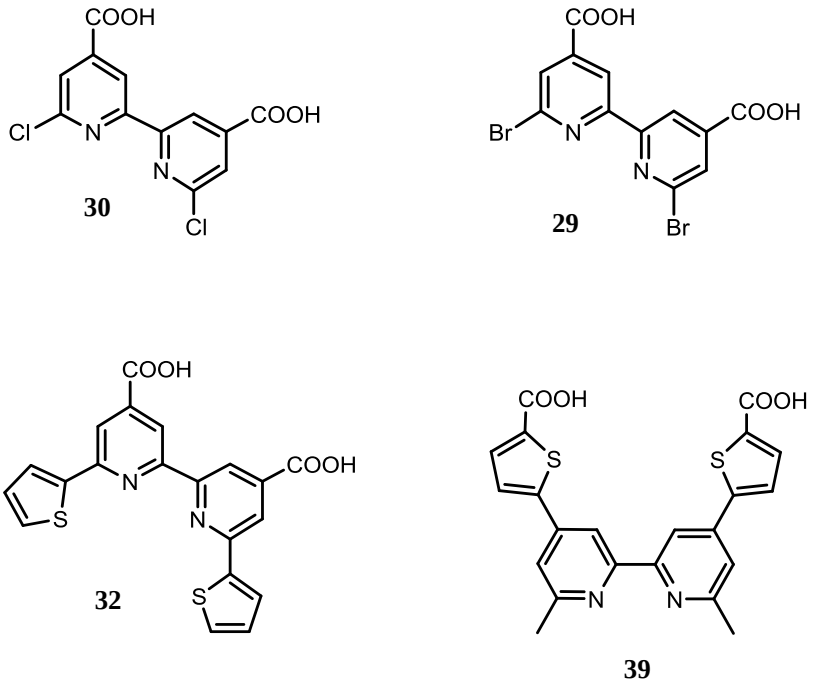

Figure 70 - target molecules from functionalisation of the 2,2'-bipyridine-4,4'-dicarboxylic acid ligand

6.2. Halide and thiophene functionalisation at the 6- and 6'-positions of a 4,4'-dicarboxy-2,2'-bipyridine ligand

6.2.1. Synthesis and characterisation of 6,6'-(bis)halide-4,4'-dicarboxy-2,2'-bipyridine ligands and copper(I) complexes (33 and 34)

The synthetic route (Scheme 4) towards the 6,6'-(bis)halide substituted target molecules began with oxidation of the commercially available 4,4'-dimethyl-2,2'-bipyridine to generate compound **24.** This step was initially carried out with $KMnO_4$,[10] however an alternative method[11] using $Na_2Cr_2O_7.2H_2O$ was found to afford species **24** in far better yield. Acid catalysed esterification[10] generated diester **25**, which was followed by synthesis of ligands **26** and **27** according to literature methods.[12] Oxidation of the 2,2'-bipyridine functionalities with H_2O_2 in acetic acid produced the pyridine *N*-oxide species, **26**. This step served to activate the pyridine ring for nucleophilic substitution at the 6- and 6'-positions through reaction with $POCl_3$, resulting in ligand **27**. At this point, the 6,6'-dichloro ligand was either hydrolysed to produce compound **30**, or else converted to the 6,6'-dibromo analogue.

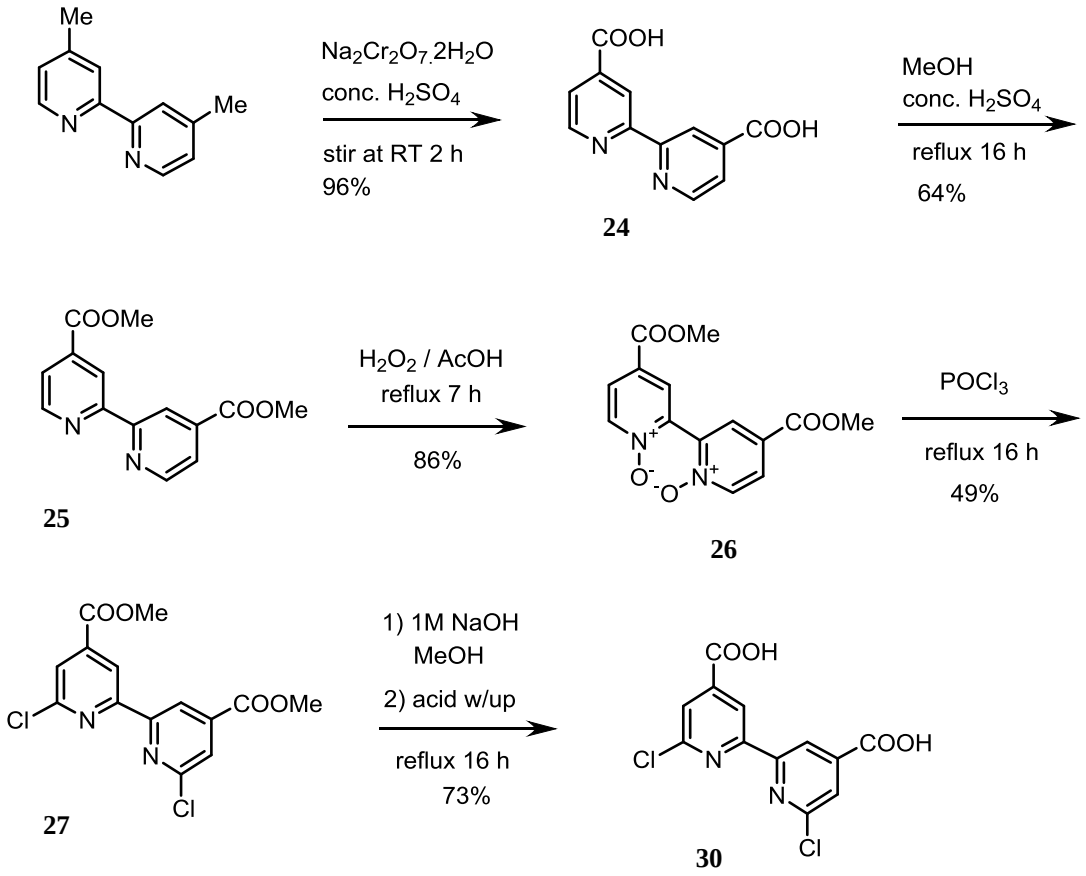

Scheme 4 – route towards 6,6'-dichloro-4,4'-dicarboxy-2,2'-bipyridine (30)

Bromination was carried out either with HBr (48% in H_2O), to directly reach the free acid complex, **29**, or with HBr (45% in acetic acid), which retained the ester groups intact, to acquire ligand **28** (Scheme 5).[12] Hydrolysis of **28** could then be carried out. The ^{1}H NMR spectra of ligands **30** and **29** were very similar with just a slight downfield shift of 0.14 ppm for H^2 in compound **29** relative to **30** to differentiate the two species (see labelling in Figure 71).

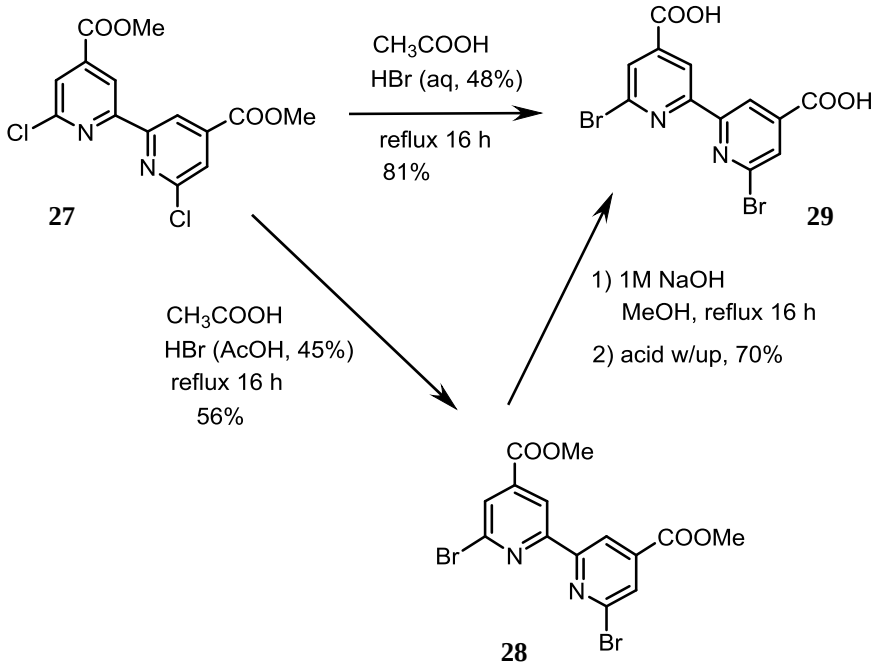

Scheme 5 – bromination of compound 27

Compounds **24–28** are known.[10-12] Ligands **29** and **30** have not previously been reported according to literature searches. The ^{1}H NMR spectra obtained for molecules **24, 25** and **27** were in agreement with literature data. There were no NMR data reported for **26**. Although compounds **24–28** are known, there was an absence of some characterisation data and structural assignments in the literature for **25-28**. Therefore ^{1}H and ^{13}C {^{1}H} NMR data are presented for the first time for ligand **26**, and ^{13}C {^{1}H} NMR data are reported for the first time for ligands **27** and **28**. Full data was acquired for the new ligands **29** and **30**. 2D-NMR data were obtained for all ligands, however full structural assignments could not be made once the halide had been installed in the structure due to difficulty in unambiguously identifying C^1, C^3 and C^6 (see labelling in Figure 71). Assignments were made as far as possible; however, even an HMBC experiment with a long acquisition time could not

unequivocally resolve the identity of the quaternary carbons, due to the absence of any key identifying cross-peaks. The aromatic C-H assignments were made *via* HMQC/HSQC experiments. Where NMR experiments could not elucidate between H^2/C^2 and H^5/C^5 in ligands **27** to **30**, assignments were assumed to be the same as those observed with previous, similar, molecules in the reaction scheme and also as the similar molecules presented in Scheme 6, where proton H^5 is always downfield of H^2.

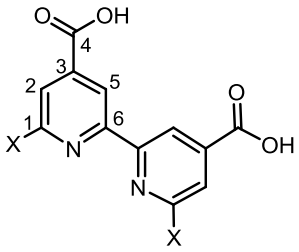

Figure 71 – Labelled structure of ligands 30 (where X=Cl) and 29 (where X=Br)

Ligands **30** and **29** were then complexed to copper(I) to produce species **33** and **34** (Figure 72). The copper(I) precursor was $[Cu(CH_3CN)_4][PF_6]$, dissolved in MeCN, and this solution was added *via* cannula into a stirring solution of two equivalents of the ligand, usually in MeOH. The ligands were partially soluble in MeOH, however a common issue was that if not all of the ligand was solubilized before the reaction, it would not all complex to copper and had to be filtered out after the reaction. The reactions occurred at room temperature with an immediate colour change upon addition of the copper(I) precursor solution, resulting in a light red/brown coloured complex **33** and a darker red/purple complex **34**. Both were partially soluble in MeOH.

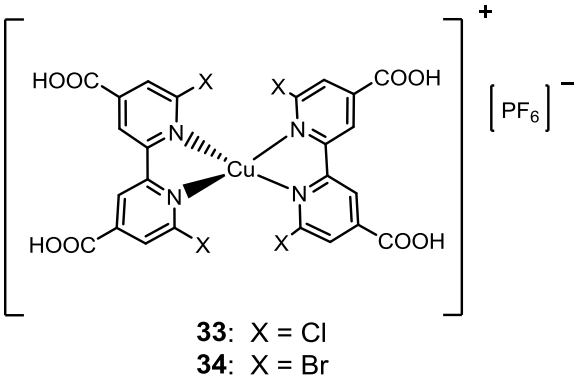

33: X = Cl
34: X = Br

Figure 72 – structures of the [Cu(6,6'-(bis)halide-4,4'-dicarboxy-2,2'-bipyridine)$_2$]$^+$ complexes

Characterisation and analysis of compounds **33** and **34** was carried out as far as possible. ^{1}H and ^{13}C $\{^{1}H\}$ NMR data were obtained for complex **34**, although only 5 of the 6 carbons were detected. The molecular ion of **34** was weakly detected by +ve MALDI mass spectrometry at m/z 866.7, which is consistent with $[M\text{-}PF_6]^+$, and the structure was also confirmed by elemental analysis. However the choice of solvent had an important bearing on stability. When **34** was studied by ^{1}H NMR in acetone-d_6 there were initially two aromatic singlets visible, attributed to the copper(I) complex. However, after a few days, the same NMR sample was re-run and there were four singlets of an almost equal integration present. The two new peaks were identified through their chemical shifts as free ligand, **29**. In CD_3OD compound **34** appeared more stable, although a small second set of singlet peaks started to appear after 48 hours in solution.

The solubility and stability in solution of **33** was poorer, therefore obtaining reasonable characterisation data was difficult. A ^{13}C $\{^{1}H\}$ spectrum was not obtained and although some batches of the dye did show two aromatic singlets for H^2 and H^5, shifted downfield of where the free ligand peaks had been. These peaks were broad and there were other impurities visible in the spectrum. The molecular ion for the complex was not detected in ESI or MALDI mass spectrometry. An elemental analysis was fairly close to that expected for the desired complex, but did not confirm the structure. Reactions using the sodium salt of ligand **30** were carried out for improved solubility, as were reactions with equivalents of NEt_3. Purification through a Sephadex column was also attempted. However a pure sample of **33** was not obtained.

It was concluded that the complexes were probably susceptible to solvent attack in solution. The larger bromine substituents were affording a more stable *pseudo* tetrahedral geometry whereas the chloro-substituted complex was less stable to attack from coordinating solvents. Given their instability and questionable purity, particularly of **33**, only a limited study with these dyes was conducted. UV/Vis and electrochemistry data were collected and DSCs were constructed.

6.2.2. Analysis of complexes 33 and 34

The UV/Vis spectra of complexes **33** and **34** (Figure 73) are very similar. The MLCT $\lambda_{(max)}$ and molar extinction coefficient values for complex **33** are 488 nm and 2775 M^{-1} cm^{-1} respectively, and for complex **34** they are 493 nm and 4186 M^{-1} cm^{-1}. There is a slight bathochromic shift on moving from the chloro- to bromo-substituents. Halogens are electron withdrawing through induction but the presence of their lone pair means they are also electron donating through resonance. There will be competition between these two effects that may influence the HOMO-LUMO gap by changing the electron density of the 2,2'-bipyridine ring.

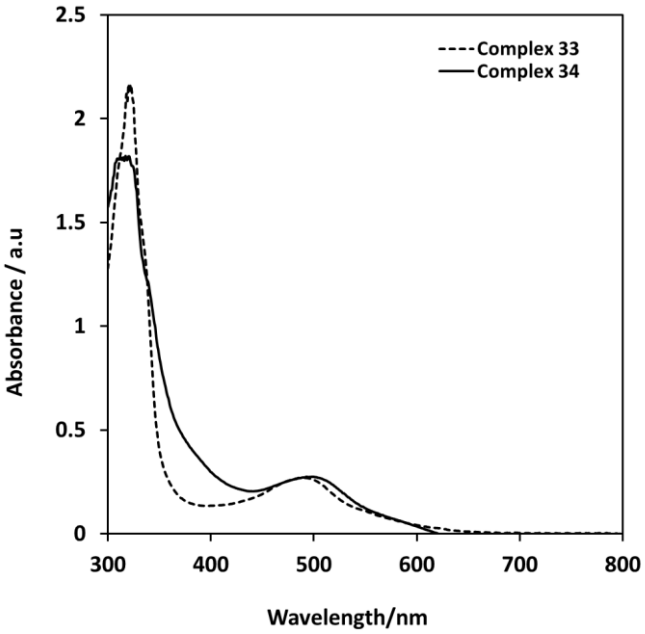

Figure 73 - UV/Vis spectra of complexes 33 and 34 at 0.1 mM in MeOH

The electrochemistry of complexes **33** and **34** were studied on the surface of FTO glass by cyclic voltammetry. No electrochemical response was observed when dyed TiO_2 films were used as the working electrodes (WE), therefore a small quantity of the dye in MeOH was dropped onto a cleaned piece of FTO glass and the solvent allowed to evaporate. This method was found to work appropriately. A platinum CE and a Ag/AgCl RE (3 M KCl) were used and the background electrolyte was 0.1 M TBAHFP in MeCN. The CVs for the two complexes are very similar (Figure 74 and Figure 75).

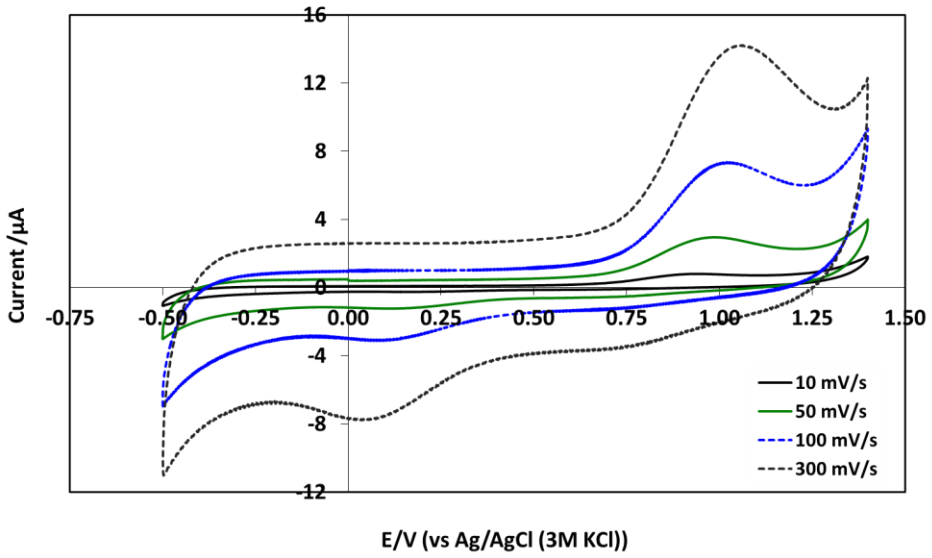

Figure 74 - CV at increasing scan rates of complex 33 on an FTO surface

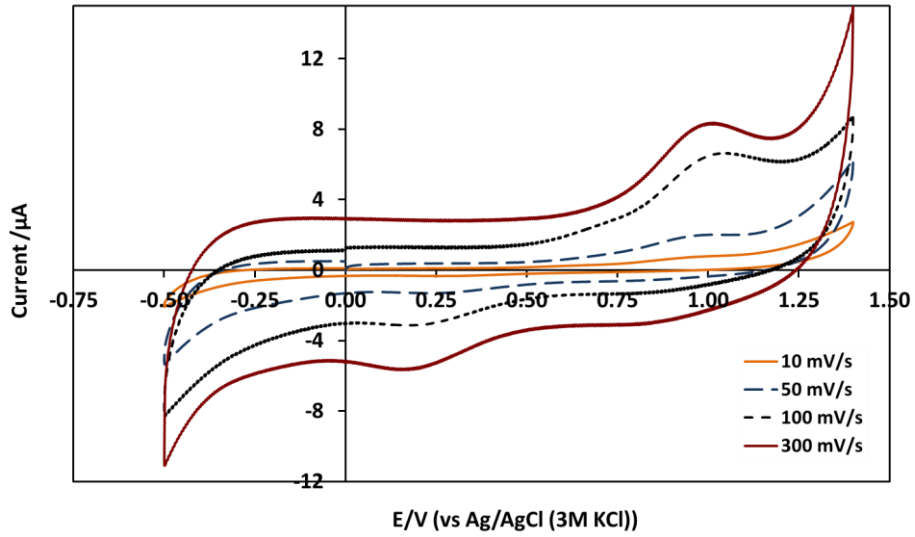

Figure 75 - CV at increasing scan rates of complex 34 on an FTO surface

The copper(I) to copper(II) oxidation takes place at ~ +1.00 V in both cases. On the reverse wave there is a reduction at ~ +0.1 V present at all scan rates, however at faster scan rates a second reduction is visible at ~ +0.75 V. This could be reduction of a second species, forming due to the instability of the dyes, or it may be due to a rearrangement of the same species. During the oxidation the complex could be switching from a tetrahedral to square

planar geometry. At slow scan rates there was enough time for this transformation to occur, whereas at fast scan rates the tetrahedral species was still detected. The large peak potential separation also suggests a large reorganization energy needs to be overcome.

Using TiO_2 films prepared according to ***method 1*** (Chapter 3.3.1) and the standard electrolyte recipe, 1 cm^2 DSCs were constructed with complexes **33** and **34.** However the cells were not promising, with $\eta \leq 0.056\%$. A higher J_{SC} was obtained when dye **34** was used, which can be linked to its higher molar extinction coefficient. Overall, work with these dyes was not pursued due to the stability and synthesis problems, the mediocre preliminary DSC efficiencies, and the fact that the synthesis route was relatively harsh, with the use of chromium reagents, concentrated acid and $POCl_3$, which would render their use inherently less sustainable. Moving forwards, the focus was shifted to synthesising the thiophene-functionalised ligands and complexes.

6.2.3. Functionalisation of the 6,6'-(bis)halide-4,4'-dicarboxy-2,2'-bipyridine ligands with thiophene moieties

From ligands **28** and **29**, synthesis of the previously unreported thiophene-functionalised target molecules, **31** and **32,** could be attempted (Figure 76).

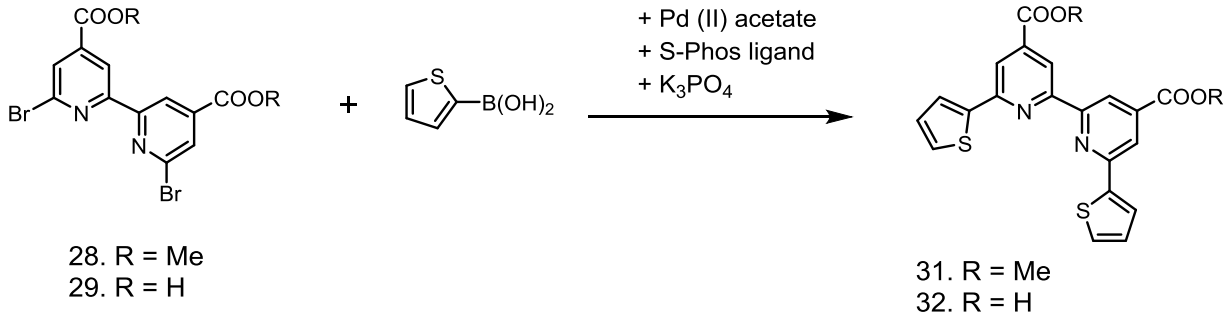

Figure 76 – synthesis of ligands 31 and 32 *via* a Suzuki-Miyaura cross-coupling

Initially a Suzuki–Miyaura cross-coupling reaction[9] of the ester **28** was tried. When conducted with conventional heating in THF, the desired reaction did not occur. A small amount of mono-coupled product was obtained and the majority of starting material recovered. In a microwave reactor, at higher temperatures, the reaction proceeded in both a

dioxane:water (5:1) and a toluene:water (5:1) solvent combination, although only partial conversion was achieved and in both cases starting material was again recovered. A pure sample of ligand **31** was isolated from column chromatography and identified from ^{1}H NMR and mass spectrometry. Only 9 of the 11 carbon peaks were detected in the ^{13}C $\{^{1}H\}$ NMR spectrum, due to the low quantity of product obtained.

A microwave cross-coupling with the free acid, ligand **29**, was also attempted in order reach compound number **32**. This time an ethanol:water (5:1) solvent combination was used for better solubility. It was difficult to tell through TLC analysis when the starting material had been consumed due to the difficulty in separating highly polar carboxylic acids on silica. ^{1}H spectroscopic NMR analysis of the crude reaction mixture showed the compound **32** as the major product, some of the starting ligand **29**, as well as the remaining boronic acid and S-Phos reagents. Although different solvent systems were tried in column chromatography of the crude reaction mixture, isolation of the pure product could not be achieved in this way. The purest sample of product was obtained when the reaction solvent was allowed to evaporate at room temperature and a white residue precipitated out. This was identified by ^{1}H NMR spectroscopy and mass spectrometry, although a ^{13}C $\{^{1}H\}$ NMR spectrum could not be acquired due to the low quantity of product.

Unfortunately, insufficient quantities of ligands **31** and **32** were eventually obtained in order to proceed to the copper(I) complexation step. It would be useful to return to this ligand synthesis again in the future to generate more of starting ligand **28**. From this point, optimisation of the cross-coupling reaction could be carried out, followed by hydrolysis of the ester group and finally the synthesis of the copper(I) complex.

6.3. Thiophene functionalisation at the 4- and 4'-positions of a 2,2'-bipyridine ligand

6.3.1. Synthesis and characterisation of a 6,6'-dimethyl-5,5'-[2,2'-bipyridin-4,4'-diyl]-bis[thiophene-2-carboxylic acid ligand] (39) and copper(I) complex, (42)

The second part of this chapter details the incorporation of thiophene groups into the 4- and 4'- positions of a 2,2'-bipyridine ligand, *i.e.* between the bipy ligand and the anchoring carboxylic acid groups. As mentioned previously, the target ligand was similar to that complexed to ruthenium(II) by Mishra. However here, steric bulk needed to be installed at the 6- and 6'-positions to retain geometric stability. For this reason, a synthesis was planned which had some similarity in its initial steps to that reported by Constable and co-workers[13] for the 6,6'-dimethyl-2,2'-bipyridine-4,4'-dicarboxylic acid ligand, but starting from 2-thiophenecarboxaldehyde rather than 2-furaldehyde (Scheme 6).

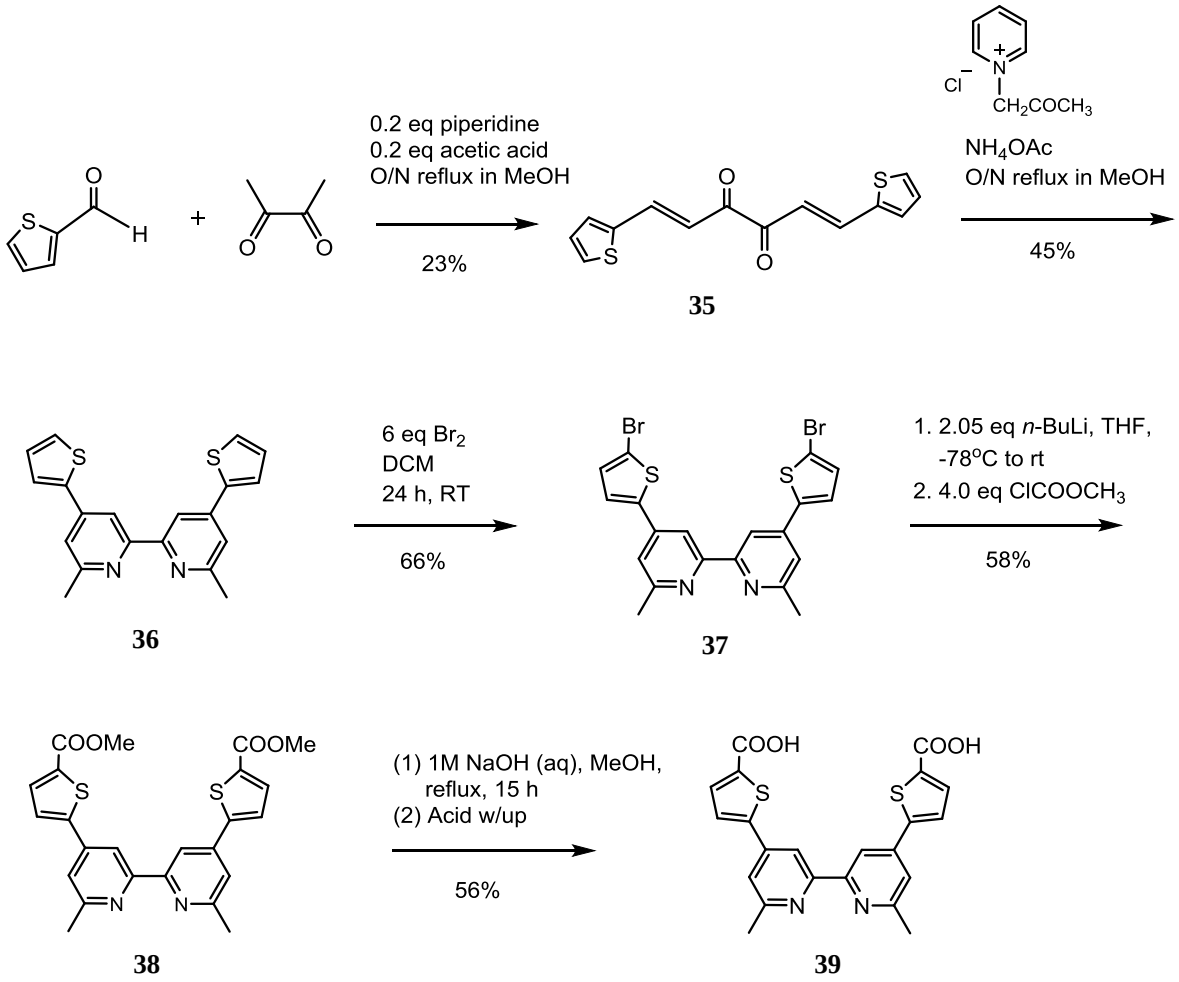

Scheme 6 – synthetic route to 6,6'-dimethyl-5,5'-[2,2'-bipyridin-4,4'-diyl]-bis[thiophene-2-carboxylic acid], 39

The first step was modified slightly from the procedure used for the analogous 2-furaldehyde reaction.[14] According to a report from Takada,[15] 0.2 equivalents of acetic acid were included in addition to the other reagents, and the reaction mixture was refluxed overnight. This offered an improved yield, albeit still a relatively low one. It is speculated that the role of the acetic acid is both to activate the carbonyl on the thiophene ring towards nucleophilic attack by the 2,3-butanedione and also to facilitate the keto-enol tautomerism required for this nucleophilic attack to occur. Increasing the heating time did not result in any significant increase in yield. When this work commenced diketone **35** had not been reported, however its synthesis has very recently been reported by other groups.[16-18] The second step of the synthesis was the Kröhnke pyridine formation to access compound **36**, which proceeded in the same way as with the analogous furan precursor, with a comparable (and moderate) yield. The next step was to derivatise the thiophene rings with the necessary anchoring moieties. In order to add carboxylic acid groups, bromination of the thiophene rings in the 2- and 2'- positions was first performed. As discussed previously, bromination will occur preferentially in this position rather than at the 3- and 4-positions. No over-bromination was observed, although some optimisation of the bromine equivalents and reaction time had to be carried out in order to minimize the amount of mono-brominated product formed. As an easier and safer alternative to bromine, *N*-Bromosuccinimide (NBS) was tried for the bromination step. However this method was not as effective and a mixture of product and starting material was obtained. A lithium-halogen exchange on **37** was the next step, using *n*-BuLi and methyl chloroformate to install a methyl ester group. The product, **38**, was isolated by column chromatography and hydrolysed under basic conditions to yield the final ligand, **39**. All of the compounds above, except **35**, are previously unreported and they have all been fully characterised and assigned using 2D-NMR experiments. Crystal structures for ligands **36** (Figure 77 (a) and (b)) and **37** (Figure 78 (a) and (b)) were obtained from slow evaporation of solvent. Key bond lengths and bond angles are listed in Table 9 (ligand **36**) and Table 10 (ligand **37**).

Ligand **36** crystallised in the monoclinic crystal system with a $P2_1/n$ space group. A comparison of bond parameters for **36** with those of the analogous bis-furan ligand[13] is provided in Table 9. Ligand **36** adopts the same trans-configuration and the ligand orientation is close to planar. The C-C bond lengths within the bipyridine ring and forming the bridge between bipyridine and the heteroaromatic are very similar for the two molecules. Due to the larger size of sulphur, the C-S bonds are longer than the C-O bonds

(1.712(3) and 1.649(4) versus 1.370(2) and 1.358(2)), and are consistent with thiophene bond lengths and angles reported in the literature.[19]

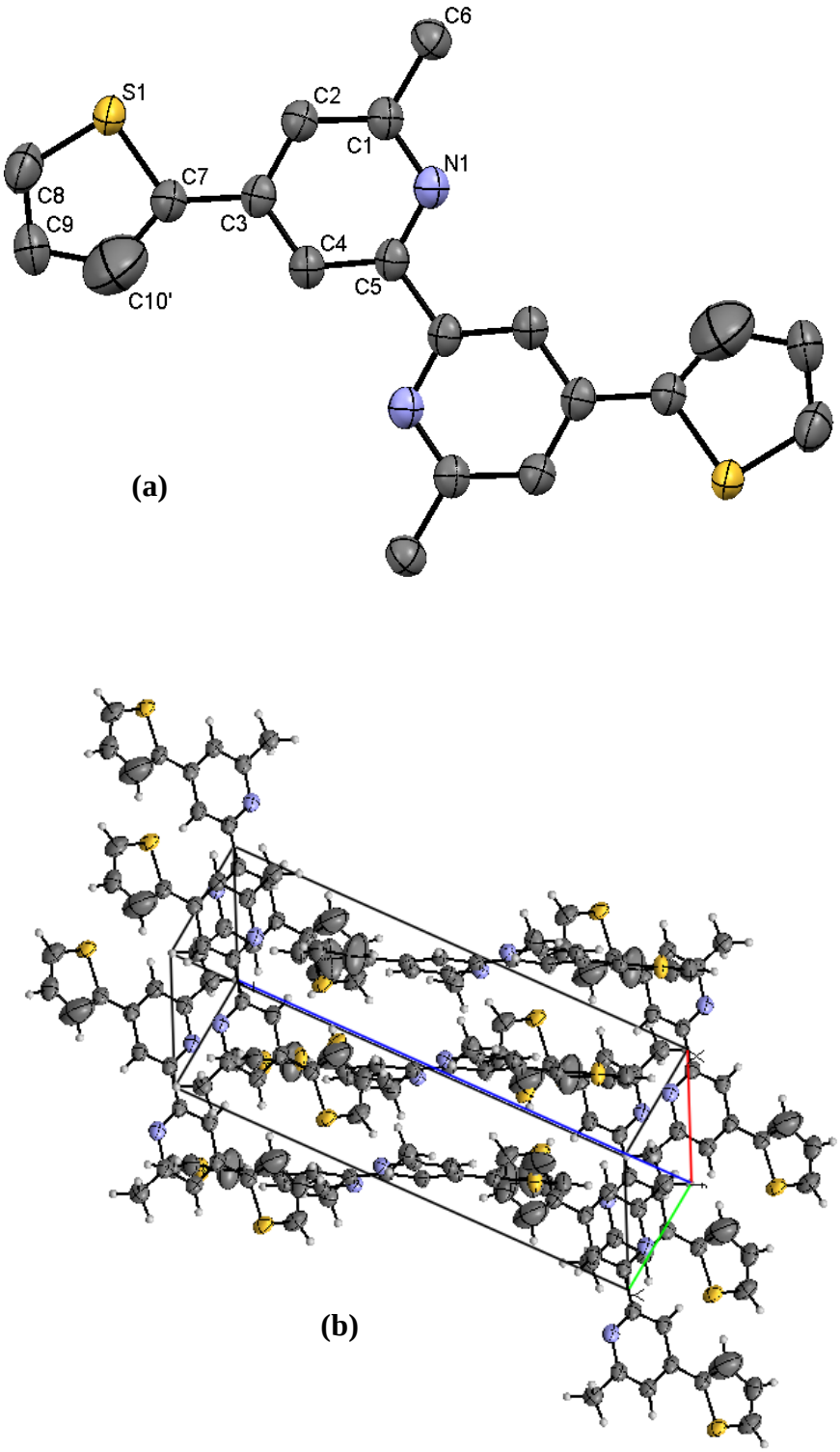

Figure 77 – (a) crystal structure for ligand 36. Thermal ellipsoids are shown at the 30 % probability level. The thiophene ring was disordered over two positions in a 65:35 ratio – the major form is shown; (b) crystal packing structure for ligand 36

Table 9 - Selected bond lengths (A˚) and bond angles (°) of 36 and the analogous bis-furan ligand

6,6'-dimethyl-4,4'-di(thiophen-2-yl)-2,2'-bipyridine (compound 36)		6,6'-dimethyl-4,4'-di(2-furyl) -2,2'-bipyridine	
Bond/Angle	**Bond length (Å) /Angle (°)**	**Bond/Angle**	**Bond length (Å) /Angle (°)**
C(1)-C(6)	1.489(4)	C(1)-C(6)	1.503(2)
C(3)-C(7)	1.469(3)	C(3)-C(7)	1.455(2)
C(5)-C(5)#1	1.495(5)	C(5)-C(5)#1	1.493(3)
C(7)-C(10)	1.373(5)	C(7)-C(10)	1.349(3)
C(7)-S(1)	1.712(3)	C(7)-O(1)	1.370(2)
C(8)-C(9)	1.337(5)	C(8)-C(9)	1.326(3)
C(8)-S(1)	1.649(4)	C(8)-O(1)	1.358(2)
C(9)-C(10')	1.377(5)	C(9)-C(10')	1.449(3)
C(8)-S(1)-C(7)	92.10(18)	C(8)-O(1)-C(7)	106.8(2)

Ligand **37** crystallised in the monoclinic crystal system, with a *C*2/c space group. The trans-geometry, bond lengths and angles are analogous to those of ligand **36** and the C-Br bond length is typical for a bromine atom attached to an aromatic carbon atom.[20] The packing of **37** in the unit cell (Figure 78 (b)) shows that the molecules orient in layers due to the π–π stacking between the aromatic rings. This arrangement is similarly reported for 6,6'-dimethyl-4,4'-di(2-furyl)-2,2'-bipyridine[13] and the intermolecular distance is similar (3.520 Å for **37** versus 3.39 Å).

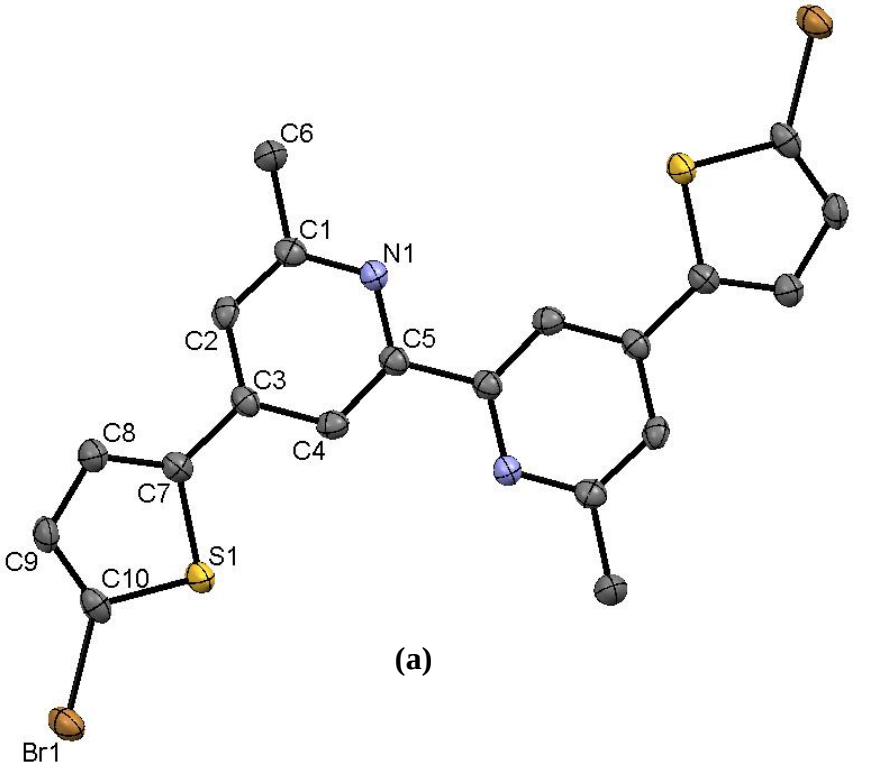

(a)

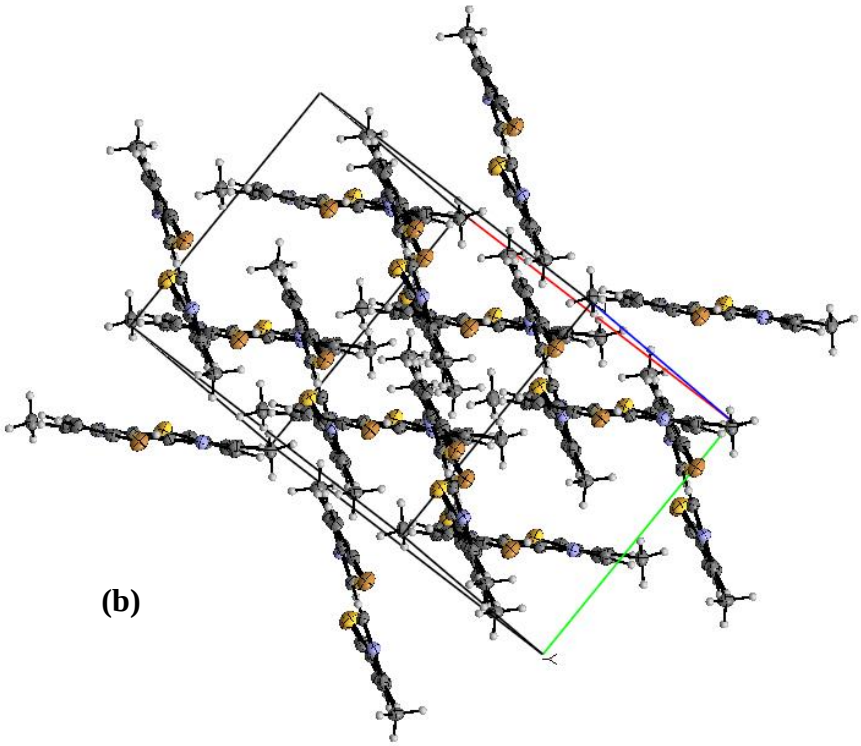

(b)

Figure 78 – (a) crystal structure for ligand 37. Thermal ellipsoids are shown at the 30% probability level; (b) crystal packing structure for ligand 37

Table 10 - Selected bond lengths (A˚) and bond angles (°) of 37

6,6'-dimethyl-4,4'-di(5,5'-bromothiophen-2-yl)-2,2'-bipyridine (compound 37)	
Bond/Angle	**Bond length (Å) /Angle (°)**
C(1)-C(6)	1.506(4)
C(3)-C(7)	1.469(5)
C(5)-C(5)#1	1.497(6)
Br(1)-C(10)	1.874(3)
C(7)-S(1)	1.735(3)
C(8)-C(9)	1.414(4)
S(1)-C(10)	1.718(3)
C(9)-C(10)	1.352(5)
C(10)-S(1)-C(7)	91.63(16)

Solubility of the ligand, **39**, and the copper(I) complex was partial in MeOH and low in other organic solvents. Therefore in the first few metal complexation reactions there was residual ligand present, visible in the ^{1}H NMR spectrum. Separation of free ligand from the complex was attempted through a Sephadex column however this was unsuccessful. A copper(I) dye (**41**) with the methyl ester ligand (**38**) was prepared and a basic hydrolysis of it was attempted. However, the reaction conditions degraded the complex and the red solution of dye changed to pale yellow, with precipitation of the free ligand. Other attempts to generate fully complexed dye included using an excess of the copper(I) precursor, refluxing the reaction, and introducing an Fmoc ester rather than a methyl group, which could be removed post-metal complexation under more mildly basic conditions. In the end, further purification of ligand **38** by a second chromatography column resulted in improved solubility of ligand **39**, leading to a pure batch of the desired dye, **42,** being synthesised.

Complexation of the free acid ligand to copper(I) was carried out under N_2 using $[Cu(CH_3CN)_4][PF_6]$, dissolved in MeCN. A cannula transfer of the copper(I) precursor into a solution of **39** stirring at room temperature in basic MeOH (i.e. containing a quantity of aq. 1 M NaOH) was carried out. Formation of a clear, dark red, solution was immediate. This was stirred overnight under N_2 followed by reduction of the reaction mixture volume under vacuum and acidification to pH 4 with aq. 1 M HCl. A dark red solid precipitated, **42**,

and was isolated, washed with diethyl ether, dried and used without further purification. Only this batch of dye was used for the analysis discussed in the following chapter.

Similar solubility of the complexes and free ligands meant NMR experiments could be conducted in the same solvent and therefore directly compared. The ^{1}H NMR spectrum of **42** showed the chemical shifts for the thiophene and bipyridine protons had shifted downfield following metal complexation; from δ 7.71 and 7.61 ppm to δ 7.97 and 7.64 ppm for the thiophene shifts, and from δ 8.31 and 7.63 ppm to δ 8.79 and 7.85 ppm for the bipyridine protons. The effect is most pronounced for the bipyridine protons and the least pronounced for H^2, the proton furthest from the metal centre (see labelling in Figure 79). This trend was also observed with the analogous complexes **40** and **41** (Figure 79), which used the ligand in its methyl ester form and the ligand prior to the bromination step, and with complexes **33** and **34**.

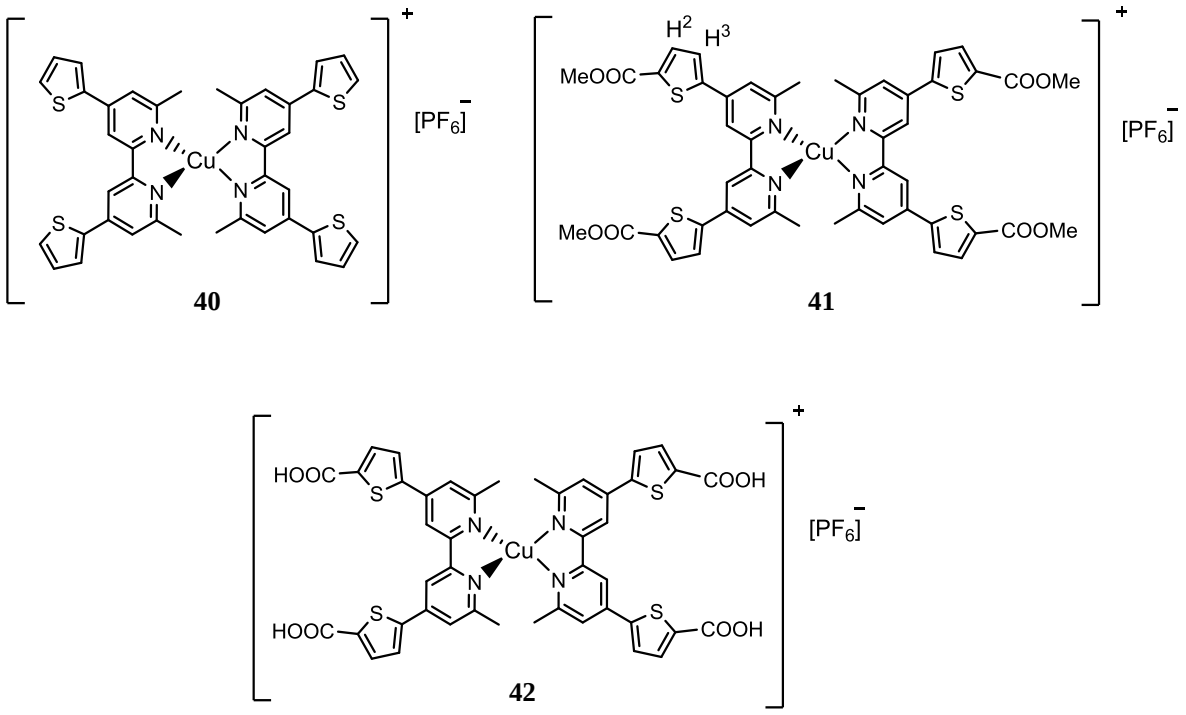

Figure 79 – Structures of the copper(I) complexes prepared with ligands 36, 38 and 39

Although their lack of binding groups prevented complexes **40** and **41** from being suitable for application in DSCs; better quality characterisation data could be obtained, compared to

the free acid complex, due to their better solubility. All of the complexes were a dark red colour in solution and dye **42** also produced dark red coloured TiO_2 films (Figure 80).

Figure 80 – Complex 42 in MeOH and on the surface of a TiO_2 film

The presence of the $[PF_6]^-$ counter ion for the complexes was confirmed through ^{31}P $\{^1H\}$ NMR. 2D-NMR data of **41** enabled complete proton and carbon assignment. The presence of two methyl groups aided the quaternary carbon assignments and the carbonyl carbon cross-peak with H^2 allowed differentiation of the thiophene protons. An extended ^{13}C $\{^1H\}$ acquisition detected 8 of the 9 aromatic carbons and the methyl carbon in compound **42**. Unfortunately the carbonyl carbon and one of the quaternary carbons were not visible therefore a full assignment could not be made. However the chemical shifts that were identified were very similar to those of complex **41** and some structural assignments were possible using HMBC data.

With the desired complex in hand, a full analysis of the dye and its viability in dye sensitized solar cells could be conducted. These data are presented in Chapter 7.

6.4. Conclusions

A number of new ligands (**29** and **30**, **31** and **32**, **36**-**39**) and copper(I) complexes (**33** and **34**, **40**-**42**) have been reported in this chapter and their synthesis described. They have been characterised and structurally assigned as far as possible.

Although synthesis of copper(I) complexes with ligands **31** and **32** was not realised, synthesis of complexes **33** and **34** en-route was completed and they were analysed for application in DSCs. Solar power-to-conversion efficiencies with the dyes were low, possibly due to their instability in solution. The bromine substituents conferred better stability to the complexes than the smaller chlorine atoms and consequently complex **34** was better characterised and purer than **33**. The complexes were studied by UV/Vis spectroscopy, recording fairly broad absorbance bands and moderate molar extinction coefficients in the visible region. Cyclic voltammetry of the dyes on an FTO glass surface identified a redox cycle with a large peak-to-peak separation of ~0.9 V. This suggests there may be some structural reorganisation of the dye taking place. Had the complexes offered better stability and a more straightforward synthesis, then optimisation of the cross-coupling reactions generating ligands **31** and **32** would have been pursued. Copper(I) complexes with these ligands have the potential to be interesting and would be useful to compare to complex **42**, therefore continuing the synthesis in the future, perhaps *via* an alternative route, is a possibility.

The most promising complex, **42,** incorporates thiophene groups in the 4- and 4'-positions between the 2,2'-bipyridine ligand and the carboxylic acid anchoring groups. The dark red dye is fairly soluble in MeOH and strongly dyes TiO_2 films the same colour. A computational study (described in Chapter 7.3) indicates the LUMO and LUMO+1 orbitals should be favourably located on the thiophene rings and carboxylic acid groups, which is important for electron injection into the TiO_2 conduction band. Complex **42** will be studied in more detail in Chapter 7.

6.5. References

1. A. Abbotto and N. Manfredi, *Dalton Trans.*, 2011, **40**, 12421-12438.
2. M. K. Nazeeruddin, E. Baranoff and M. Grätzel, *Sol. Energy*, 2011, **85**, 1172-1178.
3. T. W. Hamann, R. A. Jensen, A. B. F. Martinson, H. Van Ryswyk and J. T. Hupp, *Energ. Environ. Sci.*, 2008, **1**, 66-78.
4. N. Robertson, *Angew. Chem.-Int. Edit.*, 2006, **45**, 2338-2345.
5. A. Mishra, N. Pootrakulchote, M. K. R. Fischer, C. Klein, M. K. Nazeeruddin, S. M. Zakeeruddin, P. Bauerle and M. Grätzel, *Chem. Commun.*, 2009, 7146-7148.
6. B. Bozic-Weber, E. C. Constable, C. E. Housecroft, P. Kopecky, M. Neuburger and J. A. Zampese, *Dalton Trans.*, 2011, **40**, 12584-12594.
7. X. Q. Lu, S. X. Wei, C. M. L. Wu, S. R. Li and W. Y. Guo, *J. Phys. Chem. C*, 2011, **115**, 3753-3761.
8. B. Bozic-Weber, S. Y. Brauchli, E. C. Constable, S. O. Furer, C. E. Housecroft, F. J. Malzner, I. A. Wright and J. A. Zampese, *Dalton Trans.*, 2013, **42**, 12293-12308.
9. N. Miyaura and A. Suzuki, *Chem. Rev.*, 1995, **95**, 2457-2483.
10. D. Miyoshi, H. Karimata, Z.-M. Wang, K. Koumoto and N. Sugimoto, *J. Am. Chem. Soc.*, 2007, **129**, 5919-5925.
11. G. M. Greenway, A. Greenwood, P. Watts and C. Wiles, *Chem. Commun.*, 2006, 85-87.
12. C. Barolo, M. K. Nazeeruddin, S. Fantacci, D. Di Censo, P. Comte, P. Liska, G. Viscardi, P. Quagliotto, F. De Angelis, S. Ito and M. Grätzel, *Inorg. Chem.*, 2006, **45**, 4642-4653.
13. E. C. Constable, A. H. Redondo, C. E. Housecroft, M. Neuburger and S. Schaffner, *Dalton Trans.*, 2009, 6634-6644.
14. P. Karrer, C. Cochand and N. Neuss, *Helv. Chim. Acta*, 1946, **29**, 1836-1841.
15. Y. Takada, K. Nomura and S. Matsubara, *Org. Lett.*, 2010, **12**, 5204-5205.
16. C. R. Sinu, E. Suresh and V. Nair, *Org. Lett.*, 2013, **15**, 6230-6233.
17. Y.-F. Sun, Z.-Y. Chen, L. Zhu, S.-H. Xu, R.-T. Wu and Y.-P. Cui, *Color. Technol.*, 2013, **129**, 165-172.
18. Y.-F. Sun, L. Zhong, X.-M. Hou, S.-Y. Ma, W.-Z. Duan and R.-T. Wu, *Color. Technol.*, 2012, **128**, 331-339.
19. T. Eicher, S. Hauptmann and A. Speicher, *The Chemistry of Heterocycles: Structures, Reactions, Synthesis, and Applications*, 3rd edn., Wiley-VCH, 2012.
20. M. N. G. James and G. J. B. Williams, *Acta Crystallogr. B*, 1973, **29**, 1172-1174.

Chapter 7 - Analysis of [Cu(6,6'-dimethyl-5,5'-[2,2'-bipyridin-4,4'-diyl]-bis[thiophene-2-carboxylic acid])$_2$][PF_6], (42), for application in a DSC

7. Analysis of [Cu(6,6'-dimethyl-5,5'-[2,2'-bipyridin-4,4'-diyl]-bis[thiophene-2-carboxylic acid])$_2$][PF_6], (42), for application in a DSC

7.1. Introduction

This chapter analyses complex **42** (Figure 81) with respect to its application in a DSC. For details of synthesis please refer to Chapter 6.3.

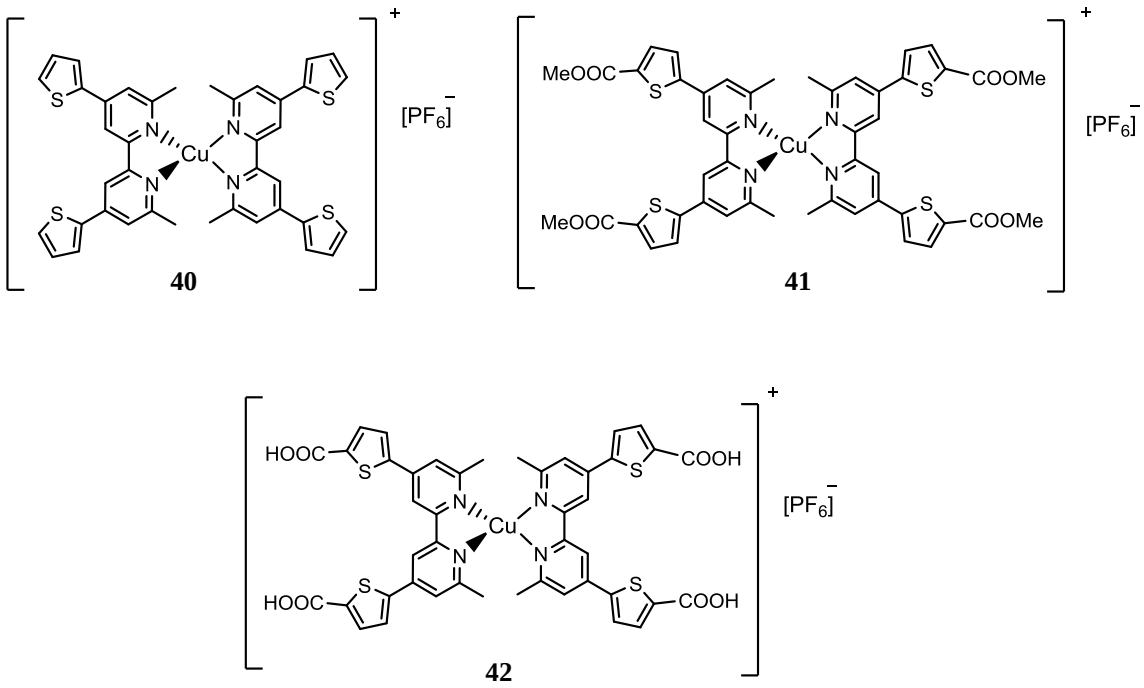

Figure 81 - [Cu(6,6'-dimethyl-5,5'-[2,2'-bipyridin-4,4'-diyl]-bis[thiophene-2-carboxylic acid])$_2$][PF_6], (42), and its analogues 40 and 41

7.2. UV/Vis and emission spectroscopy studies

As noted in previous chapters, the electronic transitions in the visible region are vital to the function of the dye in a DSC. UV/Vis spectra were acquired and molar extinction coefficients calculated for complexes **40**, **41** and **42** (Table 11). The solution and surface adsorbed UV/Vis spectra for **42** are shown in Figure 82.

Table 11 – Maximum visible region absorbance bands for 40, 41 and 42

Complex	ε (M^{-1} cm^{-1})	λ_{max} (nm)	Solvent
40	17,540	495	acetone
41	10,500	514	acetonitrile
42	9,030	506	methanol

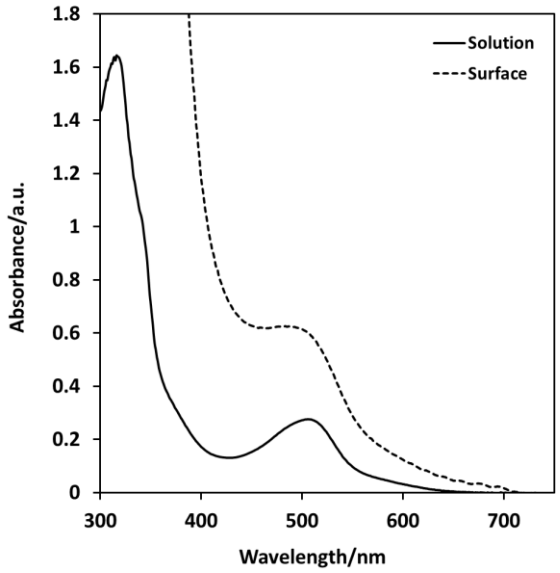

Figure 82 – UV/Vis spectrum of complex 42 in MeOH (32 µM) and adsorbed on a TiO_2 film

The presence of the electron-withdrawing ester and carboxylic acid groups is seen to shift the MLCT absorbance band to longer wavelengths relative to the carboxylate-free complex **40**, reducing the optical band gap. The molar extinction coefficients are similar for complexes **41** and **42**, although they are lower than that measured for **40**. Due to solubility issues, the measurements were conducted in different solvents therefore there could be solvatochromatic effects to take into account, i.e. interactions between the solvent and dye which can affect the wavelength and intensity of an absorbance band. The molar extinction coefficient of **42** is comparable to the other homoleptic copper(I) complexes reported for DSC application, which are typically around 10,000 M^{-1} cm^{-1}, [1, 2] and also to the copper(I) biquinoline complex, **20**. The absorption spectrum for **42** adsorbed on the TiO_2 surface is

broad but shows the same peak absorbance at around 500 nm that was observed in solution. There is also a very strong absorbance in the UV region, at $\lambda_{(max)}$ 316 nm, which has a molar extinction coefficient of 50,000 M^{-1} cm^{-1}. This is assigned to a π-π^* transition on the ligand.

Complex **42** was studied by emission spectroscopy. Its solubility was best in MeOH however it is known that MeOH can quench emission from copper(I) complexes.[3] Therefore experiments were first tried in CH_2Cl_2. All solutions were degassed prior to the experiment and measurements were carried out at room temperature. It was observed that **42** was strongly emissive at 380 nm following excitation at 320 nm, which was attributed to emission from a ligand based π^* state (Figure 83) (Note that this emission spectroscopy work was carried out on a different fluorimeter to the data presented in Chapter 5.5 therefore the intensity scale is different.) An excitation acquisition confirmed the wavelength responsible for this emission and the wavelength agreed with the absorbance maxima observed in the electronic absorption spectrum. Emissive behaviour was probed further by exciting across a range of visible wavelengths. There was a fairly weak emission signal at 500 nm after excitation at 400 nm (Figure 84) but nothing was observed following excitation at longer wavelengths.

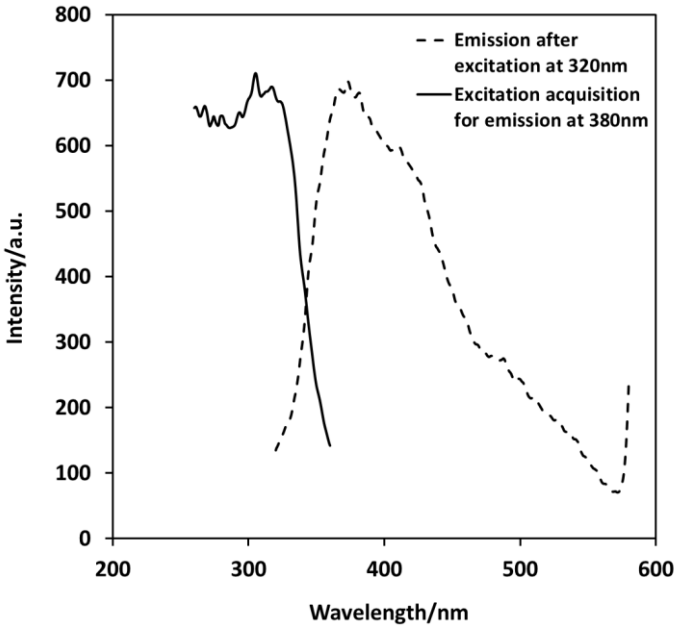

Figure 83 - excitation and emission spectra of complex 42 in CH_2Cl_2 at room temperature, following excitation at 320 nm

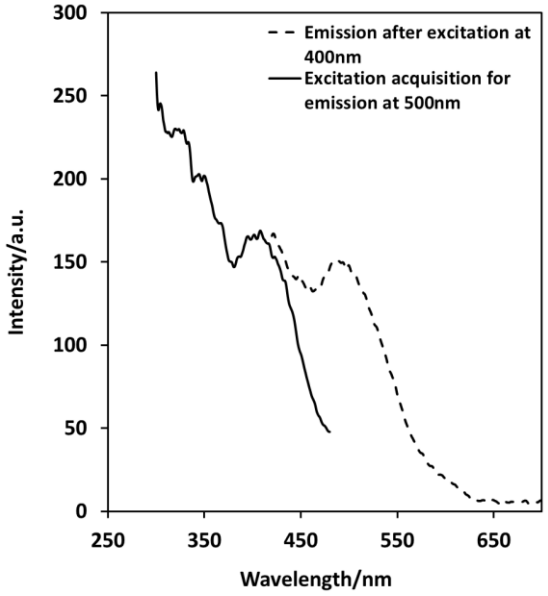

Figure 84 - excitation and emission spectra of complex 42 in CH_2Cl_2 at room temperature, following excitation at 400 nm

Experiments were also conducted in degassed MeOH for comparison. Strongly emissive behaviour, analogous to the response of the dye in CH_2Cl_2, was observed following excitation at 320 nm and it was interpreted in the same way. There was also a very weak emission at 550 nm after excitation at 510 nm (Figure 85), which is assigned as fluorescence from the MLCT. This correlates with the visible region absorbance maxima observed at 506 nm.

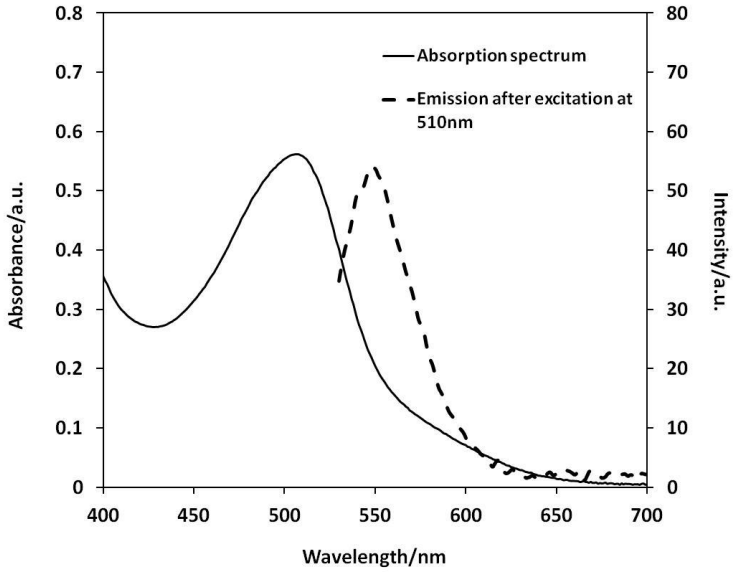

Figure 85 – absorption and emission spectra of complex 42 in MeOH at room temperature, following excitation at 510 nm

The emissive behaviour of complex **40** was also studied in 0.1 mM degassed solutions of acetone and EtOH (Figure 86). **40** was strongly emissive at the same wavelength (530 nm) in both solvents at room temperature following excitation at wavelengths between 460 and 480 nm, which correlates reasonably well with the absorption data ($\lambda_{(max)}$ = 495 nm) for the MLCT transition.

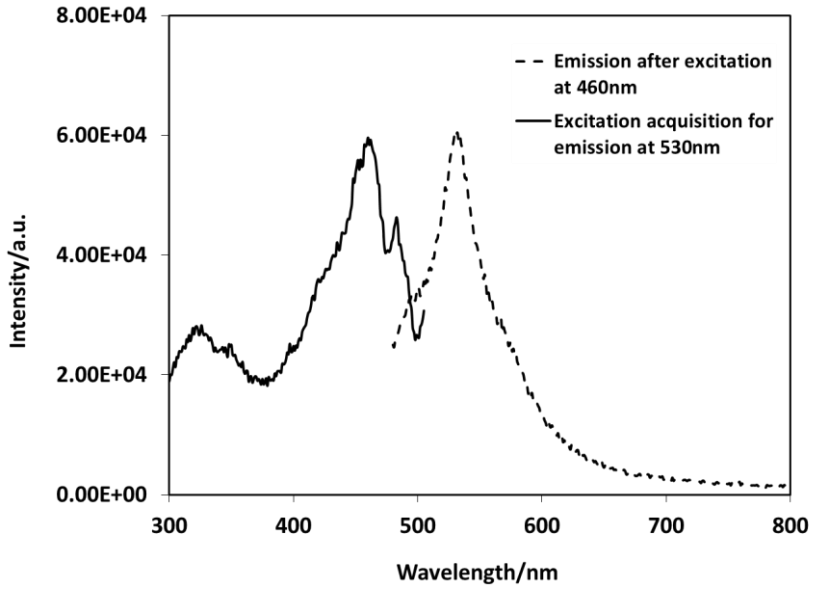

Figure 86 - excitation and emission spectra of complex 40 in EtOH at room temperature, following excitation at 460 nm

7.3. Computational analysis of complex 42

In the same manner as described for complex **20**, a computational analysis of the complex **42** cation was carried out to help assess whether the dye would be suitable for DSCs. The LANL2DZ basis set was used with the M06 functional and solvent effects were taken into consideration for MeOH. Analysis of this structure indicated that the position of the LUMO and LUMO+1 orbitals should be favourably distributed over the thiophene rings and carboxylic acid groups, which is important for efficient electron injection into the TiO_2. The HOMO and HOMO-1 are located over the copper centre and display dominant metal contributions. Molecular orbital diagrams for the two highest and lowest occupied/unoccupied orbitals are shown in Figure 87.

The simulated electronic absorption spectrum from TD-DFT is shown in Figure 88. A MLCT was predicted to occur at 555 nm with the major contributions to this transition being HOMO-1→LUMO (22%), HOMO-1→LUMO+1 (24%), HOMO→LUMO (26%) and HOMO → LUMO+1 (20%). This energy is 50 nm shifted of that observed in the experimental data however other similar work has noted discrepancies of between 50 and 80 nm in their computational analyses.[4, 5] The computed transition in the UV region more closely reproduces the experimental results, with $\lambda_{(max)}$ at 319 nm versus 316 nm observed experimentally. These, and other significant transitions, are summarised in Table 12 and the energies and copper composition of the higher occupied molecular orbitals are presented in Table 13.

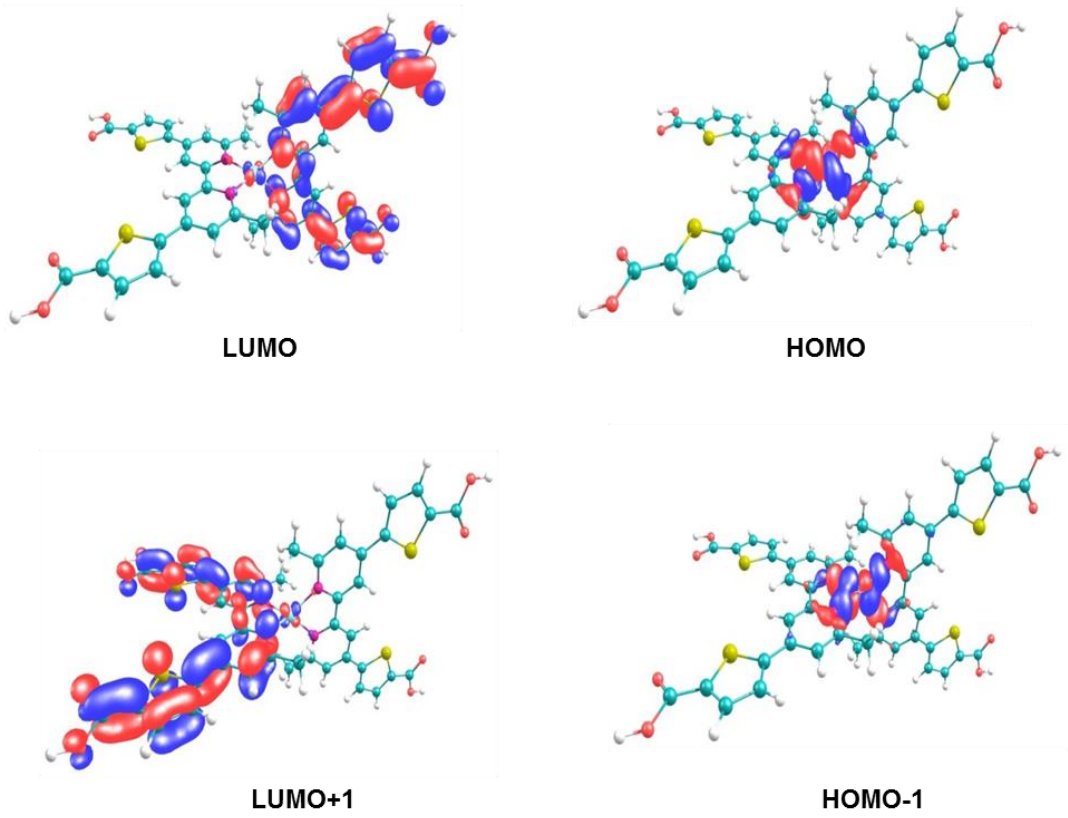

Figure 87 - plots of the two highest occupied and unoccupied molecular orbitals of [42]$^+$

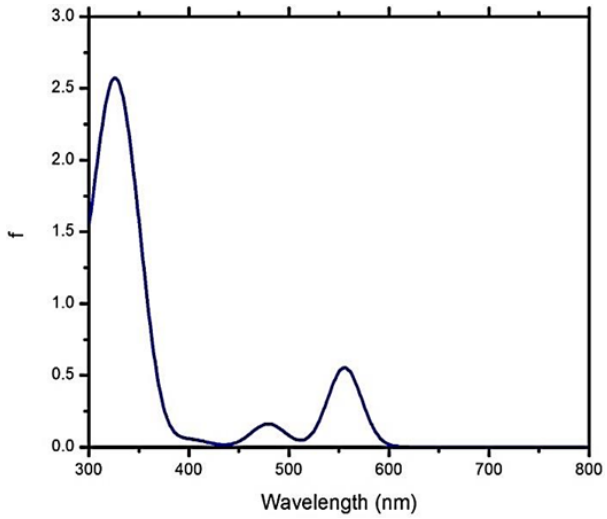

Figure 88 - Simulated UV/Vis spectrum of $[42]^+$ in MeOH

Table 12 - Wavelength, oscillator strength and composition of the most important optical transitions

λ (nm)	f	Composition
555.66	0.55	H-1→LUMO (22%), H-1→L+1 (24%) HOMO→LUMO (26%), HOMO→L+1 (20%)
480.65	0.08	H-1→L+2 (46%), HOMO→L+2 (49%)
477.26	0.08	H-1→L+3 (53%), HOMO→L+3 (40%)
403.74	0.02	H-3→LUMO (81%)
347.12	0.69	H-3→L+2 (63%), H-3→L+3 (29%)
338.56	0.36	H-7→LUMO (82%)
337.16	0.30	H-6→L+1 (73%)
327.55	0.10	H-5→LUMO (25%), H-5→L+1 (25%)
327.51	0.11	H-5→LUMO (22%), H-5→L+1 (29%)
319.09	1.43	H-9→LUMO (42%), H-8→LUMO (13%) H-8→L+1 (15%)
315.77	0.07	H-9→LUMO (12%), H-9→L+1 (12%) H-8→L+1 (37%), H-6→L+3 (19%)
314.55	0.02	H-6→L+3 (20%), H-5→L+3 (24%) H-1→L+6 (12%), HOMO→L+6 (14%)

Table 13 - Energies and Composition of the Higher Occupied and Lower Unoccupied Molecular Orbitals of [42]$^+$

MO	occ	E(eV)	Cu (% contribution)
LUMO+5	0	-1.82	
LUMO+4	0	-1.83	
LUMO+3	0	-2.54	
LUMO+2	0	-2.54	
LUMO+1	0	-2.72	
LUMO	0	-2.74	
HOMO	2	-5.80	64(d_{xy})
HOMO-1	2	-5.82	64(d_{xz})
HOMO-2	2	-6.73	84(d_{yz})
HOMO-3	2	-6.80	64(d_z^2)
HOMO-4	2	-7.02	92($d_{x^2-y^2}$)
HOMO-5	2	-7.16	

It can be seen that several transitions are responsible for the dominant bands of 555 and 319 nm, due to the energetic similarity between the two highest occupied and two lowest unoccupied molecular orbitals. This is in contrast to the principal computed MLCT band of complex **20** (563 nm, discussed in Chapter 5.7), which is dominated by a HOMO-1 → LUMO+1 transition (79%) and displays a larger difference between HOMO/HOMO-1 and LUMO/LUMO+1 energy levels. There is also more copper character in the lower lying HOMO levels for complex **42** (between 64% and 92% for HOMO-2 to HOMO-4) than for complex **20** (between 22% and 43% for HOMO-2 to HOMO-4), i.e. for complex **20** the HOMOs are distributed more evenly over ligands and metal. This may suggest that the back migration of an injected electron from the TiO_2 to the oxidised dye is less likely with complex **42** than with complex **20**, due to better charge separation.[4]

The energy levels for the HOMO and LUMO were calculated, in MeOH, to be -5.80 and -2.74 eV respectively, giving a band gap of 3.06 eV. As mentioned previously, the HOMO energies for N3 and N719 are -5.6 eV[6] and -5.5 eV[7] respectively, versus vacuum. The calculated LUMO energy is also adequately matched to the conduction band edge of TiO_2. These values can be compared to experimentally derived energy levels later in the chapter.

7.4. DSC assembly and analysis with complex 42

A range of DSCs were manufactured under varying conditions with complex **42** and the results will be presented and discussed here. Initially the effect of the TiO_2 film thickness and electrolyte recipe were studied. Mishra and colleagues[8] reported that the ruthenium(II) dye, BTC-1 (Figure 67, Chapter 6.1), outperformed N719 cells made under the same conditions when thinner films (<6 μm) were used. The TiO_2 films used in this work were prepared *via* ***method 2*** (Chapter 3.3.1) and resulted in film thicknesses typically between 6 and 7 μm or between 14 and 15 μm for single and double layer depositions respectively. Single and double layer refers to one or two layers of 3M Scotch tape™ used to mark out the area of glass for deposition. Mishra also noted the use of 3-methoxypropionitrile as the electrolyte solvent, which will be discussed in more detail later in this section.

Cells in the following studies were made to a 1 cm^2 dyed area, unless otherwise stated, and all cells were measured at an illumination intensity of 1 sun. Although there was some natural variation between the quality of each cell, general trends can be observed and discussed. Consistency in cell preparation was facilitated as far as possible by maintaining the same procedures, timings and techniques throughout cell preparation. Full details can be found in Chapter 3.3. Figure 89 shows examples of DSCs with complex **42**. The dye appeared heat-stable during the cell sealing process and also in contact with the I^-/I_3^- electrolyte. Some cells were re-tested a period of time after assembly (exact times will be noted in each specific experiment) and there was no visual change in the cells over time.

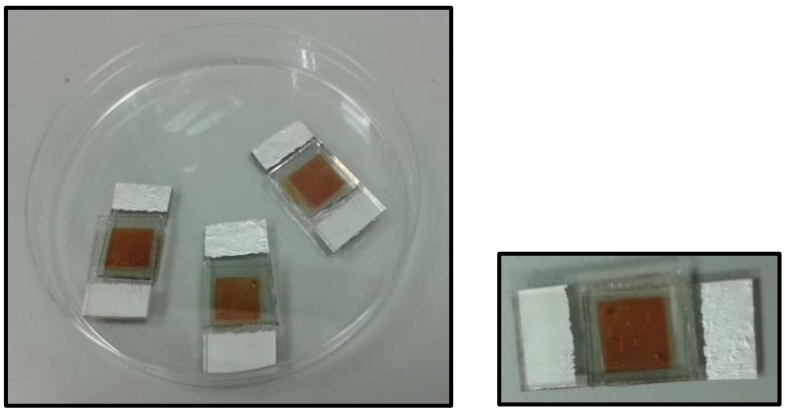

Figure 89 – 1 cm^2 DSCs constructed with complex 42

Two electrolytes, labelled **E5** and **E6**, were used in the course of these experiments. They comprised the following:

- Electrolyte 5: 0.1 M LiI, 0.05 M I_2, 0.5 M 1-methylbenzimidazole and 0.6 M 1-butyl-3-methylimidazolium iodide in 3-methoxypropionitrile
- Electrolyte 6: 0.03 M I_2, 0.05 M LiI, 0.6 M 1-propyl-3-methylimidazolium iodide, 0.5 M 4-TBP and 0.1 M guanidine thiocyanate in 85:15 MeCN:valeronitrile

E5 is the formulation used in the literature for use with copper(I) DSCs[2] and E6 is used for high efficiency ruthenium(II) DSCs.[9] A mixture of MeCN and valeronitrile is typically used to reduce the volatility of the electrolyte (relative to using only MeCN). 3-methoxypropionitrile is less volatile still and is the solvent used by Mishra's group in their studies. In E5, 1-methylbenzimidazole is used as an alternative to the 4-TBP employed in E6. It imparts the same favourable properties to the cell, in that the cell V_{OC} is increased, but as a solid it is less volatile than 4-TBP therefore is often used when concentrating on longer-term stability.[10] 1-butyl-3-methylimidazolium iodide and 1-propyl-3-methylimidazolium iodide are ionic liquids, which have certain features which make their inclusion in DSC electrolytes favourable, for example their high chemical and thermal stability, negligible vapour pressure, low volatility and high conductivity. However, their high viscosity can cause diffusion limitations for the I_3^- redox species, resulting in less efficient reduction of the oxidised dye.[11] Therefore they are generally diluted with organic solvents from the nitrile group for use in DSCs.

In the first experiment, four cell environments were studied. TiO_2 film thickness was controlled either by a single or double layer of scotch tape and cells were made either with E5 or E6. In Table 14 the average of the cell parameters measured for three DSCs with complex **42** are presented from each set of conditions, as well as N719 control cell parameters. Cell efficiencies were very promising, with the average measurement ranging between 0.61 and 0.74 %.

Table 14 –cell parameters of DSCs constructed with complex 42. Values for complex 42 are an average of 3 DSC measurements. N719 values are from 1 DSC. All cells had an area of 1 cm^2 and were tested on day 1 (where day 0 is the day of cell construction)

Experiment number/dye	Electrolyte	TiO_2 layers	V_{OC} (mV)	J_{SC} (mA)	*FF* (%)	η (%)
1 – complex 42	**5**	**Double**	**564**	**1.65**	**66.0**	**0.61**
1 – N719	5	Double	708	9.8	52.8	3.66
2 – complex 42	**6**	**Double**	**572**	**1.58**	**69.1**	**0.63**
2 – N719	6	Double	691	9.43	58.4	3.8
3 – complex 42	**5**	**Single**	**584**	**2.04**	**62.7**	**0.74**
3 – N719	5	Single	722	8.91	54.3	3.49
4 – complex 42	**6**	**Single**	**585**	**1.83**	**66.2**	**0.71**
4 – N719	6	Single	735	3.66	63.6	1.71

The experiment found that cells with thinner TiO_2 films displayed a modest improvement in short-circuit photocurrent, open-circuit photovoltage and overall solar-to-electrical power conversion efficiency compared to those assembled from thicker TiO_2 films. Although with thinner films Mishra's group found the BTC-1 dye produced higher efficiency cells than N719, efficiencies for both dyes were still higher in cells with thicker TiO_2 films. However, our doctor bladed double layer films are thicker than those used in Mishra's experiments therefore it is difficult to directly compare. Mishra's group compared film thicknesses of 3.3 µm, 5.5 µm and a 7 µm film plus 5 µm scattering layer, whereas the "thin" and "thick" films used here are double the magnitude.

The group attributed the better performance of the thiophene functionalised dye in thinner films to its high molar extinction coefficient. Using a highly absorbing dye means that recombination losses can be reduced through using thinner films, while reasonable photocurrents can still be obtained. Increasing the dye loading on the TiO_2 surface by increasing the film thickness will only be advantageous up to a point. Although more dye will be adhered to a thicker film, it appears from the lower photocurrents obtained that this additional dye is not leading to an improved electron collection efficiency. Thicker films can also lead to an increase in electron losses through recombination.[12]

The electrolyte composition did not affect overall cell efficiency. In both the double and single layer film thickness cells the short-circuit current was higher with E5 and the fill

factor was lower. The photovoltage with E6 was slightly higher with double thickness cells but with single layers the difference was negligible. The cells were re-tested a week later. For the DSCs with complex **42** shown in Table 14, η had decreased for 8 cells and increased for 4 cells. However it should be noted that some of the cells had dried out over the week, which resulted in negligible, or significantly lower, power output. From the 4 cells that registered an improved efficiency, three of these displayed an increase in J_{SC} of between 0.11 and 0.14 mA and a decrease in photovoltage of between 3 and 9 mV. The fourth cell exhibited a decrease in photocurrent and an increased photovoltage. There was little change in fill factor across the four cells. This "ripening" effect in cells over time, consisting of an increase in J_{SC}, was noted by Constable and co-workers with their copper(I) cells.[2, 13]

Optimisation of DSCs with complex **42** was then carried out. In the literature, headline efficiencies reported by groups are generally for small cells (dyed area <1 cm^2) with a TiO_2 scattering layer and often with a post-sintering $TiCl_4$ treatment. The initial experiments indicated that a single layer of mesoporous TiO_2 was better than a double layer and that the two electrolyte compositions produced similar cells. Reducing the cell size and employing these additional treatments resulted in a top cell efficiency for a DSC with complex **42** of 1.41% (Figure 90, data in Table 18).

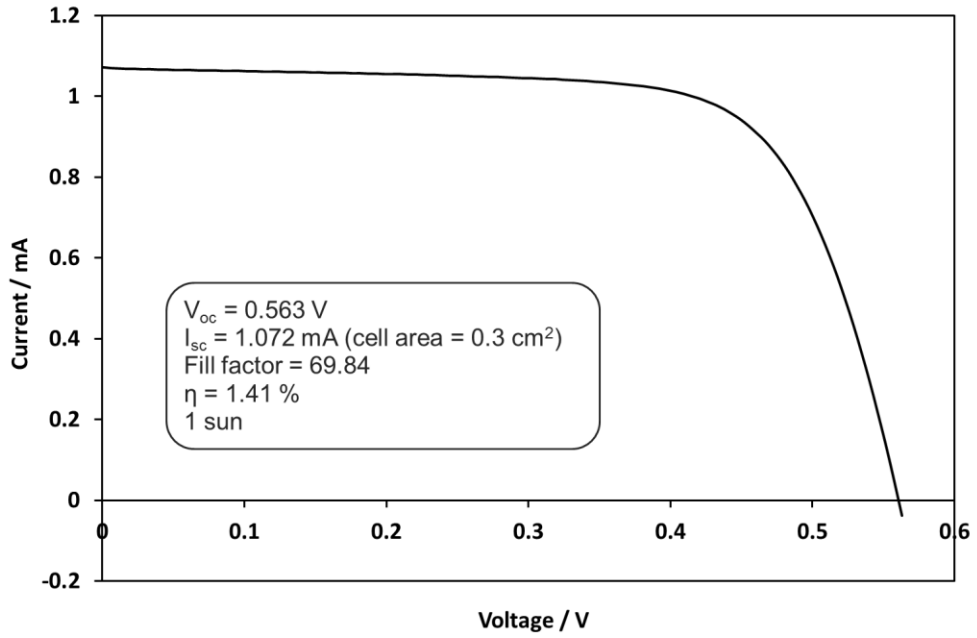

Figure 90 – *I-V* curve for a DSC constructed with complex 42. Electrolyte 6 was used and this measurement was made on day 1. Data for this cell is given in Table 18.

Data acquired from the cells constructed in these optimisation experiments are shown in Table 15 to Table 18. Table 15 and Table 16 compare the same cells on day 0 and day 1 (where day 0 is the day of assembly), and Table 17 and Table 18 are comparing the same batch of cells on day 0 and day 1. The cell area was reduced for some of the cells and in each case 1 cm^2 control cells with complex 42 and N719 were assembled. All cells had a scattering layer and the cells in Table 17 and Table 18 had undergone a $TiCl_4$ treatment post-sintering. The positive effects of applying a $TiCl_4$ treatment and a scattering layer were noted in Chapter 5.9. In this set of experiments the improvements observed from leaving the cell to "rest" overnight after assembly are more consistent. By comparing the results for the cells when they were tested on day 0 (Table 15 and Table 17) to measurements made on the same cells a day later (Table 16 and Table 18) the most obvious area of improvement was the short-circuit photocurrent, which led to higher cell efficiencies being recorded. An increase in J_{SC} of between 3 and 6 % for the cells in Table 15 and Table 16 was observed. More of an improvement in J_{SC} (between 15 and 22 %) was noted in cells which had received the $TiCl_4$ treatment. *I-V* curves for these DSCs (those compared in Table 17 and Table 18 are plotted in Figure 91, where the increase in J_{SC} with time is clear.

Table 15 – Comparing cell parameters for DSCs with a single layer of TiO_2 and a scattering layer (particle size 150-250 nm). Day = 0

TESTING ON DAY 0						
Dye	**Cell area (cm^2)**	**$TiCl_4$?**	**V_{OC} (mV)**	**J_{SC} (mA)**	***FF* (%)**	**η (%)**
N719	1	N	712	11.60	52.2	4.31
42	1	N	579	2.33	62.6	0.84
N719	0.20	N	717	12.14	58.0	5.05
42	0.25	N	571	2.34	73.9	0.99
42	0.25	N	586	2.64	34.9	0.54

Table 16 - Comparing cell parameters for DSCs with a single layer of TiO_2 and a scattering layer (particle size 150-250 nm). Day = 1

TESTING ON DAY 1						
Dye	**Cell area (cm^2)**	**$TiCl_4$?**	**V_{OC} (mV)**	**J_{SC} (mA)**	***FF* (%)**	**η (%)**
N719	1	N	715	11.77	53.3	4.49
42	1	N	580	2.47	60.0	0.86
N719	0.20	N	718	11.41	59.1	4.84
42	0.25	N	583	2.42	75.3	1.06
42	0.25	N	588	2.74	32.4	0.52

Table 17 - Comparing cell parameters for DSCs with a single layer of TiO_2 and a scattering layer (particle size 150-250 nm) with $TiCl_4$ treatment. *I-V* curves shown in Figure 91. Day = 0

TESTING ON DAY 0							
Dye	**Cell ID**	**Cell area (cm^2)**	**$TiCl_4$?**	**V_{OC} (mV)**	**J_{SC} (mA)**	***FF* (%)**	**η (%)**
N719		1	Y	687	7.89	52.1	2.82
42		1	Y	544	1.71	64.3	0.60
N719		0.30	Y	657	9.42	50.5	3.12
42	Cell 1	0.30	Y	552	2.95	71.3	1.16
42	Cell 2	0.25	Y	579	2.88	62.6	1.04
42	Cell 3	0.275	Y	560	3.01	62.9	1.06

Table 18 - Comparing cell parameters for DSCs with a single layer of TiO_2 and a scattering layer (particle size 150-250 nm) with $TiCl_4$ treatment. *I-V* curves shown in Figure 91. Day = 1

TESTING ON DAY 1							
Dye	**Cell ID**	**Cell area (cm^2)**	**$TiCl_4$?**	**V_{OC} (mV)**	**J_{SC} (mA)**	***FF* (%)**	**η (%)**
N719		1	Y	705	6.15	53.8	2.33
42		1	Y	552	2.02	62.1	0.69
N719		0.30	Y	670	9.24	40.9	2.53
42	Cell 1	0.30	Y	563	3.60	69.8	1.41
42	Cell 2	0.25	Y	593	3.30	59.9	1.17
42	Cell 3	0.275	Y	575	3.57	54.6	1.12

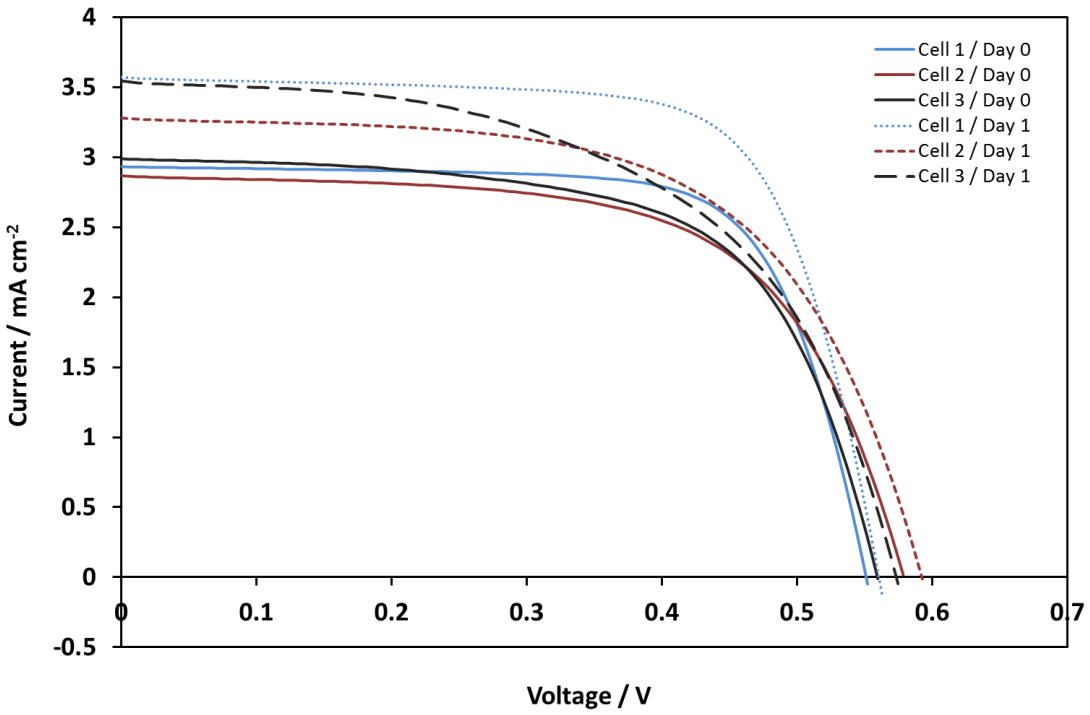

Figure 91 – *I-V* curves recorded at 1 sun on day 0 and day 1 of cells assembled with complex 42. Cell parameters are given in Table 17 and Table 18

This ageing effect of copper(I) DSCs, most noticeable through an increased J_{SC}, is also observed by other groups.[2, 13, 14] The reason for this effect is poorly understood, however the groups suggest reorganization, or aggregation, of dye molecules on the TiO_2 surface may be responsible.[13, 14] The response could also be linked to similar photocurrent increases observed with ruthenium(II) DSCs following light soaking.[15]

The cells with complex **42** from Table 17 and Table 18 were also retested after 6 weeks in the dark and the data is shown in Table 19. Cells 1 and 3 still retained a very respectable performance. Cell 2 had dried out a little which will have contributed to its greater loss of performance. All cells measured an increased V_{OC} of between 10 and 16 mV. There were minimal changes in the fill factors for cells 1 and 3. The main loss over this longer period of time was in the J_{SC}, and could be due to some dye desorption from TiO_2 or a degradation of the dye due to the electrolyte or presence of water over time.[16, 17] However, with good cell sealing, complex **42** appears stable under DSC conditions at least for a matter of weeks.

Table 19 - Comparing cell parameters for DSCs with a single layer of TiO_2 and a scattering layer (particle size 150-250nm) with $TiCl_4$ treatment. Day = 43

TESTING ON DAY 43							
Dye	**Cell ID**	**Cell area (cm^2)**	**$TiCl_4$?**	**V_{oc} (mV)**	**J_{sc} (mA)**	**FF (%)**	**η (%)**
42	Cell 1	0.30	Y	579	2.92	71.6	1.21
42	Cell 2	0.25	Y	603	0.64	55.5	0.21
42	Cell 3	0.275	Y	589	2.76	54.8	0.89

The DSC efficiencies achieved here are very promising and indicate that complex **42** is suited to DSC application. Given that the batch of N719 control cells from Table 17 and Table 18 were of a lower standard than usual for these experiments, it is speculated that even higher efficiencies with complex **42** may be possible.

7.5. IPCE measurements

The IPCE spectrum for a 1 cm^2 DSC with complex **42** (labelled cell 6) is shown in Figure 92 and is compared to that of an N719 cell (labelled N719-1). Both cells were prepared with a double layer of TiO_2 paste (film thickness ~ 14 μm) and there was no scattering layer or $TiCl_4$ treatment used. It can be seen that there is a broad spectral reponse from ~600 nm with complex **42** and the peak visible-region maxima is 17% at 500 nm. Spectra recorded for other DSCs with **42**, including ones with a single TiO_2 layer, showed the same shape and the maximum IPCE was always between 14% and 17%. The maximum IPCE value at around 500 nm is comparable to the response observed in the UV/Vis spectrum. The IPCE of complex **42** is lower than the N719 control cell, which peaks at 62% at 530 nm. All spectra recorded for N719 DSCs exhibited similar IPCE values (typically ~57%) at the same wavelength. IPCE (external quantum efficiency) depends on light absorption, electron injection efficiency and charge collection efficiency. The low external quantum efficiency of **42** is therefore due to one, or a combination of, these factors. Charge collection efficiency can be reduced if there is a high degree of recombination of injected electrons with the oxidised redox mediator. The effective electron lifetime, or electron diffusion length, are measurable indicators of this and will be discussed for these two cells later in this chapter. It is interesting to note that the IPCE spectrum for complex **42** continues to rise into the UV region of the spectrum, whereas the response with N719 decreases steadily after the peak at 530 nm up until around 350 nm when it begins to increase again.

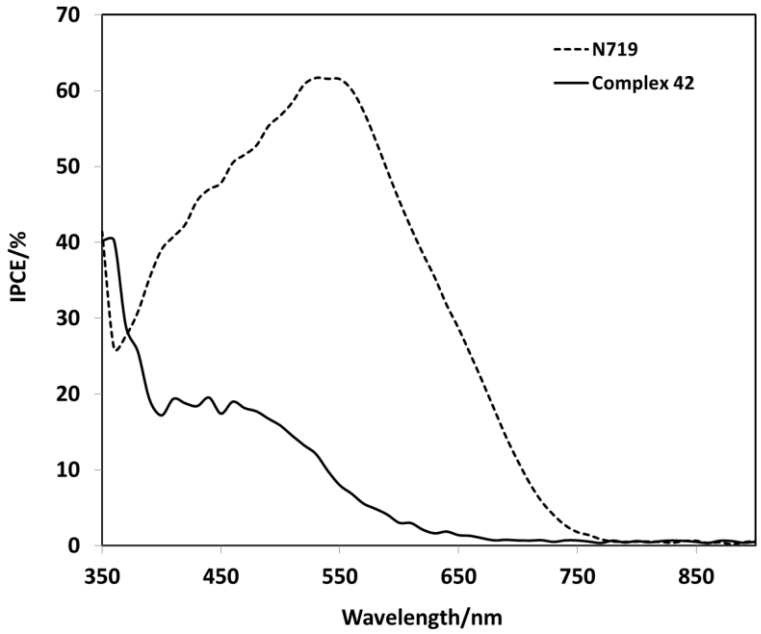

Figure 92 - IPCE spectra for complex 42 (cell ID, "complex 42-6") and N719 (cell ID, "N719-1")

7.6. Cyclic voltammetry of complex 42 and estimation of energy levels

Cyclic voltammetry of complex **42** immobilised on a TiO_2 film was studied and the working electrodes were prepared as described previously (see Chapter 3.5.1 and the graphic in Chapter 2.3). Undyed TiO_2 films were used for background scans, the CE was a platinum wire and the RE was Ag/AgCl (3 M KCl). Experiments were first conducted in a 0.2 M aqueous KNO_3 background electrolyte. CVs were measured at increasing scan rates and finally a 10 scan experiment was carried out at 0.3 V/s to assess dye stability to the redox cycling. From Figure 93 and Figure 94 it can be seen that an oxidation process is visible at slow scan rates ($\leq$ 0.3 V/s), which becomes better defined as the scan rate is increased. At scan rates $\geq$ 0.5 V/s a reduction peak appears which also increases in magnitude with increasing scan rate. At the fastest scan rate recorded, 20 V/s, the cycle is close to reversible. The peak oxidation and reduction potentials separate at increasing scan rates; at 1 V/s they are E_p^{ox} = +0.56 V and E_p^{red} = +0.47 V and at 20 V/s they are E_p^{ox} = +0.65 V and E_p^{red} = +0.40 V. Three TiO_2 films were studied in this way and showed the same behaviour. There is a linear relationship between the peak current and scan rate (Figure 95) which confirms the electrochemical response is due to activity of a surface adsorbed species.

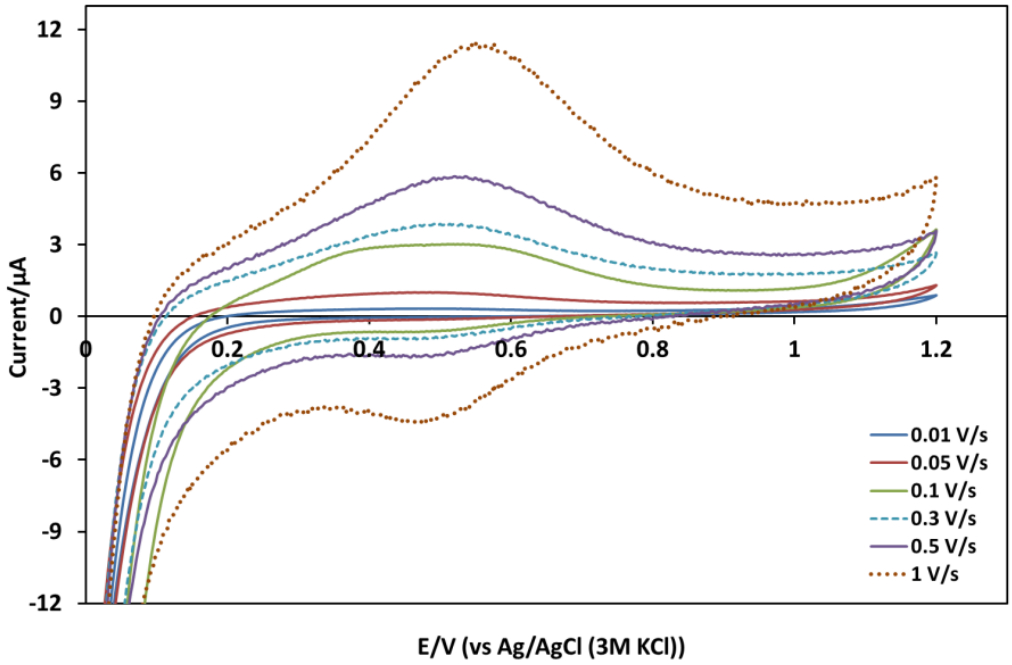

Figure 93 – cyclic voltammogram of a complex 42 dyed TiO_2 film at increasing scan rates (from 0.01-1 V/s). The background electrolyte is 0.2 M aqueous KNO_3.

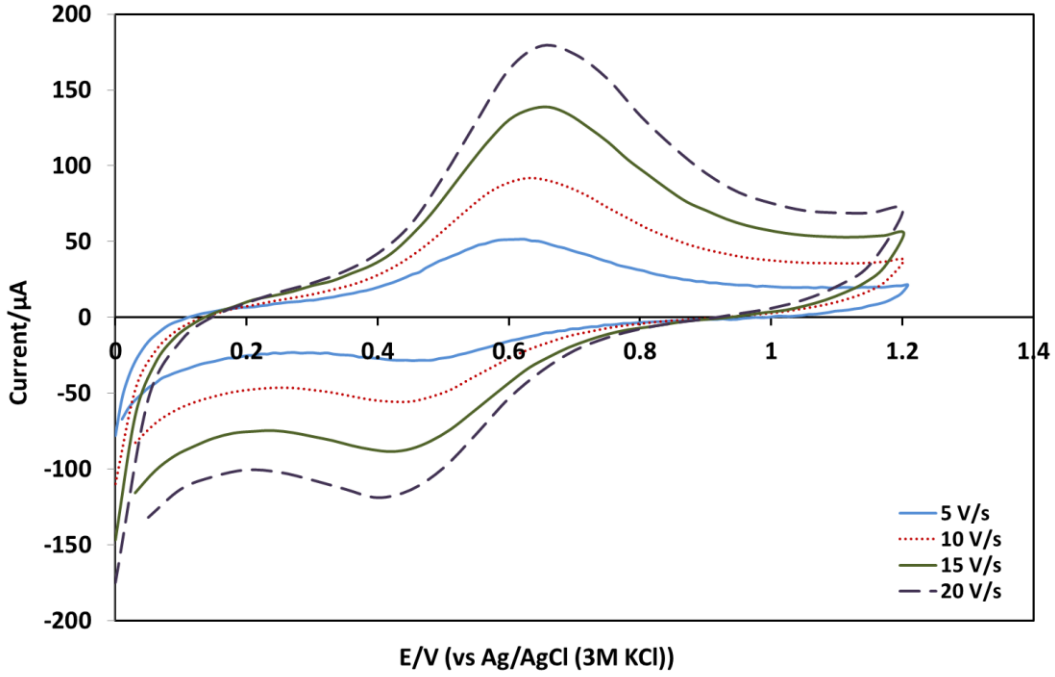

Figure 94 - cyclic voltammogram of a complex 42 dyed TiO_2 film at increasing scan rates (from 5-20 V/s). The background electrolyte is 0.2 M aqueous KNO_3.

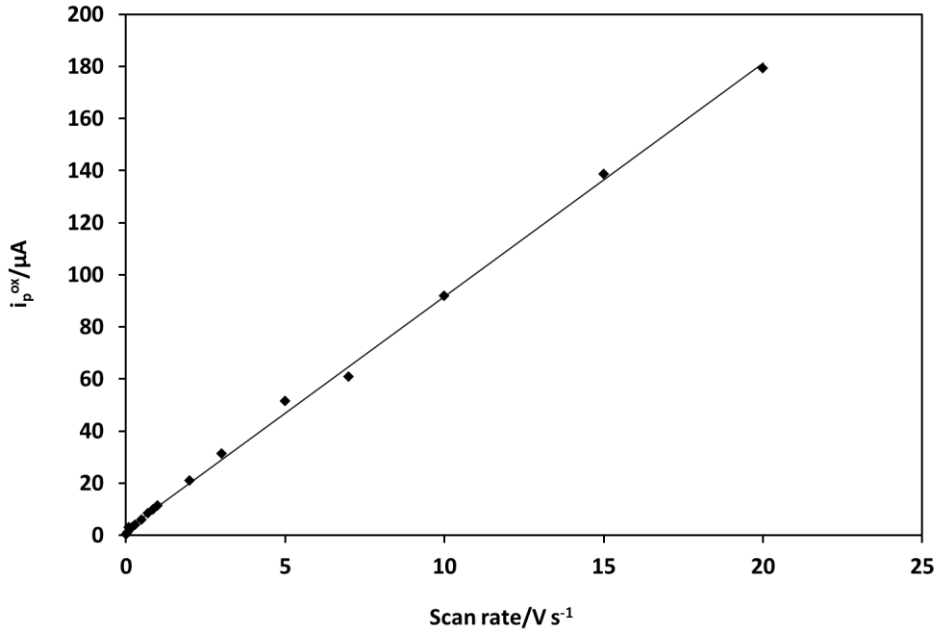

Figure 95 – plot showing the dependence of the peak anodic current on scan rate for complex 42

As discussed in Chapter 2.3, there are certain characteristics which define an electron transfer process as reversible. For example, the position of the peak potentials (E_p) should be independent of scan rate. It can be seen from Figure 93 and Figure 94 that this is not applicable here, where ΔE_p increases with scan rate. Both the appearance (or not) of a reduction peak at different scan rates and the variation in peak potential separation with scan rate can be attributed to the response of a quasi-reversible system. A quasi-reversible system responds more slowly to the applied potential, therefore a larger overpotential is required as the scan rate is increased, i.e. ΔE_p increases. With respect to the dependence of the reduction peak on scan rate, at slower scan rates the oxidised species can be lost by diffusion or *via* a chemical reaction before the overpotential is reached. Therefore a reduction peak will not be observed, or it will be very small.

It is speculated that the lack of ideal reversibility is due to some instability of the complex in its oxidised form. The absence of a reduction peak at slow scan rates suggests that the oxidised species reacts/degrades chemically before it can be electrochemically reduced. During a consecutive 10 scan experiment at a 0.3 V/s scan rate (Figure 96), there is a clear decrease in peak anodic current over time. If the Cu(II) species is not being reduced, then a

drop in anodic current would be expected over multiple scans as the surface concentration of the Cu(I) species decreases.

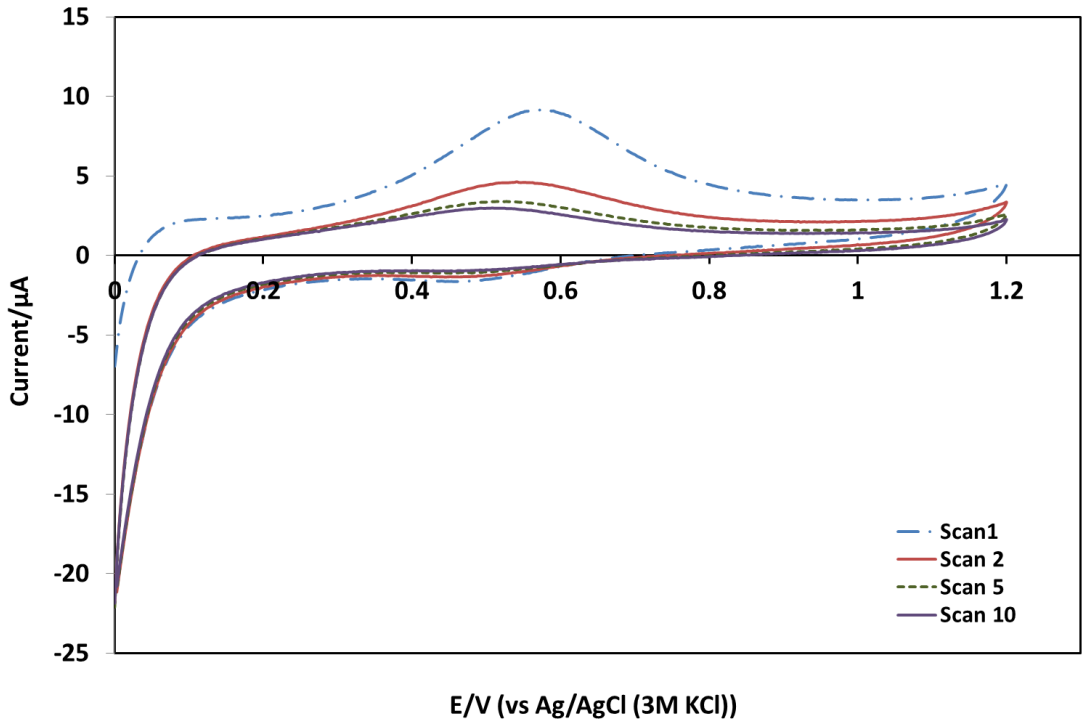

Figure 96 - CV of a complex 42 dyed TiO_2 film, cycled through 10 scans at a rate of 0.3 V/s; scan 1 (--), scan 2 (-), scan 5 (--), scan 10 (-). The background electrolyte is 0.2 M aqueous KNO_3.

It was also noted during these experiments that there was a sharp increase in negative current in the reverse scan, from an onset of +0.1 V, when a dyed film was used as the working electrode. This effect was not observed when a blank TiO_2 film was used and there was not a loss of cathodic current with repeated scanning, as there was for the anodic current (Figure 96). This effect could be caused by reduction of the TiO_2, O_2 or solvent. The photocatalytic activity of TiO_2 has already been documented in terms of water splitting[20] and oxygen reduction, [21] however both of processes require exposure of the system to UV light, or visible light if the TiO_2 surface is sensitized with a dye. For all of these measurements the apparatus was set up in a Faraday cage i.e. in the dark, therefore this is not applicable. However electrochemical reduction of oxygen is known to be catalysed by surface adsorbed copper complexes.[18-20] A report from Dias[18] and colleagues studied reduction of oxygen by a Cu(I)-TPT complex (where TPT = 2,4,6-tris(2-piridil)-1,3,5-

triazine), adsorbed on a graphite electrode. The group proposed the formation of an adduct between an oxygen molecule and the catalytically active Cu(I) complex, which is followed by the transfer of electrons *via* the metal complex to produce the reduction product, water. Therefore to probe the possible role of complex **42** as an electrocatalyst for oxygen reduction, the CV experiments were repeated under degassed conditions using the same background and dyed films. The apparatus (Figure 97) was degassed by bubbling with nitrogen for 15 minutes prior to scanning but all other conditions were kept the same.

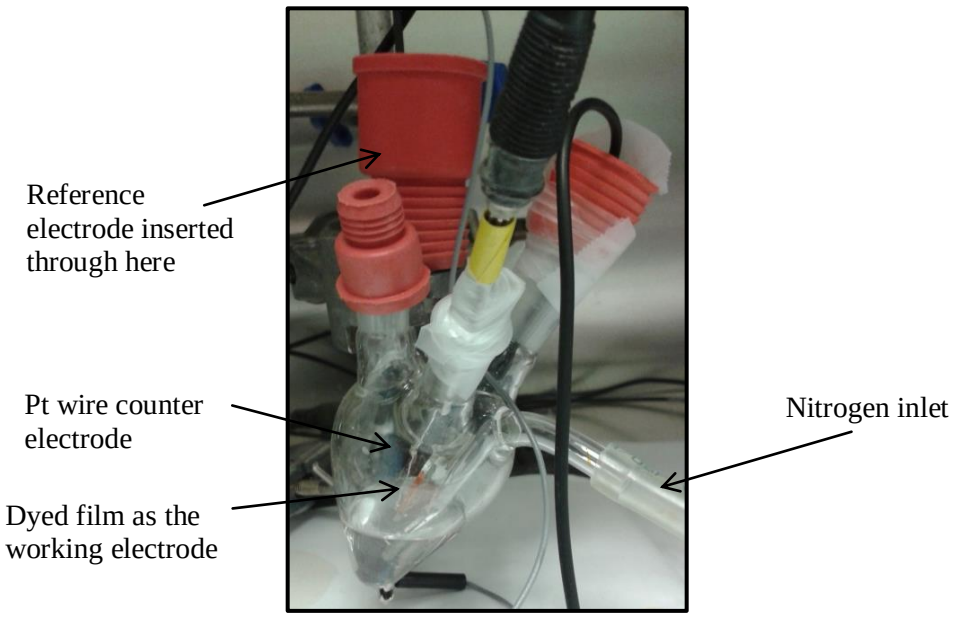

Figure 97 – electrochemical cell setup for degassed CV measurements. Clear plastic tubing on the right hand side shows nitrogen flow inlet.

As Figure 98 shows, there was a decrease in the magnitude of the cathodic current when a dyed film was used as the WE in a degassed system. It was also noted that there was a slight positive shift (~80 mV) in the peak anodic potential when oxygen had been removed. Presumably the ground state of the dye is more stabilised on the TiO_2 film in the absence of oxygen. This experiment implies that there is some interaction between complex **42** and oxygen.

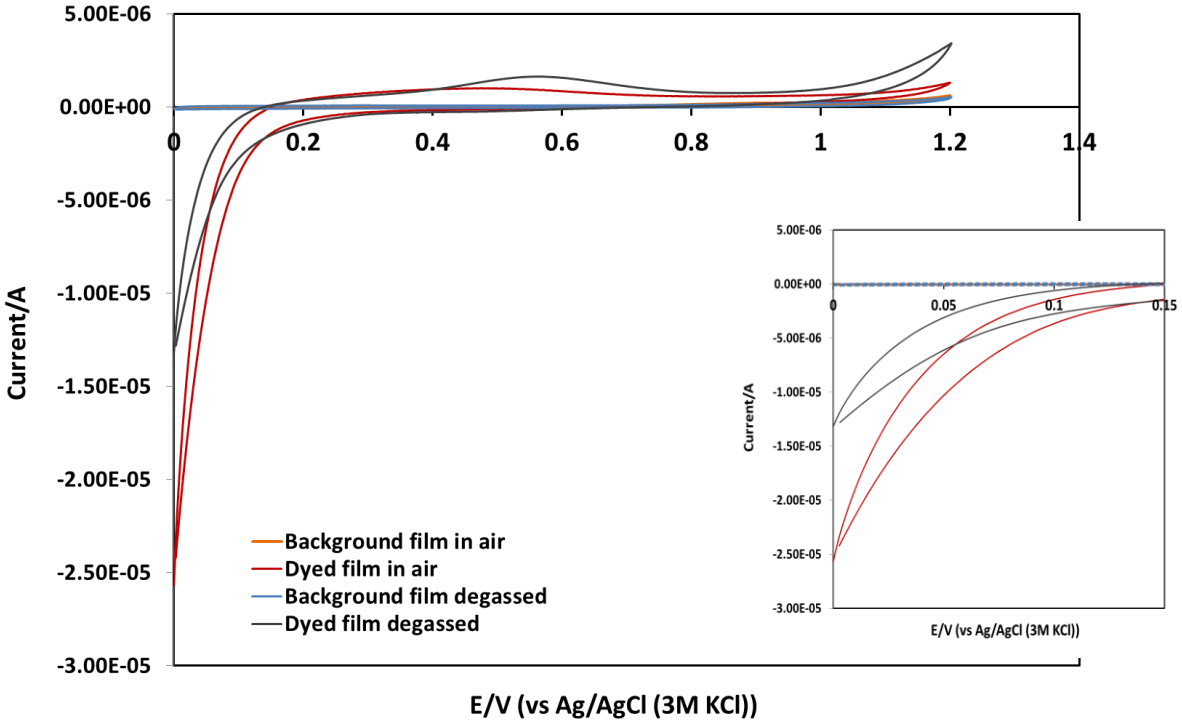

Figure 98 – CVs comparing blank and dyed TiO_2 films as the WEs in a degassed experiment and in air. All scans were recorded at 50 mV/s and the background electrolyte is 0.2 M aqueous KNO_3. Inset shows a zoomed-in image of the cathodic current

The same experiments were repeated in a non-aqueous environment (MeCN); firstly, to study whether the same response was measured and, secondly, as a better representation of the DSC environment. Cyclic voltammetry was repeated using the same dyed films in a background electrolyte of 0.1 M TBAHFP in MeCN. The experiments were conducted in air and also in degassed solutions. A disadvantage of using MeCN with a Ag/AgCl reference electrode is that Ag/AgCl is an aqueous electrode, therefore a higher solution resistance in the experiment is experienced due to a higher junction potential.

In MeCN the same quasi-reversible form of the CVs was observed (Figure 99 and Figure 100), with an oxidation peak visible at slow scan rates and a reduction peak which appeared only at faster scan rates. The peaks are more widely separated than in the aqueous solution and the separation increases with scan rate, with E_p^{ox} = +0.79 V and E_p^{red} = +0.38 at 1 V/s and E_p^{ox} = +0.90 V and E_p^{red} = +0.24 at 15 V/s. This trend is again attributed to the effect of solution resistance, especially given the higher junction potential in this case. It can be seen that there are no sharp cathodic currents recorded with dyed films in these scans.

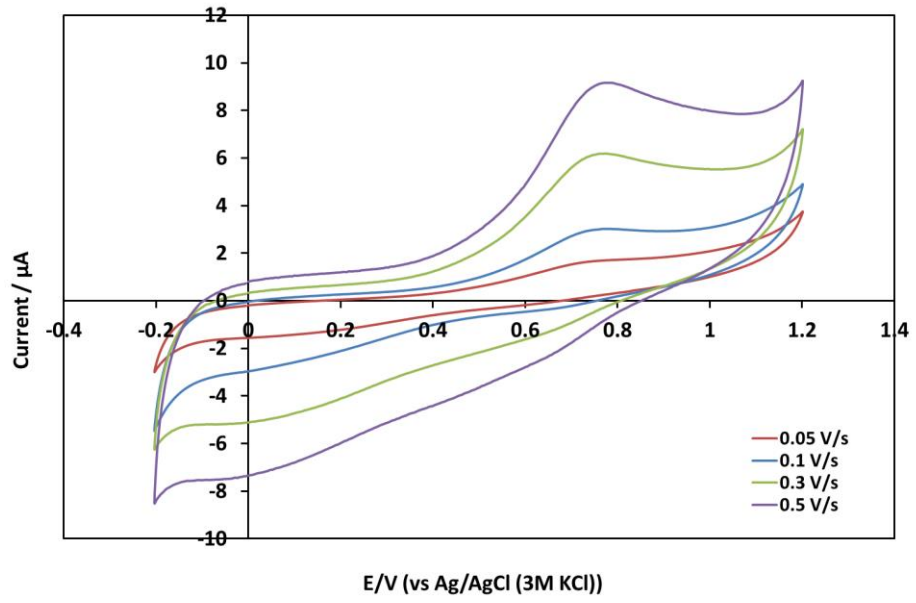

Figure 99 – CV (in air) of a complex 42 dyed TiO_2 film at increasing scan rates, from 0.05-0.5 V/s (measurements made on the same film as used in Figure 93 and Figure 94)

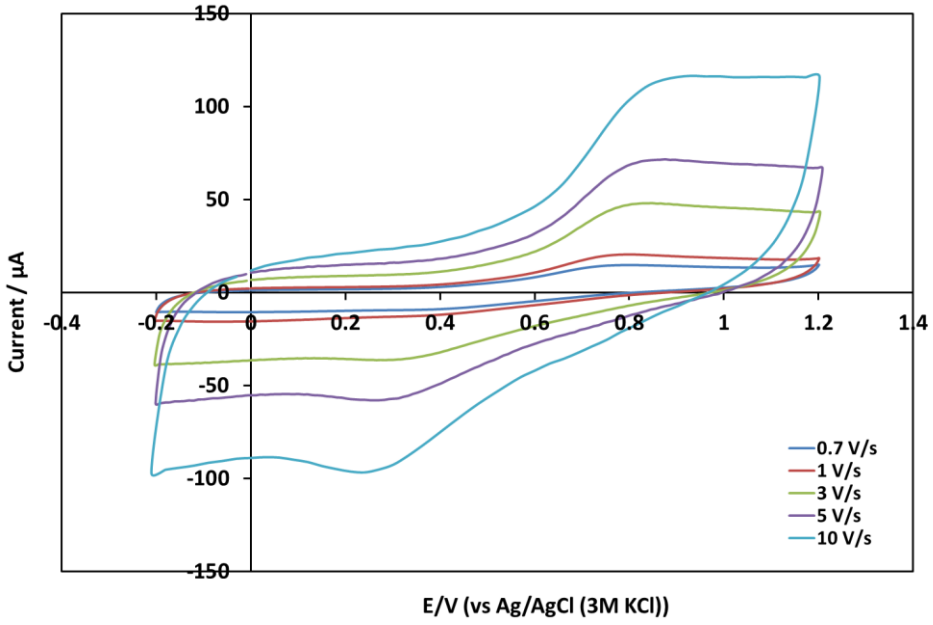

Figure 100 – CV (in air) of a complex 42 dyed TiO_2 film at increasing scan rates, from 0.7-10 V/s (measurements made on the same film as used in Figure 93 and Figure 94)

The experiment was repeated following degassing for 15 minutes with nitrogen. The only change was a slightly positive shift (~90 mV) in the anodic peak potential again, as observed under aqueous conditions. If electrochemical oxygen reduction is occurring in the case of the aqueous system, then it is speculated that the same cathodic current is not

observed under MeCN conditions due to the lack of protons available to form water. A 10 scan experiment of a dyed film at 0.3 V/s under MeCN conditions (Figure 101) found no drop in current over repeated cycling, implying that **42** is more stable on the TiO_2 surface in an MeCN environment.

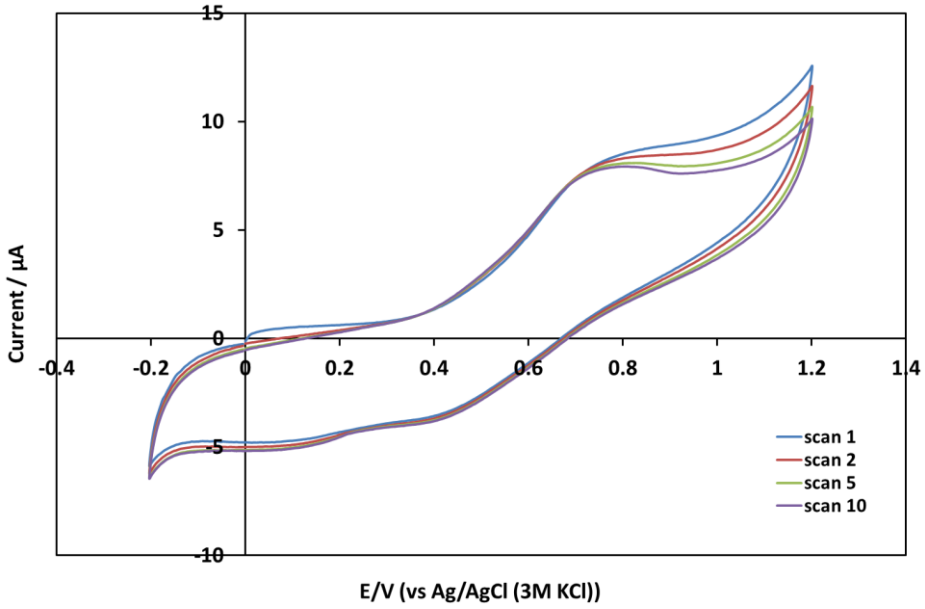

Figure 101 – CV of a complex 42 dyed TiO_2 film in MeCN background electrolyte, cycled through 10 scans at a rate of 0.3 V/s

As described in Chapter 5.6, the HOMO for the complex can be calculated from the CV data. The $E_{1/2}$ value was almost the same from the two sets of experiments. In 0.2 M KNO_3, $E_{1/2}$ (which should be independent of scan rate) was +0.53 V. This potential was confirmed by calculating $E_{1/2}$ for the most reversible scan rates (7, 10, 15 and 20 V/s) and the values were consistent (0.530 V is the average with values in the range of 0.526 V to 0.541 V). In MeCN, $E_{1/2}$ was calculated to be 0.57 V and this was consistent over the range of scan rates. Using the value from the MeCN experiments, the HOMO energy level of the dye can be estimated as: HOMO = $[(-4.5) - (0.210 + E_{1/2})] = -5.28$ eV.

Using the absorption onset of 640 nm from the UV/Vis spectrum (Figure 82) the resulting band gap and LUMO energy are calculated as 1.94 eV and -3.33 eV respectively. Referring to the emission data in Figure 85, $E^{0\text{-}0}$ is at 530 nm which results in an excited state energy of -2.94 eV after addition to $E_{1/2}$. Both of these values are adequate for injection into the

TiO_2 conduction band.[6] The computed LUMO is -2.74 eV, which correlates well with the excited state energy and is higher in energy than the experimental LUMO. The computed HOMO is in fairly good agreement with the experimental data, although is a little lower in energy.

7.7. Studying DSCs with complex 42 by EIS

Assembled DSCs were studied by electrochemical impedance spectroscopy (EIS). As discussed in Chapter 2.4, EIS can be used to calculate the electron diffusion length, L_n, and the effective electron lifetime, τ_n. The electron diffusion length (equation 18, Chapter 2.4) is the average distance an electron diffuses through the TiO_2 film before it is lost in a recombination reaction and the effective electron lifetime (equation 19, Chapter 2.4) is the average time an electron will remain free before it undergoes a recombination reaction. EIS was initially used on N719 DSCs, as a system whose EIS behaviour is well-established. Cell number N719-1 corresponds to the same cell whose IPCE response is shown in Figure 92. Impedance measurements under two different light intensities (photon fluxes of 2.66×10^{15} and 3.64×10^{15} s^{-1} cm^{-2}) were recorded at open-circuit potential and data was interpreted using the Z-View software. The equivalent circuit used was developed by Bisquert[21] and is shown in Figure 102. Typically a Warburg element would also be included in series with R1 however, since no Warburg impedance was observed in the experimental data, it was removed from the model.

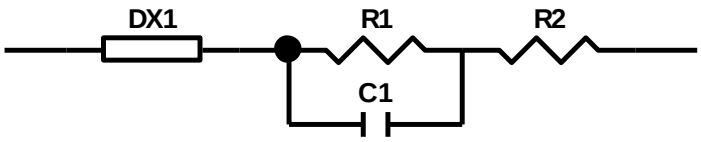

Figure 102 – the equivalent circuit model used for studying DSCs with N719 (slightly modified *DX type 11-Bisquert #2)*

R2 is the series resistance, R1 is the charge transfer resistance associated with electron transfer at the cathode, C1 is the double layer capacitance at the cathode and the built-in extended element (DX type 11-Bisquert #2) represents the electron processes in the TiO_2 film.

An EIS spectrum for cell N719-1 is shown in Figure 103. From fitting to the equivalent circuit in Figure 102, values for the recombination resistance between electrons in the TiO_2 film and ions in the electrolyte, r_{rec}; the transport resistance for electrons in the TiO_2 film, r_{tr}; and the chemical capacitance, c_μ; were acquired. In addition, values for the series resistance and for electron transfer processes at the counter electrode were obtained (see Table 20).

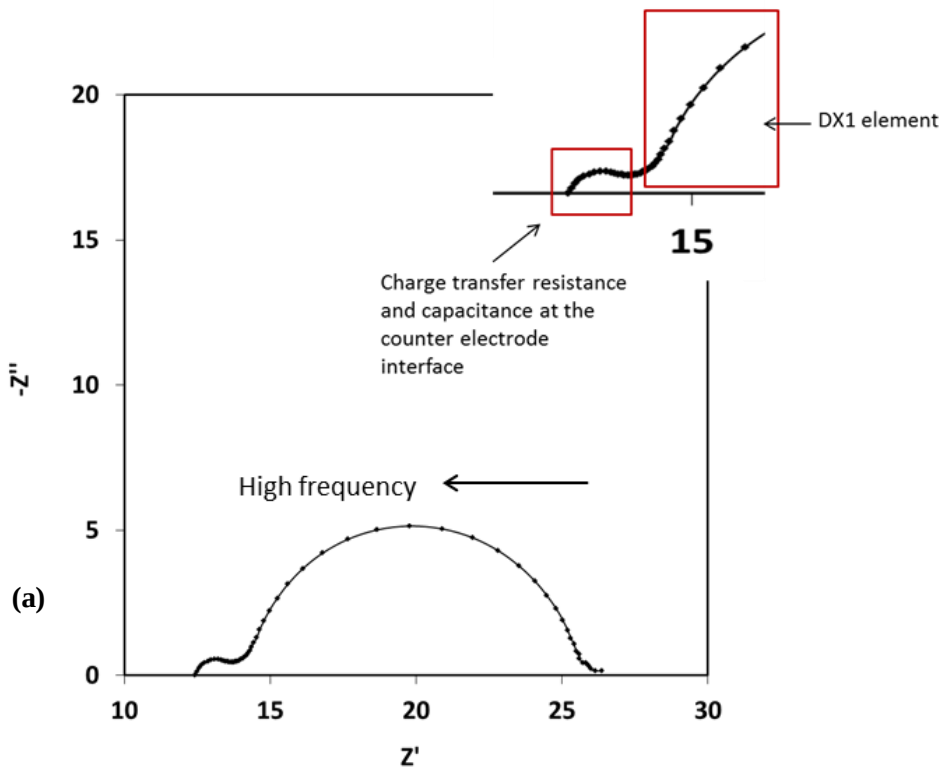

Figure 103 – (a) EIS spectrum for N719-1 at a photon flux of 3.64×10^{15} s^{-1} cm^{-2}, modelled using the equivalent circuit shown in Figure 102. (The DX1 element encompasses the whole larger semi-circle) (b) A zoomed in view of the high frequency data.

The small semi-circle at high frequency (inset Figure 103) corresponds to processes at the counter electrode interface, R1 and C1. The DX1 element, visible as a straight line extending ~45° away from the x-axis and as the larger semicircle, relates to the transport resistance of electrons in the TiO_2. The lower frequency semi-circle provides the r_{rec} and c_μ in the TiO_2 film. For an efficient DSC it is necessary that $r_{rec}>r_{tr}$. Using these values the electron diffusion length and effective electron lifetime were calculated (Table 20). It can be seen that L_n/L is between 2 and 2.5, which satisfies the requirement for the electron diffusion length to be greater than the TiO_2 film thickness, L.

Table 20 – parameters obtained from modelling the impedance response of two N719 DSCs at two light intensities

Cell number	Photon flux (s^{-1} cm^{-2})	Film thickness	V_{OC}	R2 (Ω)	R1 (Ω)	C1 (μF)
N719 - 1	2.66×10^{15}	13.2 μm	0.680	12.56	0.995	13.58
	3.64×10^{15}	13.2 μm	0.682	12.47	0.905	14.38
N719 - 2	2.66×10^{15}	6.5 μm	0.704	15.43	3.493	15.37
	3.64×10^{15}	6.5 μm	0.712	15.34	3.482	15.34

Cell number	Photon flux (s^{-1} cm^{-2})	r_{tr} (Ω)	r_{rec} (Ω)	c_{μ} (mF)	L_n (μm)	τ_n (ms)
N719 - 1	2.66×10^{15}	3.48	15.38	1.58	27.7	24.3
	3.64×10^{15}	2.71	11.51	1.90	27.2	21.9
N719 - 2	2.66×10^{15}	2.98	18.65	1.39	16.3	25.9
	3.64×10^{15}	2.61	14.27	1.74	15.2	24.8

There is little variation in L_n with change in light intensity, which concurs with discussion in the literature.[22] It has been found that $L_n = (D_n\tau_n)^{½}$, where D_n is the effective electron diffusion coefficient, and it has been established that D_n and τ_n exhibit an opposite response to an increase in light intensity (D_n tends to increase with light intensity whereas τ_n tends to decrease). This renders L_n more or less constant. In this case the effective electron lifetimes for the two cells are similar and range between 22 and 26 ms, with both cells having shorter lifetimes at the higher light intensity. Typically τ_n is between 1 ms and 1 s, depending on the light intensity.[23] It can be seen in Table 20 that both r_{tr} and r_{rec} also decrease as the light intensity is increased.

These factors can all be understood by considering the effects of the higher light intensity on the electron density in the TiO_2 film. At higher light intensities the cell V_{OC} is larger, E_f is higher and there are more electrons in the TiO_2 film. The trap states become filled therefore the free electron density is higher. Consequently electron transport is faster.

The higher concentration of conduction band electrons also leads to higher rates of recombination, which can be understood from the quasi-static approximation (Equations 22 and 23); where τ_n is the effective electron lifetime, τ_0 is $1/k_{br}[I_3^-]$ (where k_{br} is the rate constant for the back reaction of electrons), n_c is the free/conduction band electron density

and n_t is the density of trapped electrons. The $\delta n_t/\delta n_c$ term shows how the trapped and free electron densities vary with the position of E_f. The effective electron lifetime decreases as the light intensity is increased, since n_c varies more rapidly than $g({}_nE_F)$. This causes a decrease in the $\delta n_t/\delta n_c$ term, which leads to a corresponding decrease in effective electron lifetime according to Equation 22. Therefore the rate of recombination is increased at higher light intensities. In the same way, the chemical capacitance increases with light intensity due to the increased amount of electronic charge being stored in the TiO_2 film.

$$\tau_n = \left(1 + \frac{\partial n_t}{\partial n_c}\right)\tau_0$$

Equation 22

$$\frac{\partial n_t}{\partial n_c} = g({}_nE_F)\frac{k_B T}{n_c}$$

Equation 23

Measurements were then made for DSCs containing complex **42**. Data for two cells (including cell "complex **42**-6", whose IPCE response is shown in Figure 92) is presented in Table 21. The impedance response and fitting for cell 5 at a photon flux of 3.64×10^{15} $s^{-1}cm^{-2}$ is shown in Figure 104. DSCs with complex **42** exhibited slightly different impedance responses than observed with N719. Fitting of the data was initially tried with the DX type 11-Bisquert #2 model. However since the counter electrode impedance was not clearly visible, the R1 and C1 elements were removed, resulting in an equivalent circuit model modified as shown in Figure 104(b).

It is noted that comparisons between the N719 and complex **42** EIS measurements can only be made for the electron diffusion length. Due to the variation in V_{OC} of the cells with the two dyes, there will be a different amount of charge present in the TiO_2 films. For DSCs with complex **42**, the V_{OC} is lower relative to DSCs with N719 measured at the same light intensity. This means there is less charge in the TiO_2 films of the copper(I) cells, therefore r_{tr} will be higher. However L_n should be fairly constant at different light intensities therefore comparisons of this parameter can be made. As observed with the N719 DSCs, r_{rec} and r_{tr}

decrease, and c_μ increases, with an increase in light intensity. The transport resistance values are larger for the copper(I) cells than for the N719 cells, which may be due to the lower photovoltages. A low free electron density in the semiconductor film increases the transport resistance since there is more likelihood of the electrons being retained in multiple trapping/de-trapping processes. The electron diffusion lengths are adequate relative to the TiO_2 film thickness; however it can be seen that they are shorter than calculated for the N719 DSCs. This is probably a contributing factor to the lower efficiencies and IPCE obtained for DSCs with complex **42**.

Table 21 - parameters obtained from modelling the impedance response of complex 42 DSCs

Cell number	Photon flux (s^{-1} cm^{-2})	Film thickness	V_{oc}	R2 (Ω)	r_{tr} (Ω)	r_{rec} (Ω)	c_μ (mF)	L_n (μm)	τ_n (ms)
Complex **42**-5	2.66×10^{15}	15.4 μm	0.526	7.87	38.5	70.0	0.11	20.8	7.70
	3.64×10^{15}	15.4 μm	0.537	9.83	34.1	49.0	0.13	18.1	6.11
Complex **42**-6	2.66×10^{15}	15.4 μm	0.527	8.77	20.6	69.4	0.13	28.2	9.03
	3.64×10^{15}	15.4 μm	0.537	9.34	19.0	51.0	0.16	25.2	8.11

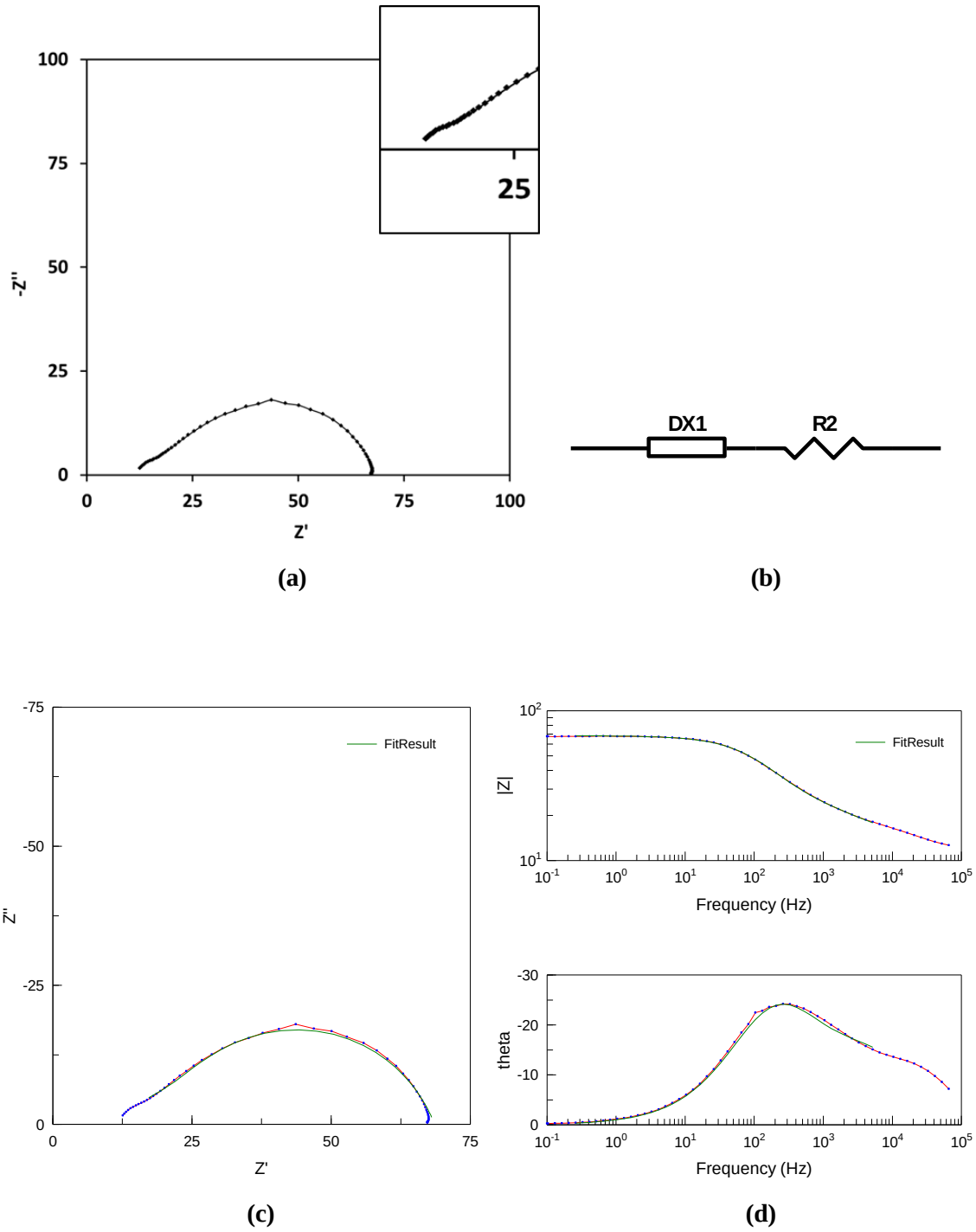

Figure 104 – (a) EIS spectrum of cell "Complex 42-5" at a photon flux of 3.64×10^{15} s^{-1} cm^{-2}; (b) the equivalent circuit model used for cells "Complex 42-5" and "Complex 42-6"; (c) Nyquist plot with fitting (d) Bode plot with fitting

7.8. Conclusions

The novel complex [Cu(6,6'-dimethyl-5,5'-[2,2'-bipyridin-4,4'-diyl]-bis[thiophene-2-carboxylic acid])$_2$][PF_6] has been studied and assessed for viability in a DSC.

The complex exhibited two absorbance bands in the electronic absorption spectrum at 316 nm and 506 nm, with ε values of 50,000 M^{-1} cm^{-1} and 9030 M^{-1} cm^{-1} respectively. The presence of the thiophene rings resulted in an improved molar extinction coefficient and maximum absorbance relative to the unfunctionalised copper(I) bipyridine complex, **1**, which has ε = 6800 $M^{-1}cm^{-1}$ at $\lambda_{(max)}$ 491 nm. The dye was strongly emissive in both CH_2Cl_2 and MeOH, following excitation at 320 nm. Weak fluorescence was observed in MeOH following excitation at 510 nm, which was assigned to emission from the MLCT state and correlates with the UV/Vis data for this transition. The E^{0-0} energy obtained from these data was used in conjunction with electrochemical measurements to calculate an excited state energy of -2.94 eV, which indicates enough driving force for electron injection into the TiO_2 conduction band.

Solar-to-power-conversion efficiencies were highly promising with this complex. In smaller DSCs (cell areas between 0.25 cm^2 and 0.3 cm^2) average efficiencies of ~1% were obtained, with a peak efficiency of 1.41 % recorded. The two electrolyte compositions used, which differed in the volatility of their components, did not particularly affect the DSC performance. However cells with thinner TiO_2 films (6-7 μm) displayed a modest improvement in short-circuit current, open-circuit photovoltage and overall solar-to-electrical power conversion efficiency compared to those assembled from thicker TiO_2 films (14-15 μm). Generally, thicker TiO_2 films are beneficial as they enable more dye uptake and hence greater light harvesting. However there is always a balance between this advantage and a possible increase in recombination losses of the electrons which would lead to a decrease in charge collection efficiency. A "ripening" effect in the cells was noted when comparing *I-V* measurements from the day of construction to measurements made the following day. The largest improvement was noted in the short-circuit photocurrent. This trait has been observed in other copper(I) DSC research and is generally attributed to a favourable reorganisation of the dye on the surface.

Cyclic voltammetry using dyed TiO_2 films as the working electrodes was carried out. The dye underwent redox cycling, attributed to the Cu(I)/Cu(II) transitions, in both aqueous and MeCN background electrolyte solutions. An oxidation reaction was always observed, however the reduction was found to be scan rate dependent. The system was reversible at

very fast scan rates (>10 V/s) but at scan rates <0.1 V/s there was no reduction process measured. There was a larger peak potential separation in the MeCN experiment and in both solvents the peak separation increased with scan rate. This was attributed to increased solution resistance. Electron transfer limitations were discounted due to the fact that the reversibility of the system was better at faster scan rates. Consecutive 10-scan experiments implied that dye stability was better in the MeCN environment than in aqueous solution. The measured $E_{1/2}$ for the dye was very similar in the two background electrolytes. From the MeCN experiments the value of $E_{1/2}$ was +0.57 V and this was used to obtain an estimation of the HOMO energy level; -5.28 eV. The LUMO was calculated, using this value and an absorption onset of 640 nm, to be -3.33 eV.

DSCs with complex **42** were studied using EIS and compared to the response of N719 DSCs. For N719 cells, L_n/L was between 2 and 2.5, resulting in adequate electron diffusion lengths, and electron lifetimes between 22 and 26 ms. The fitting of an equivalent circuit to these cells was straightforward and used a slightly modified version of the DX type 11-Bisquert #2 model. Fitting of data from DSCs with complex **42** was a bit more difficult due to the lack of resolution between the high and low frequency responses and the DX-1 element. However DSCs were studied and modelled with an equivalent circuit lacking the RC counter electrode element to obtain reasonable values. The EIS data estimated fairly short effective electron lifetimes (between 6 and 9 ms). The electron diffusion lengths were greater than the TiO_2 film thickness, as required, although shorter than those calculated for the N719 cells. This may be a contributing factor to the low IPCE observed, which was only 17% in the key visible region wavelength range, and to the lower solar conversion efficiencies compared to N719.

However it can be concluded that the required electron kinetic processes (injection, collection efficiency and dye regeneration) are taking place reasonably effectively, as evidenced by the solar-to-power-conversion efficiencies recorded. Very respectable DSC performances for a copper(I) dye have been reported, with a top efficiency of 1.4%.

7.9. References

1. B. Bozic-Weber, E. C. Constable, C. E. Housecroft, P. Kopecky, M. Neuburger and J. A. Zampese, *Dalton Trans.*, 2011, **40**, 12584-12594.
2. B. Bozic-Weber, S. Y. Brauchli, E. C. Constable, S. O. Furer, C. E. Housecroft, F. J. Malzner, I. A. Wright and J. A. Zampese, *Dalton Trans.*, 2013, **42**, 12293-12308.
3. S. M. Scott, K. C. Gordon and A. K. Burrell, *Inorg. Chem.*, 1996, **35**, 2452-2457.
4. B. Bozic-Weber, V. Chaurin, E. C. Constable, C. E. Housecroft, M. Meuwly, M. Neuburger, J. A. Rudd, E. Schoenhofer and L. Siegfried, *Dalton Trans.*, 2012, **41**, 14157-14169.
5. T. E. Hewat, L. J. Yellowlees and N. Robertson, *Dalton Trans.*, 2014, **43**, 4127-4136.
6. G. Boschloo and A. Hagfeldt, *Accounts Chem. Res.*, 2009, **42**, 1819-1826.
7. M. Grätzel, *Accounts Chem. Res.*, 2009, **42**, 1788-1798.
8. A. Mishra, N. Pootrakulchote, M. K. R. Fischer, C. Klein, M. K. Nazeeruddin, S. M. Zakeeruddin, P. Bauerle and M. Grätzel, *Chem. Commun.*, 2009, 7146-7148.
9. S. W. Wang, K. L. Wu, E. Ghadiri, M. G. Lobello, S. T. Ho, Y. Chi, J. E. Moser, F. De Angelis, M. Gratzel and M. K. Nazeeruddin, *Chemical Science*, 2013, **4**, 2423-2433.
10. A. Fischer, H. Pettersson, A. Hagfeldt, G. Boschloo, L. Kloo and M. Gorlov, *Sol. Energ. Mat. Sol. Cells*, 2007, **91**, 1062-1065.
11. M. Gorlov and L. Kloo, *Dalton Trans.*, 2008, 2655-2666.
12. S. Ito, S. M. Zakeeruddin, R. Humphry-Baker, P. Liska, R. Charvet, P. Comte, M. K. Nazeeruddin, P. Pechy, M. Takata, H. Miura, S. Uchida and M. Gratzel, *Adv. Mater.*, 2006, **18**, 1202-1205.
13. B. Bozic-Weber, S. Y. Brauchli, E. C. Constable, S. O. Fuerer, C. E. Housecroft and I. A. Wright, *Phys. Chem. Chem. Phys.*, 2013, **15**, 4500-4504.
14. M. Sandroni, M. Kayanuma, A. Planchat, N. Szuwarski, E. Blart, Y. Pellegrin, C. Daniel, M. Boujtita and F. Odobel, *Dalton Trans.*, 2013, **42**, 10818-10827.
15. A. Listorti, C. Creager, P. Sommeling, J. Kroon, E. Palomares, A. Fornelli, B. Breen, P. R. F. Barnes, J. R. Durrant, C. Law and B. O'Regan, *Energ. Environ. Sci.*, 2011, **4**, 3494-3501.
16. N. Heo, Y. Jun and J. H. Park, *Sci. Rep.*, 2013, **3**, 1712.
17. B. Macht, M. Turrion, A. Barkschat, P. Salvador, K. Ellmer and H. Tributsch, *Sol. Energ. Mat. Sol. Cells*, 2002, **73**, 163-173.
18. V. L. N. Dias, E. N. Fernandes, L. M. S. da Silva, E. P. Marques, J. J. Zhang and A. L. B. Marques, *J. Power Sources*, 2005, **142**, 10-17.
19. C. X. Cai, K. H. Xue, X. Y. Xu and Q. H. Luo, *J. Appl. Electrochem.*, 1997, **27**, 793-798.
20. A. L. B. Marques, J. Zhang, A. B. P. Lever and W. J. Pietro, *J. Electroanal. Chem.*, 1995, **392**, 43-53.
21. J. Bisquert and F. Fabregat-Santiago, *Dye-Sensitized Solar Cells*, EPFL Press, 2010, Chapter 12, p. 457.
22. L. M. Peter and K. G. U. Wijayantha, *Electrochim. Acta*, 2000, **45**, 4543-4551.
23. B. E. Hardin, H. J. Snaith and M. D. McGehee, *Nat. Photonics*, 2012, **6**, 162-169.

Chapter 8 – Conclusions and outlook

8. Conclusions and outlook

This thesis has been a highly multidisciplinary study of copper(I) dyes for application in dye-sensitized solar cells (DSCs). A number of new ligands and copper(I) complexes have been synthesised and studied. Analysis has focussed not only on their structural characterisation as new molecules, but has also probed their electrochemical, photochemical and photophysical properties with respect to suitability for DSCs.

Work began by reproducing one of the initially reported copper(I) dyes by Constable; [Cu(6,6'-dimethyl-2,2'-bipyridine-4,4'-dicarboxylic acid)$_2$][Cl], complex **1**. The aim of this work was to gain a greater understanding of the dye as a "model complex" and as a starting point for novel dye synthesis. The copper(I) complex had been structurally characterised in detail in the literature but there was no analysis of its electrochemistry or stability in a DSC reported. Therefore our work sought to address these areas of characterisation. The DSC efficiencies obtained during this thesis were comparable to, or higher than, those reported by the authors. It was found that the V_{OC} and cell efficiency decreased for DSCs assembled with TiO_2 films that had been dyed overnight, relative to those dyed for up to 5 hours. Aggregation on the surface was implied by the UV/Vis measurements however dye degradation may also be an issue. There were two redox processes identified by cyclic voltammetry and an ECE mechanism was speculated. Following oxidation, copper(II) complexes are susceptible to solvent attack in the axial positions due to a flattening of the structure from tetrahedral to square planar. This type of reaction/degradation process may occur if the complex and its ligands are too flexible. The effects of aggregation and dye solvation could be better studied by recording UV/Vis measurements for the dye in a range of different solvents (solubility permitting) as well as on the TiO_2 film. This would help to assess what effects are due to aggregation of dye on the surface and what is due to solvatochromatic effects in the dye solution. In terms of dye stability, it would be useful to revisit the effect of oxygen on the complex. A starting point for this would be repeating the electrochemistry under degassed conditions to probe whether the second reduction peak was still present.

From this work it was also highlighted that a broader light absorption profile would be an appropriate improvement to the 2,2'-bipyridine structure. Therefore work moved onto studying a more conjugated 2,2'-biquinoline copper(I) complex (**20**), which offered better light absorption at longer wavelengths as well as being sterically bulky. The tetrahedral geometry conferred by the ligand to the copper(I) centre was confirmed through X-ray

crystallography, which also revealed the anionic form of the [Cu(2,2'-biquinoline-4,4'-dicarboxylic acid)$_2$]$^-$ fragment, being charge balanced by a triethylamine cation. The similar effect of increased dye time linking to decreased cell efficiencies and photovoltages was also noted here.

A detailed assessment of the copper(I) 2,2'-biquinoline-4,4'-dicarboxylic acid dye was made, including electron lifetime calculations from open-circuit photovoltage decay and both experimental and computed energy level estimations. Low solar cell efficiencies mean that complex **20** is not well-suited to DSC application; however the reasons for poor cell performance were explored in this thesis. The two main rationales are limited electron injection and limited dye regeneration. Evidence for and against both justifications were acquired in the course of this work. Both the experimental and computational calculations indicated that the energetic position of the LUMO/first excited state was appropriate for electron injection into the TiO_2 conduction band. In support of this, electron injection from a copper(I) 2,2'-biquinoline complex into the TiO_2 conduction band was studied by Meyer, who found that electron injection was occurring as required. However the low photocurrents and cell efficiencies obtained in our measurements suggested that this was not the case. Meyer's group additionally report that ligands with low lying π^* orbitals could trap electrons after injection, hence limiting charge collection efficiency, which may be the issue here rather than electron injection. In terms of dye regeneration, it is acknowledged that the thermodynamic driving force for regeneration of **20** calculated from our electrochemical measurements is on the low side for ensuring rapid dye ground state regeneration. However it was also observed that regeneration of the dye's ground state with LiI in a cyclic voltammetry experiment took place effectively. Therefore it is possible that both electron injection/collection and dye regeneration are contributing factors to the low cell efficiencies.

Work towards a ligand improvement strategy for 2,2'-biquinoline was introduced in Chapter 5, which involves the installation of electron donating groups to raise the energetic position of the LUMO. This would serve to improve electron injection if energy level matching was a problem. Although a (bis)chloro-functionalised 2,2'-biquinoline copper(I) complex did not offer any improvement to DSCs, the more electron-donating bis(amino)-functionalised complex would likely have more of an influence. However the limited solubility of the ligand hindered characterisation and would hinder complexation to

copper(I). Other electron donating substituent options which could be considered are alkyl groups and hydroxyl groups.

The penultimate and final chapters described the synthesis and study of halide and thiophene functionalised 2,2'-bipyridine ligands and subsequent copper(I) complexes. The most successful sensitizer was obtained when thiophene rings were incorporated into the 4- and 4'-positions of the 2,2'-bipyridine framework, creating complex **42**; [Cu(6,6'-dimethyl-5,5'-[2,2'-bipyridin-4,4'-diyl]-bis[thiophene-2-carboxylic acid])$_2$][PF_6]. From DFT analysis the location of the LUMO and LUMO+1 were found to be favourably placed over the thiophene rings and the carboxylic acid groups. Promising DSC efficiencies of >1% were obtained and an assessment of the dye's electrochemistry, emissive behaviour and its IPCE spectrum were also recorded. EIS showed that the electron diffusion lengths and electron lifetimes in DSCs with complex **42** were adequate, although a little shorter than obtained with N719 DSCs. These factors may be preventing the attainment of higher solar conversion efficiencies. It would be useful to obtain comparative electron diffusion lengths measurements from intensity-modulated photovoltage/photocurrent spectroscopy (IMVS/IMVS) to compare to the EIS values. Given the observations in Chapters 4 and 5 that shorter dye times afford better DSC performances in the case of dyes **20** and **1**, a study to identify the optimal dye time for complex **42** would also be worthwhile to further improve cell efficiencies.

In terms of synthesis, producing more of ligand **28** is not ruled out. The Suzuki–Miyaura cross-coupling reaction between 2-thienylboronic acid and both ligands **28** and **29** was achieved however completion to the metal complexes was not realised. Once ligand **28** is reached, only a hydrolysis (in the case of the ester) followed by metal complexation is required. It would be interesting to compare copper(I) complexes consisting of the 6- and 6'-thiophene functionalised 2,2'-bipyridine ligand with the 4- and 4'-functionalised complex **42**. There are also opportunities for further functionalisation with ligand **37**, using the bromine substituents as the point for further derivatisation. For example, installation of a second set of thiophene rings could be carried out to further improve the light harvesting of the dye. Alternatively, bulkier groups may result in dyes more suited to application with a $Co^{2+/3+}$ mediator.

The use of other heteroaromatics was not discussed in this work, however investigations along that route have been pursued in the scope of this work. In the same manner that 1,6-

di(thiophen-2-yl)hexa-1,5-diene-3,4-dione was synthesied, the novel ligand 1,6-di(2-*N*-methyl-pyrrole)hexa-1,5-diene-3,4-dione was produced and fully characterised. However the first step of the synthesis, reaction between the 2,3-butanedione and *N*-methyl-2-pyrrolecarboxaldehyde, was very low yielding (only 3 %) which made it difficult to obtain sufficient material to proceed through the synthesis, as well as being a wasteful process. Offering the greatest aromatic character, thiophene substituents are preferable to pyrrole or furan moieties therefore this synthetic route will probably not be pursued.

There has been a lot of progress made with copper(I) dyes in recent years and the method of *in situ* heteroleptic complex formation has been greatly exploited to generate a wide range of sensitizers. In addition, the use of phosphonate anchoring groups has found success with improved DSC performances demonstrated over analogous complexes with carboxylic acid binding groups. Success with copper(I) dyes used in conjunction with a $Co^{2+/3+}$ mediator has also very recently been reported.

Therefore there is still scope for improvement and utilisation of DSCs with copper(I) sensitizers. The primary aim must be to increase the solar-to-power conversion efficiencies, which at present peak at 3.77% for Constable's copper(I) dye containing an ancillary bipyridine ligand appended with hole-transporting triphenylamino moieties. If efficiencies of ~5 to 6 % could be reached then perhaps small scale applications could become financially viable relative to DSCs containing the standard ruthenium(II) dyes. It is worth remembering that synthesis and purification of copper(I) dyes is simpler than for ruthenium(II) dyes, which is important when considering device manufacturing on a larger, manufacturing scale. However, ligand synthesis also needs to be as facile and high-yielding as possible in order to further minimise costs, time and the environmental impact of using copper(I) dyes.

One avenue yet to be explored is the use of copper(I) dyes in solid-state DSCs, for example with a hole conducting polymer rather than a liquid electrolyte. Thinner TiO_2 films ($\leq$2 μm) typically need to be used in solid state DSCs therefore more strongly light-absorbing copper(I) dyes would be needed. Co-sensitization with copper(I) dyes has also not been trialled to the best of our knowledge. In recent years co-dyeing with two or three sensitizers has proved successful, providing the sensitizing process is carefully controlled to optimise dye loading and minimise recombination events. If improvements along these lines could be achieved and with more focus on the larger scale processing aspects (such as shorter

sintering times and faster dye times), then copper(I) DSCs still have much to offer in the future of photovoltaic technologies.

Appendix 1: NMR spectra

[Cu(2,2'-biquinoline-4,4'-dicarboxylic acid)$_2$][HNEt$_3$], 20

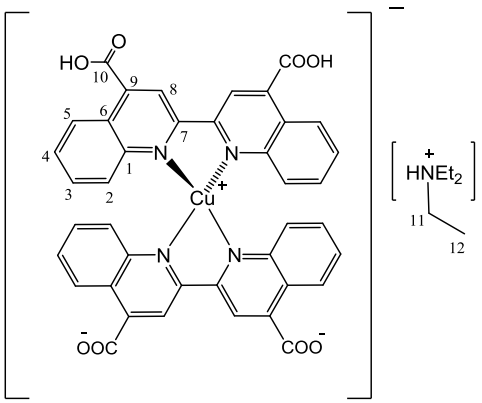

^{1}H NMR (CD$_3$OD), 20

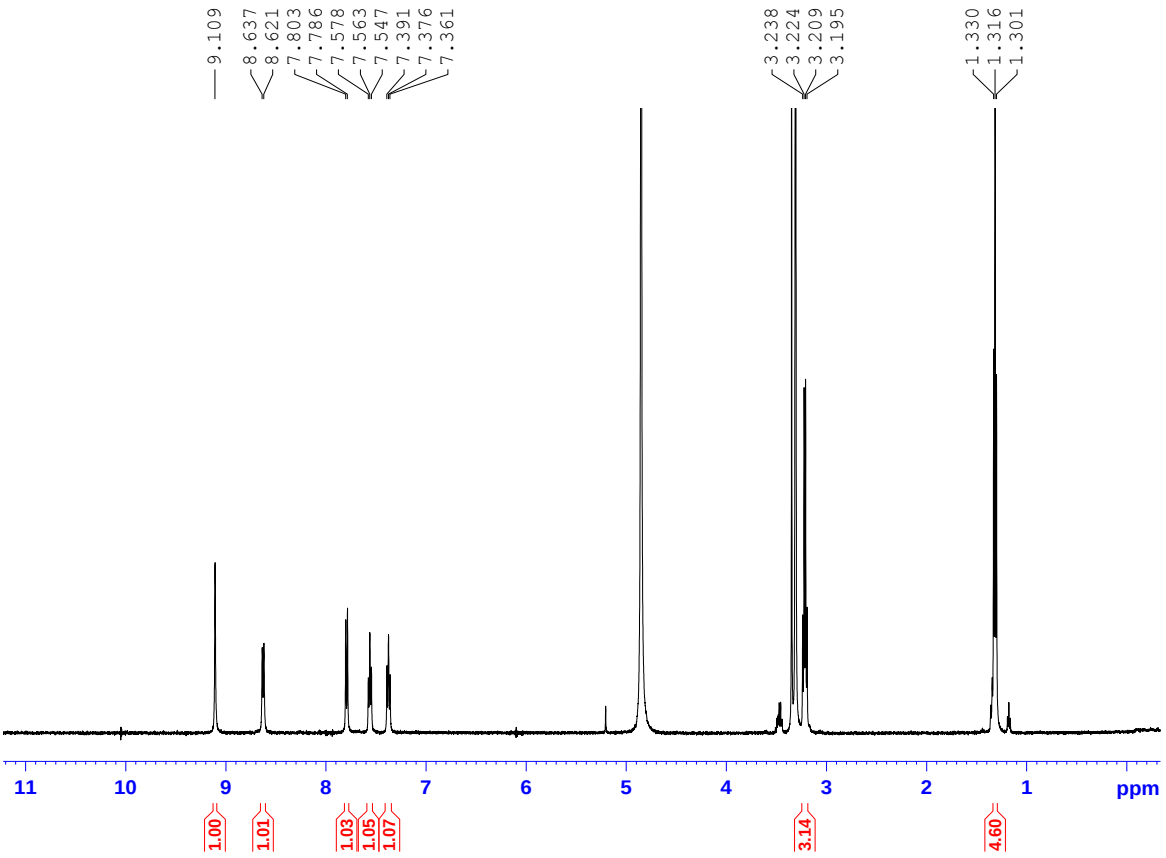

^{13}C {^{1}H} NMR (CD_3OD), 20

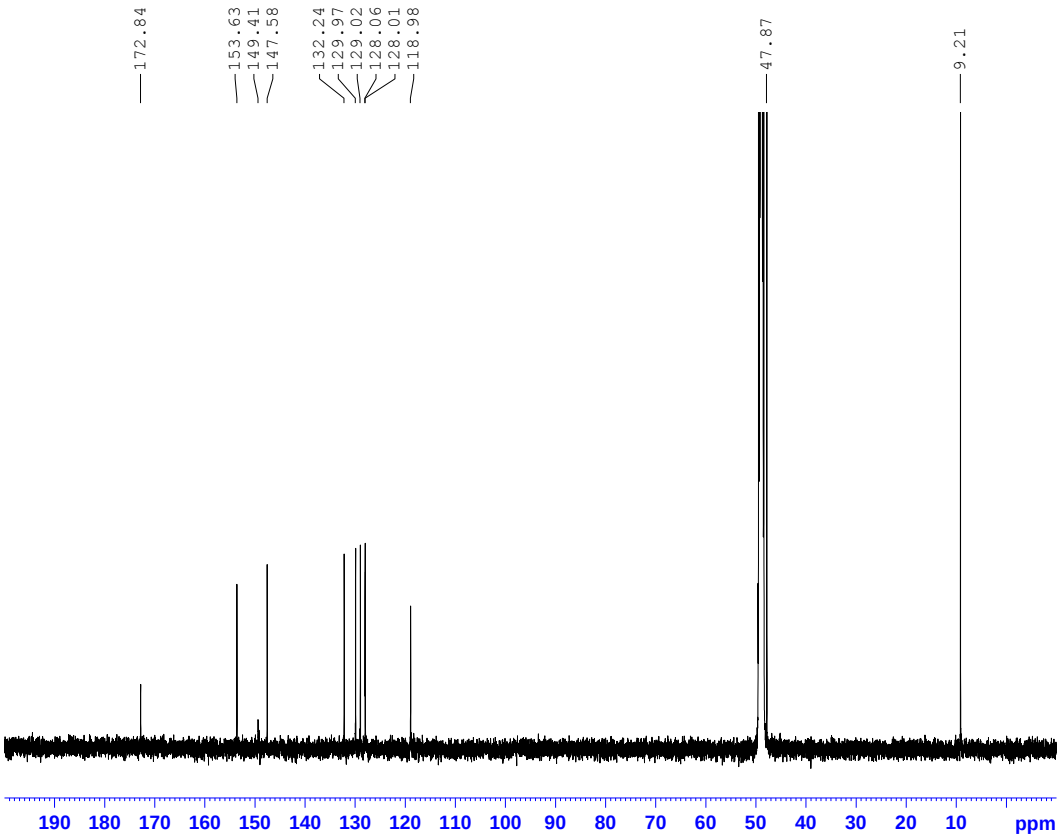

COSY (CD_3OD), 20

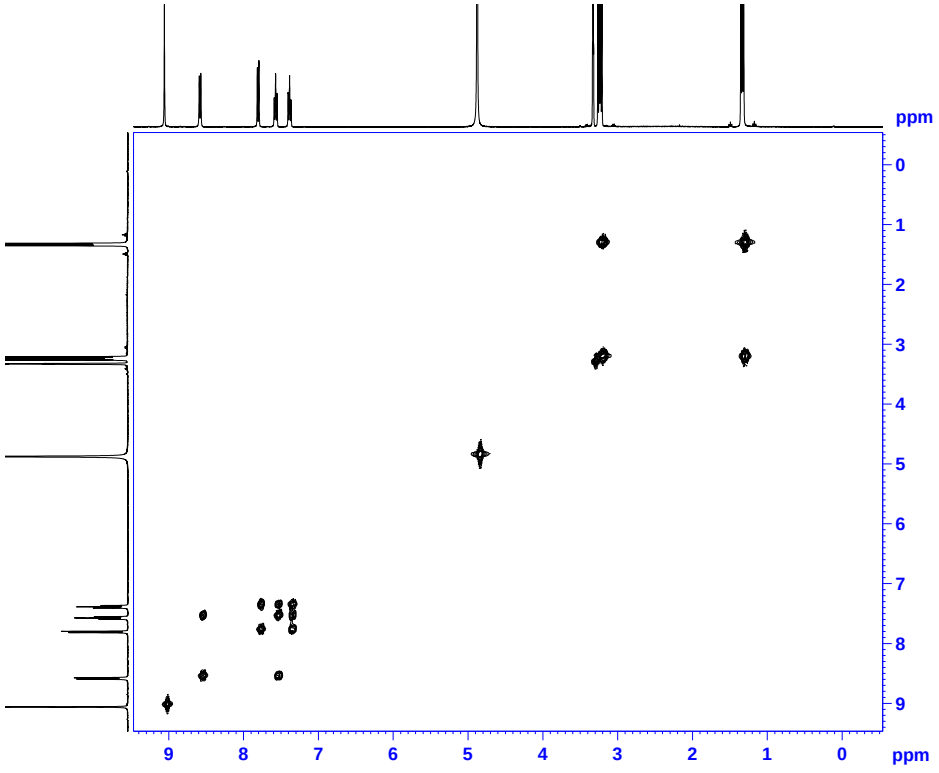

HMQC (CD_3OD), 20

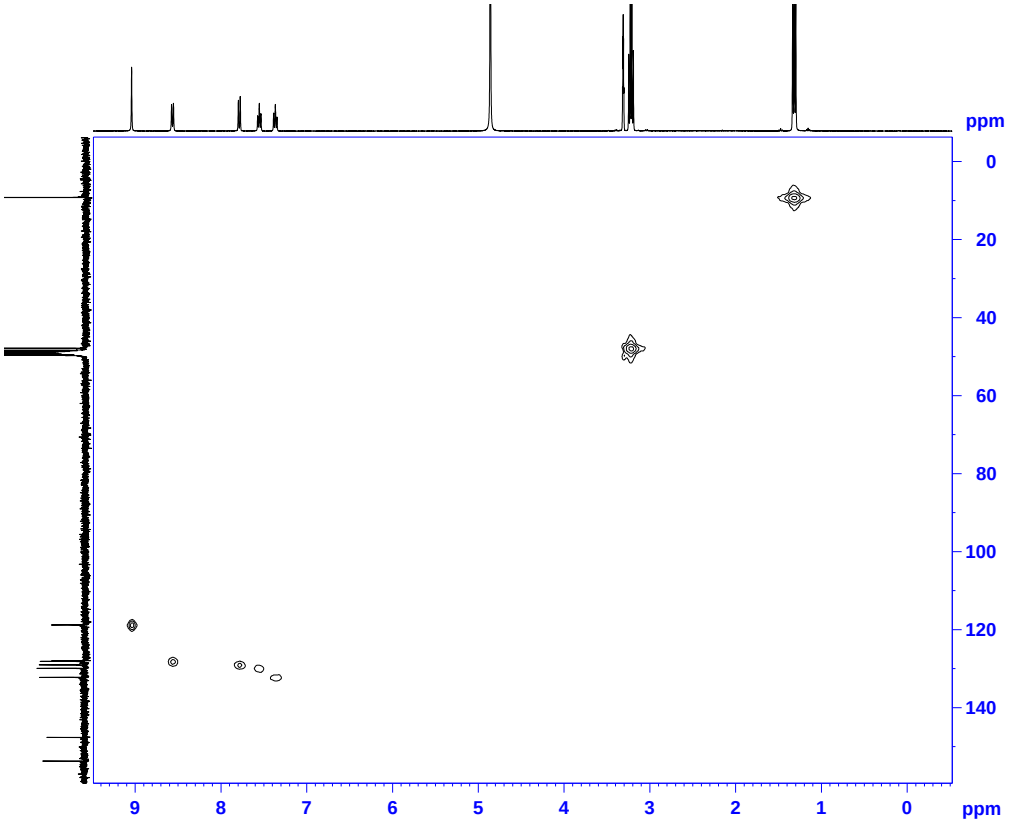

HMBC (CD_3OD), 20

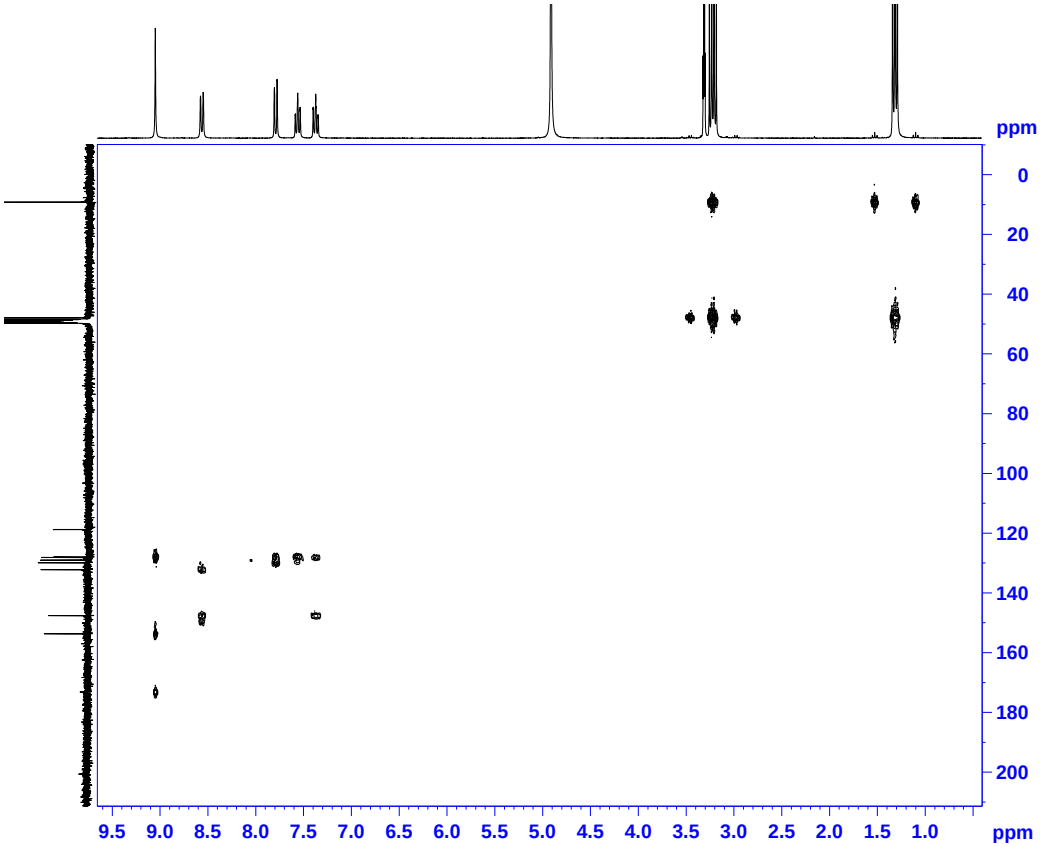

6,6'-dichloro-[2,2'-biquinoline]-4,4'-dicarboxylic acid, 21

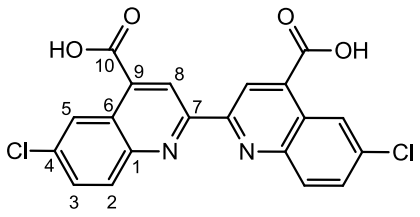

^{1}H NMR (CD_3OD with a drop of 1 M NaOH), 21

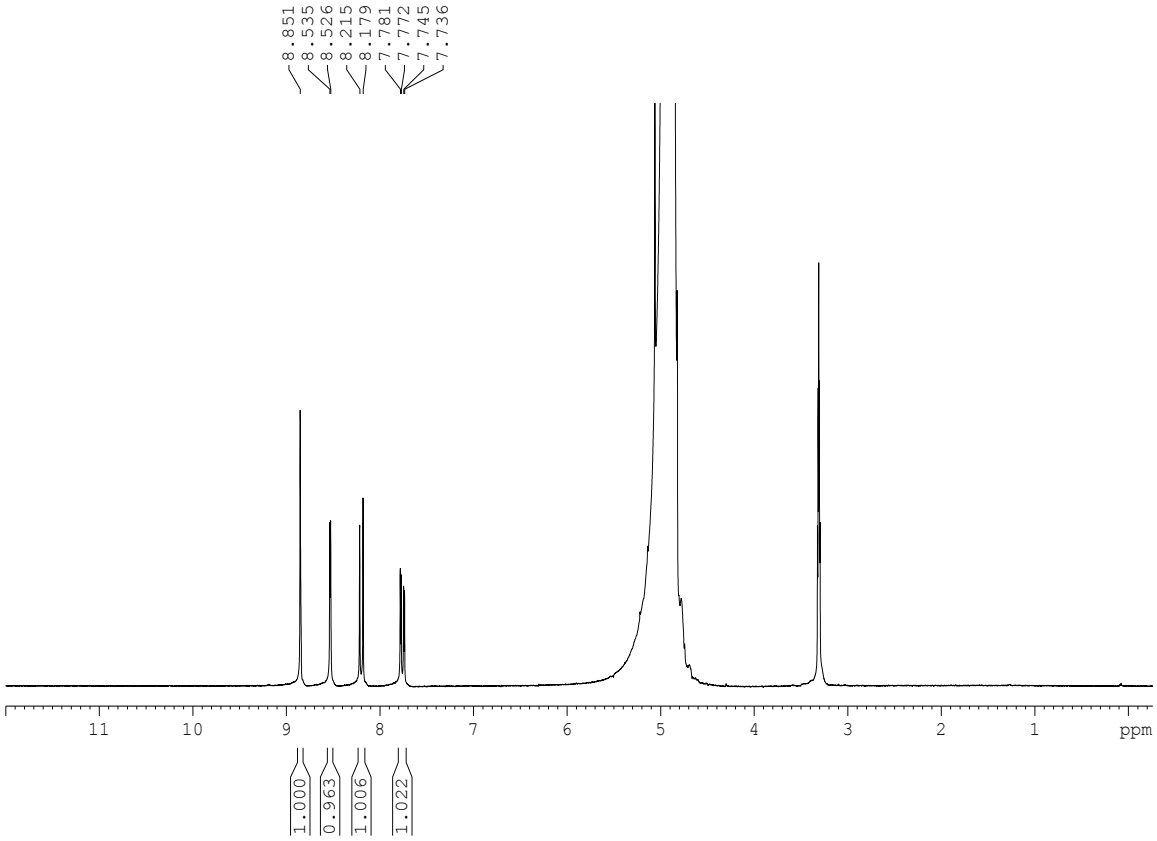

^{13}C {^{1}H} NMR (CD_3OD with a drop of 1 M NaOH), 21

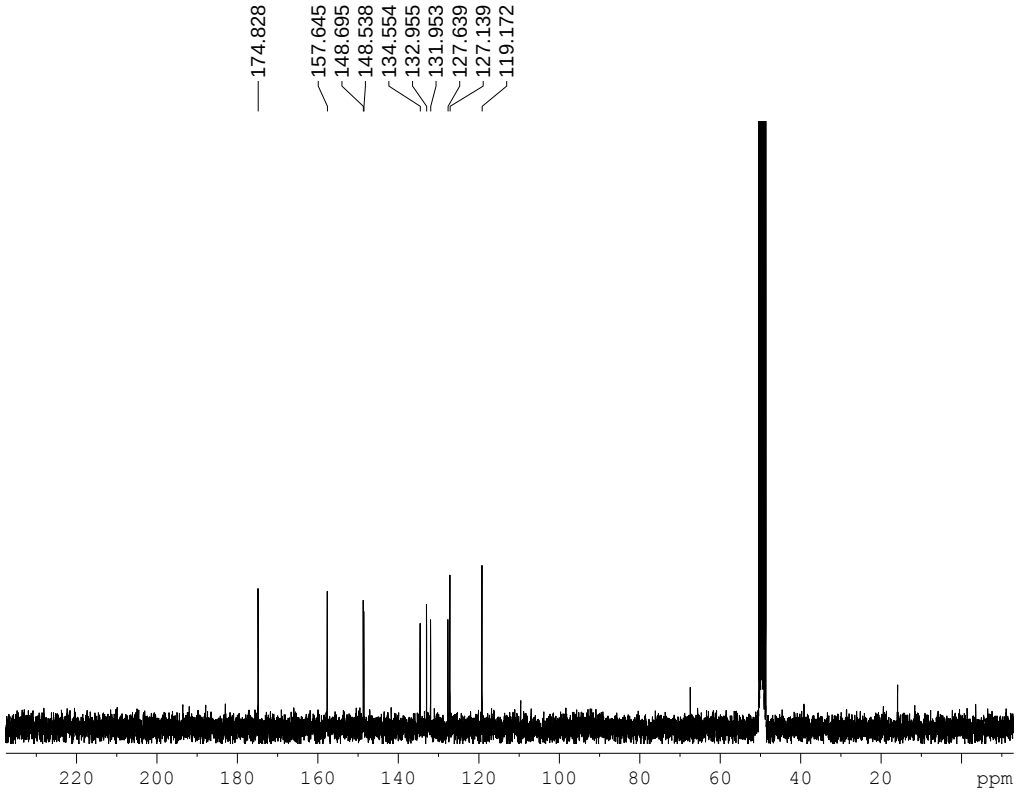

COSY (CD_3OD with a drop of 1 M NaOH), 21

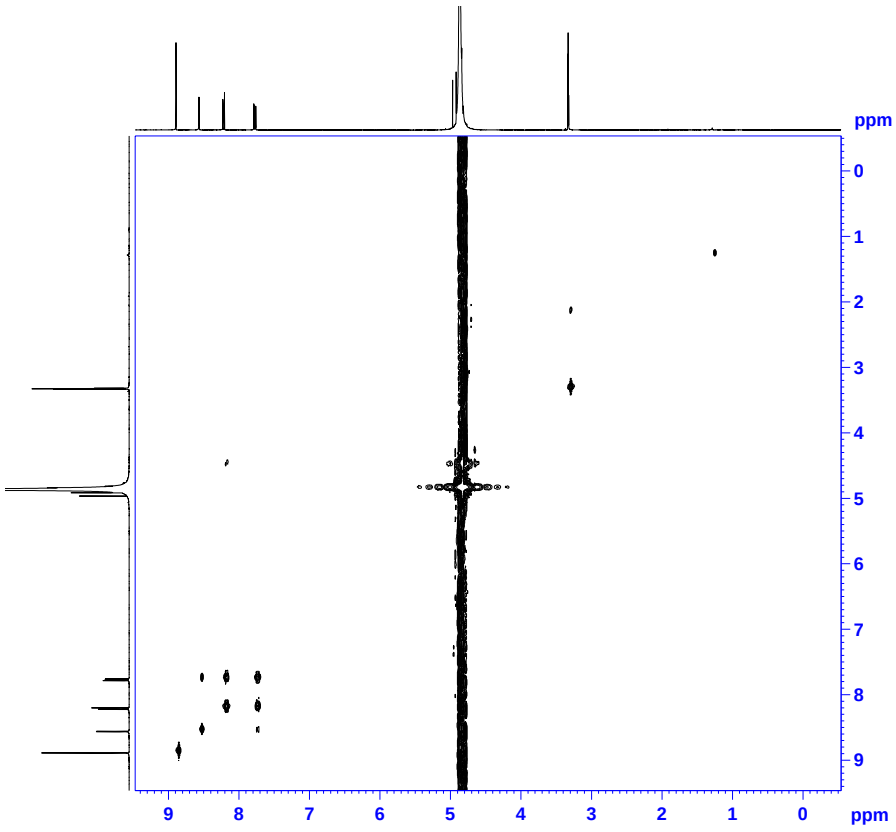

HSQC (CD_3OD with a drop of 1 M NaOH), 21

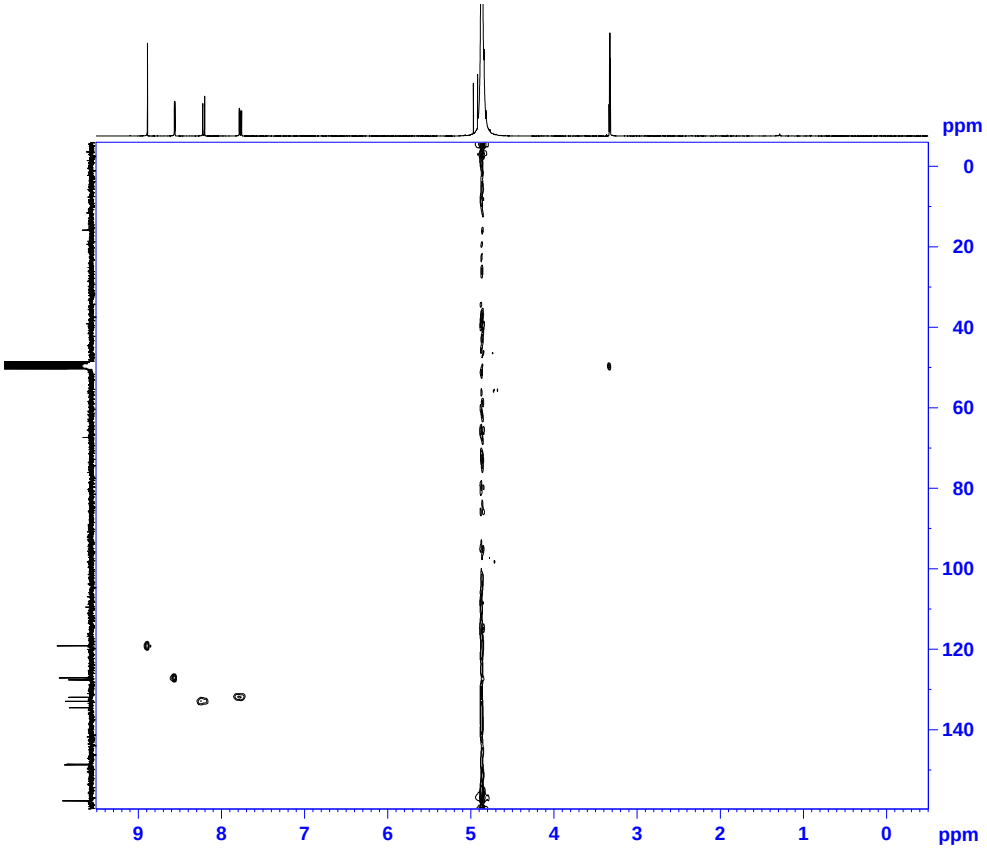

HMBC (CD_3OD with a drop of 1 M NaOH), 21

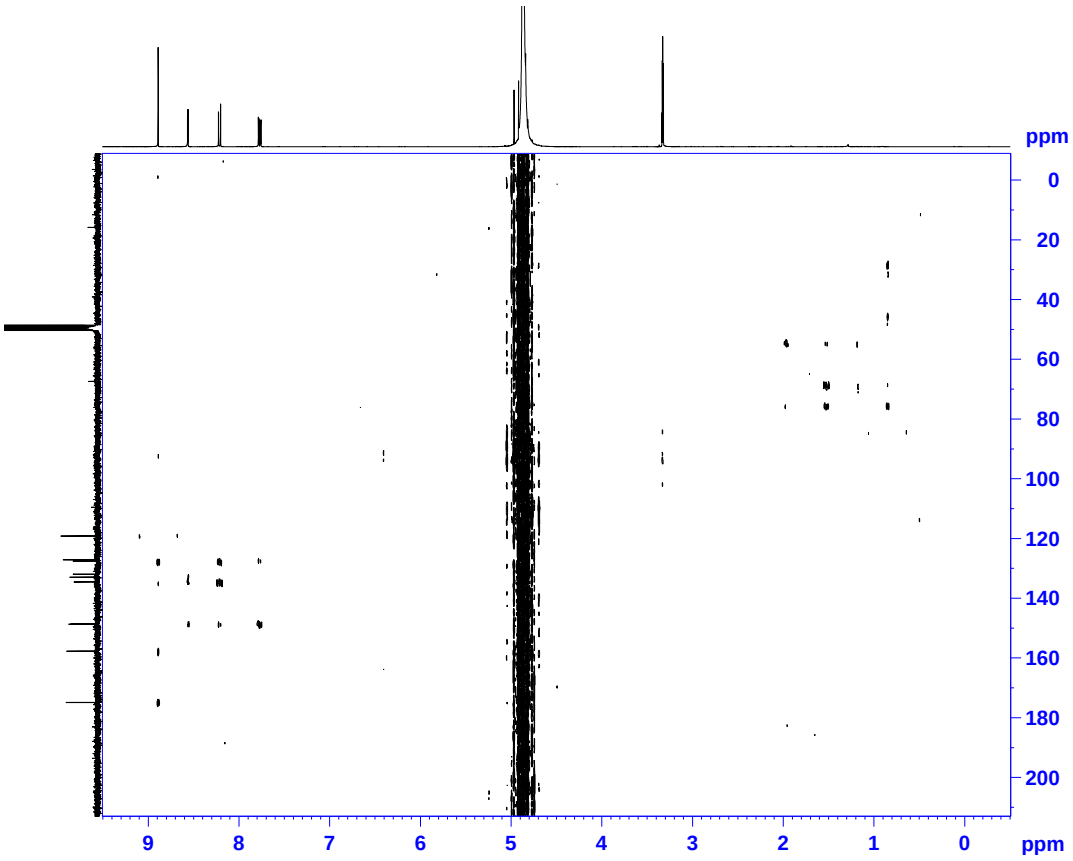

[Cu(6,6'-dichloro-[2,2'-biquinoline]-4,4'-dicarboxylic acid)$_2$][HNEt$_3$], 22

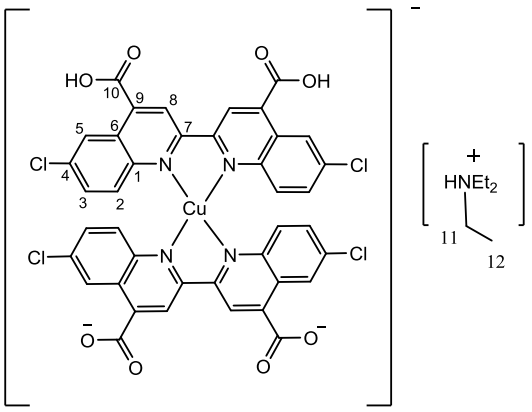

^{1}H NMR (CD_3OD), 22

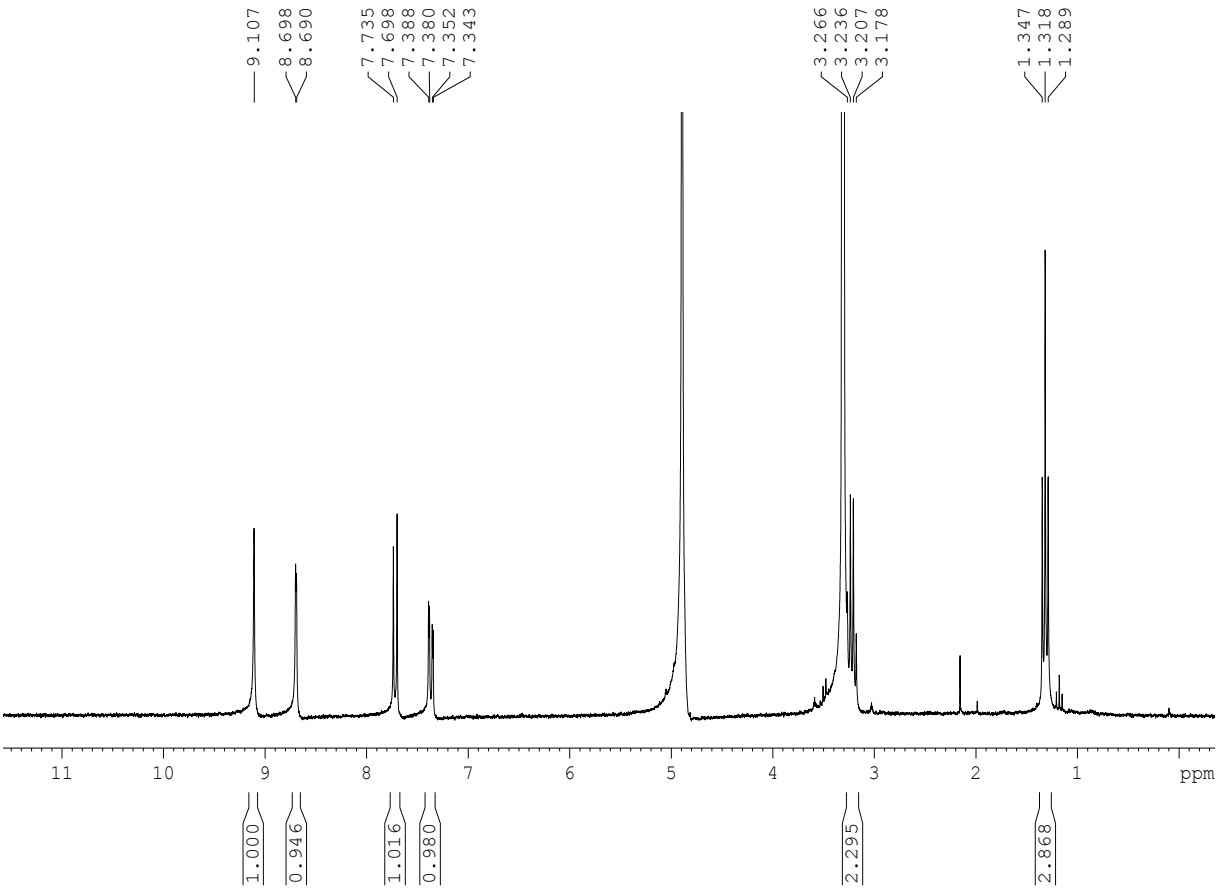

^{13}C {^{1}H} NMR (CD_3OD), 22

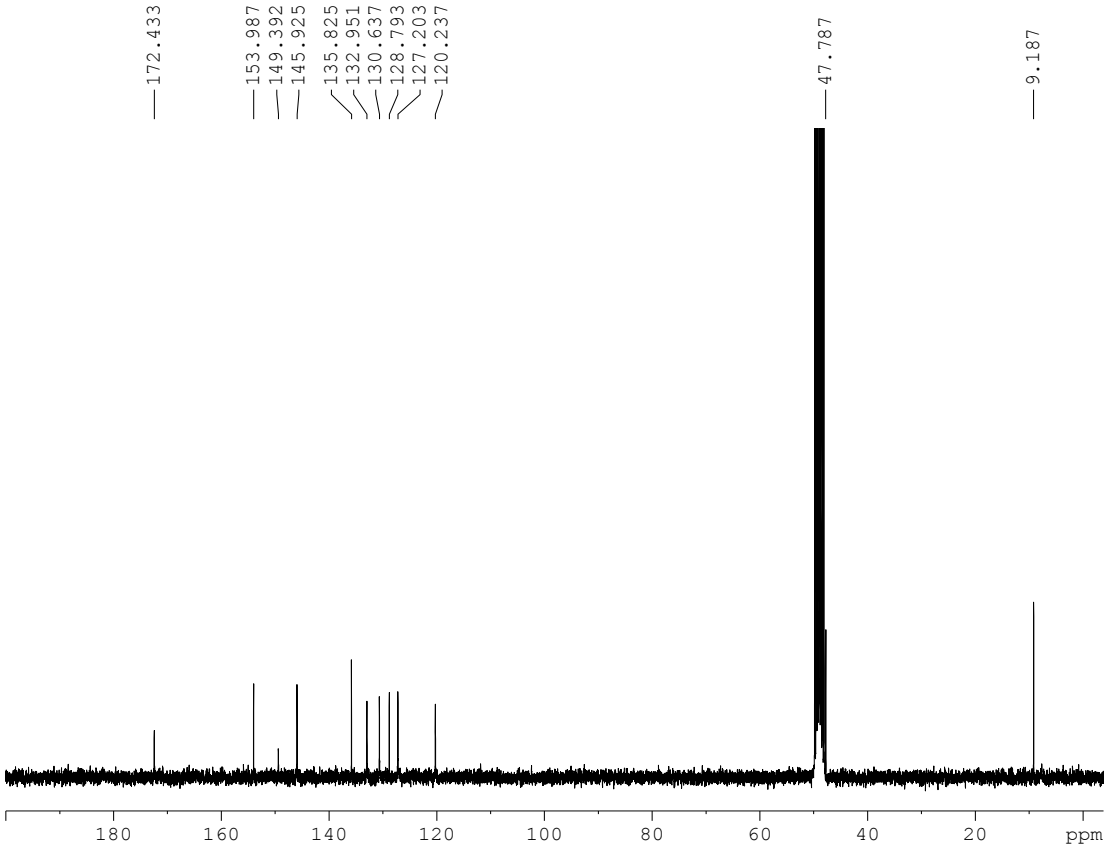

HSQC (CD_3OD), 22

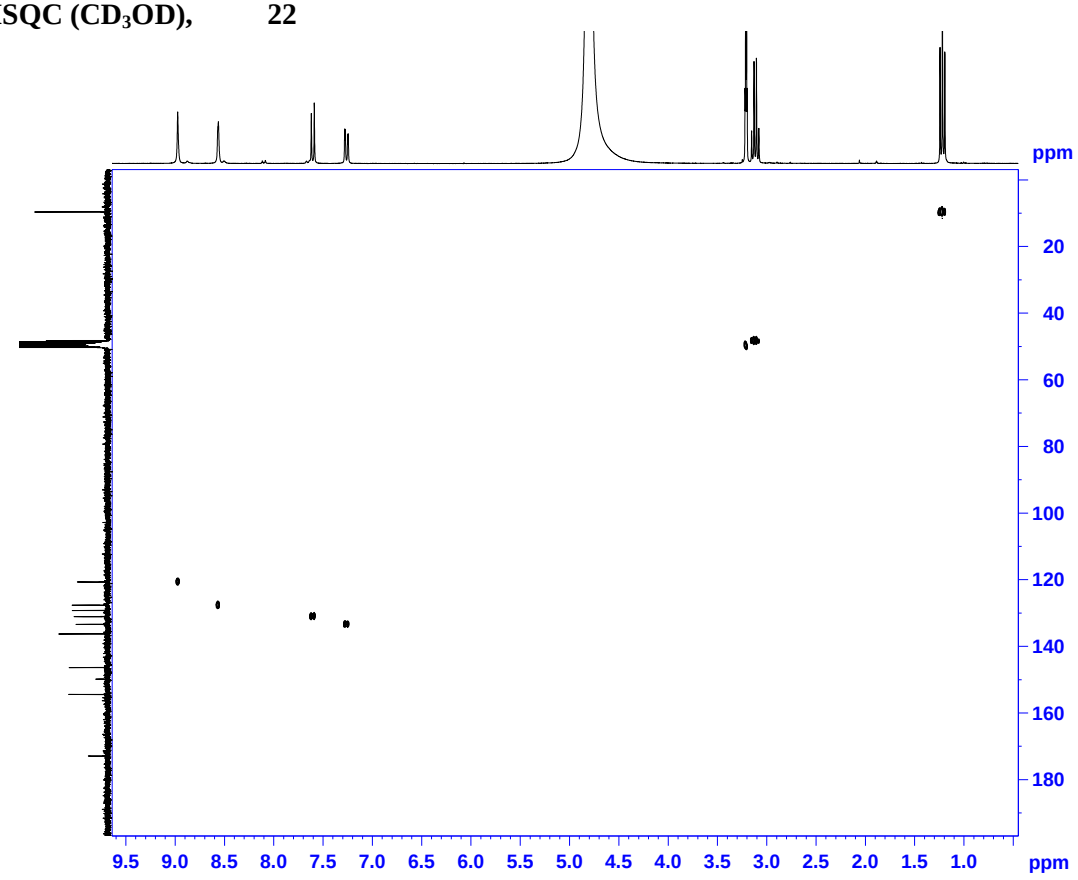

HMBC (CD_3OD), 22

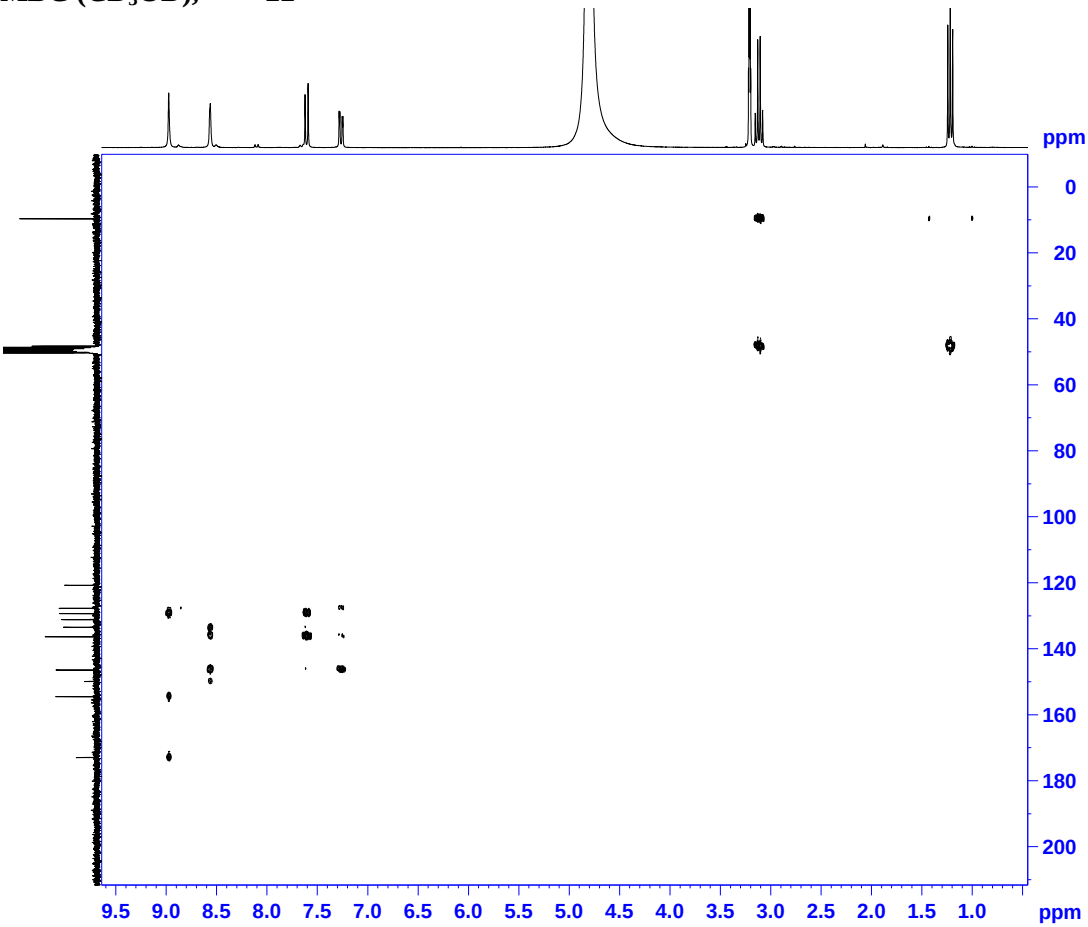

6,6’-dibromo-4,4’-dicarboxy-2,2’-bipyridine, 29

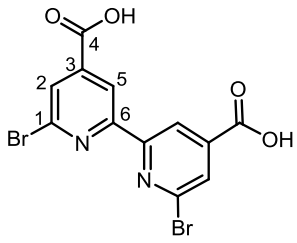

^{1}H NMR (CD_3OD), 29

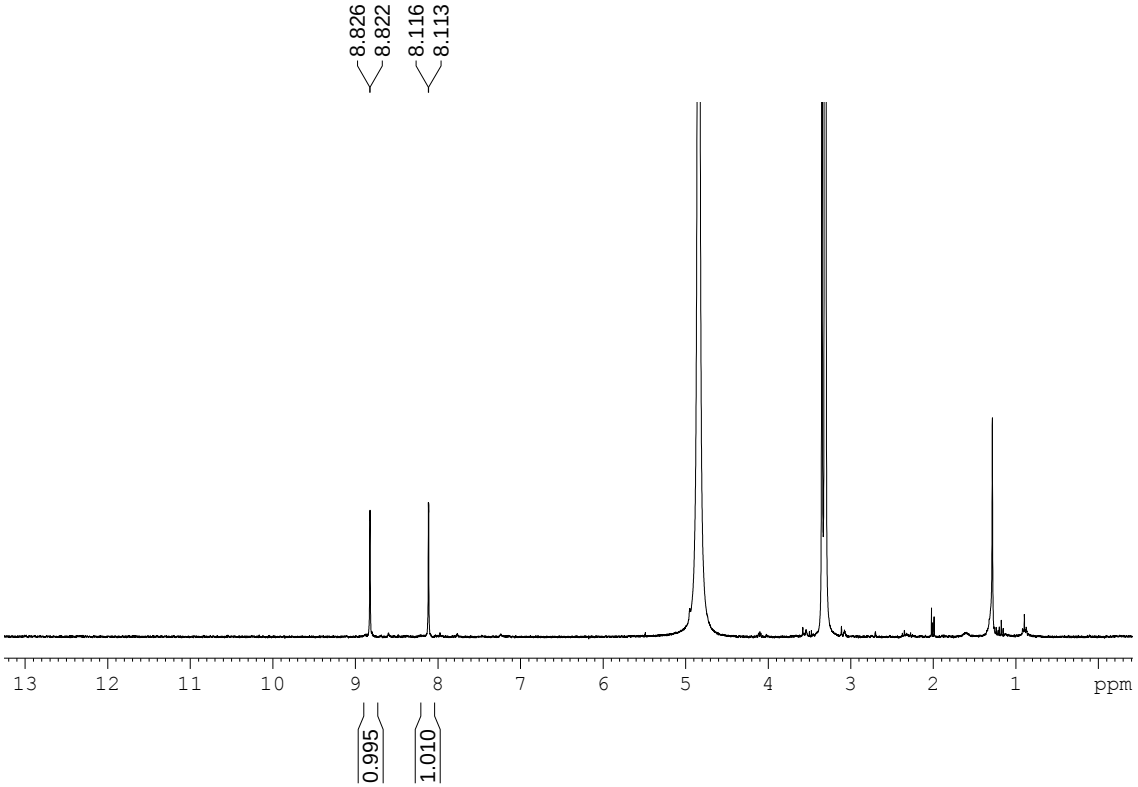

^{13}C {^{1}H} NMR (CD_3OD), 29

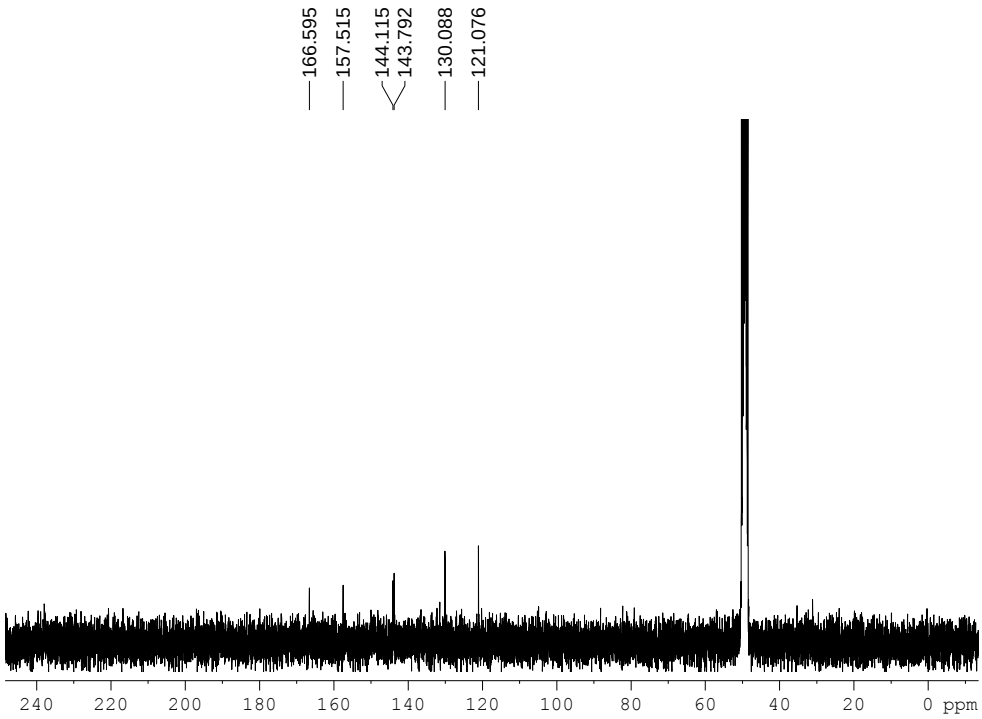

HSQC (CD_3OD), 29

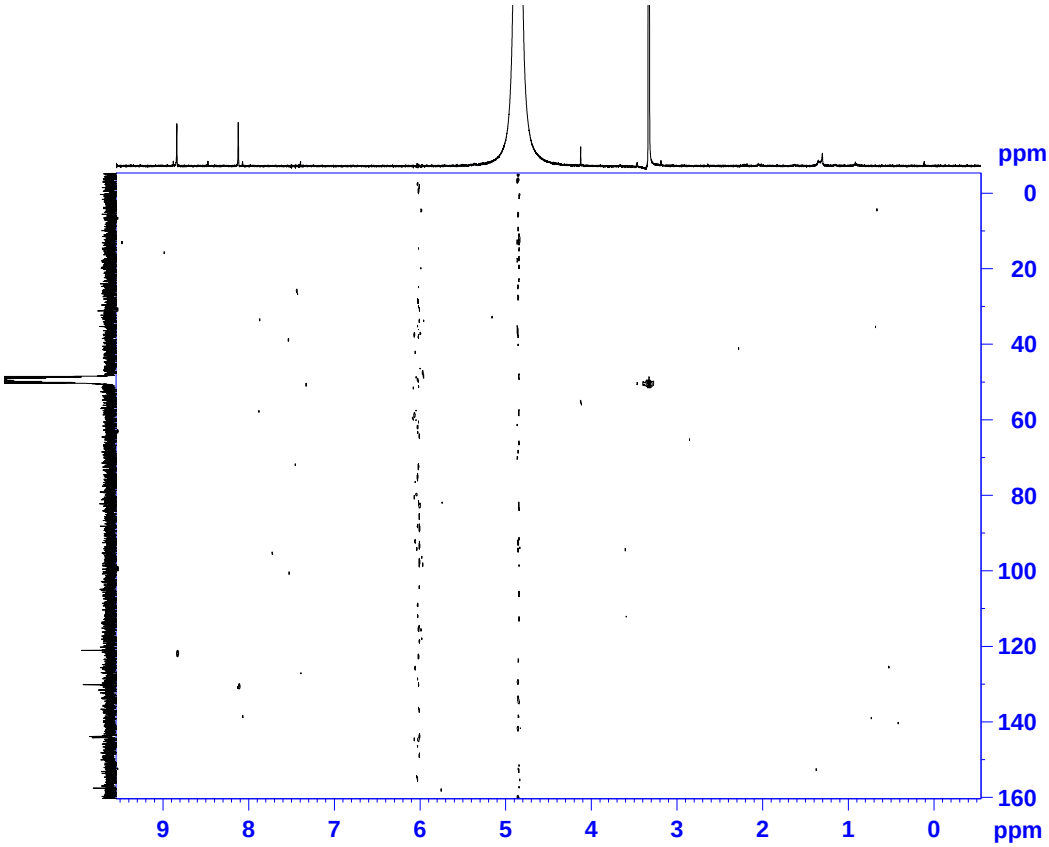

HMBC (CD_3OD), 29

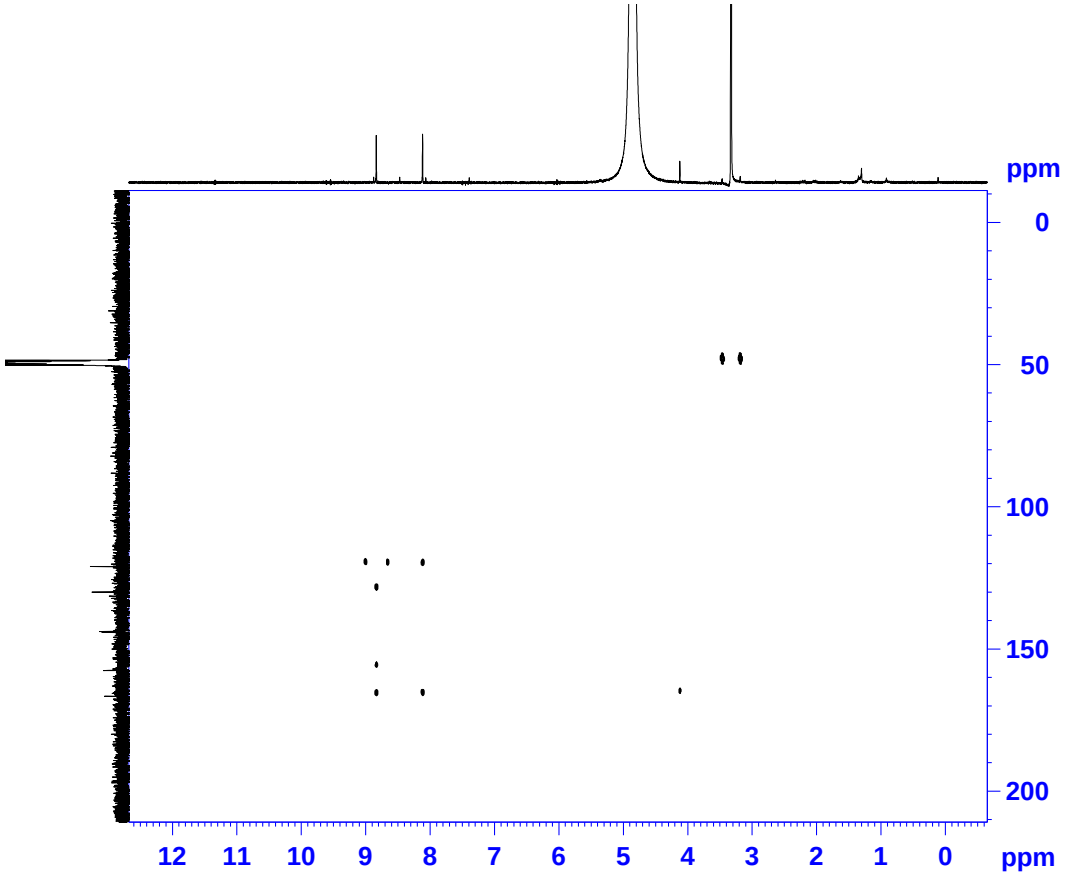

6,6’-dichloro-4,4’-dicarboxy-2,2’-bipyridine, 30

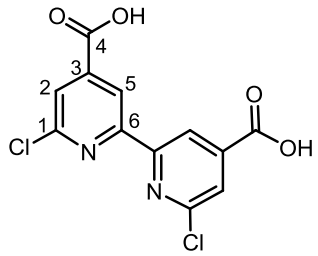

^{1}H NMR (CD_3OD), 30

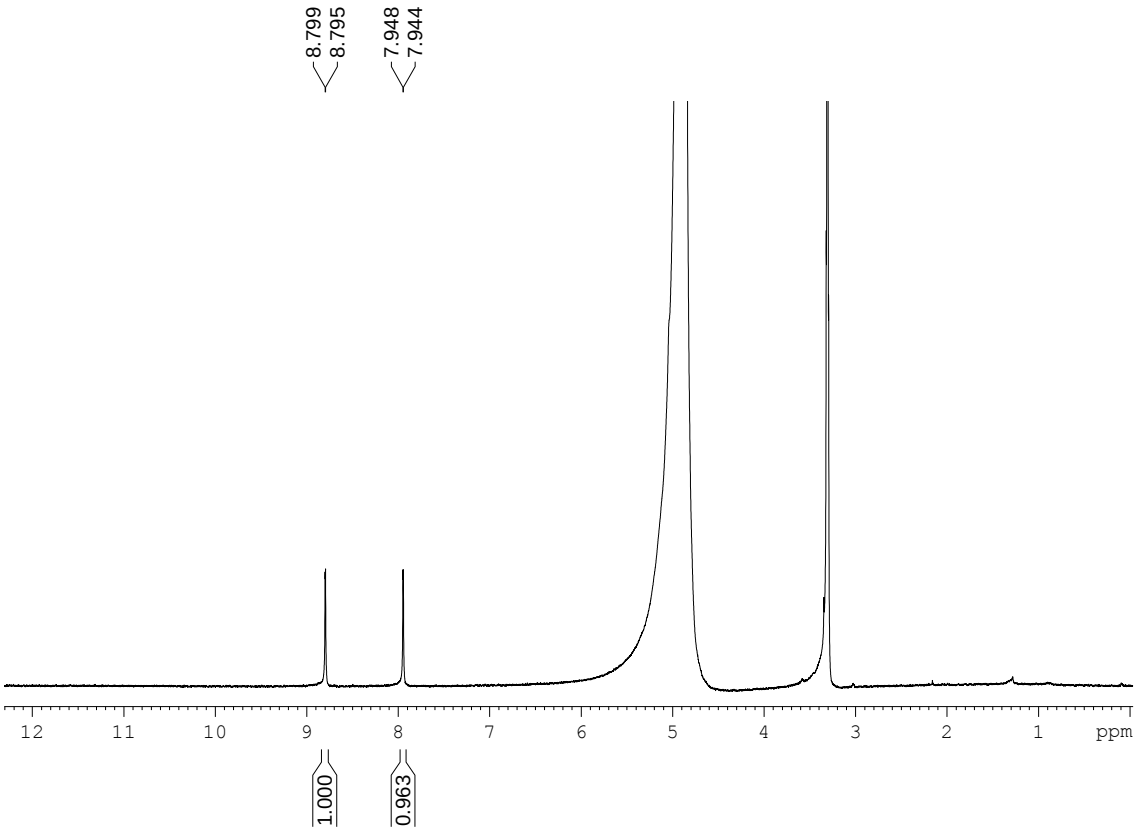

^{13}C {^{1}H} NMR (CD_3OD), 30

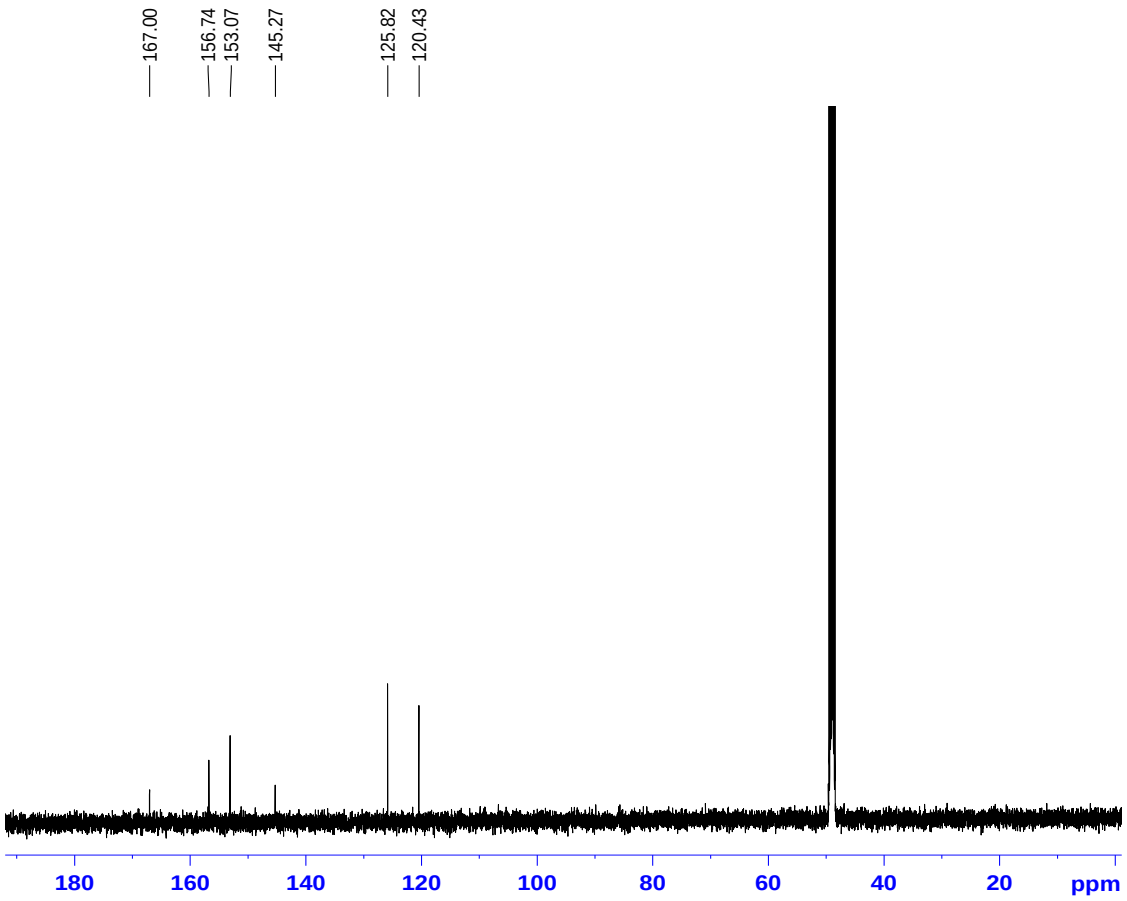

HSQC (CD_3OD), 30

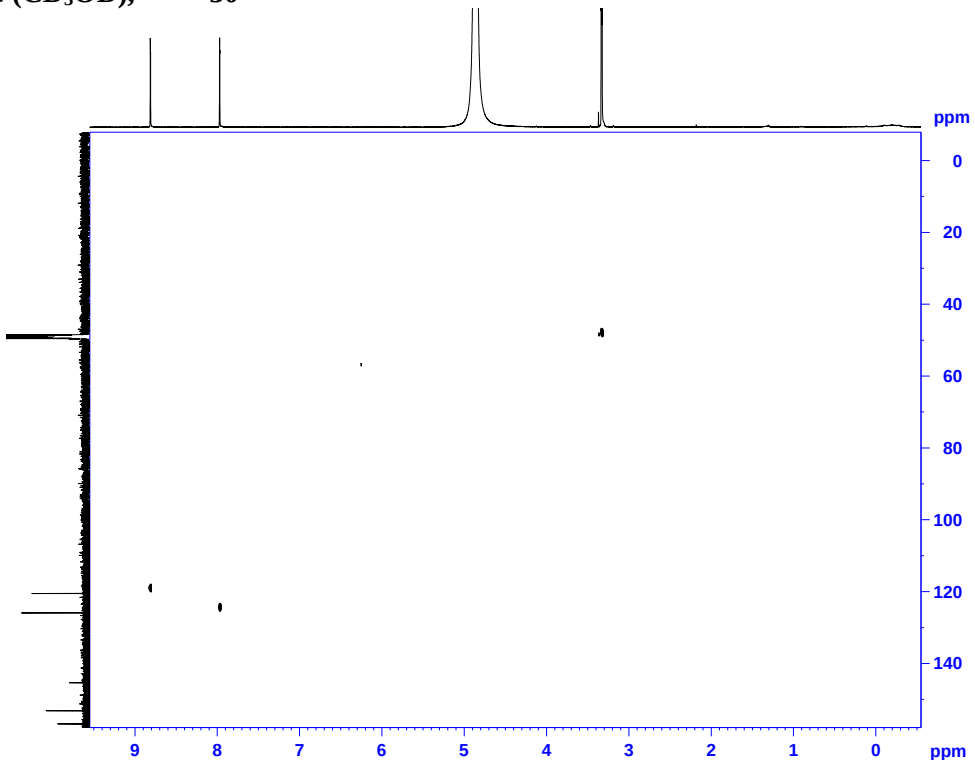

HMBC (CD_3OD), 30

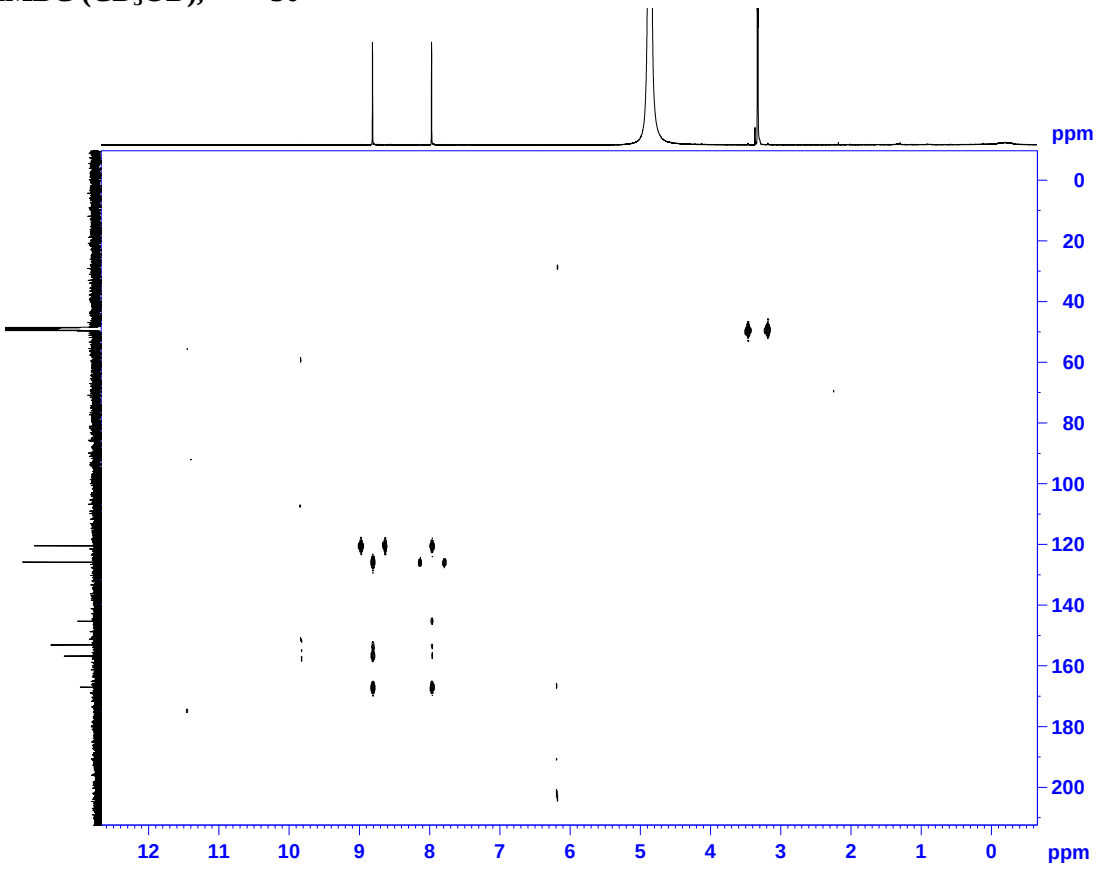

6,6'-bisthiophene-4,4'-dimethoxycarbonyl-2,2'-bipyridine, 31

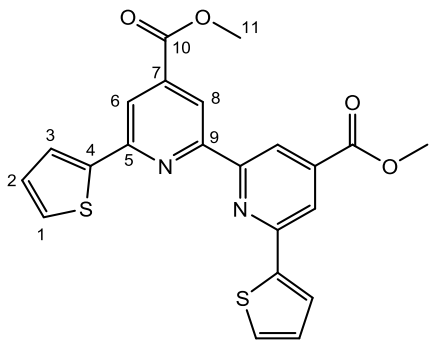

^{1}H NMR ($CDCl_3$), 31

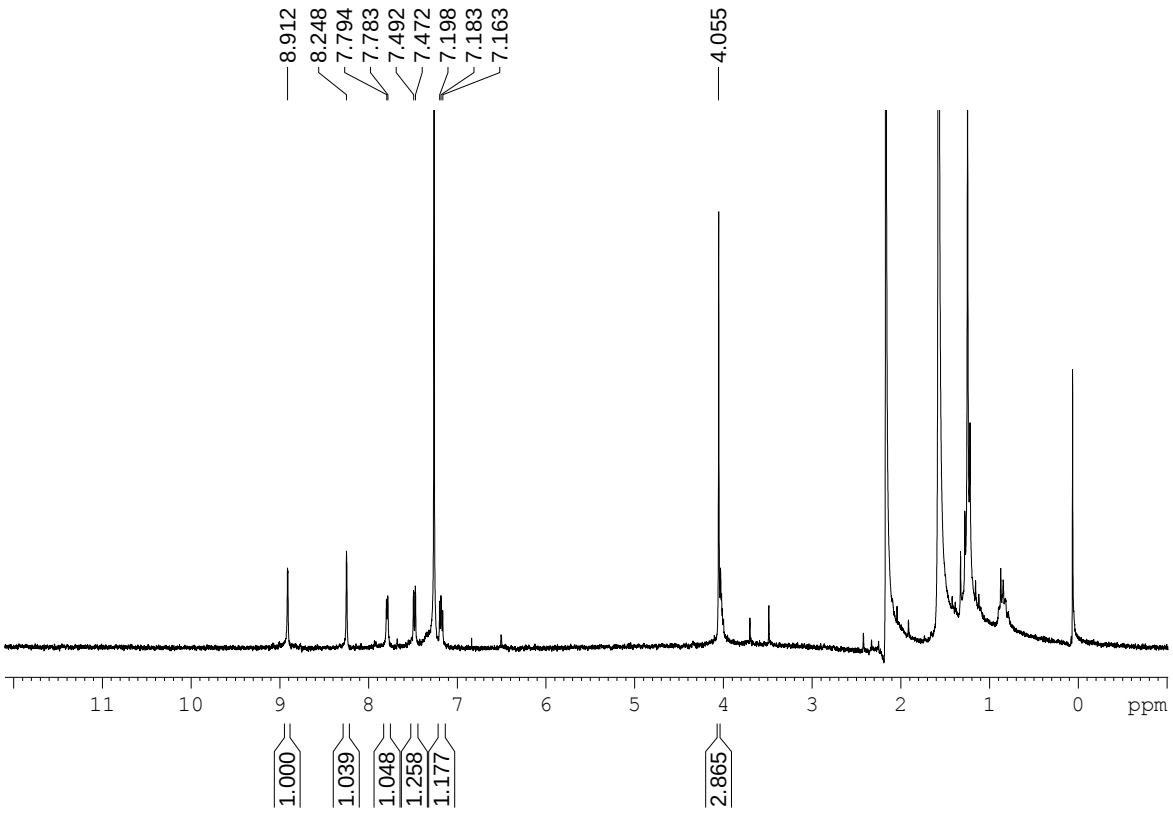

^{13}C {^{1}H} NMR ($CDCl_3$), 31

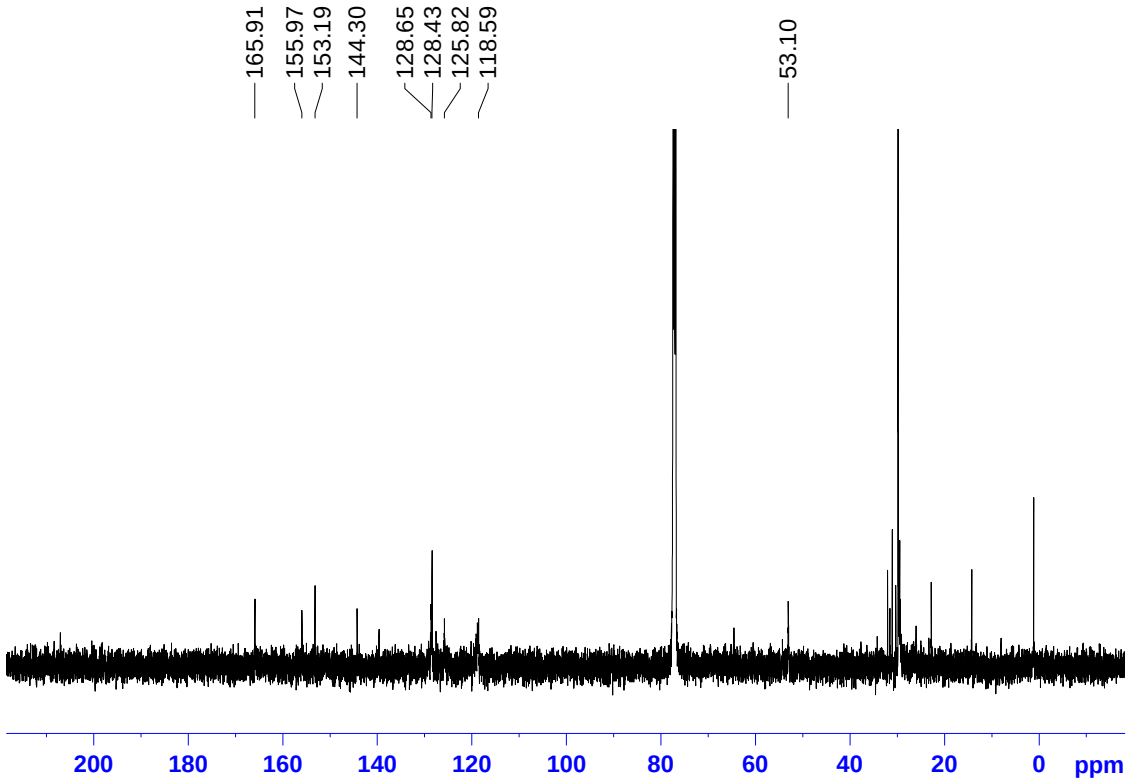

6,6'-bisthiophene-4,4'-dicarboxy-2,2'-bipyridine, 32

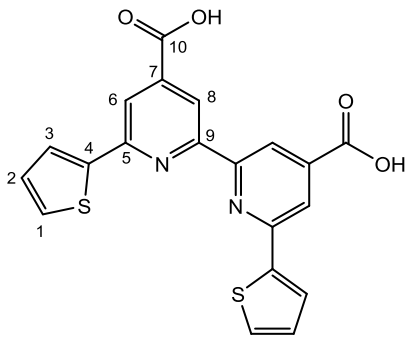

^{1}H NMR (CD_3OD), 32

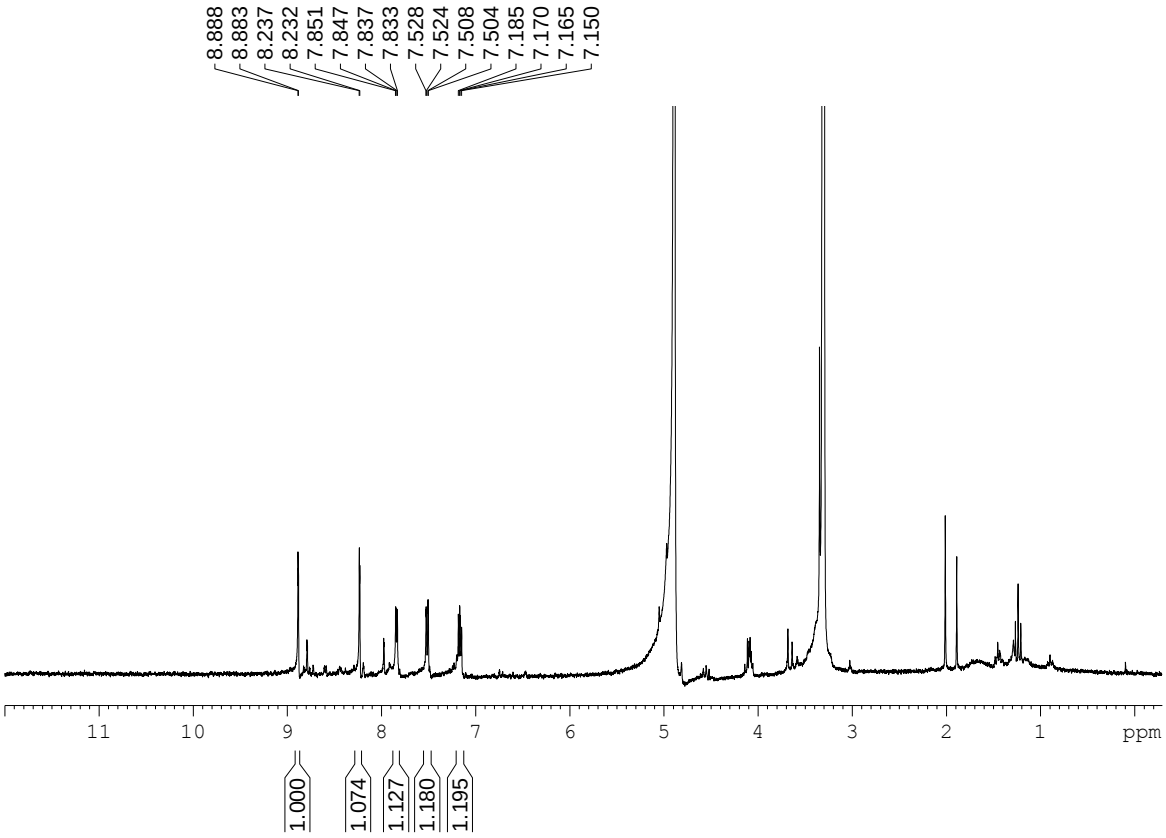

[Cu(6,6'-dichloro-4,4'-dicarboxy-2,2'-bipyridine)$_2$][PF$_6$], 33

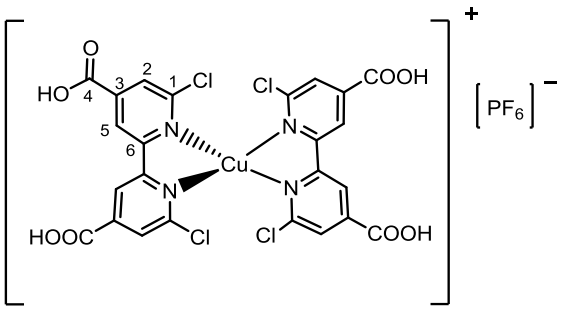

^{1}H NMR (CD_3OD), 33

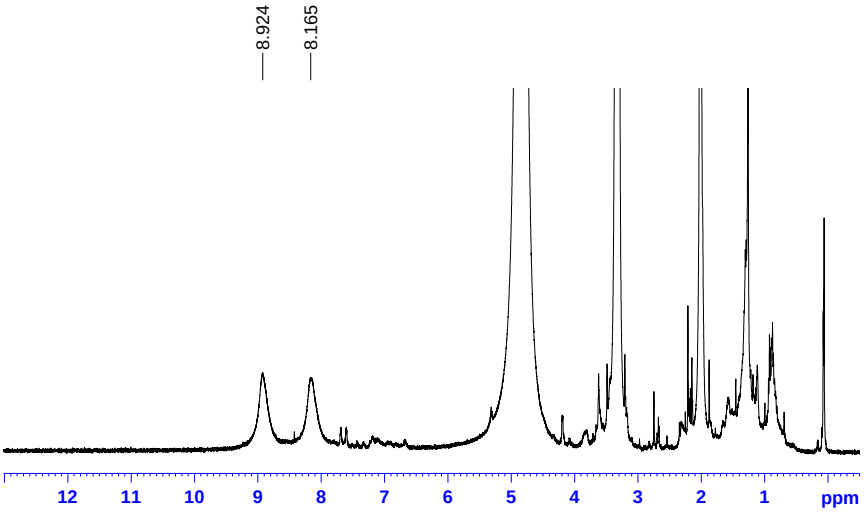

[Cu(6,6'-dibromo-4,4'-dicarboxy-2,2'-bipyridine)$_2$][PF$_6$], 34

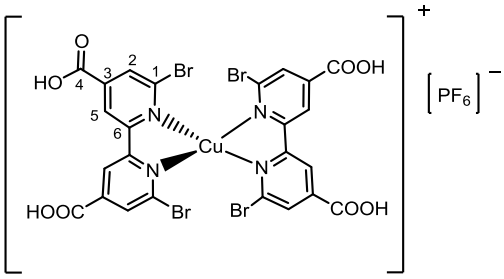

^{1}H NMR (CD$_3$OD), 34

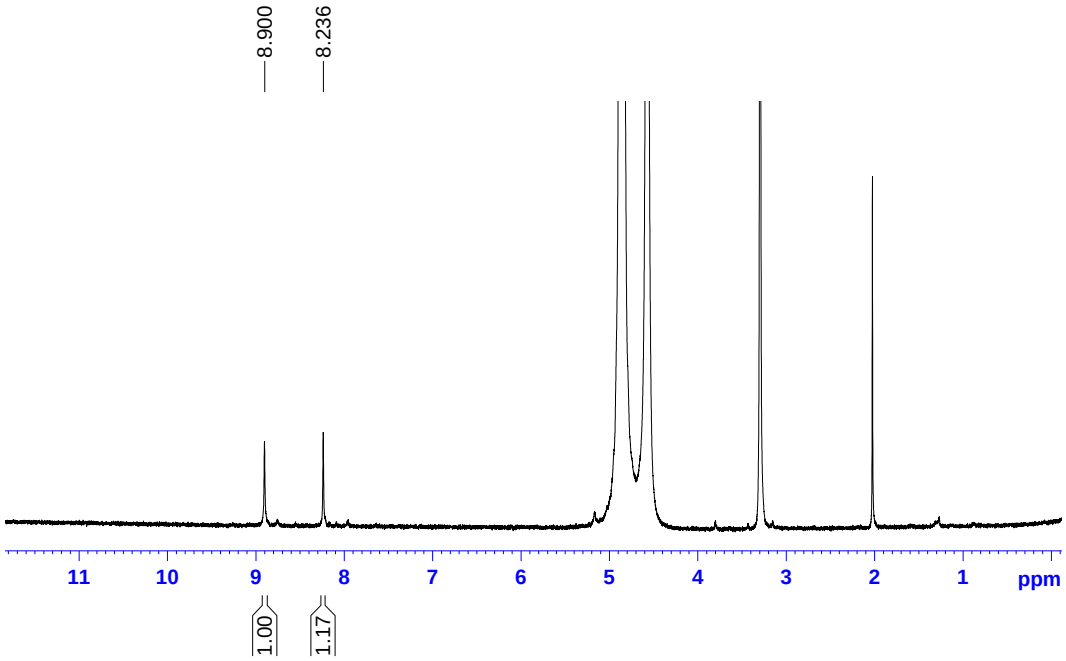

^{13}C {^{1}H} NMR(CD$_3$OD), 34

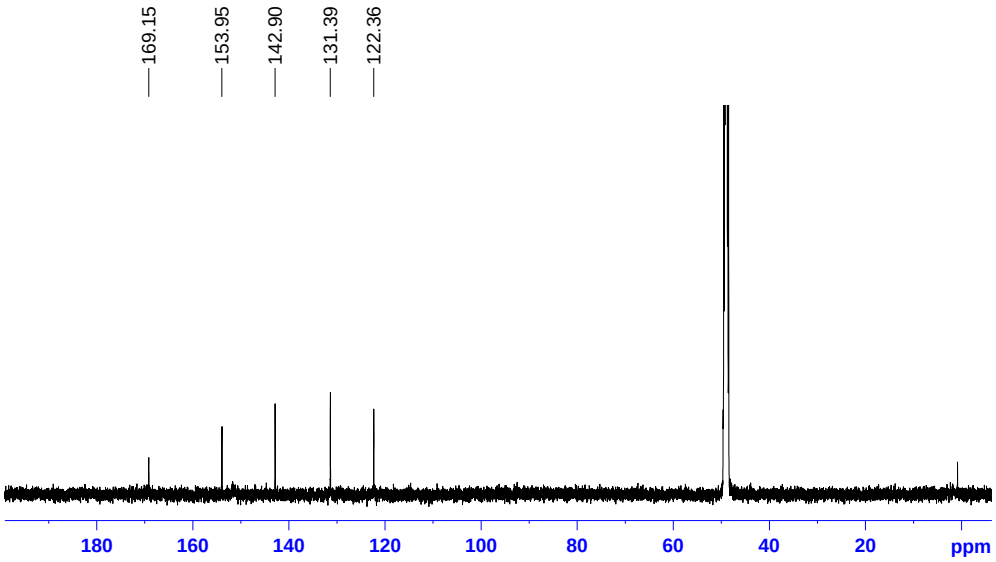

1,6-di(thiophen-2-yl)hexa-1,5-diene-3,4-dione, 35

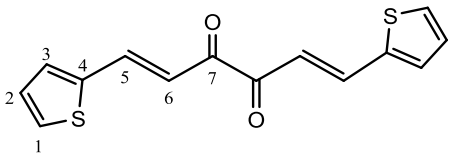

^{1}H NMR ($CDCl_3$), 35

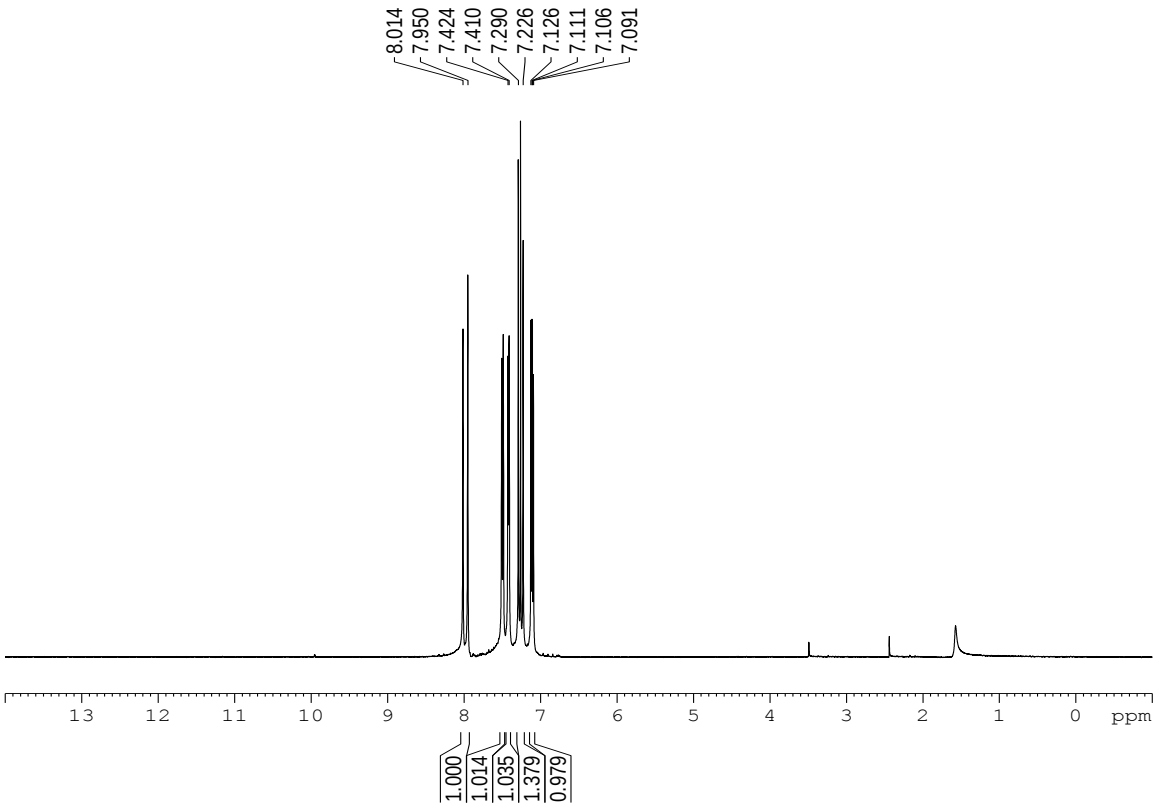

^{13}C {^{1}H} NMR ($CDCl_3$), 35

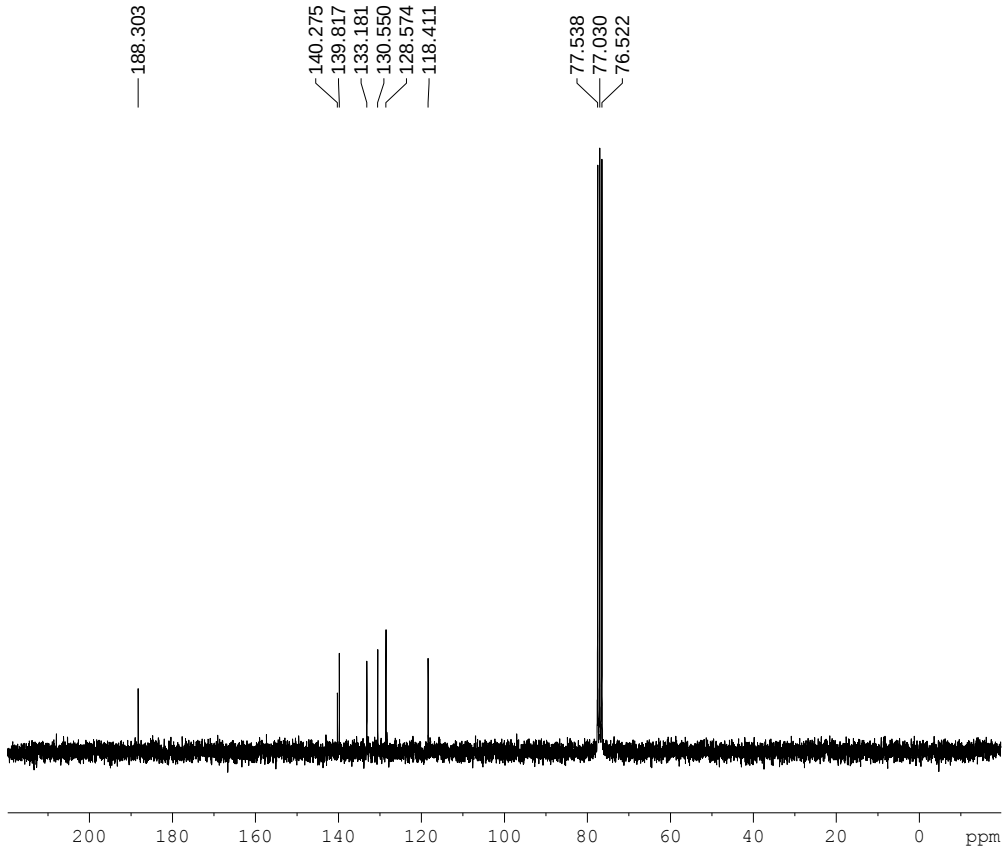

COSY ($CDCl_3$), 35

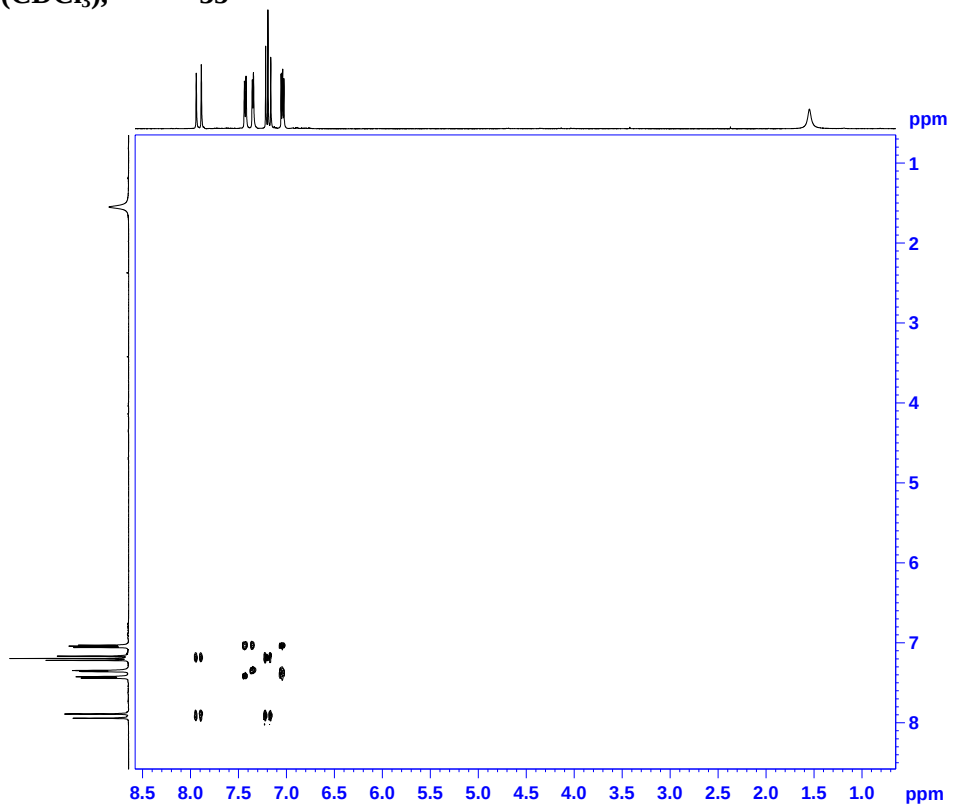

HMQC ($CDCl_3$), 35

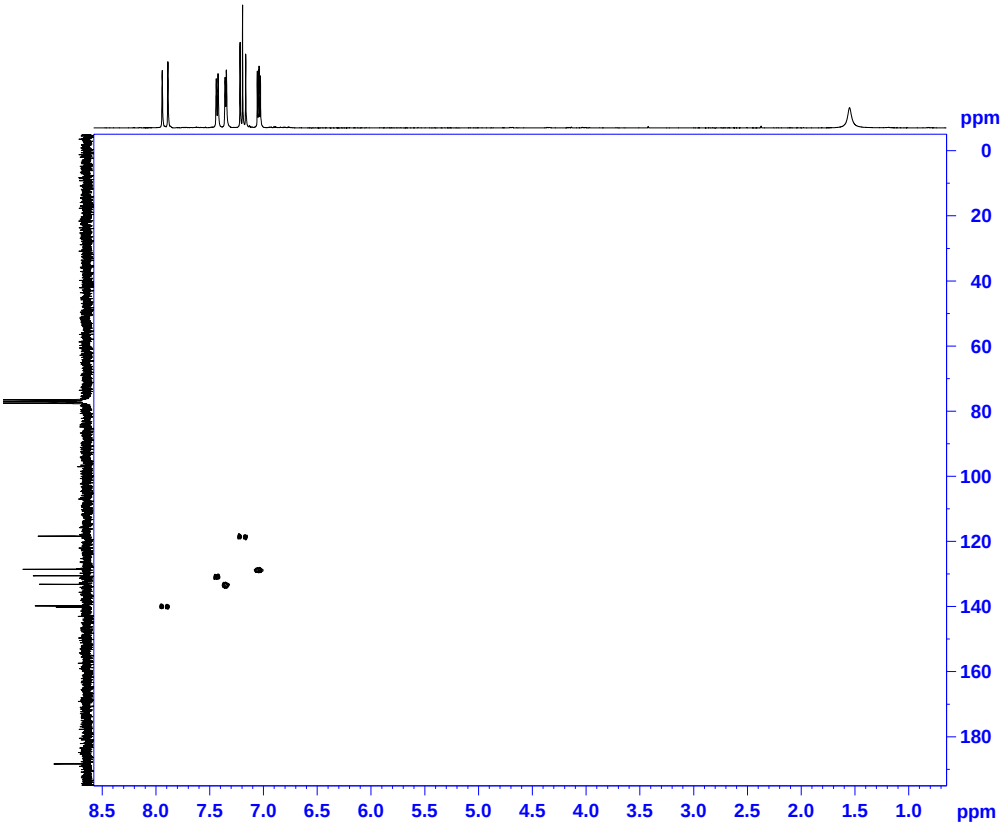

HMBC ($CDCl_3$), 35

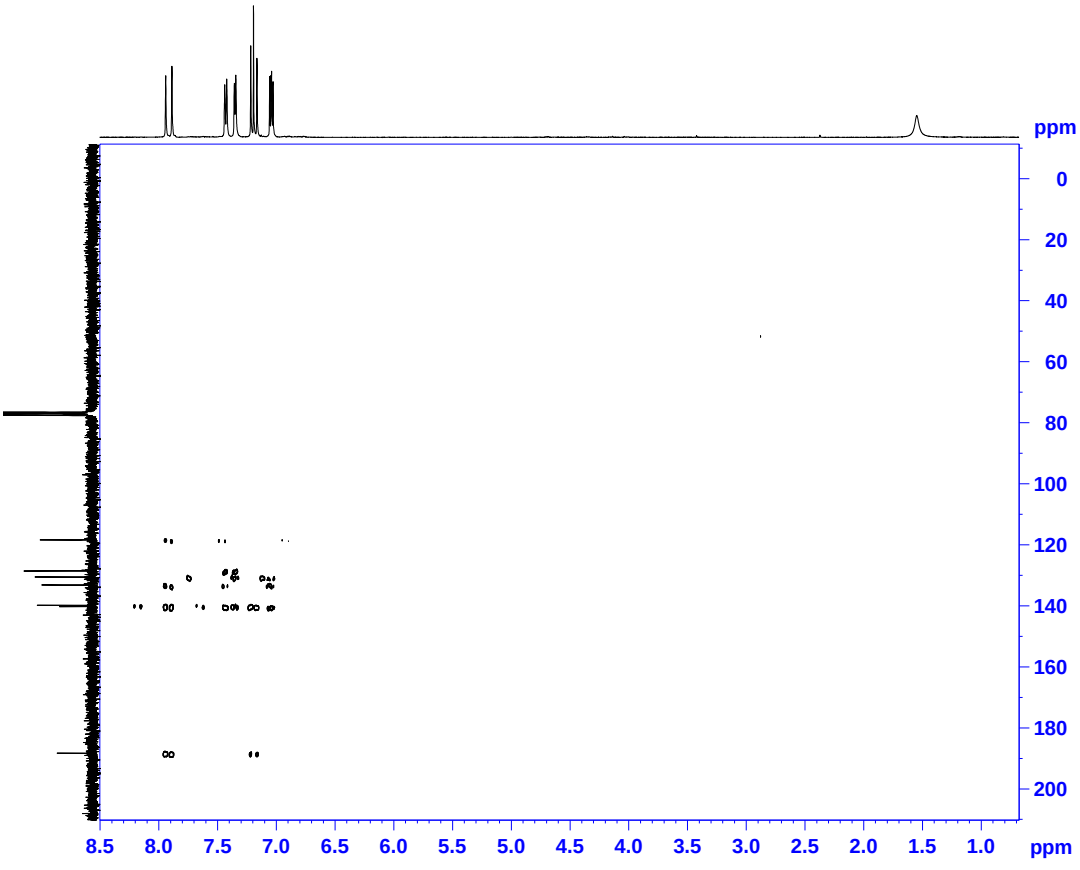

6,6'-dimethyl-4,4'-di(thiophen-2-yl)-2,2'-bipyridine, 36

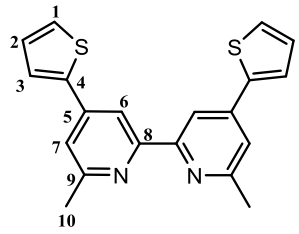

^{1}H NMR ($CDCl_3$), 36

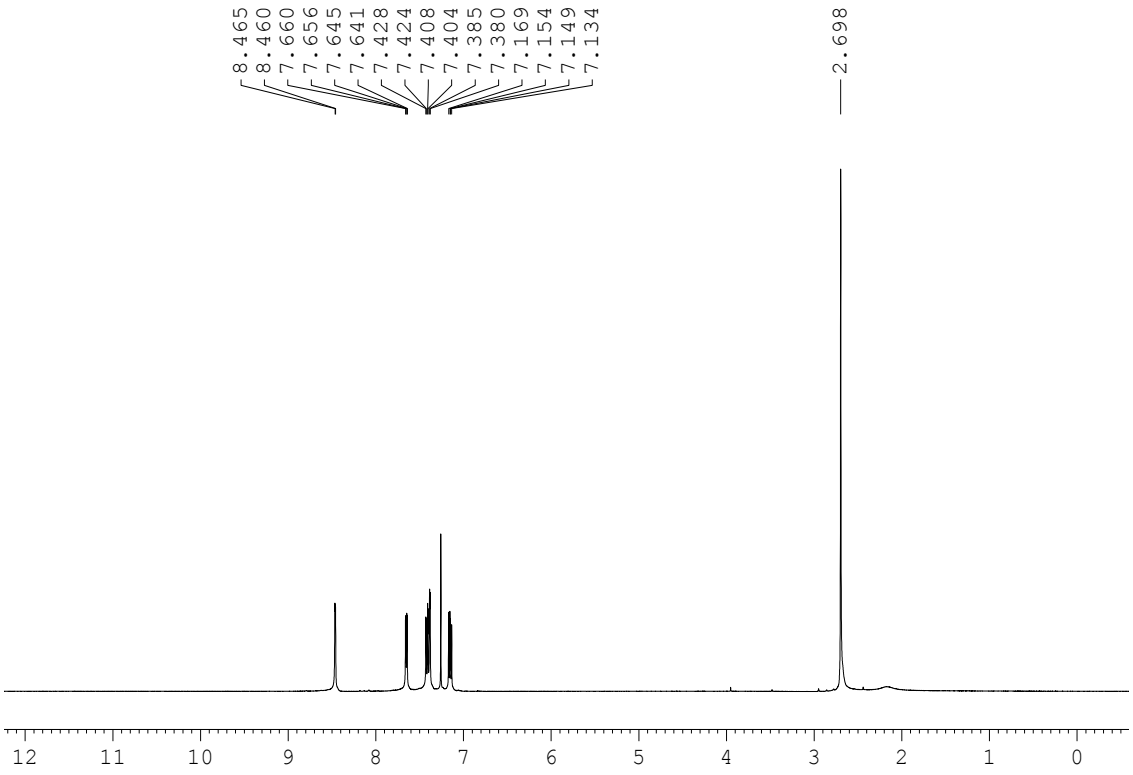

^{13}C {^{1}H} NMR ($CDCl_3$), 36

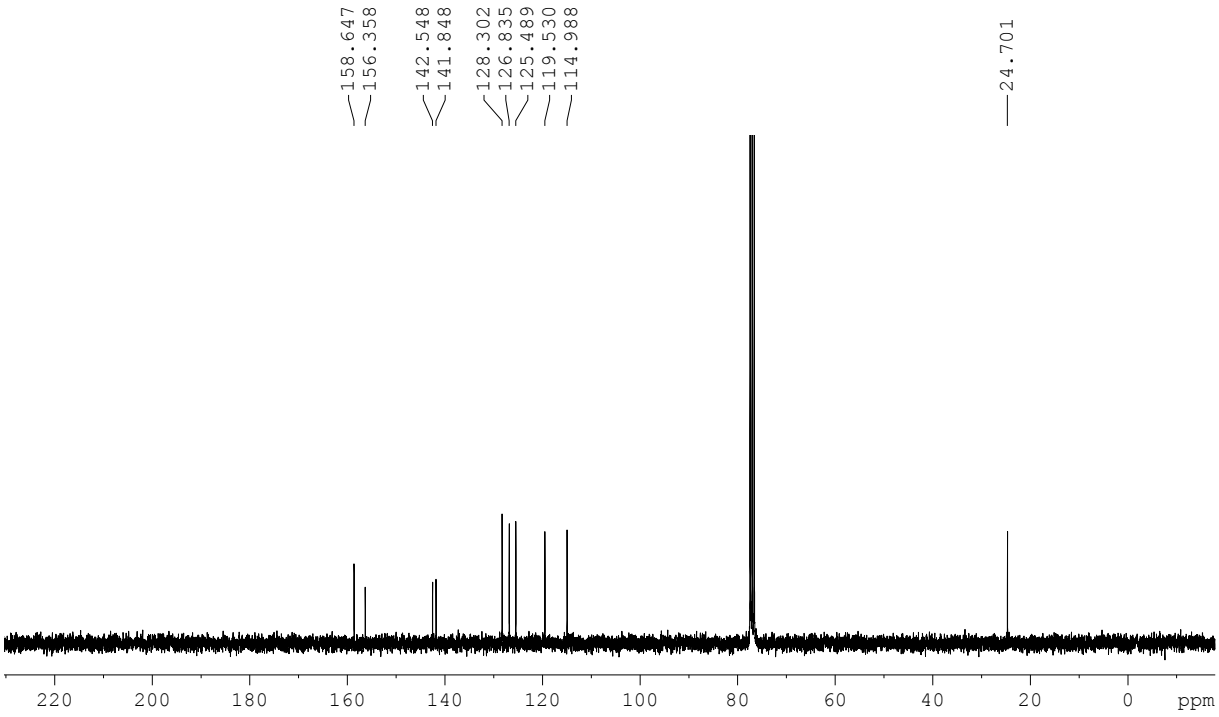

COSY ($CDCl_3$), 36

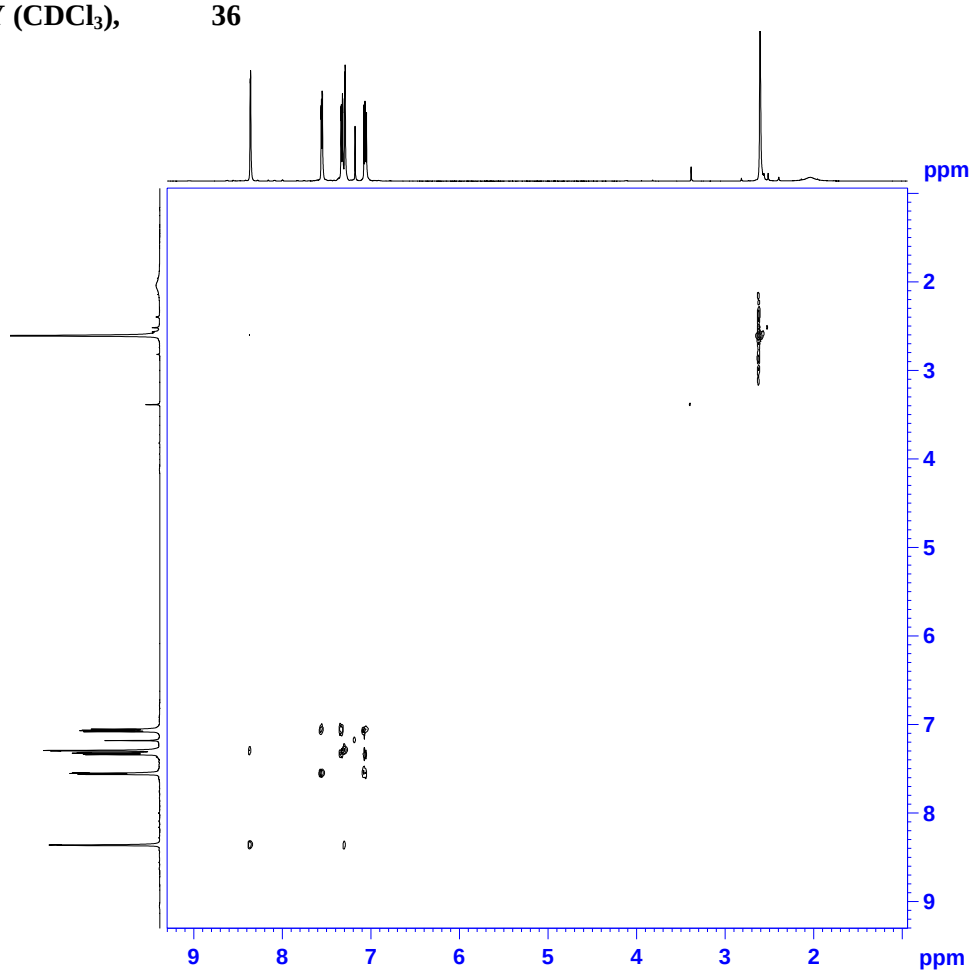

HSQC ($CDCl_3$), 36

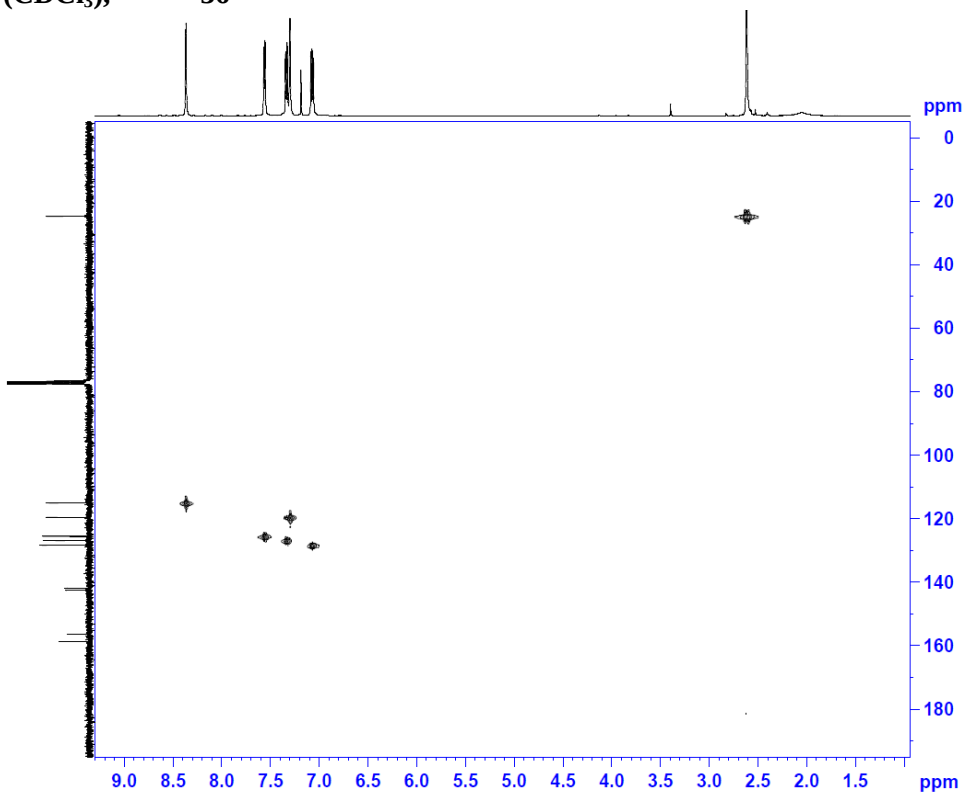

HMBC ($CDCl_3$), 36

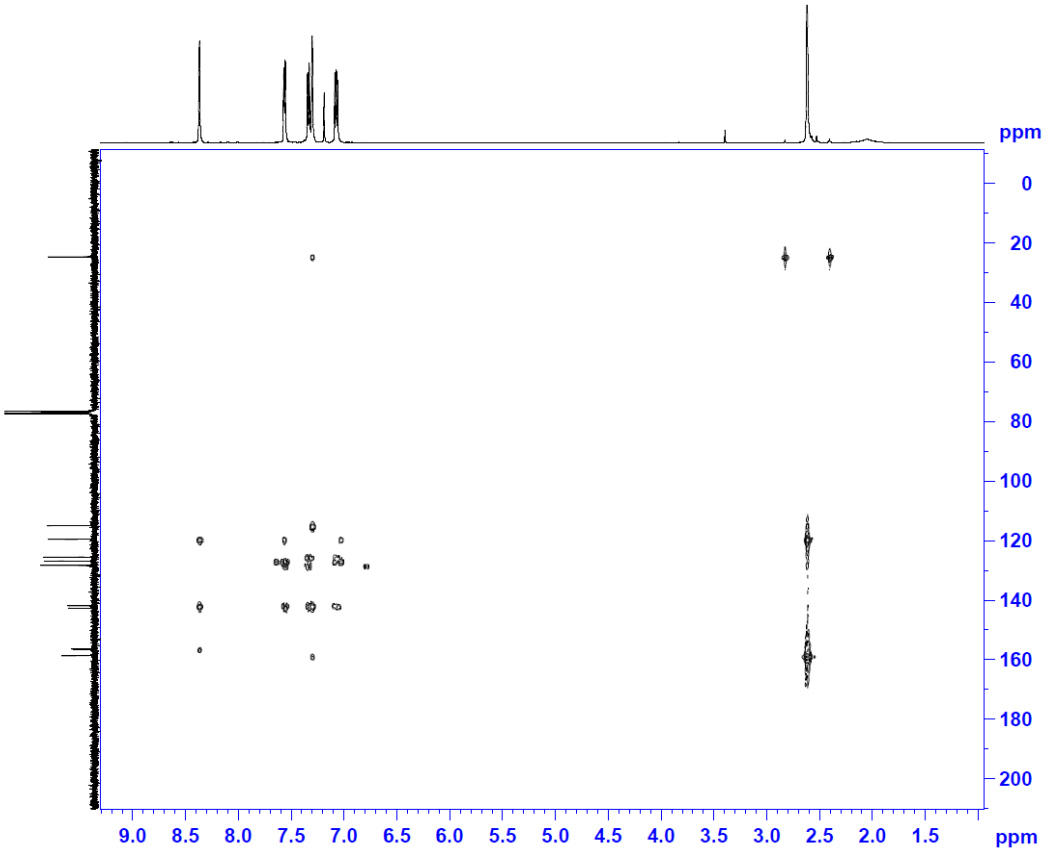

6,6'-dimethyl-4,4'-di(5,5'-bromothiophen-2-yl)-2,2'-bipyridine, 37

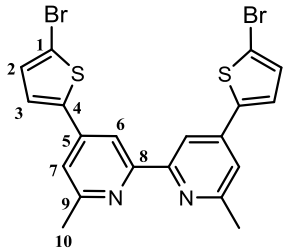

^{1}H NMR ($CDCl_3$), 37

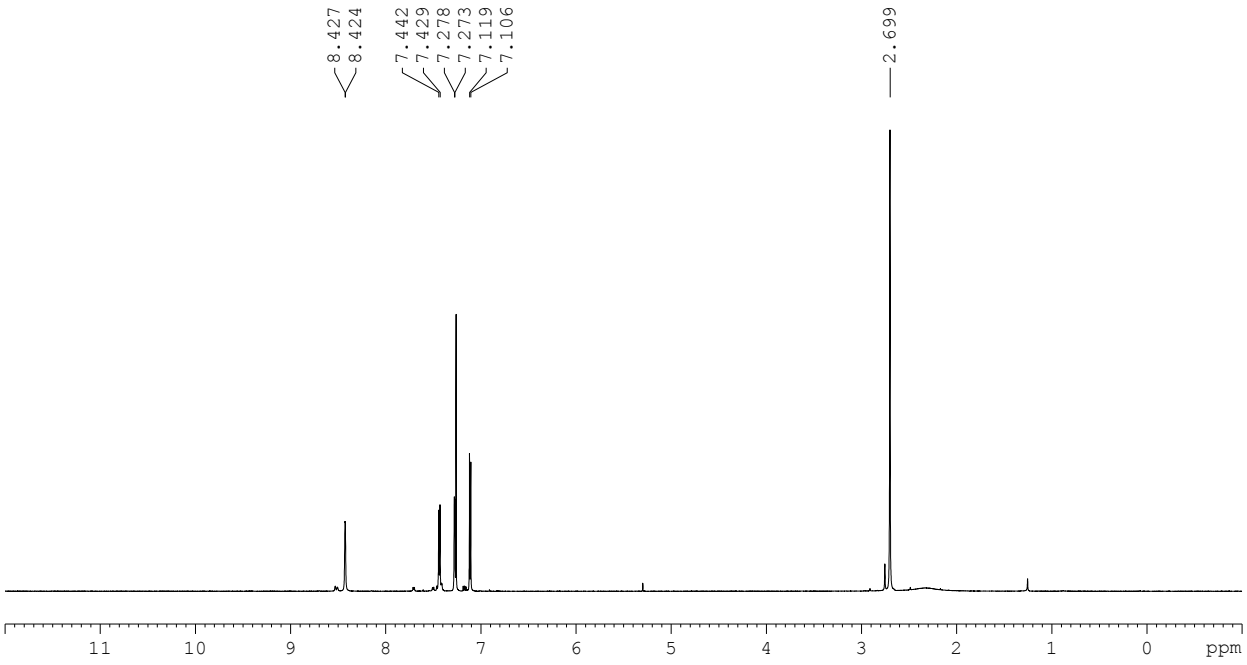

^{13}C {^{1}H} NMR ($CDCl_3$), 37

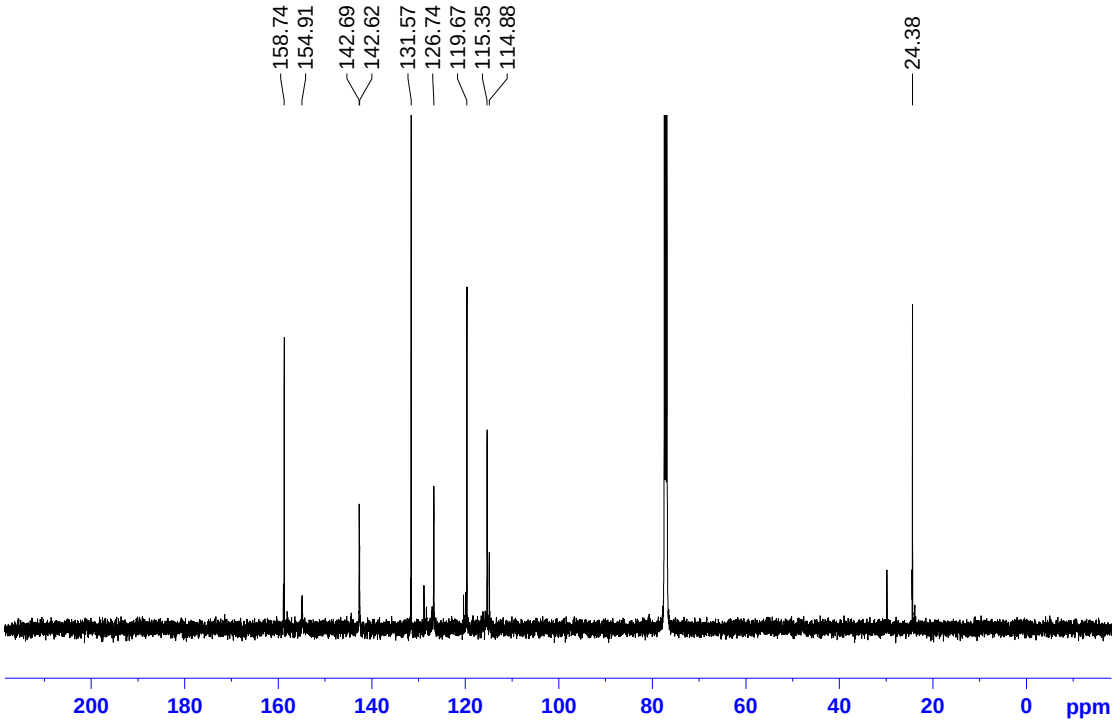

COSY ($CDCl_3$), 37

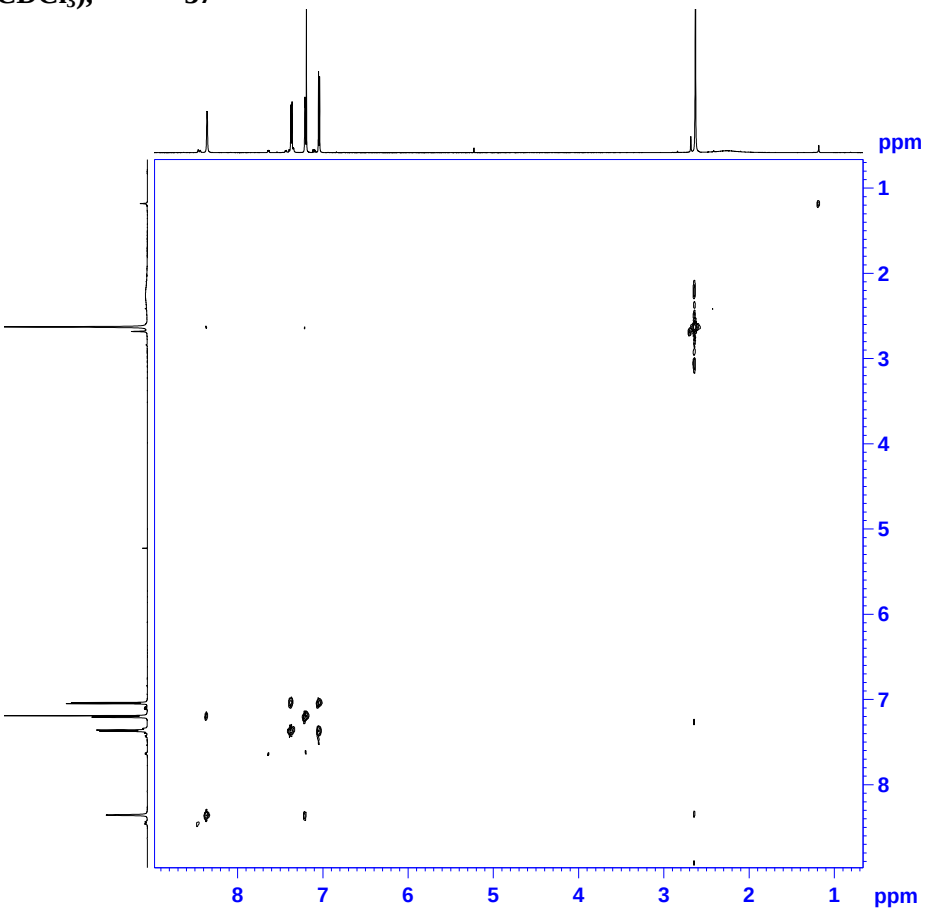

HMQC ($CDCl_3$), 37

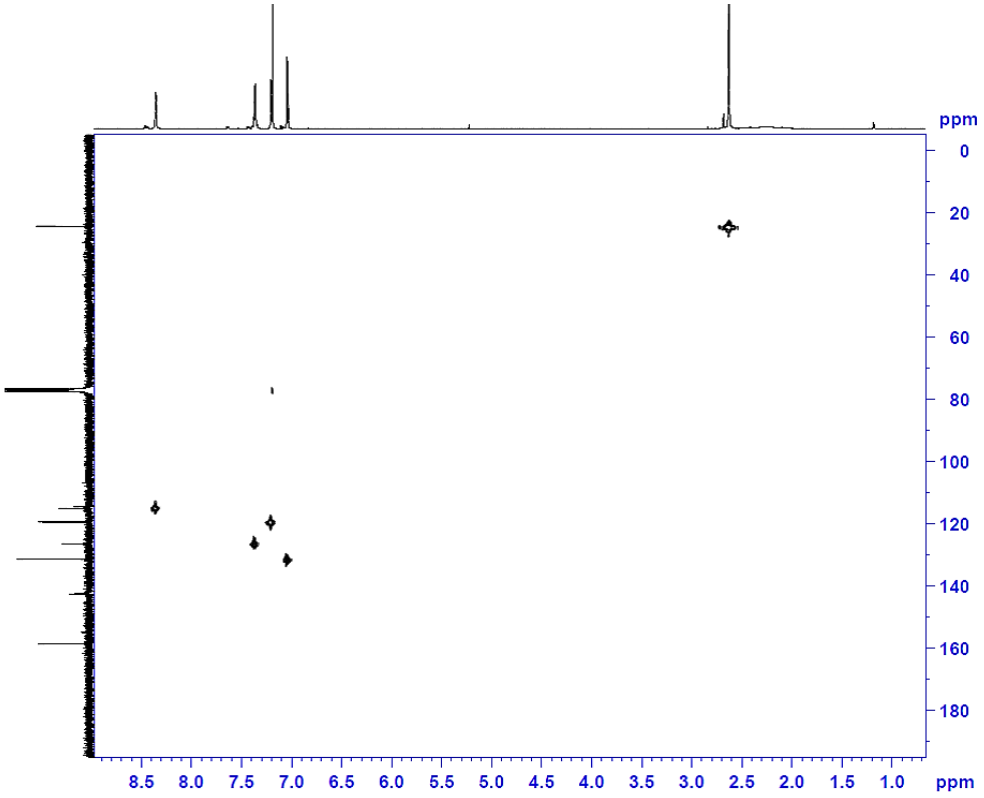

HMBC ($CDCl_3$), 37

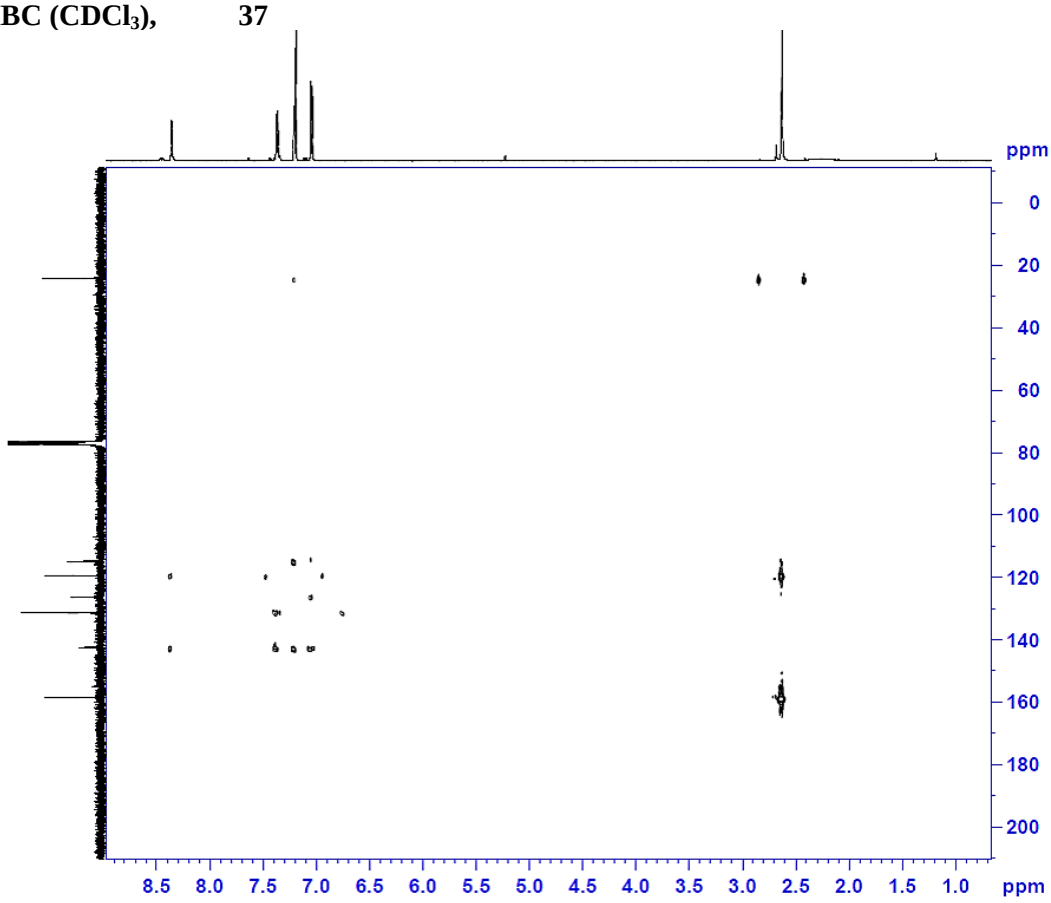

6,6'-dimethyl-5,5'-[2,2'-bipyridin-4,4'-diyl]-bis[thiophene-2-methanoate], 38

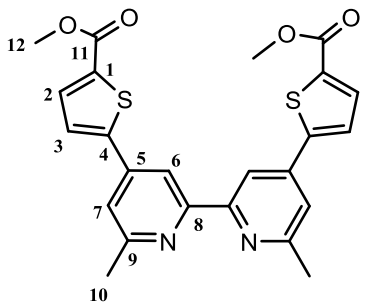

^{1}H NMR ($CDCl_3$), 38

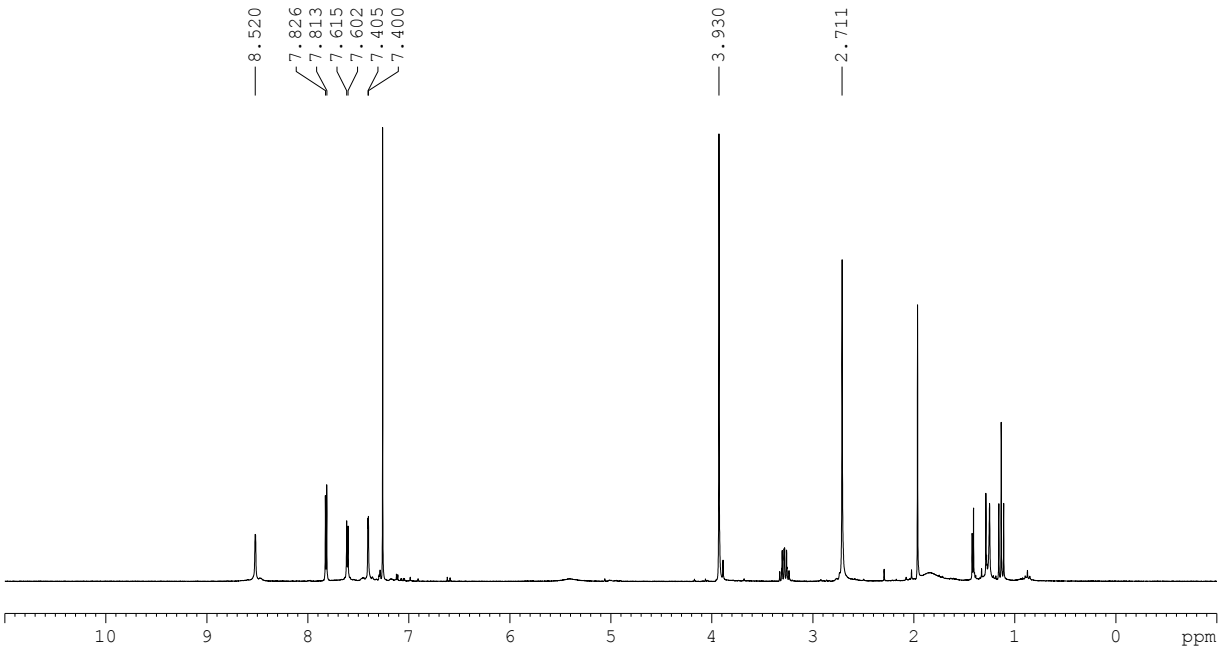

^{13}C {^{1}H} NMR ($CDCl_3$), 38

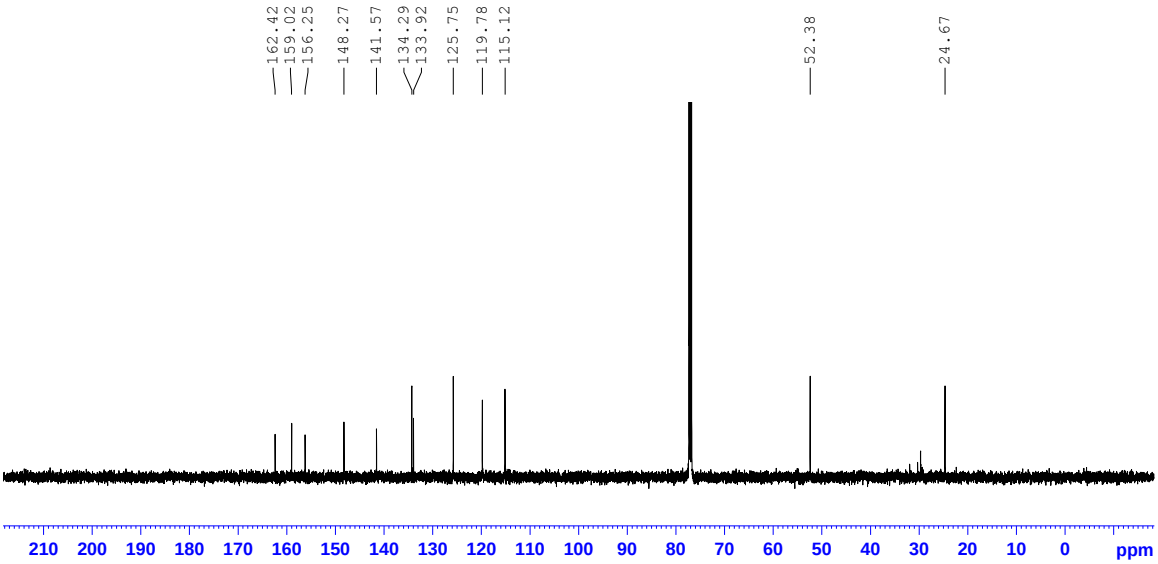

COSY ($CDCl_3$), 38

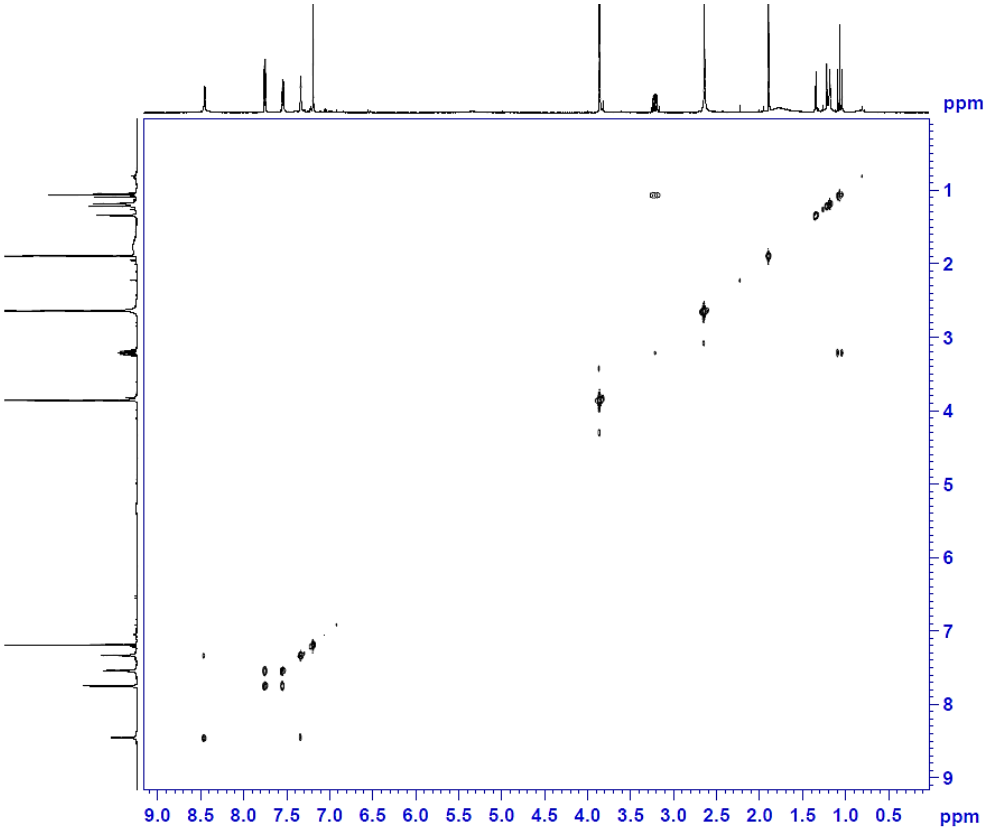

HSQC ($CDCl_3$), 38

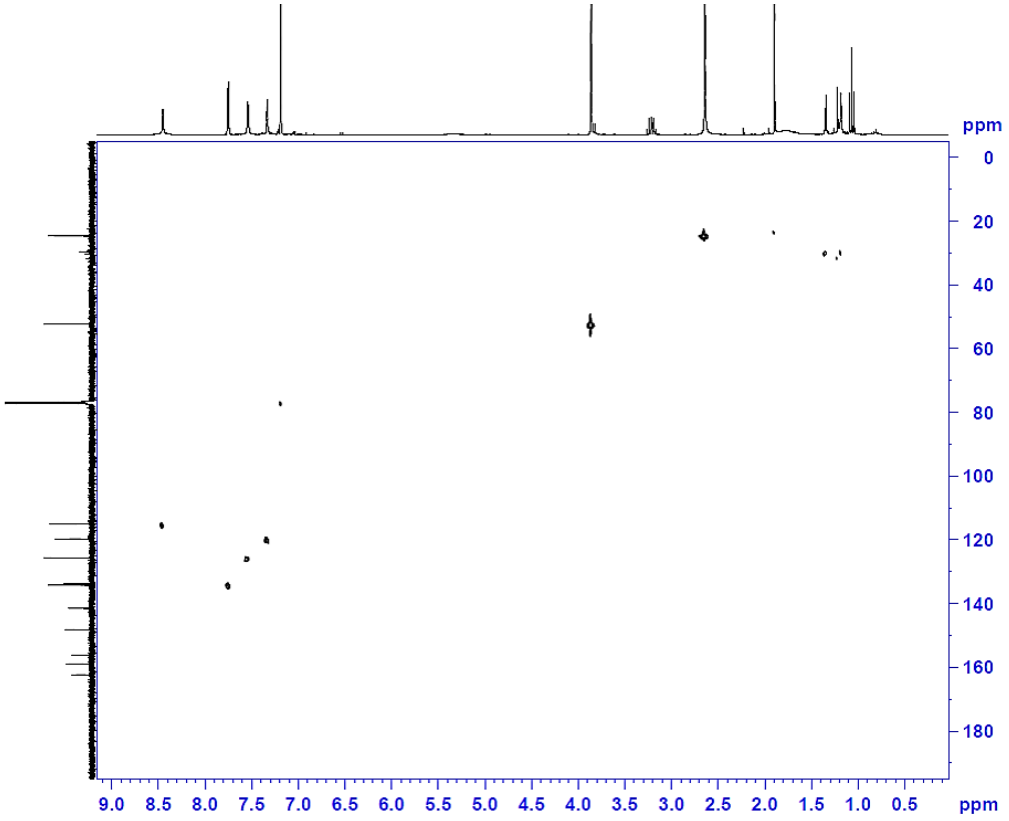

HMBC ($CDCl_3$), 38

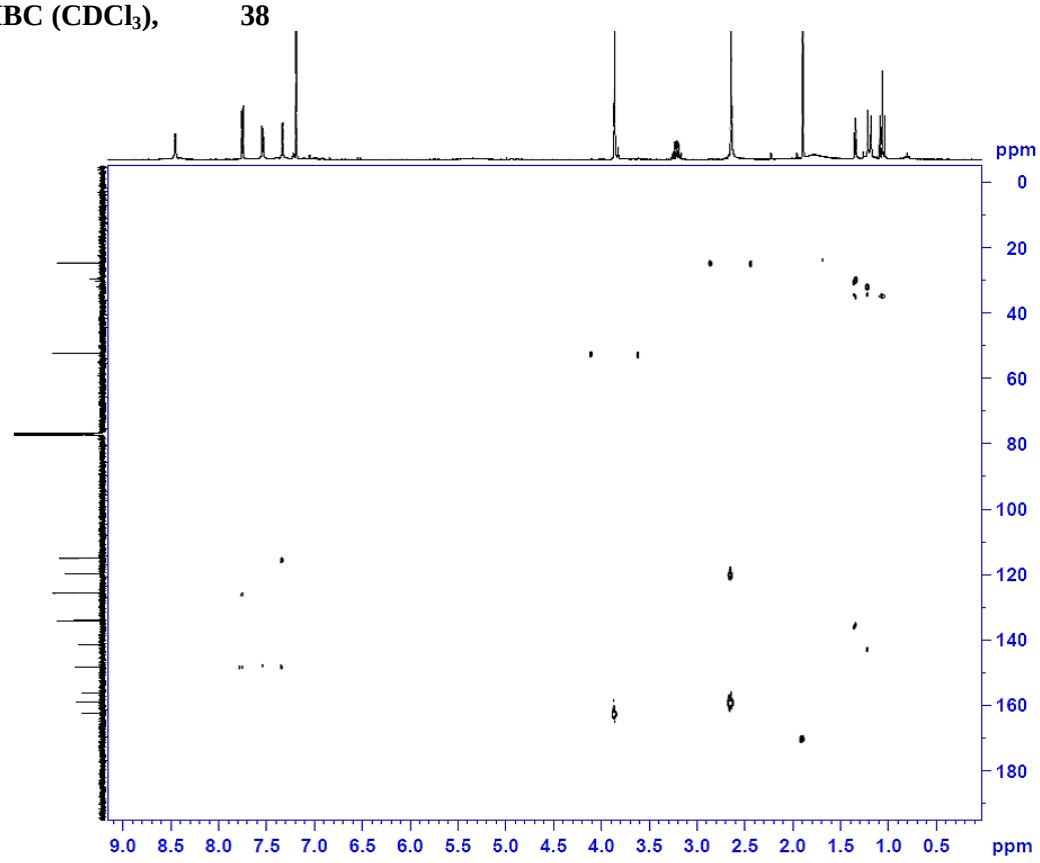

6,6'-dimethyl-5,5'-[2,2'-bipyridin-4,4'-diyl]-bis[thiophene-2-carboxylic acid], 39

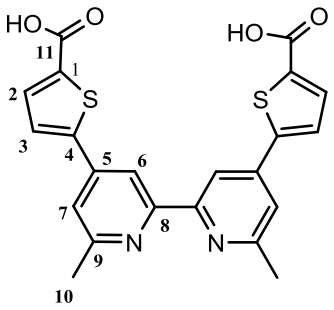

^{1}H NMR (CD_3OD, with a drop of 1 M NaOH), 39

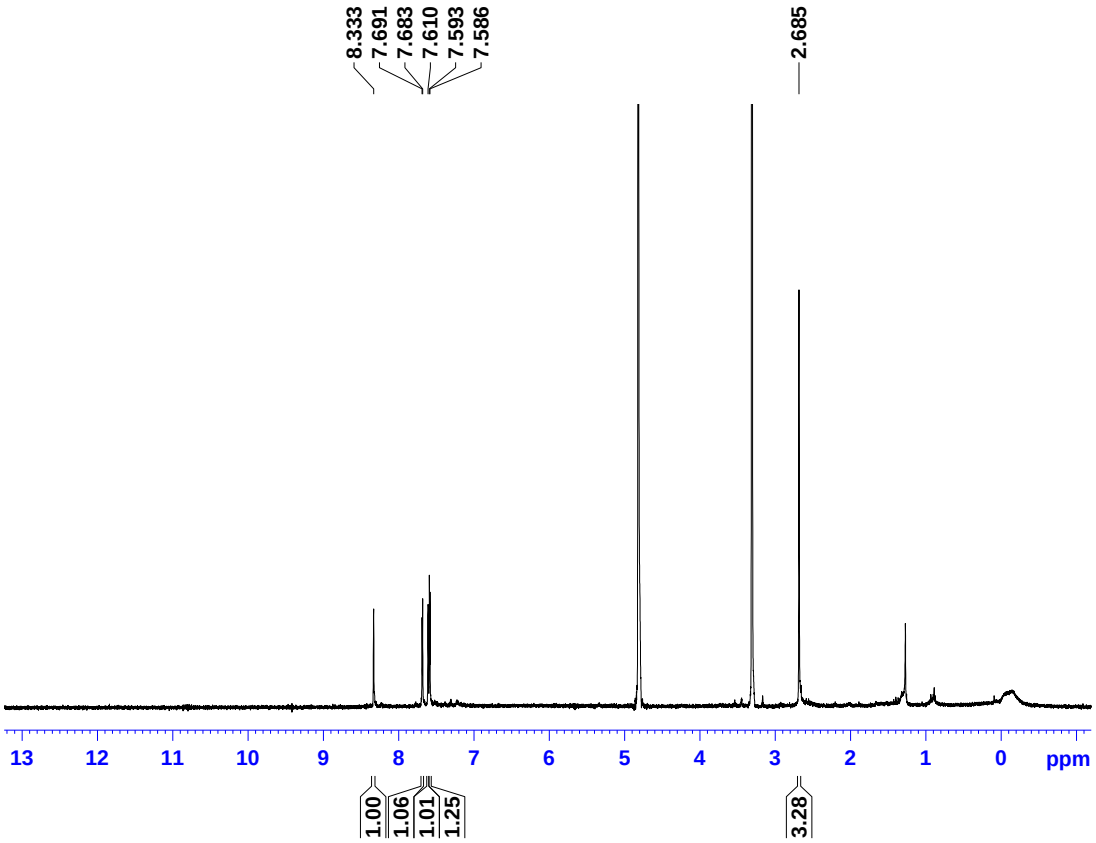

^{13}C {^{1}H} NMR (CD_3OD, with a drop of 1 M NaOH), 39

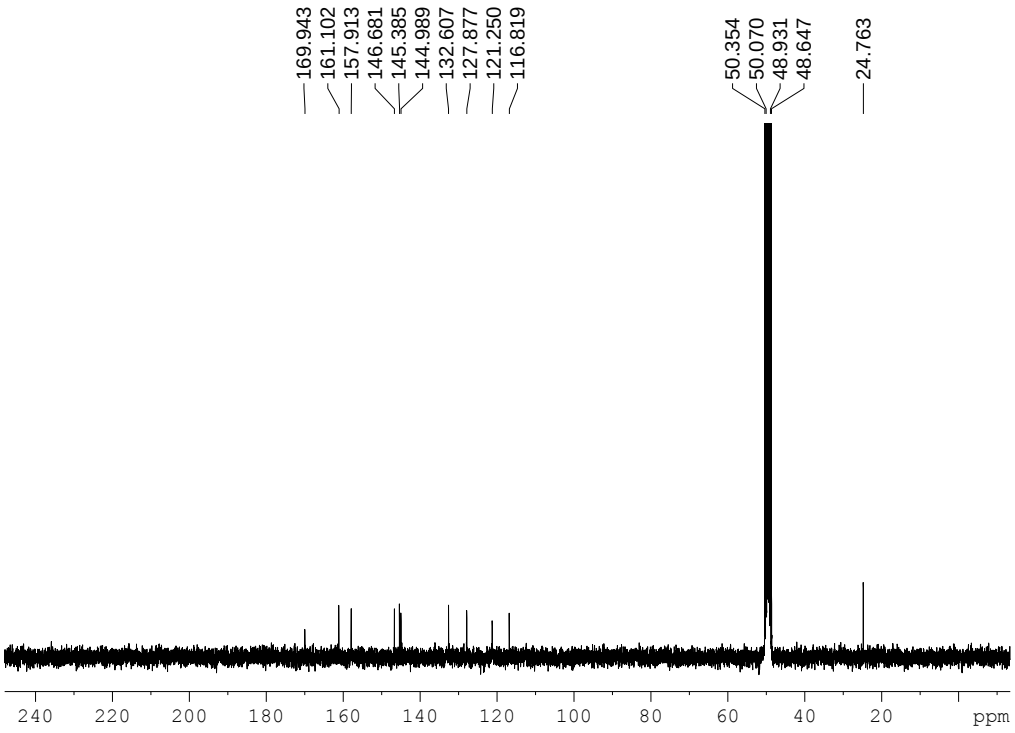

COSY (CD_3OD), 39

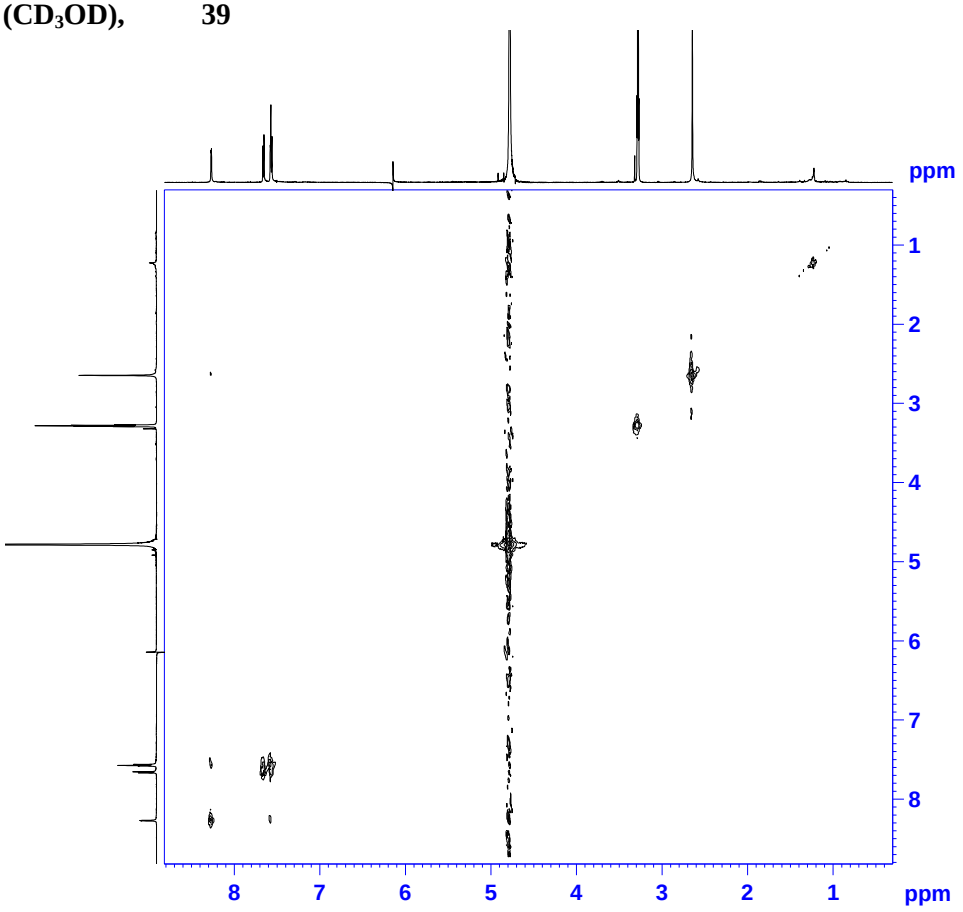

HMQC (CD_3OD), 39

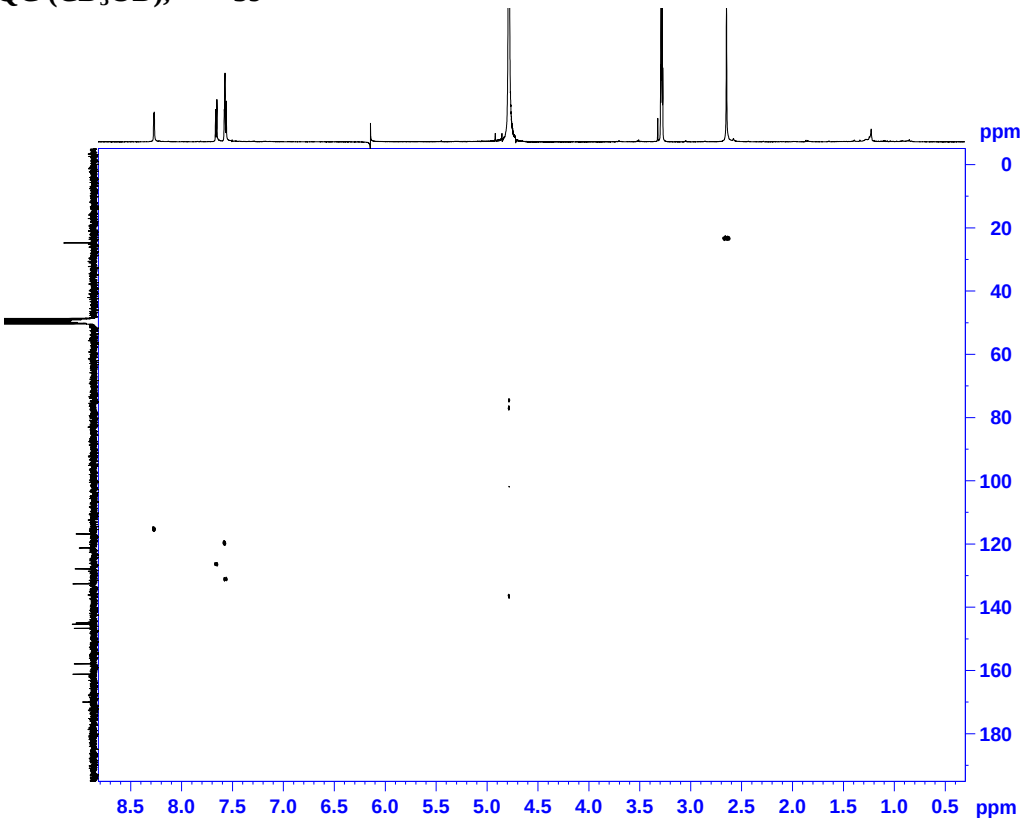

HMBC (CD_3OD), 39

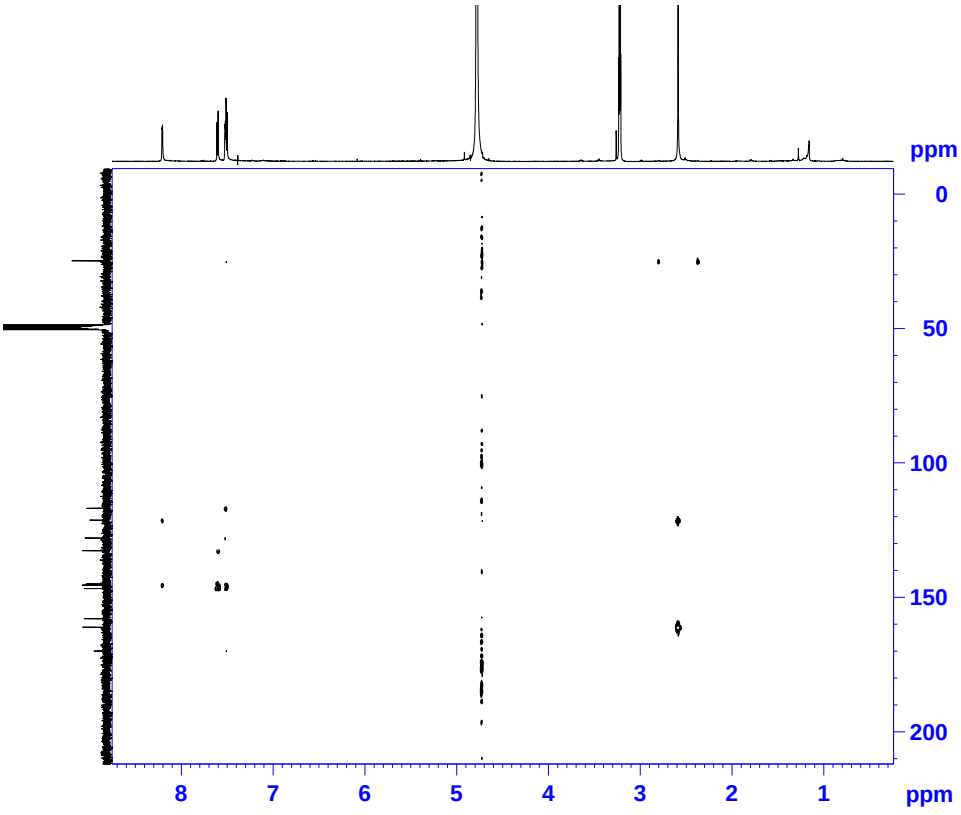

[Cu(6,6'-dimethyl-4,4'-di(thiophen-2-yl)-2,2'-bipyridine)$_2$][PF$_6$], 40

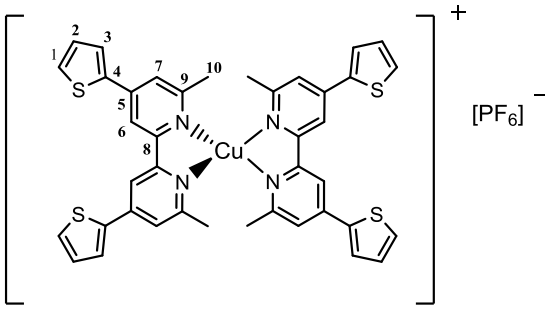

^{1}H NMR (DMSO-d$_6$), 40

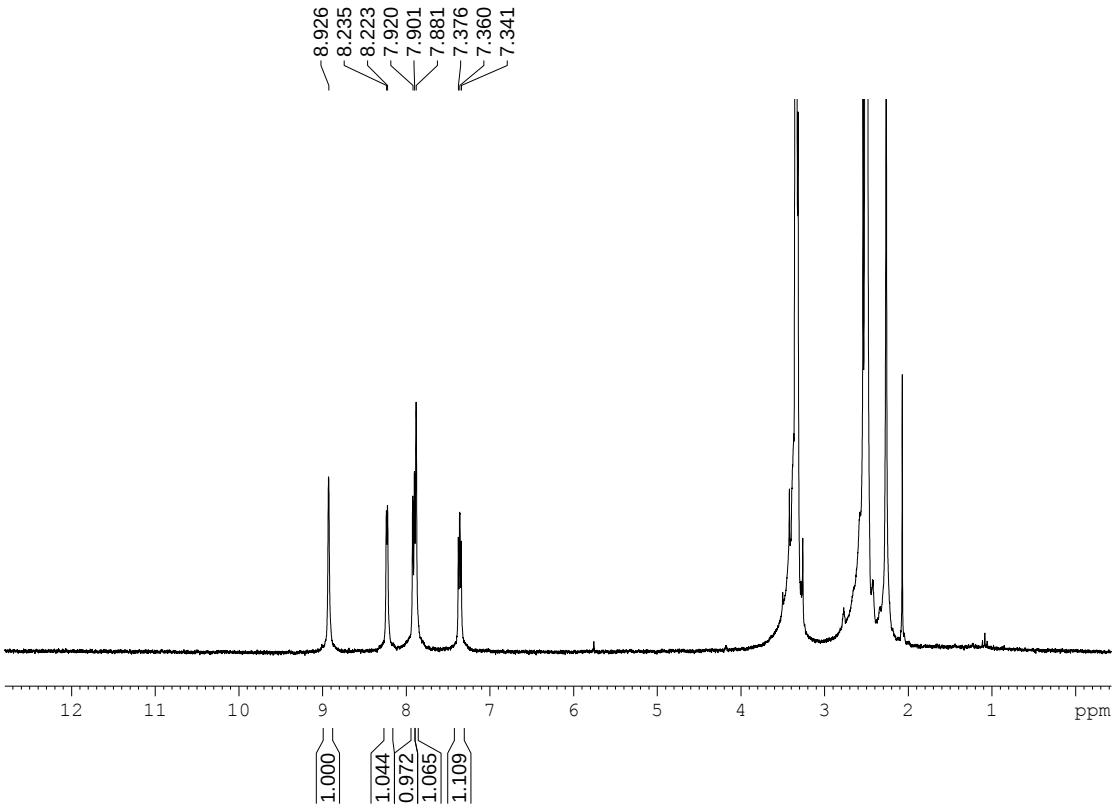

^{13}C {^{1}H} NMR (DMSO-d_6), 40

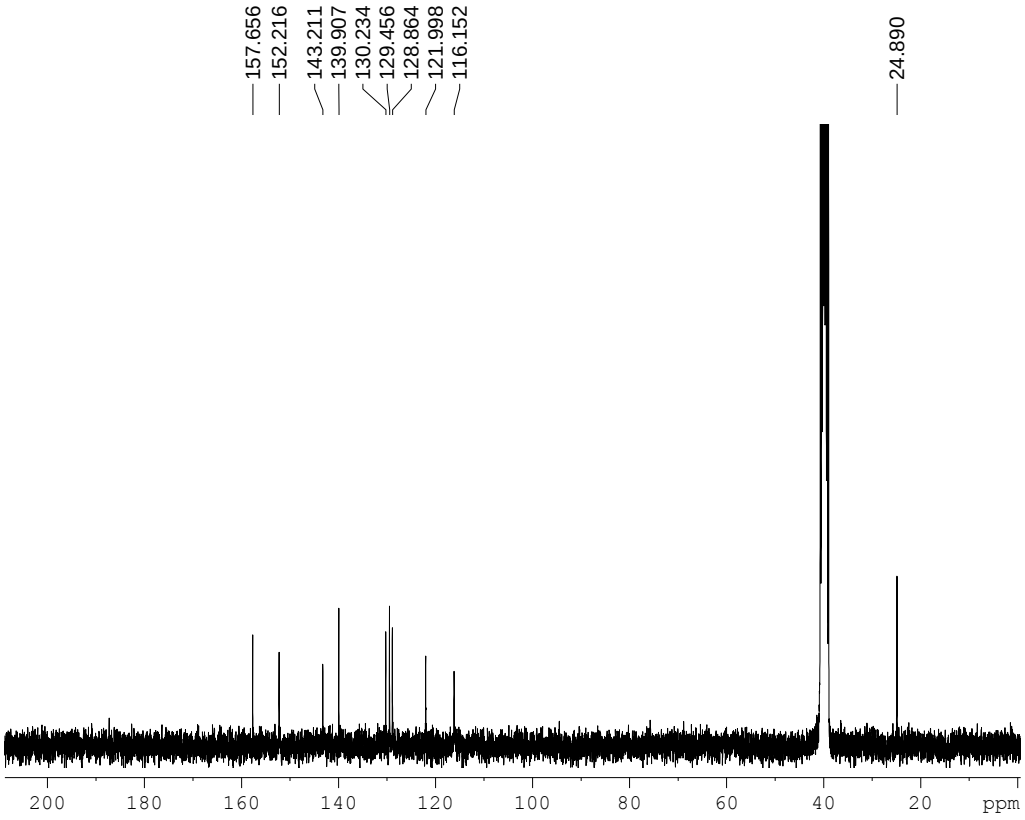

[Cu(6,6'-dimethyl-5,5'-[2,2'-bipyridin-4,4'-diyl]-bis[thiophene-2-methanoate)$_2$][PF$_6$], 41

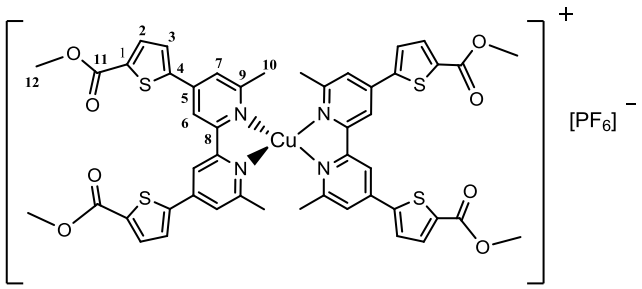

^{1}H NMR (acetone-d$_6$), 41

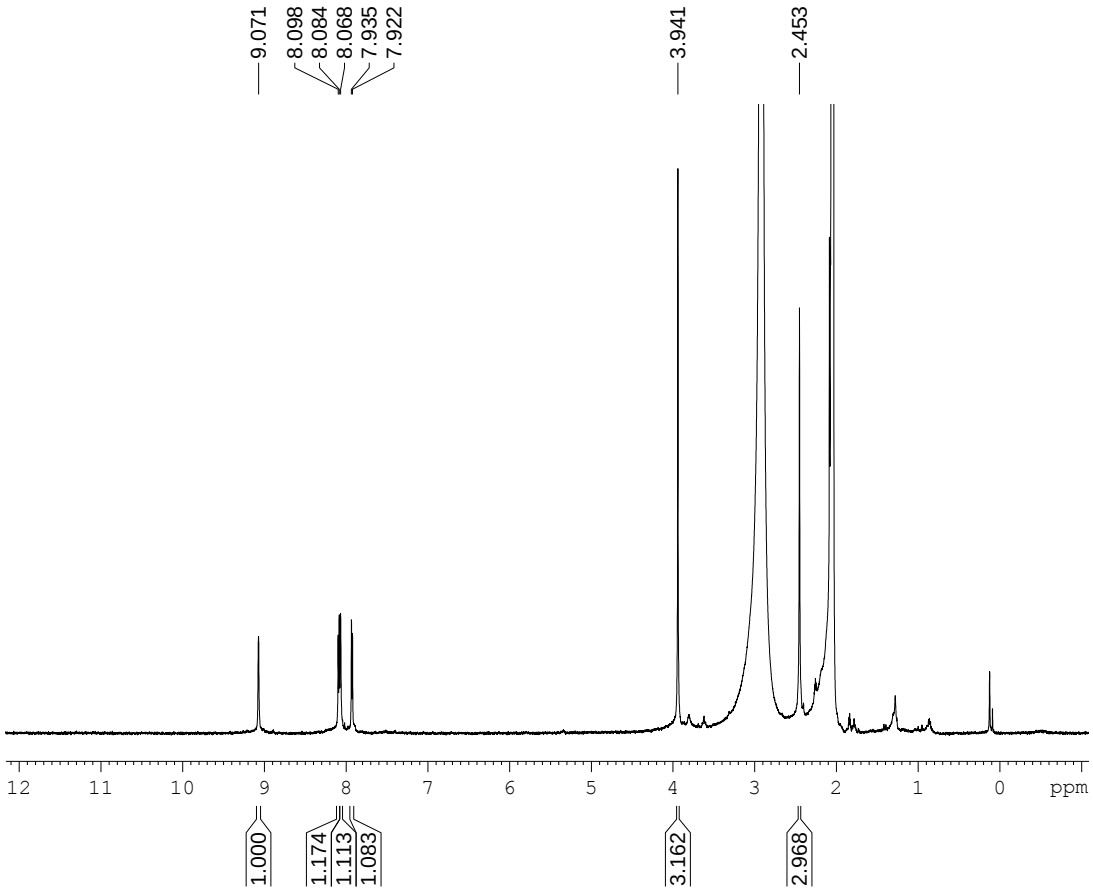

^{13}C {^{1}H} NMR (acetone-d_6), 41

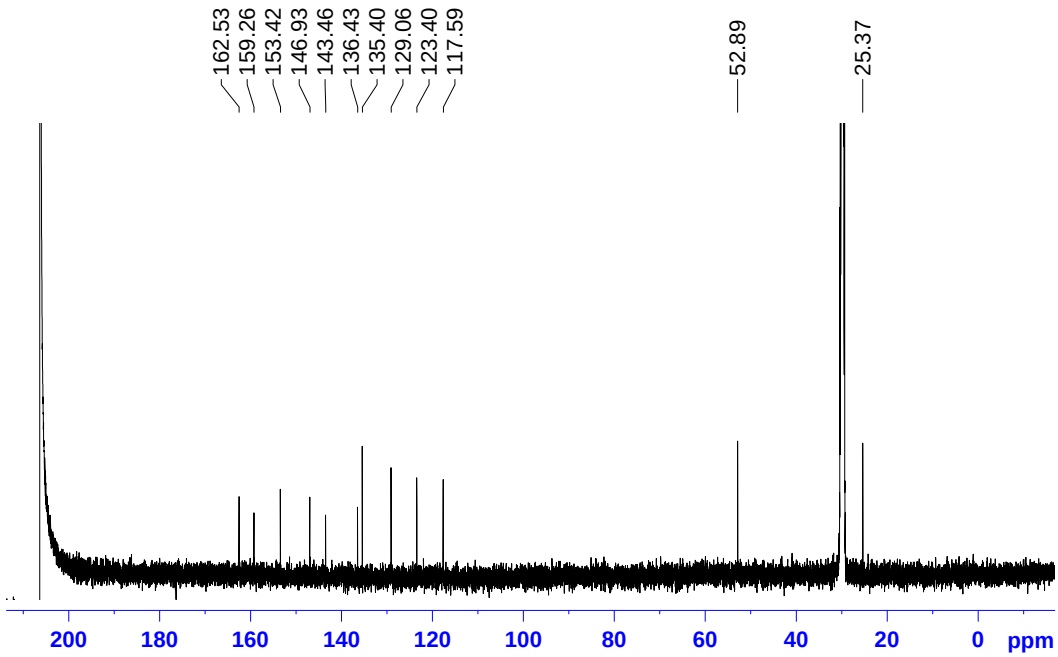

COSY (acetone-d_6), 41

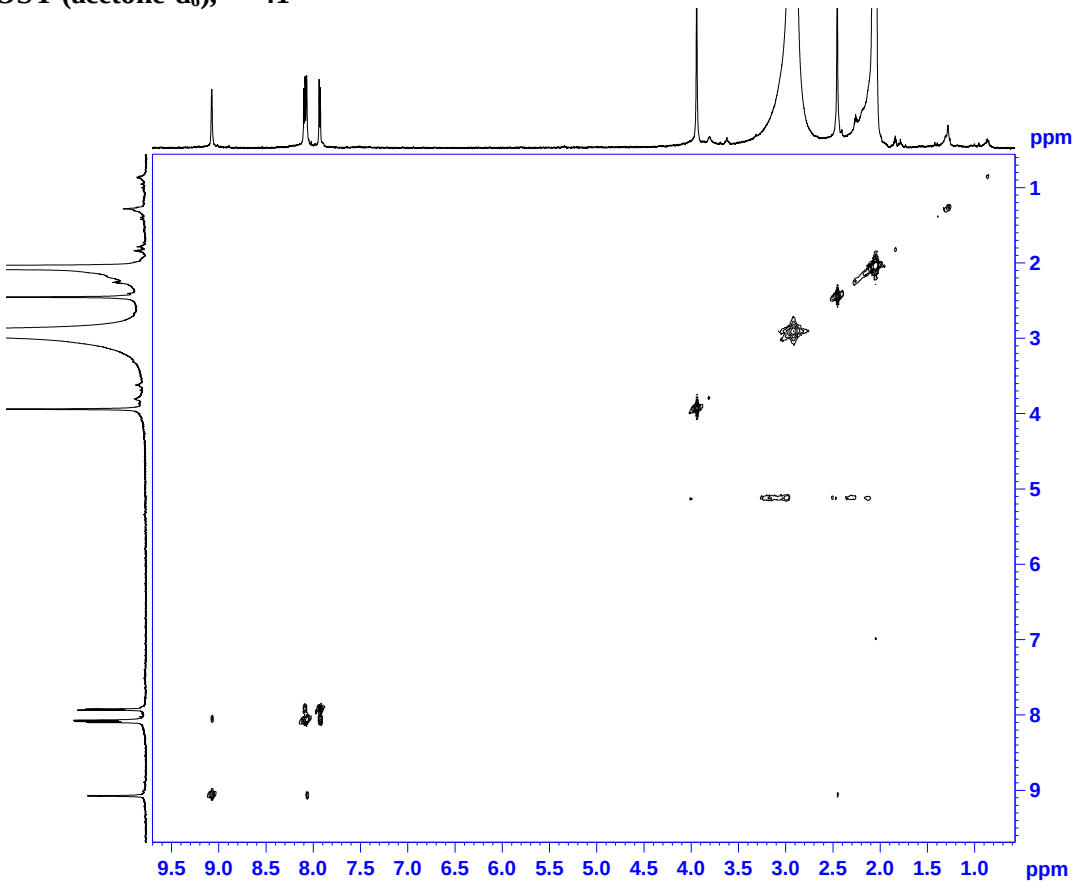

HSQC (acetone-d_6), 41

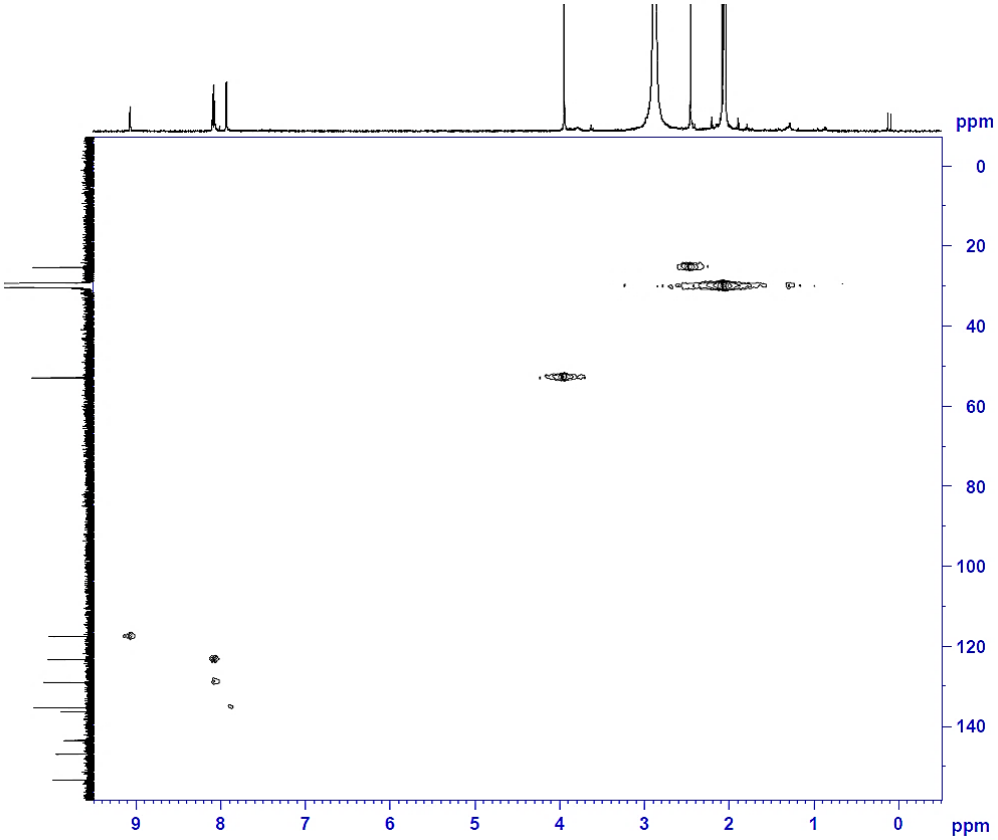

HMBC (acetone-d_6), 41

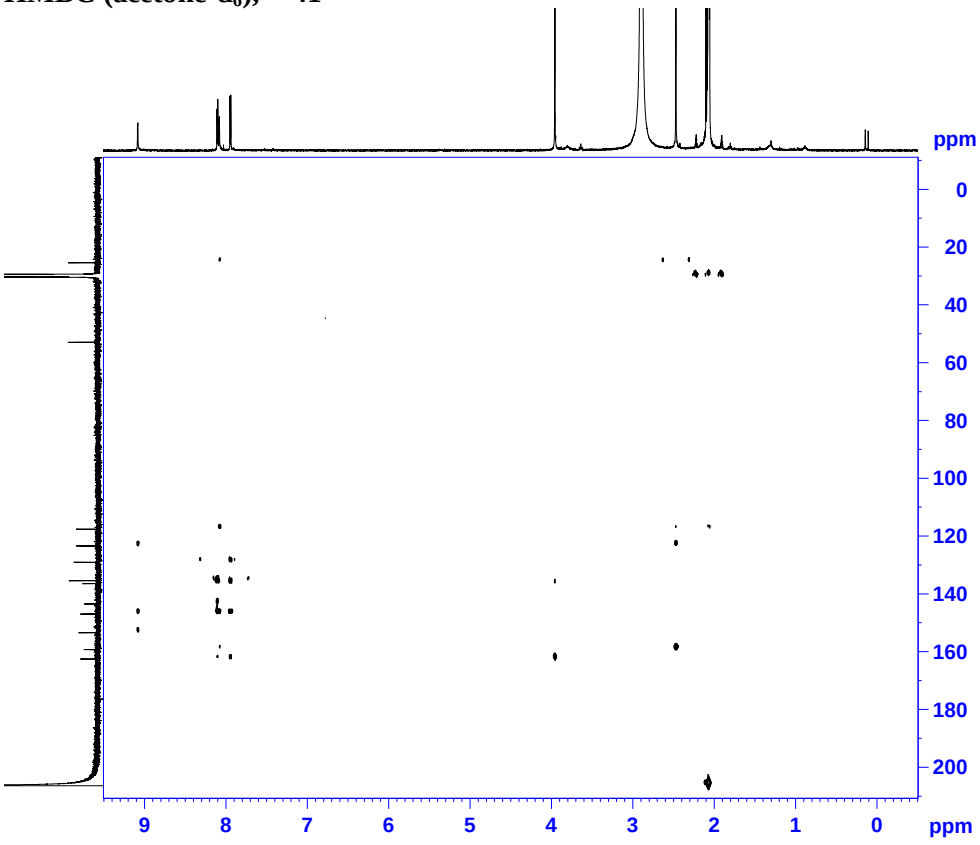

[Cu(6,6'-dimethyl-5,5'-[2,2'-bipyridin-4,4'-diyl]-bis[thiophene-2-carboxylic acid])$_2$][PF$_6$], 42

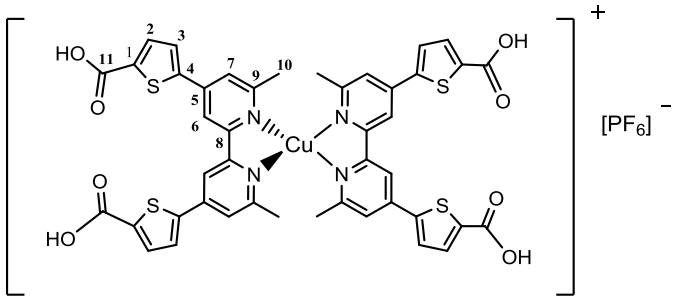

^{1}H NMR (CD$_3$OD), 42

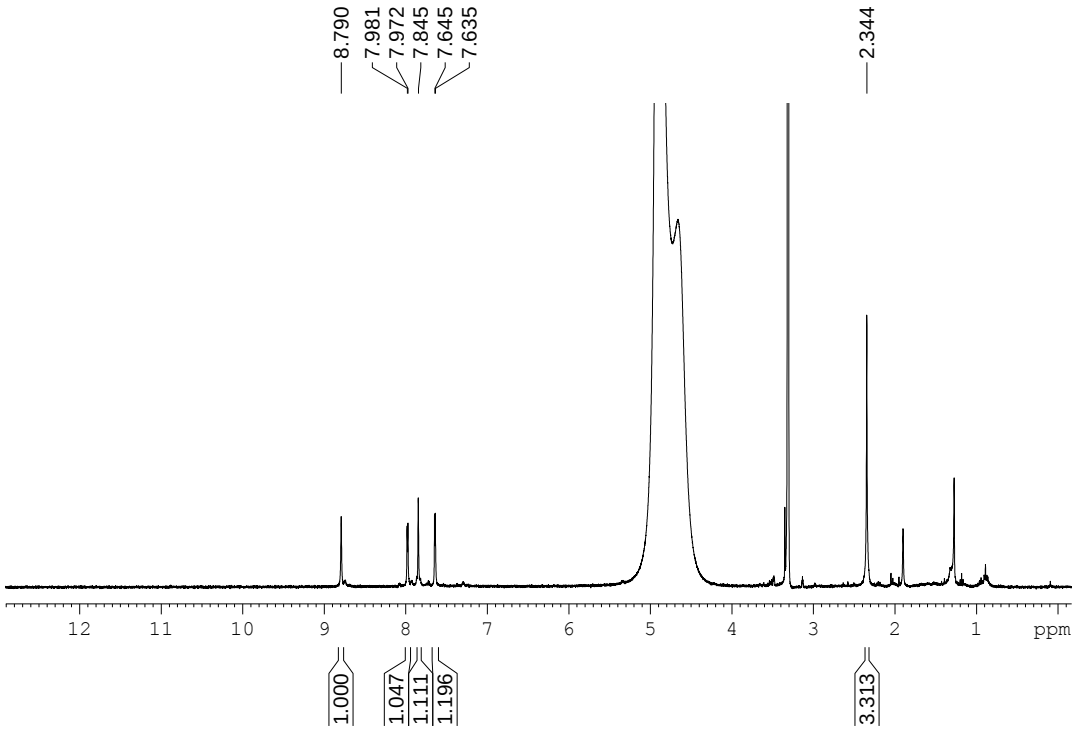

^{13}C {^{1}H} NMR (CD_3OD), 42

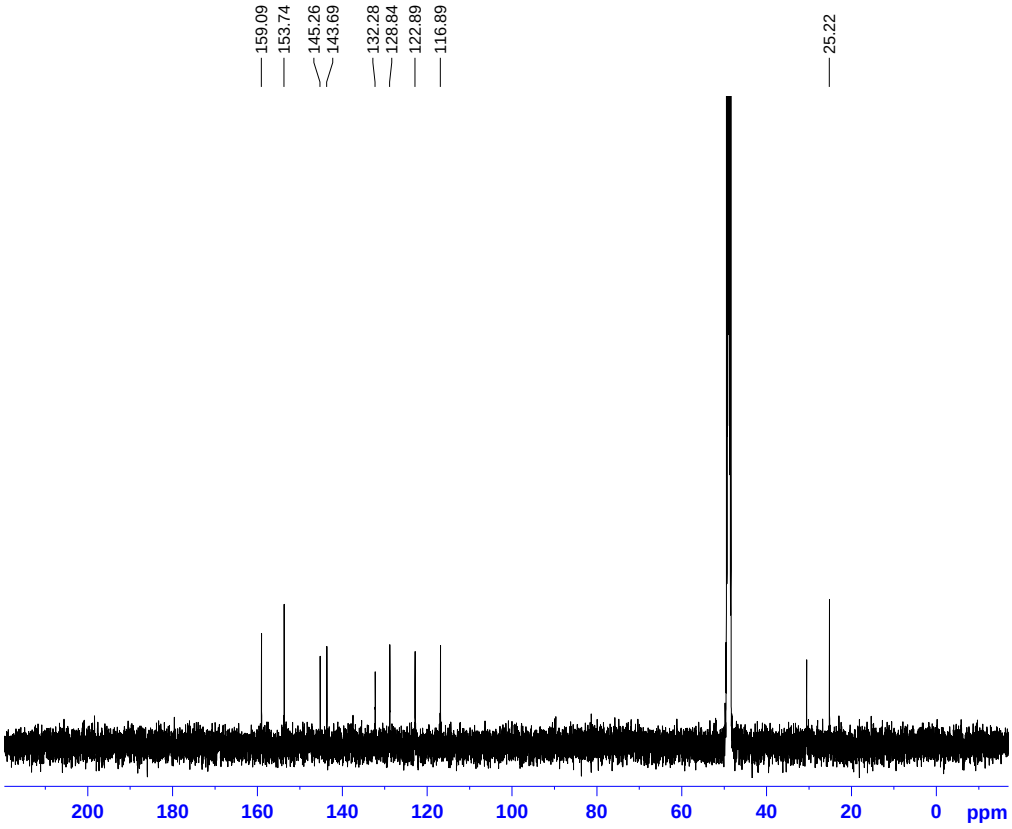

HMBC (CD_3OD), 42

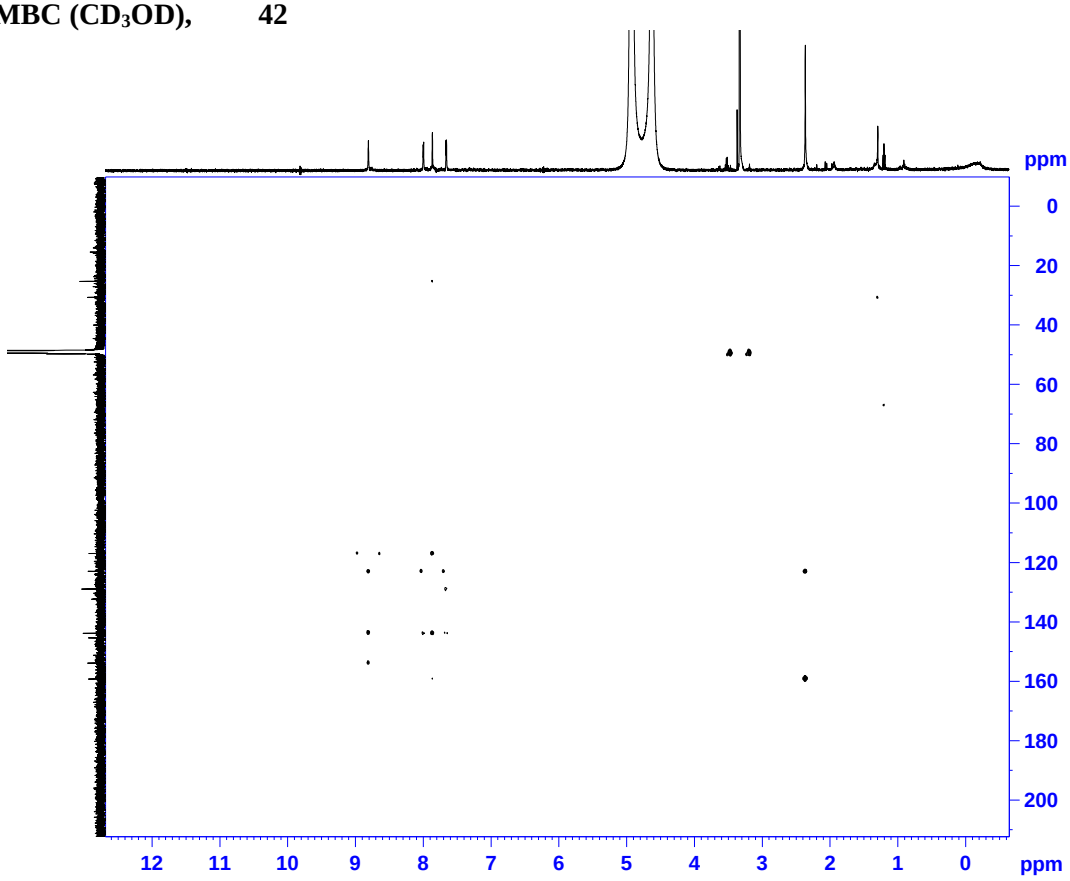

1,6-di(2-furyl)hexa-1,5-diene-3,4-dione, 43

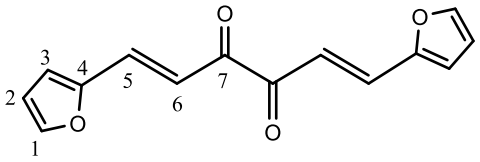

^{1}H NMR ($CDCl_3$), 43

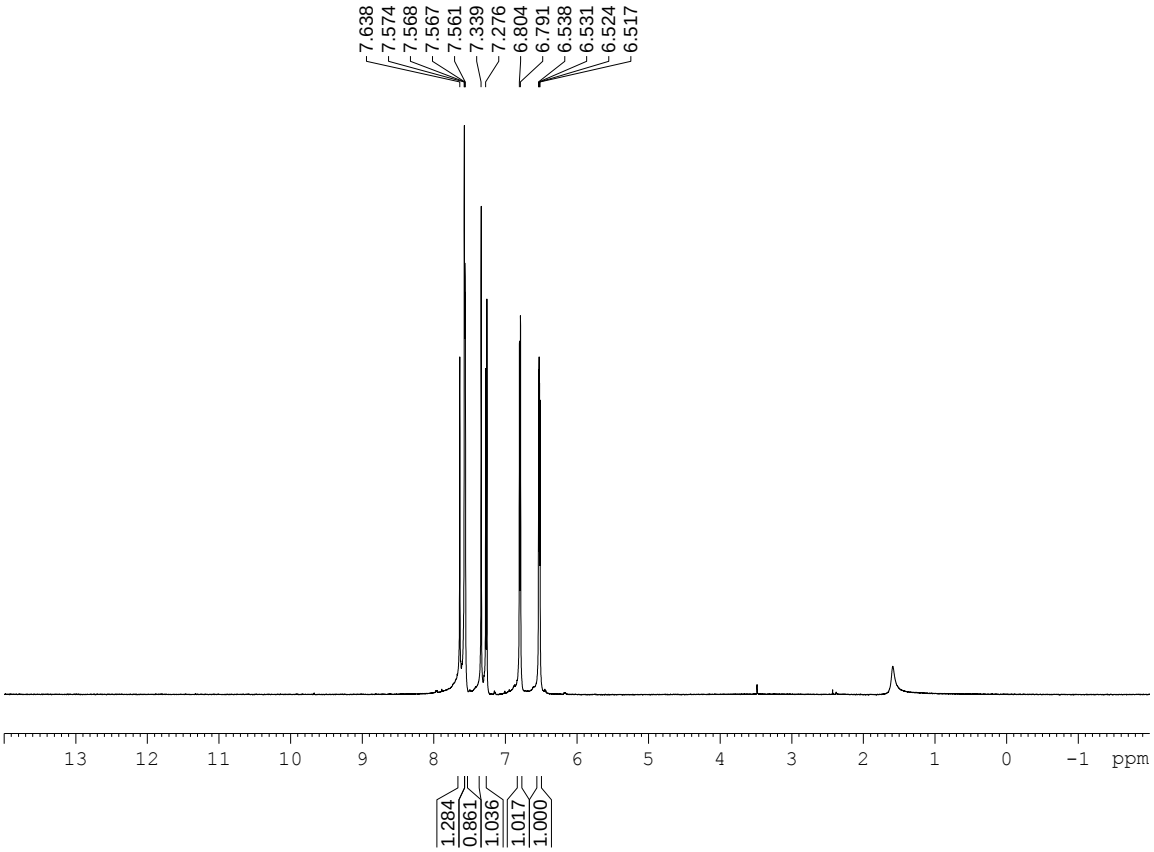

^{13}C {^{1}H} NMR ($CDCl_3$), 43

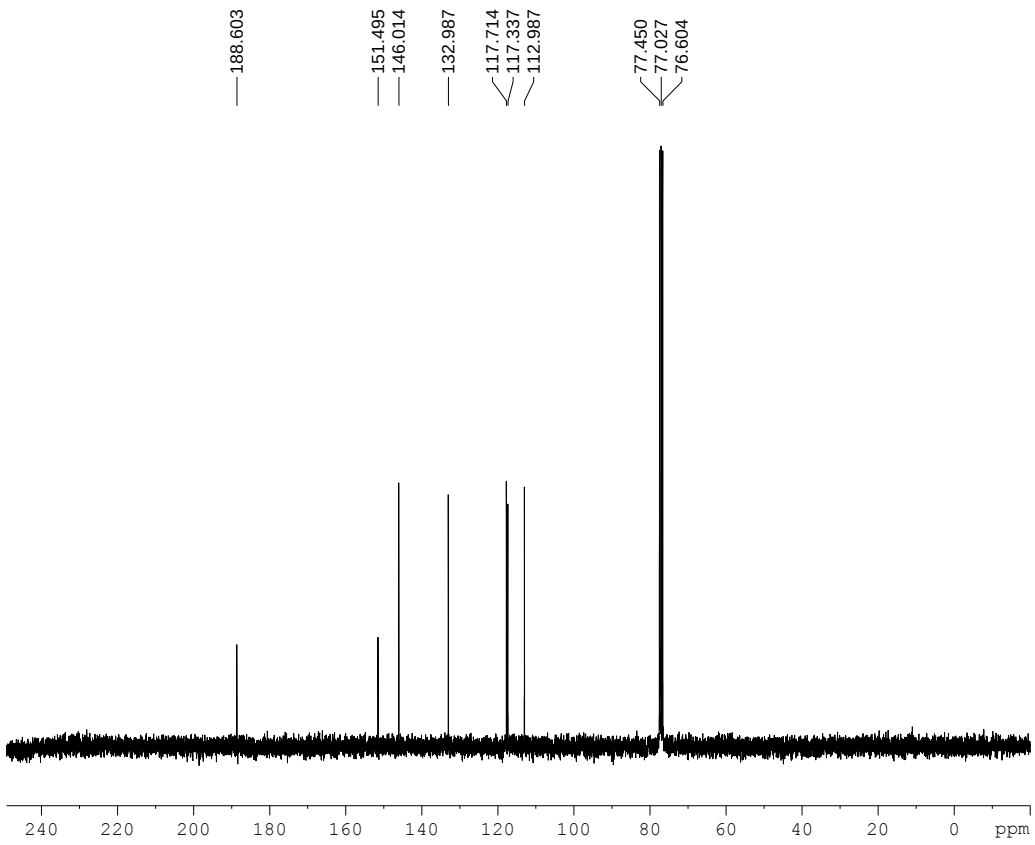

4,4'-di(2-furyl)-6,6'-dimethyl-2,2'-bipyridine, 44

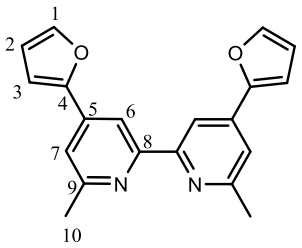

^{1}H NMR ($CDCl_3$), 44

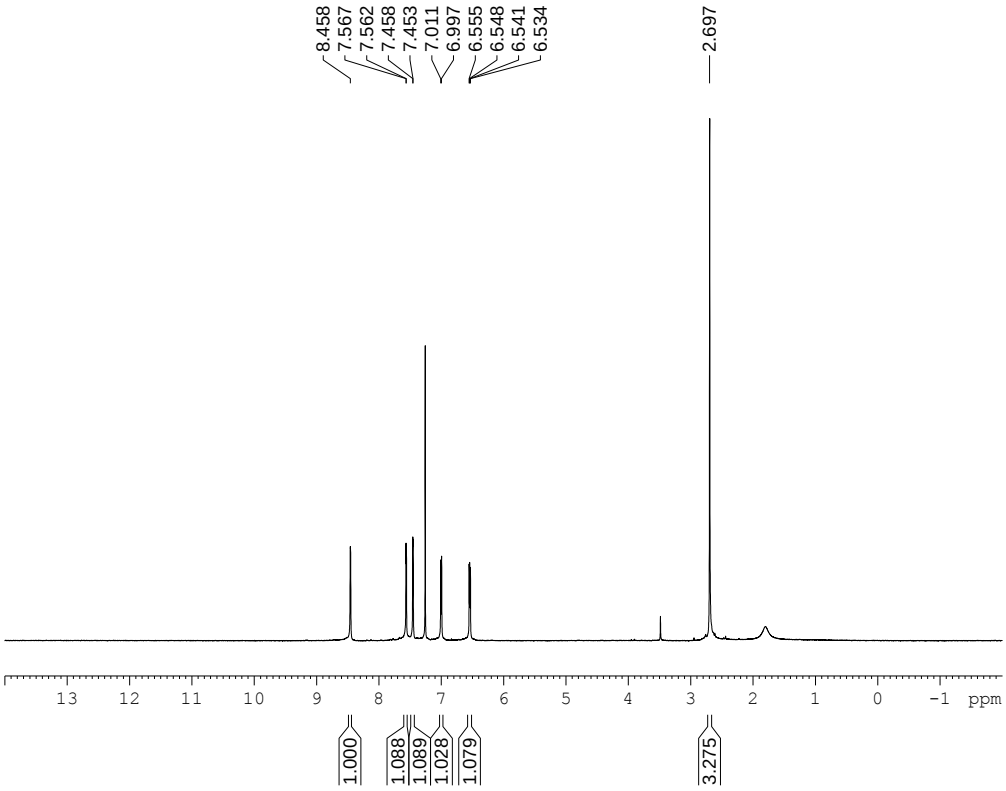

^{13}C {^{1}H} NMR ($CDCl_3$), 44

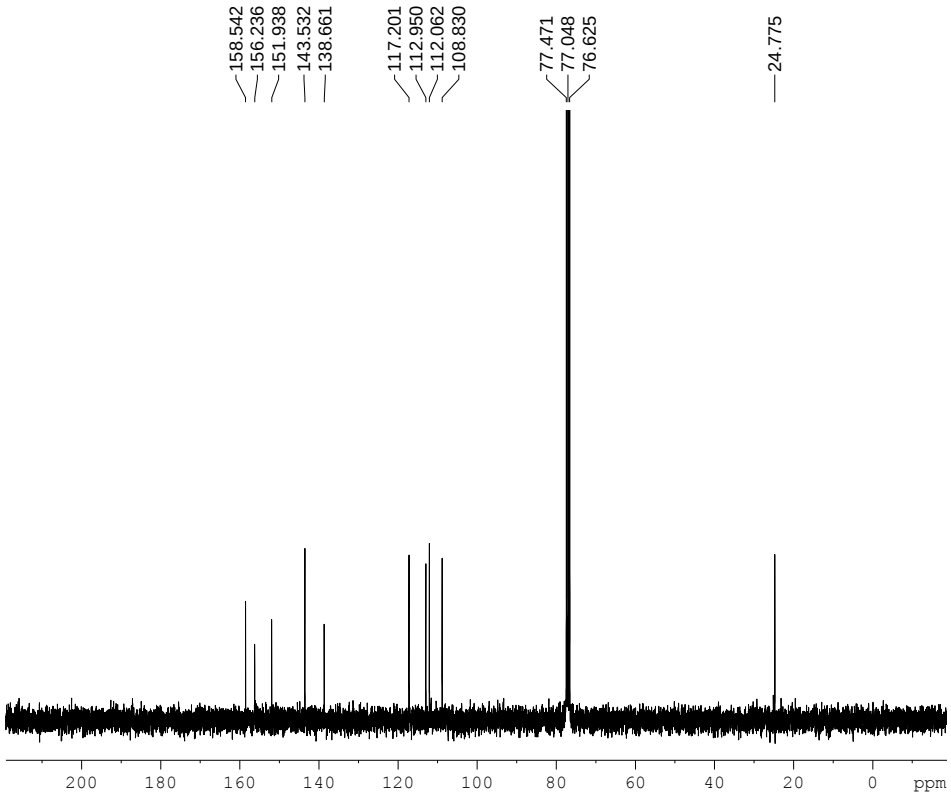

6,6'-Dimethyl-2,2'-bipyridine-4,4'-dicarboxylic acid, 45

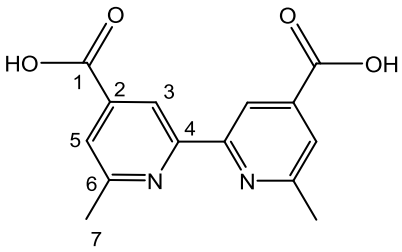

^{1}H NMR (DMSO-d_6), 45

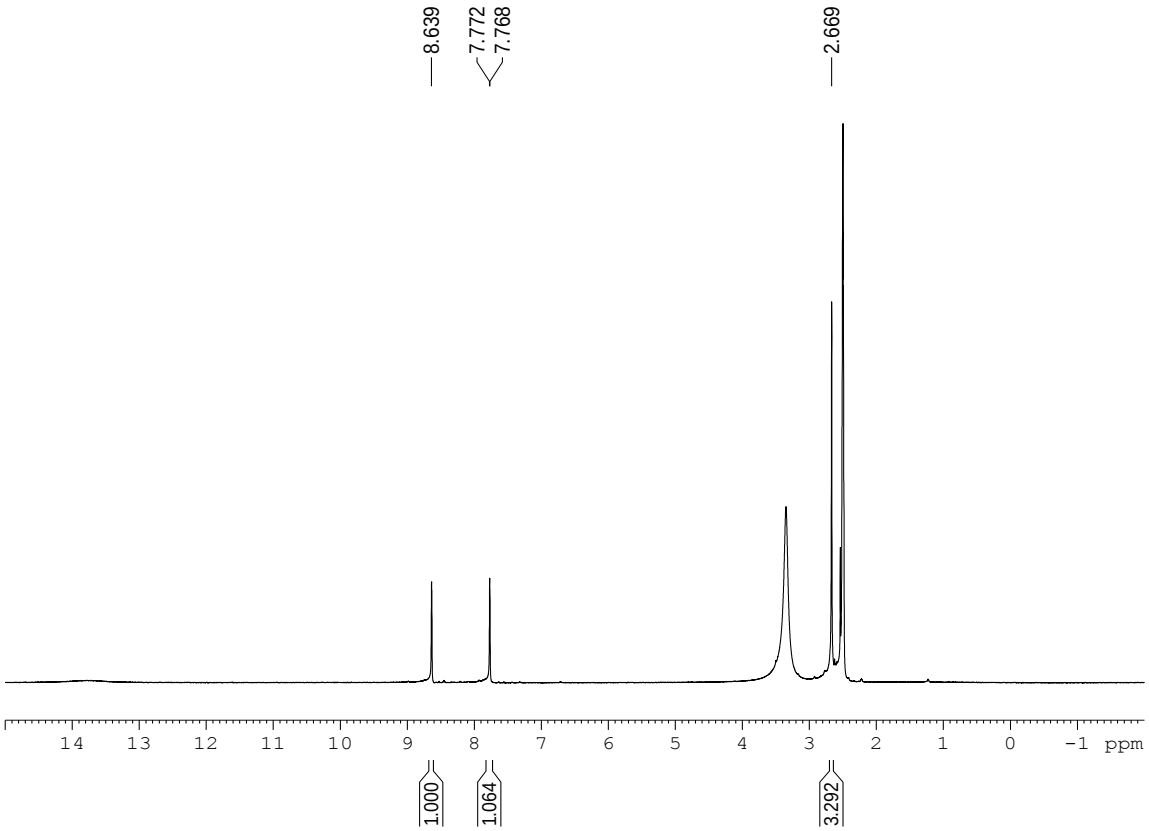

^{13}C {^{1}H} NMR (DMSO-d_6), 45

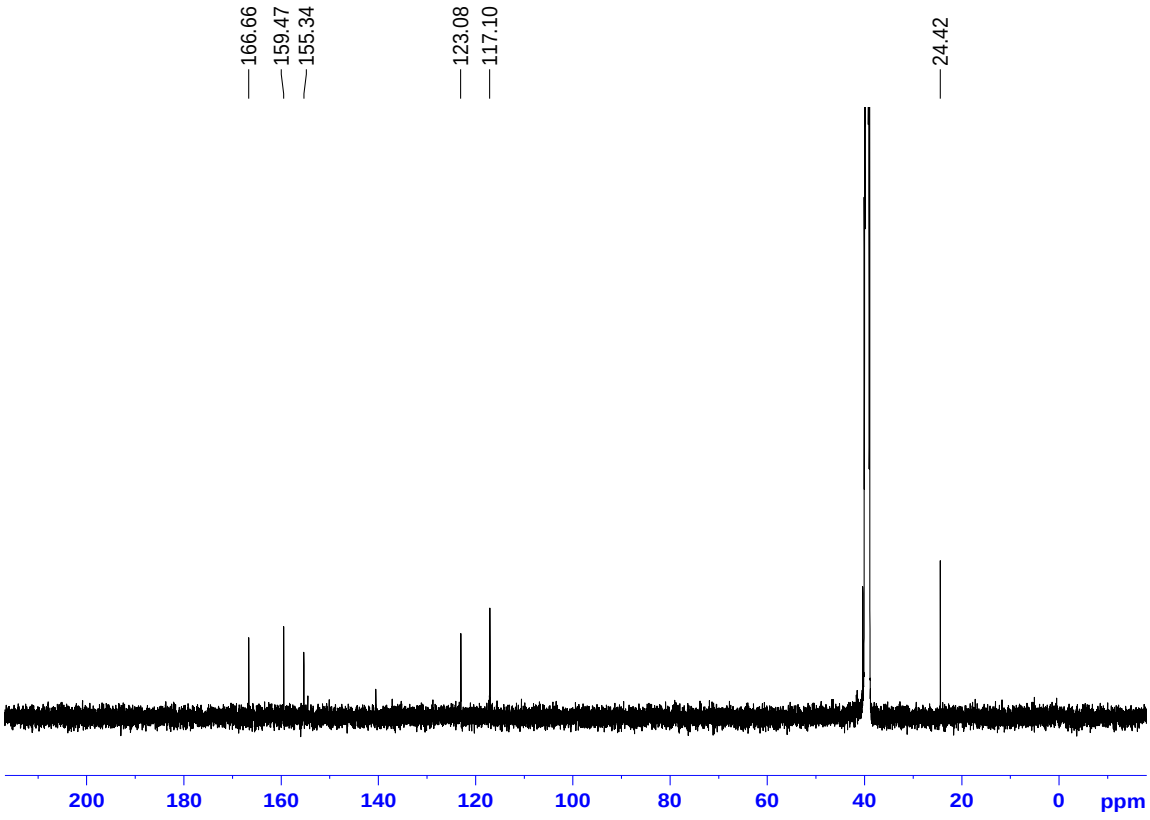

[Cu(6,6'-dimethyl-2,2'-bipyridine-4,4'-dicarboxylic acid)$_2$][Cl], 1

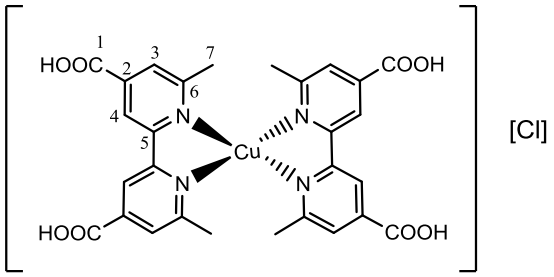

^{1}H NMR (CD_3OD), 1

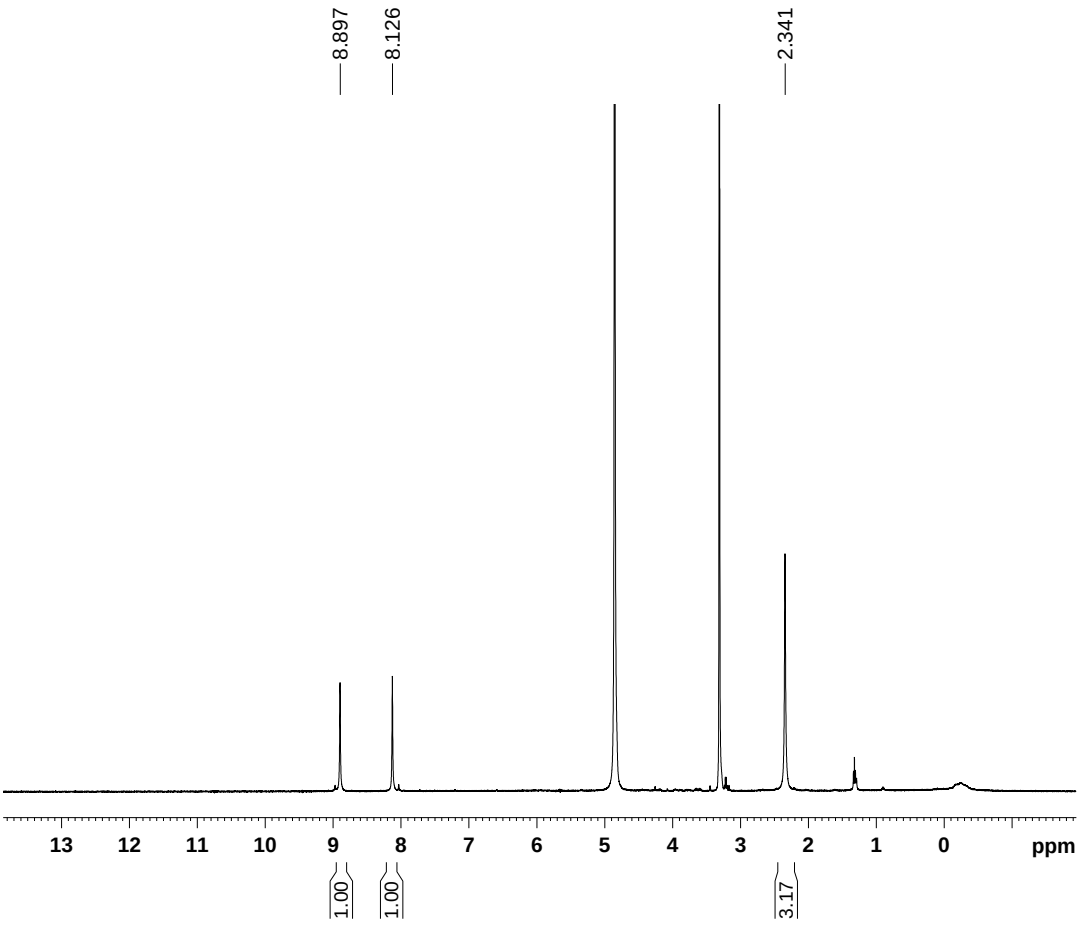

^{13}C {^{1}H} NMR (D_2O), 1

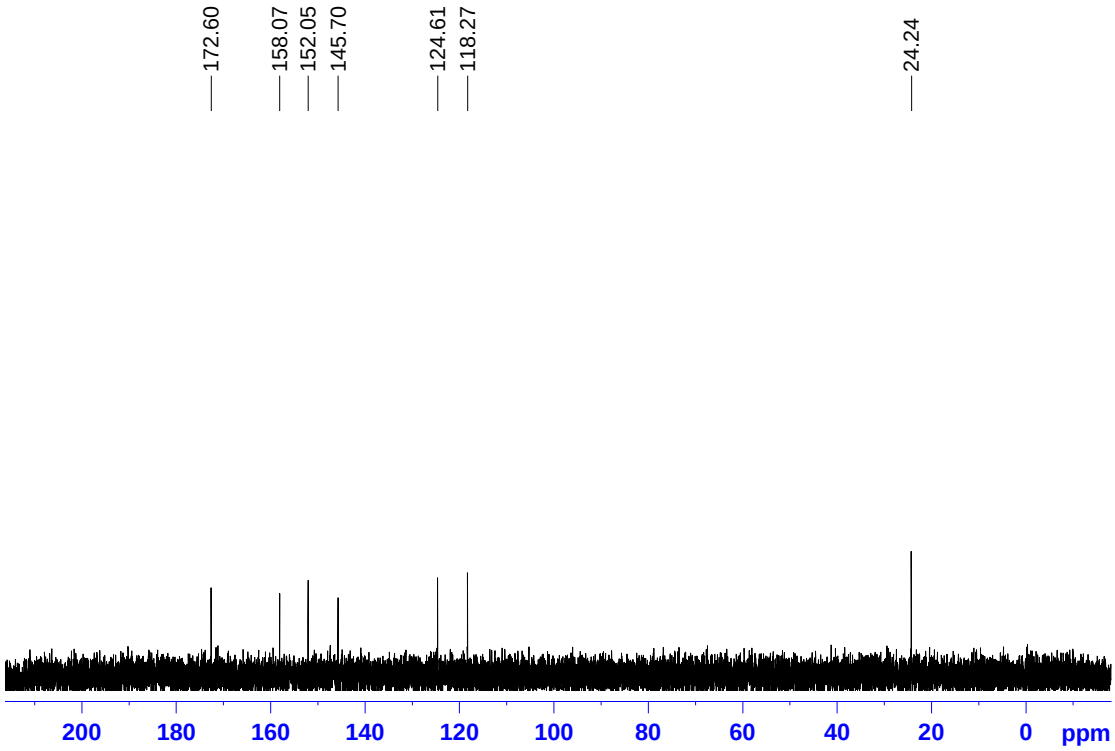

Appendix 2: Crystallographic data

Crystal data and structure refinement for compound **20**

Identification code	h13mdj03
Empirical formula	C188 H172 Cu4 N20 O40
Formula weight	3605.62
Temperature	150(2) K
Wavelength	0.71073 A
Crystal system, space group	monoclinic, C 2/c
Unit cell dimensions	a = 33.0460(13) A alpha = 90 deg. b = 13.2840(5) A beta = 116.035(2) deg. c = 22.9630(9) A gamma = 90 deg.
Volume	9057.5(6) A^3
Z, Calculated density	2, 1.322 Mg/m^3
Absorption coefficient	0.545 mm^-1
F(000)	3752
Crystal size	0.2 x 0.1 x 0.2 mm
Theta range for data collection	3.58 to 25.03 deg.
Limiting indices	-39<=h<=39, -15<=k<=15, -27<=l<=27
Reflections collected / unique	48089 / 7882 [R(int) = 0.1592]
Completeness to theta = 25.03	98.5 %
Refinement method	Full-matrix least-squares on F^2
Data / restraints / parameters	7882 / 3 / 627
Goodness-of-fit on F^2	1.103
Final R indices [I>2sigma(I)]	R1 = 0.0643, wR2 = 0.1444
R indices (all data)	R1 = 0.1009, wR2 = 0.1644
Largest diff. peak and hole	0.607 and -0.490 e.A^-3

Crystal data and structure refinement for compound **36**

Identification code	h12mdj13	
Empirical formula	C20 H16 N2 S2	
Formula weight	348.47	
Temperature	150(2) K	
Wavelength	0.71073 A	
Crystal system, space group	Monoclinic, $P2_1/n$	
Unit cell dimensions	a = 10.0680(16) A b = 4.6940(10) A c = 17.749(2) A	alpha = 90 deg beta = 91.419(9) deg gamma = 90 deg
Volume	838.5(2) A^3	
Z, Calculated density	2, 1.380 Mg/m^3	
Absorption coefficient	0.320 mm^-1	
F(000)	364	
Crystal size	0.10 x 0.10 x 0.05 mm	
Theta range for data collection	4.04 to 27.52 deg.	
Limiting indices	-12<=h<=12, -6<=k<=6, -22<=l<=23	
Reflections collected / unique	9707 / 1908 [R(int) = 0.0869]	
Completeness to theta = 27.52	99.3 %	
Absorption correction	Semi-empirical from equivalents	
Max. and min. transmission	0.9842 and 0.9687	
Refinement method	Full-matrix least-squares on F^2	
Data / restraints / parameters	1908 / 4 / 136	
Goodness-of-fit on F^2	1.054	
Final R indices [I>2sigma(I)]	R1 = 0.0590, wR2 = 0.1334	
R indices (all data)	R1 = 0.1241, wR2 = 0.1679	
Largest diff. peak and hole	0.231 and -0.392 e.A^-3	

Crystal data and structure refinement for compound **37**

Identification code	h12mdj17
Empirical formula	C20 H14 Br2 N2 S2
Formula weight	506.27
Temperature	150(2) K
Wavelength	0.71073 A
Crystal system, space group	Monoclinic, *C*2/*c*
Unit cell dimensions	a = 19.3180(9) A alpha = 90 deg. b = 10.5000(6) A beta = 97.703(3) deg c = 9.2850(4) A gamma = 90 deg.
Volume	1866.36(16) A^3
Z, Calculated density	4, 1.802 Mg/m^3
Absorption coefficient	4.574 mm^-1
F(000)	1000
Crystal size	0.15 x 0.10 x 0.10 mm
Theta range for data collection	4.12 to 27.52 deg.
Limiting indices	-25<=h<=24, -13<=k<=13, -12<=l<=12
Reflections collected / unique	16070 / 2132 [R(int) = 0.0825]
Completeness to theta = 27.52	98.8 %
Absorption correction	Semi-empirical from equivalents
Max. and min. transmission	0.6577 and 0.5470
Refinement method	Full-matrix least-squares on F^2
Data / restraints / parameters	2132 / 0 / 119
Goodness-of-fit on F^2	1.028
Final R indices [I>2sigma(I)]	R1 = 0.0382, wR2 = 0.0822
R indices (all data)	R1 = 0.0779, wR2 = 0.0963
Largest diff. peak and hole	0.575 and -0.730 e.A^-3

Appendix 3: Publications

K. A. Wills, H. J. Mandujano-Ramirez, G. Merino, D. Mattia, T. Hewat, N. Robertson, G. Oskam, M. D. Jones, S. E. Lewis and P. J. Cameron, *RSC Adv.*, 2013, 23361-23369.